UNIVERSITÉ DE SHERBROOKE
Faculté de génie
Département de génie civil

PUNCHING SHEAR BEHAVIOR OF INTERIOR SLAB–COLUMN CONNECTIONS REINFORCED WITH GFRP BARS UNDER LATERAL CYCLIC LOADING

COMPORTEMENT AU POINÇONNEMENT DE JONCTIONS DALLE-POTEAU INTÉRIEUR EN BÉTON RENFORCÉES AVEC DES ARMATURES EN PRFV SOUS CHARGEMENT LATÉRAL CYCLIQUE INVERSÉ

Thèse de doctorat
Spécialité : génie civil

Mohamed Ebrahem Mohamed Ebrahem ELADAWY
(Mohamed Eladawy)

A dissertation submitted in partial fulfilment
of the requirements for the degree of
Doctor of Philosophy
(Civil Engineering)

Sherbrooke (Québec) Canada

June 2019

MEMBRES DU JURY

Prof.Brahim BENMOKRANE

Directeur

Prof. Amir FAM

Évaluateur

Prof. Abdeldjelil BELARBI “DJ”

Évaluateur

Prof. Nathalie ROY

Rapporteur

Dedication to my father …

My father gave me the greatest gift anyone could give another person, he believed in me.

ABSTRACT

In North America and much of the world, fiber–reinforced–polymer (FRP) reinforcing bars have emerged as an innovative solution to overcome the corrosion problem in concrete structures. Most investigations in the past have focused mainly on the behavior under static–loading conditions, omitting seismic design. Therefore, the feasibility of using FRP as internal reinforcement in a completely reinforced–concrete (RC) structure immune to corrosion essentially pertains to its strength, stiffness, and deformation capacity to resist seismic loads, has become questionable. Nevertheless, no tests have been conducted yet on FRP–RC slab-column connections subjected to a combination of gravity and lateral reversed cyclic loads. It should, however, be pointed out that the current North American codes and guidelines [CSA S806 (2012) and ACI 440.1R (2015)] do not include any requirements concerning the nominal punching–shear strength, stiffness, or drift capacity of flat–plate structures reinforced with FRP bars under lateral reversed cyclic loading.

This has been the main impetus to conduct the first-ever experimental study on the punching–shear behavior of glass–FRP (GFRP) slab-column connections under the combination of gravity and quasi-static reversed cyclic loading to simulate seismic loading. In this research study, a total of nine full–scale interior slab-column connections were constructed and tested to understanding and assessing the seismic performance of GFRP–reinforced two–way slab-column connections. The specimens were tested through two phases. Phase I, focused on the two–way slabs without shear reinforcement and the main test variables were: (i) flexural–reinforcement type (GFRP and steel bars); (ii) the flexural–reinforcement ratio (1.06% and 1.51%); (iii) service gravity load intensity (dead load plus 30% of the live load and dead plus live load); and (iv) concrete compressive strength (NSC and HSC). Phase II focused on the impact of using GFRP stirrups as shear reinforcement around the slab-column connection on slab seismic performance. The test variables considered in Phase II were: (i) GFRP stirrups type (closed and spiral); (ii) GFRP stirrups distribution; and (iii) service gravity load intensity (dead load plus 30% of the live load and dead plus live load).

Based on the laboratory testing results, the punching–shear performances were evaluated in terms of cracking behavior, hysteretic response, connection stiffness, energy dissipation, and ductility index. The results revealed that all GFRP specimens achieved adequate punching strength and lateral deformation capacity against punching–shear failure during and after the reversed lateral cyclic load conditions. Consequently, GFRP reinforcing bars could be used effectively as reinforcement in slab-column connections subjected to gravity and reversed lateral cyclic loads. The GFRP–RC specimens achieved lateral inter-story drift capacities over 1.50% satisfying the limits in CSA A23.3 and ACI 421.3R. The GFRP–RC specimens also had adequate drift–ductility indices, dissipated energy, and connection stiffness. On the other hand, increasing the flexural reinforcement ratio or gravity–load intensity in GFRP–RC specimen without shear reinforcement significantly affected the performance of the slab-column connection subjected to reversed lateral cyclic loads. Using high–strength concrete (HSC) in GFRP–RC specimen without shear reinforcement enhanced the slab' punching resistance.

Provision of shear reinforcement around slab-column connections was proved to be an efficient means in enhancing the overall connections' seismic performance. The GFRP stirrups, either closed or spiral, could be used effectively as shear reinforcement in the concrete slab-column connections reinforced with GFRP bars and subjected to gravity and reversed lateral cyclic loads. All GFRP–RC specimens with GFRP shear reinforcement achieved a high lateral drift of 4.0% to 7.50% with the ability to sustain the gravity load. Moreover, the specimens with shear reinforcement displayed softer punching shear failure with a gradual decrease in the lateral loads and maintained its integrity. The findings of this study will support the work of the North American technical committees engaged in developing standards and design provisions for GFRP–RC slabs subjected to lateral reversal cyclic loading.

Keywords: Concrete slab-column connection; Glass FRP (GFRP) reinforcement, Seismic loading; Lateral reversed cyclic loading, GFRP shear reinforcement; Punching shear; Connection stiffness; Energy dissipation; Drift–ductility index; Design codes; and High–strength concrete.

RÉSUMÉ

En Amérique du Nord et dans une grande partie du monde, les barres d'armature en polymère renforcé de fibres (FRP) sont devenues une solution innovante pour résoudre le problème de la corrosion dans les structures en béton. Dans le passé, la plupart des études ont principalement porté sur le comportement sous charges statiques, en omettant le calcul sismique. Par conséquent, la possibilité d'utilisation des PRF comme armatures internes dans une structure en béton armé exempte de corrosion, essentiellement sur la base de leur résistance, de leur rigidité et de leur capacité de déformation à résister aux charges sismiques n'a été que très peu explorée. En particulier, aucun essai n'a encore été réalisé sur les jonctions dalle-poteau en béton sous une combinaison de charges de gravité et de charges latérales cycliques inversées. Il convient toutefois de souligner que les codes et guides nord-américains en vigueur [CSA S806 (2012) et ACI 440.1R (2015)] ne prévoient aucune exigence concernant la résistance nominale au poinçonnement, la rigidité ou la capacité de déplacement latéral relatif des planchers-dalles en béton armé de PRF sous chargement cyclique latéral inversé.

Cela a été la principale motivation pour mener la toute première étude expérimentale sur le comportement au poinçonnement de jonctions dalle-poteau en béton armé de barres en polymère renforcé de fibres de verre (PRFV), sous la combinaison de charges de gravité et de charges cycliques inversées quasi statiques, pour simuler un chargement sismique. Dans la présente étude, un total de neuf (9) jonctions dalle-poteau intérieur pleine grandeur ont été fabriquées et testées pour étudier et évaluer la performance sismique des jonctions dalle bidirectionnelle-poteau en béton armé avec des armatures en PRFV. Les spécimens ont été testés en deux phases. La phase I comportait les dalles bidirectionnelles sans armatures de cisaillement et les principaux paramètres de l'essai étaient les suivants:(i) le type d'armature de flexion (barres d'armature en acier et en PRFV) (ii) le taux d'armature en flexion (1,06% et 1,51%) (iii) l'intensité de la charge de gravité en service (charge morte plus 30% de la charge vive ou une combinaison de charges morte et vive), et (iv) la résistance à la compression du béton (béton de résistance normale et béton à haute résistance). La phase II a porté sur l'effet

de l'utilisation d'étriers en PRFV comme armature de cisaillement autour de la jonction dalle-poteau sur la performance sismique des dalles. Les paramètres d'essai pris en compte dans la phase II étaient les suivants: (i) le type d'étriers en PRFV (fermé et en spirale), ii) la distribution des étriers en PRFV, et (iii) l'intensité de la charge de gravité en service (charge morte plus 30% de la charge vive ou une combinaison de charges morte et vive).

Sur la base des résultats des essais en laboratoire, les performances au poinçonnement ont été évaluées suivant le comportement à la fissuration, la réponse hystérétique, la rigidité de la jonction, la dissipation d'énergie et l'indice de ductilité du déplacement relatif. Les résultats ont montré que tous les spécimens en PRFV avaient une résistance et une capacité de déformation suffisantes face à la rupture par poinçonnement, pendant et après le chargement latéral cyclique inversé. Par conséquent, les barres d'armature en PRFV pourraient être utilisées efficacement comme armatures dans les jonctions dalle-poteau soumises à des charges de gravité et aux charges cycliques latérales inversées. Les spécimens en béton armé de PRFV ont atteint un déplacement relatif latéral inter étage au-delà de 1,50%, satisfaisant ainsi les limites définies dans la norme CSA A23.3 et dans le guide ACI 421.3R. Les spécimens en béton armé de PRFV présentaient également des indices de ductilité du déplacement relatif, une dissipation d'énergie et une rigidité de jonction adéquats. D'autre part, l'augmentation du taux d'armature en flexion ou de la charge de gravité dans un spécimen en béton armé de PRFV sans armatures de cisaillement a considérablement affecté les performances de la jonction dalle-poteau, soumise à des charges cycliques latérales inversées. L'utilisation de béton à haute résistance dans un spécimen en béton armé de PRFV sans armatures de cisaillement a nettement amélioré les performances de la dalle.

La disposition d'armatures de cisaillement autour des jonctions dalle-poteau a été un moyen efficace pour améliorer les performances sismiques globales des jonctions. Les étriers en PRFV, fermés ou en spirale, pourraient être utilisés efficacement comme armatures de cisaillement dans les jonctions dalle-poteau en béton armé de PRFV, et soumises aux charges de gravité et aux charges cycliques latérales inversées. Tous les spécimens avec des étriers en PRFV ont présenté des déplacements relatifs latéraux élevés de 4,0% à 7,50% avec une capacité de supporter la charge de gravité. De plus, les spécimens avec armatures de cisaillement en PRFV présentaient une rupture flexible par poinçonnement, et une diminution progressive des charges latérales et un maintien de leur intégrité. Les résultats de cette étude appuieront les

travaux des comités techniques nord-américains chargés d'élaborer les normes et les dispositions de calcul des jonctions dalle-poteau en béton armé de PRFV, soumises à une charge cyclique latérale inversée.

Mots clés: Jonction dalle-poteau, armatures en polymère renforcé de fibre de verre (PRFV), chargement cyclique latéral inversé, armature de cisaillement en PRFV, poinçonnement, rigidité de jonction, dissipation d'énergie, indice de ductilité du déplacement relatif.

Acknowledgement

First, I would like to praise Allah for His bounty He blessed me with that; He gave me the ambition, ideas, strength and endurance to go through all difficulties and achieve this work. I hope He blesses this work as an ongoing charity and a beneficial knowledge for humanity.

My warmest appreciation and deepest gratitude are due for my research advisor and dissertation committee chair Prof. **Brahim Benmokrane**. He provided invaluable advising throughout the years of this study. His deep yet very broad knowledge, continuous encouragement and support, inspiring ideas, keen supervision and meticulous revisions tremendously helped me achieve this work. I learned a lot through my rich experience with him on the academic, professional and personal levels.

Truly grateful to the Natural Science and Engineering Research Council of Canada (**NSERC**), Canada Research Chair Program, the Fonds de la recherche du Quebec–Nature et Technologie – (**FRQ–NT**) for their financial support, and Pultrall Inc. (Thetford Mines, QC, Canada) for the provided generous of the FRP materials.

My sincere appreciation is due for Prof. Benmokrane research group and technical staff at Sherbrooke University who provided valuable input through our fruitful discussions in this project. I would like to extend my special thanks to all my friends and colleagues at Sherbrooke University for their support and assistance throughout the years. Special thanks to **Ibrahim Lashin** for his support and valuable friendship.

Finally, I would like to express my sincere love and warmest gratitude to my beloved family; my great parents and my brothers. Their continuous support, encouragement and prayers greatly helped me achieve this work. I am especially grateful for **Alaa**'s love, patience and accommodation of a very busy father throughout the years of demanding studies at Sherbrooke University.

TABLE OF CONTENTS

LIST OF TABLES

LIST OF FIGURES

NOTATIONS

Δ_e	Virtual lateral deflection
Δ_y	Lateral deflection at yield point of steel bars
A_f	The total area of the reinforcing bars in one direction
A_{fv}	The cross-sectional area of the FRP shear reinforcement at a perimeter of 0.5d from column face
Ag	Gross cross-sectional area
b_1	The width of the critical section for shear measured in the direction of the span for which moments are determined
b_2	The width of the critical section for shear measured in the direction perpendicular to b_1
b_o	The perimeter of shear-critical section
d	Effective slab depth
d_b	Bar diameter
e	Distance from column centerline to the edge of the critical section
E_f	Modulus of elasticity of FRP reinforcement
E_{fv}	Modulus of elasticity of FRP stirrups, the straight portion
$f_c^{'}$	Concrete compressive strength
f_{fu}	The ultimate tensile strength of FRP bars
f_{fv}	The ultimate tensile strength of the straight portion of FRP stirrups
f_{fvb}	The ultimate tensile strength of FRP stirrups at the bend location
J_x	Polar moment of inertia of the critical shear perimeter
k	The ratio between the depth of neutral axis and reinforcement depth
M_n	The ultimate unbalanced moment at the centroid of critical shear section
n_f	The ratio between modulus of elasticity of FRP bars and modulus of elasticity of concrete
r_b	The radius of the bend
S	The spacing between the shear stirrups
V_c	Ultimate punching shear capacity provided by the concrete

v_c	Ultimate punching-shear stress provided by the concrete
v_{sf}	Ultimate punching-stress provided by the FRP shear reinforcement
V_u	The applied shearing force at failure
v_u	The maximum shear stress at critical section due to the applied force
α_s	Dimensionless coefficient equal to 4.0 for interior columns
β_c	The ratio of the long side to the short side of the column
δ	Lateral–drift ratio
$\delta_{0.8u}$	Lateral–drift ratio at 20% loss of ultimate lateral strength
δ_e	Virtual lateral–drift ratio
δ_u	Ultimate lateral–drift ratio
δ_y	Lateral–drift ratio at yield point of steel bars
ε_{fu}	Ultimate tensile strain for FRP bar
ε_y	Yield strain of steel bars
λ	Concrete density factor (1.0 for normal weight concrete)
μ_δ	The drift ductility index
ρ_b	Balanced reinforcement ratio
ρ_f	Reinforcement ratio of FRP longitudinal bars
ρ_{fv}	Shear reinforcement ratio at a perimeter at $0.5d$
Υ_v	The fraction of unbalanced moment transferred by eccentricity
ϕ_c	Concrete resistance factor

CHAPTER 1. INTRODUCTION

1.1. General Background

Two–way concrete floor systems are extensively used in numerous types of structures. Two–way concrete slabs can be assorted into two categories; slabs that are supported on beams, and slabs that are supported on columns without any beam. The beamless slabs can be further subdivided into two categories: flat slabs, which are supported on columns through a drop panel or column capital, and flat plates, which are supported directly on the columns **Figure 1.1**. Flat slab/plate buildings are one of the most widely used floor systems for offices, industrial buildings and parking garages due to their financial and functional advantages. A flat slab is a structural system with thickenings in the slab at the columns and load-bearing walls called drop panels or column capitals, that's act as T–beams over the supports which increase the shear capacity and the stiffness of the floor system under vertical loads, thus increasing the economical span range. The flat plate is a structural system consists of a slab with uniform thickness supported directly on or loadbearing walls.

Figure 1.1 Common Types of the beamless slabs.

The main advantages of flat–plates are increased clear floor height and reduce total height and weight of the structure, also easy to construct and they comparatively require a lower amount of labour and formwork, on the other hand, it considered as an architecturally favourable slab system due to the absence of beams. So flat plate construction is a very desirable structural system in view of the economy, construction, and architectural desires.

Regardless of the construction advantages of flat plates, structural engineers must consider two major problems during the design of flat plate systems: (i) large deflections at mid-span of the slabs and (ii) punching shear failure at slab-column connections. The previous problem is often associated with long–span slab systems, in which the slab thickness is designed to be relatively thin to lower the self–the weight of slabs. The reduction in slab thickness, on the other hand, reduces the flexural stiffness of slab systems, and thus, increases vertical deflections at mid-span. To deal with this issue, prestressing methods are often used to control the vertical deflections of slabs. The other problem associated with flat plate systems is more complicated. Punching failure, or two–way shear failure, is associated with a particular collapse mechanism in which the column together with an attached portion of the slab pushes through the surrounding slab **Figure 1.2**.

Figure 1.2 Punching shear failure of parking garage Smiths City, New Zealand, 2011.

The possibility of punching shear failure at slab-column connections is higher when lateral forces, due to wind or earthquake loadings, cause substantial unbalanced moments to be transferred between the slab and the column. Punching failure can be classified as a shear dominant brittle type of failure. Because of its brittle nature, it becomes almost impossible to inspect typical warnings on the structural components prior to failure. Once this happens the slab falls onto the next lower floor where the extra loading is magnified by dynamic effects. In short, a punching shear failure in one connection can lead to the progressive collapse of an entire structure.

In most multi-story reinforced concrete buildings, shear walls or other core structures specifically designed for that purpose resist lateral loads due to the wind and particularly earthquake. The remaining structural elements are then designed only for gravity loads;

however, during an earthquake event these elements must be able to sustain lateral drift. In flat–slab buildings during an earthquake, the horizontal movement of the ground induces large horizontal inertia forces and lateral drifts in the buildings. The reversed displacements make the slab-column connection rotate and produce unbalanced moments in the connection around the column area. A portion of this unbalanced moment is transferred as shear to the slab in the joint region **Figure 1.3**. Since the ultimate strength of flat–slab buildings is frequently governed by the shear or punching capacity of the slab-column connection, an increase in shear due to lateral drift will likely reduce the shear capacity available for gravity loads.

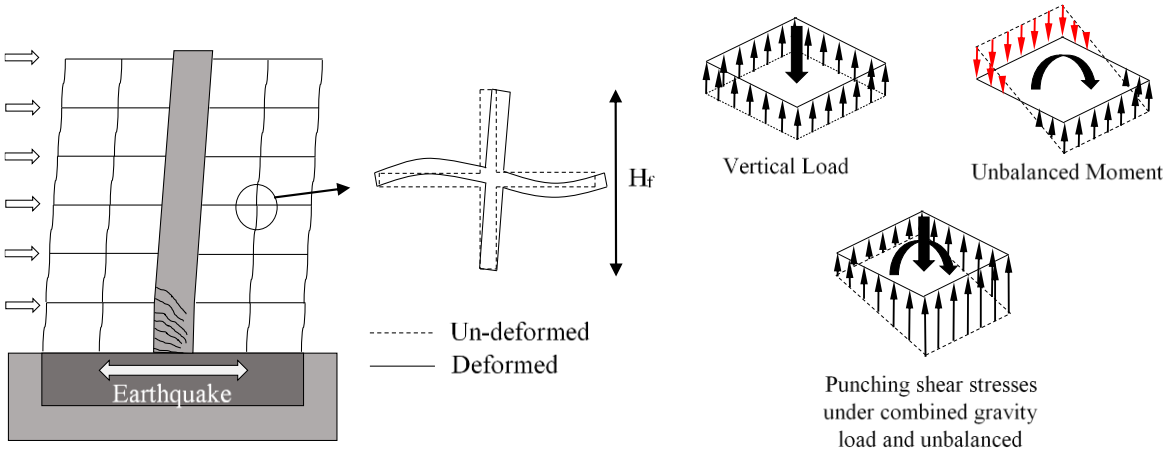

Figure 1.3 Horizontal inertia forces and lateral drifts in the buildings.

Consequently when the flat plate structural systems are employed in seismic zones, it is recommended to combine it with primary lateral force–resisting structural elements such as moment–resisting frames or shear walls. In this case, the slab–column connections must possess adequate strength against punching shear failure during and after the earthquake occurrence and adequate ductility to undergo inelastic deformations without failure, that is, the ability to undergo a specified minimum lateral inter-story drift ratio. In other words, the flat plate system must have adequate residual punching shear resistance to gravity loads after a severe earthquake.

A significant research effort over the last years has shown that fiber–reinforced polymer (FRP) reinforcing bars can be effectively used as an alternative to the steel bars in reinforced concrete structures, particularly where steel corrosion is a major concern. FRPs are not only corrosion–free and nonmagnetic materials with high strength–to–weight ratios but also their attractiveness

of usages as a kind of smart reinforcement for a reinforced concrete structural member. The concrete slabs are the most vulnerable component structural element to corrosion deteriorations because of the direct exposure to high concentration of chlorides used for snow and ice removal. Using FRP bars in reinforced concrete slabs especially for parking garages can extend the lifetime serviceability, reduce maintenance costs, and improve life–cycle cost efficiency. Moreover, FRP bars may also reduce construction costs by eliminating the need for waterproofing membranes and pavement items [Benmokrane et al. (2006)].

To date, considerable research efforts have conducted to better understand the punching shear behaviour of FRP–RC slab under concentric loading. However, to date, no research has investigated the punching shear behaviour of FRP–RC slab–column connection under seismic loading. Furthermore, using FRP as shear reinforcement in FRP–RC two–way slabs have not fully investigated. The current codes and guidelines do not include any requirements concerning the nominal punching shear strength, stiffness, and drift capacity of flat plate structures reinforced with FRP bars and shear reinforcement under cyclic lateral loading. Therefore, in order to produce a safe design for FRP–RC flat plate structure system with and without FRP shear reinforcements, these critical issues should be examined.

1.2. Research Objectives and Originality

GFRP reinforcing bars have recently gained wide acceptance as an attractive alternative to steel reinforcement in concrete structures. Because of a distinct lack of experimental evidence on flat plate connections reinforced with GFRP bars and GFRP stirrups under simulated seismic loads, ACI 440.1R and CSA S806 do not include any requirements or design guidance of such GFRP connections subjected to lateral loads. This study presents pioneer test results for full–scale interior slab-column connections reinforced with GFRP bars subjected to gravity and cyclic lateral loads. The performance of the connections in terms of strength, stiffness, drift capacity, energy dissipation, and ductility index were evaluated. Study of the data enabled identification of the most important parameters and the impact of each parameter on the performance. The research also contributed to the development of design recommendations for GFRP–RC slab-column connections subjected to lateral displacements induced by earthquakes while carrying gravity loads.

The main objectives of this research can be summarized as follows;

i. Investigate the punching shear behaviour of interior slab-column connection reinforced with GFRP bars without and with GFRP stirrups as shear reinforcement under lateral cyclic loading.
ii. Estimate the effect of the different parameters on the strength, stiffness, deformability, and drift capacity of the test specimens;
iii. Examine the current design equations provided by ACI 440.1R–2015 and CSA S806–2012 for FRP reinforced concrete two–way slabs under lateral cyclic loading.
iv. Establish design recommendations for designing a flat plate structure system reinforced with FRP bars without and with shear reinforced under lateral cyclic loading.

The specific objectives of this research

i. Assess the effect of type of the reinforcing bars (GFRP and steel) and GFRP flexural reinforcement ratio on the behaviour of slab-column connections.
ii. Evaluate the effect of concrete strength (normal and high–strength concrete) on the behaviour of slab-column connections.
iii. Assess the effect of service gravity load intensity on the behaviour of GFRP–reinforced slab-column connections with and without FRP shear reinforcement.
iv. Evaluate the effect of GFRP stirrups (closed and spiral) as shear reinforcement on the strength and behaviour of slab-column connections.
v. Investigate the effect of GFRP stirrups distribution on the punching shear strength of GFRP–reinforced slab-column connections.

1.3. Research Methodology

To achieve the main and specific objectives, the pioneer experimental program was conducted. The experimental program includes designing, preparing, constructing and testing of nine full–scale specimens represent interior slab-column connection divided into two phases. Phase I comprised five slab-column connection without shear reinforcement and reinforced with steel and GFRP bars. Different parameters are addressed such as (i) type of reinforcement (steel and GFRP), (ii) GFRP–flexural reinforcement ratio, (iii) gravity load intensity and (v) concrete compressive strength (NSC and HSC). Phase II comprised four GFRP–RC slab-column

connection with GFRP–stirrups as shear reinforcement. The effects of the following parameters were investigated: (i) stirrups extension, (ii) stirrups type (closed or spiral); and (iii) gravity load intensity. All test specimens were identical and measured 2500×2500 mm with a thickness of 200 mm. A column measuring 300 mm×300 mm measuring extended 700 mm at its centre above and below the slab surfaces. The slabs were simply supported on a 2000×2000 mm perimeter on the bottom face of the slab. These dimensions were chosen to represent the locations of lines of contra–flexure. All specimens were tested to failure under combined constant gravity load and quasi-static revered lateral cyclic loading. Also, the validity of the punching shear design equations as specified in [ACI 440.1R–15 (2015)] and [CSA S806–12 (2012)] under cyclic lateral loads were examined.

1.4. Organization of the Dissertation

- **Chapter 1:** provides an outline of the thesis with a brief description of the contents of each chapter
- **Chapter 2:** presents a literature review of relevant work concerning reinforced concrete two–way interior slab-column connections. First, the main research on steel–reinforced two–way interior slab-column connections. Then, and the recently conducted experimental research on GFRP–RC two–way interior slab-column connections are reviewed.
- **Chapter 3:** describes the experimental program of the thesis in details. It presents the geometry and reinforcement details of the test specimens including the fabrication procedure of the specimens. Description of the instrumentation and testing procedure is given as well. In addition, detailed characteristics of the used materials are provided.

The subsequent three chapters respectively correspond to three technical Articles that have submitted for publication in scientific journals

- **Chapter 4:** (Article No. I – Accepted) “Experimental Study of Interior GFRP-RC Slab-Column Connections under Lateral Cyclic Load” *ACI Structural Journal*. Presents the experimental testing results in terms of failure modes, cracking patterns, hysteretic response, connection stiffness, energy dissipation, and drift-ductility index with taking

into consideration the effects of reinforcing-bar type; GFRP flexural-reinforcement ratio, and gravity-load intensity.

- **Chapter 5:** (Article No. II – submitted) "Cyclic Testing of Interior Two–Way Slab-Column Connections Reinforced with GFRP Bars" *ASCE Journal of Composites for Construction*. Presents the laboratory results of an experimental program to investigate the seismic performance of two-way GFRP-reinforced specimens taking into consideration the effects of the reinforcing-bar type (GFRP or steel), concrete compressive strength, and using GFRP closed stirrups as shear reinforcement.
- **Chapter 6:** (Article No. III – submitted) "Effect of Stirrups on Punching Behavior of GFRP–RC Slab-Column Connections under Lateral Cyclic Load" *ASCE Journal of Structural Engineering*. Presents experimental investigation to assess the effect of GFRP stirrups type (closed and spiral), stirrup extension, and the impact of service gravity load intensity on the punching–shear behavior of GFRP–RC slab–column connections with FRP shear reinforcement under the combination of gravity and lateral reversed cyclic loading.
- **Chapter 7:** presents the thesis summary, conclusions, and recommendation for future research.

Also, further details regarding the analysis and the design of the tested specimens are presented in two appendices (Appendix A & B).

CHAPTER 2. LITERATURE REVIEW

2.1. Punching Shear Failure Mechanism

2.1.1. In the case of slabs without transverse reinforcement

The punching shear failure is characterized by low stresses in the longitudinal reinforcement and the development of a diagonal crack with variable inclination, starting from the root of the column to the tension face of the slab as shown in **Figure 2.1**. The inclination of the failure surface is dependent on the geometry of the member (depth, slenderness, column dimension to slab thickness) and the characteristics of the structural parameters (material strengths, aggregate distribution, dimension, reinforcement layout etc.). After the diagonal tension cracking has occurred in the vicinity of the critical section of the slab around the perimeter of the load area, the slab carries the shear forces by shear across the compression zone, aggregate interlock, and dowel action. However, once two–way bending occurs, the nominal ultimate shear stress that can be developed in a slab at the assumed critical section is much higher than in a beam. This increase in punching shear strength of slabs is due to the three–dimensional.

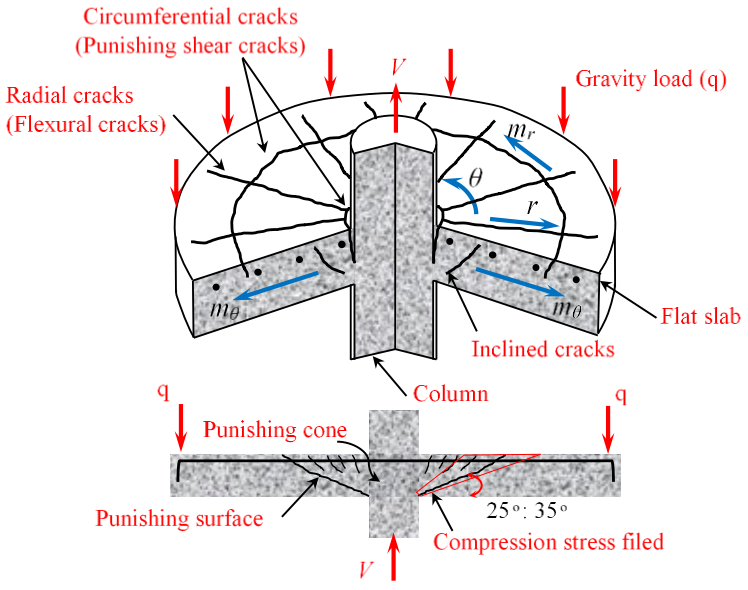

Figure 2.1 Typical cracks at interior slab-column connections.

When the load is applied to the slab, the first crack to form is a roughly circular tangential crack around the perimeter of the loaded area due to the negative bending moments in the radial direction. Radial cracks then extend from that perimeter due to negative bending moments in the tangential direction. Because the radial moment decreases rapidly away from the loaded area, a significant increase in load is necessary before tangential cracks form around the load area some distance out in the slab. The diagonal tension cracks that developed in the slab tend to originate near mid-depth and therefore more similar to the web–shear cracks than to flexural–shear cracks [Park et al. (2000)]. Test results by Kinnunen et al. (1960) reported that the first shear crack opened up at a load which ranged from 45 to 75 % of the ultimate load. In most cases, only radial cracks were observed in the slab portion situated outside the shear crack. At higher loads, some tangential cracks forming circles around the column develop. The final punching failure occurs suddenly as a result of the propagation of the outermost tangential crack.

2.1.2. In the case of slabs with transverse reinforcement

The efficacious solution to enhance ductility and punching shear strength of slab-column connections is to use shear reinforcement in the slab in the vicinity of columns [Hawkins et al. (1974)]. In order to reach yield, and therefore be fully effective, shear reinforcement has to be well–anchored. Deformations at failure in slabs with well-anchored shear reinforcement are two to three times greater than slabs without shear reinforcement [Regan et al. (1985)]. The principal effect of shear reinforcement is to restraint the discontinuity of the slab at the shear crack, so that rotation is concentrated to the vertical crack at the face of the column [Sherif (1996)]. While after the development of inclined shear cracks, the shear reinforcement transfers most of the forces across the shear cracks and delays further widening. This, in turn, increases the punching–shear and deformation capacity of the slab [Rizk et al. (2011)].

Design of slabs with shear reinforcement typically considers several potential failure modes:

i. Crushing of compression struts (see **Figure 2.2 (a)**). This failure mode becomes governing for high amounts of bending and transverse reinforcement, where large compressive stresses develop in the concrete near the column region. Crushing of concrete struts limits thus the maximum strength that can be provided by a shear

reinforcing system. This is instrumental for design as it determines the applicability of such systems with respect to the effective depth of the slab and size of the support region.

ii. Punching within the shear–reinforced zone (see **Figure 2.2 (b)**). Such failure develops for moderate or low amounts of shear reinforcement when a shear crack localizes the strains within the shear–reinforced zone. Shear strength is thus governed by the contribution of concrete and of the transverse reinforcement. For design, this failure mode is used to determine the amount of shear reinforcement to be arranged.

iii. Punching outside the shear–reinforced zone (see **Figure 2.2 (c)**), this failure mode may be governing when the shear–reinforced zone extends over a small region. A check of this failure mode is typically performed in design to determine the extent of the slab to be shear reinforced.

iv. Delamination of the concrete core (see **Figure 2.2 (d)**), when the shear reinforcement is not enclosing the flexural reinforcement, delamination of the concrete core may occur. This leads to a rather ductile failure mode but with limited strength and with loss of development on the flexural reinforcement. Typical detailing provided in codes of practice avoids the use of shear reinforcement systems leading to such failure mode.

v. Flexural yielding (see **Figure 2.2 (e)**), slabs with low flexural reinforcement ratios and with sufficient transverse reinforcement can fail by the development of a flexural plastic mechanism. Bending strength and not punching shear strength is thus governing for the strength of the slab.

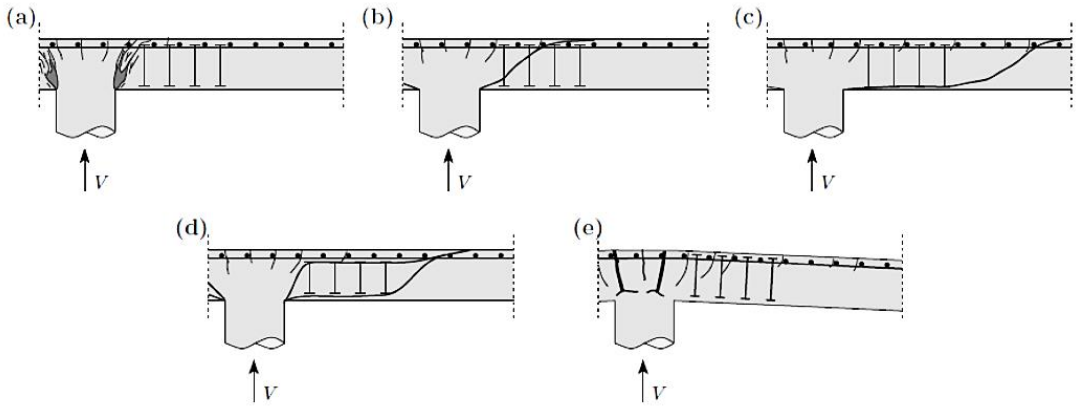

Figure 2.2 Failure modes in flat slabs.

2.2. Punching Shear Strength of Slab-Column Connections Reinforced with FRP Bars or Grids

Significant research efforts over the past years have shown that fibre–reinforced polymer (FRP) reinforcing bars can be used effectively as an alternative to the steel bars in RC structures, particularly where steel corrosion is a major concern. FRPs are corrosion–free and nonmagnetic materials with high strength–to–weight ratios, in addition to their possibility to provide embedded microwire sensors into the matrix (used as a kind of "smart" reinforcement) [Komová et al. (2008)], makes them an alternative reinforcement for concrete structures. Using FRP reinforcing bars in reinforced concrete two–way slabs such as in parking garages, the most component structural element vulnerable to corrosion deteriorations because of the direct exposure to high concentration of chlorides used for snow and ice removal, can extend the lifetime serviceability, reduce maintenance costs, and improve life-cycle cost efficiency. Moreover, FRP bars may also reduce construction costs by eliminating the need for waterproofing membranes and pavement items [Benmokrane et al. (2006)]. The FRP mechanical properties have a brittle linear elastic response (see **Figure 2.3)**, a lower modulus of elasticity, and different bond characteristics than that of steel reinforcement, which results in differences in the punching–shear behaviour.

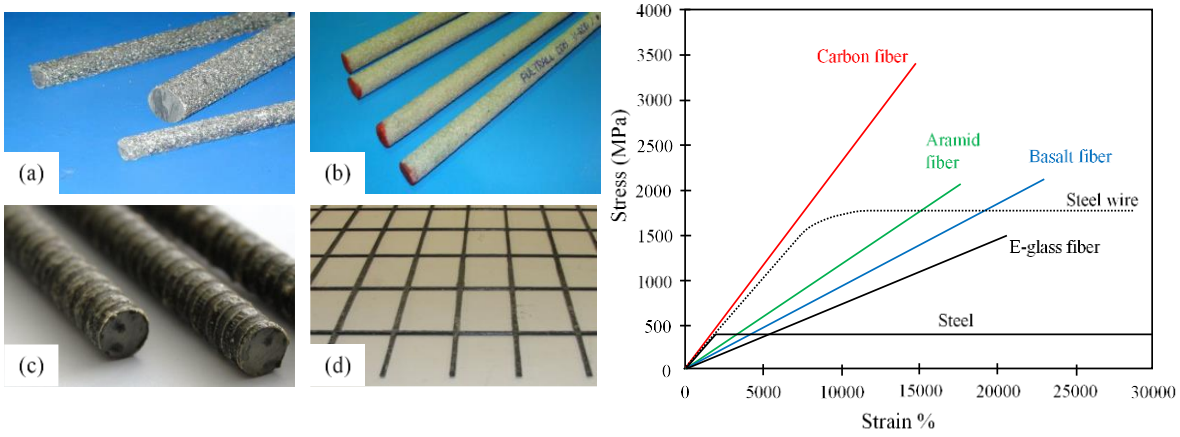

Figure 2.3 Various types of FRP bars and grids; (a) CFRP; (b) GFRP; (c) BFRP; (d) CFRP and Stress-strain curve of various FRP bars.

Numerous studies were conducted to evaluate the punching–shear behaviour of FRP bars and/or grids in RC two–way slabs reinforced with and without shear reinforcement [Matthys and Taerwe, (2000 I & II); El–Ghandour et al. (2003); Zaghloul (2004–2007); Lee et al. (2009), Hassan et al. (2013); Gouda et al. (2015) and Hussein et al. (2018)]. Through these investigations, it was demonstrated that the difference in mechanical properties and bond characteristics between FRP and steel reinforcement significantly affect the slab behavior and strength. This results in the development of wider and deeper cracks. Deeper cracks decrease the contribution to shear strength from the uncracked concrete due to the lower depth of concrete in compression. Wider cracks, in turn, decrease the contributions from aggregate interlock and residual tensile stresses. Additionally, due to the relatively small transverse strength of FRP bars and relatively wider cracks, the contribution of dowel action may be negligible [El–Gamel et al. (2005 b)]. Besides, given the difference in mechanical properties, the punching–shear equations for steel–RC flat slabs cannot be directly employed for FRP–RC sections.

Matthys and Taerwe (2000– I & II) investigate the punching shear behavior of two way concrete slabs reinforced FRP grid. A total of seventeen punching tests have been performed on square slabs with a side length of 1000 mm and a total slab thickness of 120 or 150 mm. The square concrete slabs were tested in a vertical position according to the test setup presents in **Figure 2.4**. All slabs were simply supported by eight supports arranged in a circular pattern with a diameter of 0.9 m and the load was applied concentrically with a circular steel loading plate as shown. The investigated parameters were flexural reinforcement ratio, slab thickness, and loaded area. The specimens were divided into three series: the first series had four specimens reinforced with S500 steel mesh (the reinforcement ratio "ρ" ranged between 0.58% to 1.79%); the second series had eight specimens reinforced with different types of CFRP grids (the reinforcement ratio "ρ" ranged between 0.19 to 1.05%); and the third series had five specimens reinforced with a hybrid type of FRP comprising glass and carbon FRP (the reinforcement ratio "ρ" ranged between 0.62% to 3.76%).

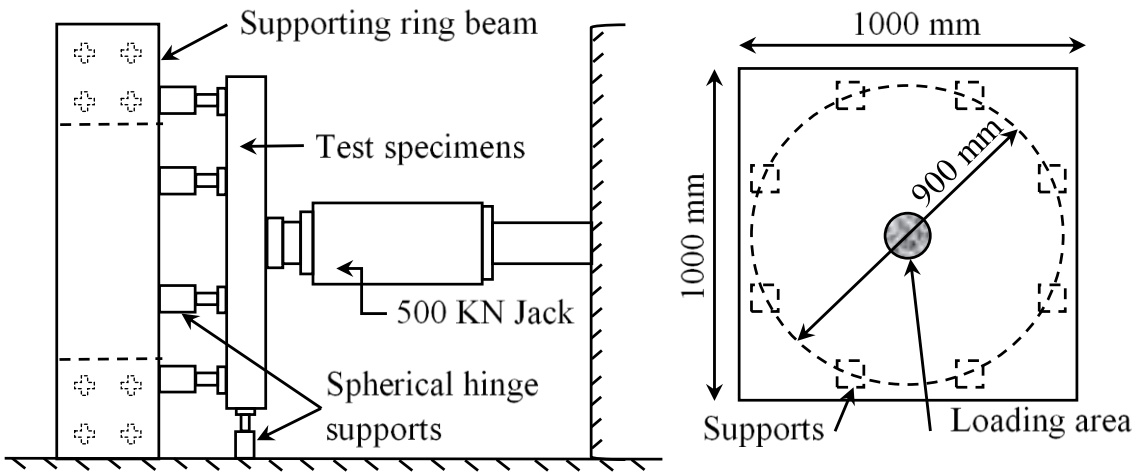

Figure 2.4 Test setup.

The test results revealed that there is a strong interaction between shear and flexural effects. However, most slabs showed a punching cone failure. The average angle of inclination for the punching cone was 30.7° for steel reinforced slabs, 29.2° for different CFRP grids and 26.8° for H type slabs. For all slabs, a slip of the flexural reinforcement was noticed near failure or shortly after cracking and the bond behaviour of the grids was of considerable influence on the crack development and brittleness of the punching failure. Furthermore, Matthys and Taerwe found that the FRP–RC specimens with similar flexural strength as the steel–reinforced reference specimens, the obtained punching load and stiffness in the cracked state were considerably less. However, for the FRP–RC specimens with an increased reinforcement ratio or an increased slab depth, the behaviour of the slabs were comparable to steel–reinforced reference slabs. In addition, higher failure loads were found with increasing loading plate diameter; however, this parameter was less important than the reinforcement ratio and slab thickness.

Matthys and Taerwe also verified the punching failure load obtained for all the specimens using some well–known empirical or code equations and compared the results with their experimental data. They found that these equations give fairly good predictions, but with an underestimation for FRP–reinforced slabs. The latter aspect was solved by introducing the equivalent reinforcement ratio $\rho_f E_f / E_s$. They suggested a modification to the empirical formula of the BS 8110–97 (1997) to adapt it for determining the punching shear capacity of FRP reinforced slabs. They multiplied the reinforcement ratio by the modular ratio E_f / E_s to obtain the modified punching capacity, as shown in the following equation:

$$V_c = 1.36 \frac{\sqrt[3]{100\rho_f \frac{E_f}{E_s} f_c'}}{d^{\frac{1}{4}}} b_{0.15d} d \qquad (2.1)$$

El–Ghandour et al. (2003) examine eight square simply supported FRP–RC two–way slabs to investigate the punching shear behavior of FRP–RC flat slabs with and without carbon fiber reinforced polymer (CFRP) shear reinforcement as shown in **Figure 2.5**. All specimens were square with 2000 mm side length, a 175 mm thickness, and a 200×200 mm square column. All specimens were tested using a concentrated load at the centre of the slabs. The first phase consisted of four specimens. Two slabs were reinforced with GFRP bars (ρ = 0.18%) and two were reinforced with CFRP bars (ρ = 0.15%). In the second phase, they increased the flexural reinforcement ratio (ρ) to 0.38%. In the first phase, the specimens had rather low reinforcement ratio and wide spacing between the reinforcement bars and consequently failed due to bond slip of the flexural bars at loads less than their expected flexural and punching shear capacities.

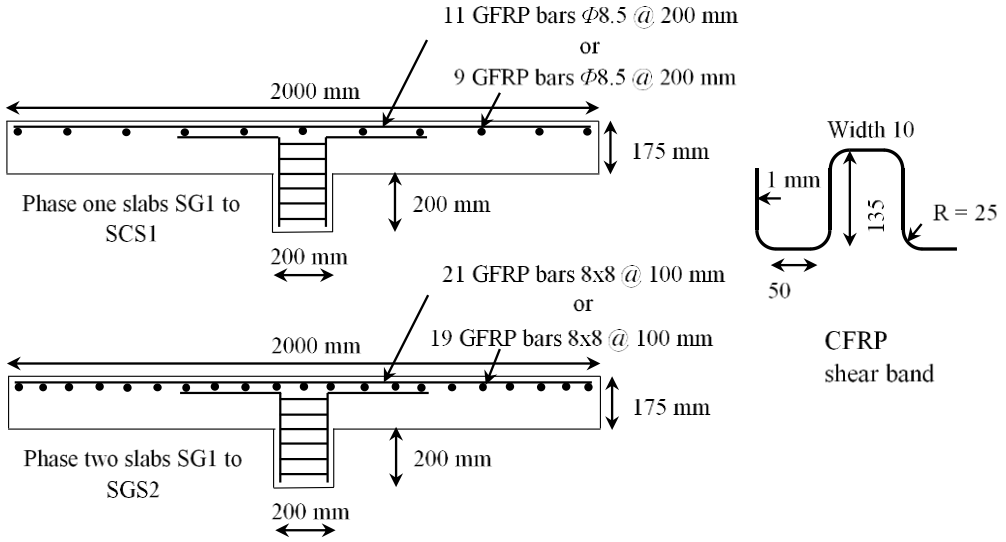

Figure 2.5 Slab layout and reinforcement details in tested slabs.

Based on his research result he concluded that the shear reinforcement increased the slab load capacity, and it hampered slip initiation but did not eliminate it. In the second phase, the smaller flexural bar spacing eliminated the problems of concrete splitting and prevented the bond slip failure in these slabs, which failed in punching shear. The shear reinforcement increased the apparent bond of the flexural reinforcement and reduced its slippage. It also prevented splitting of concrete around flexural bars, consequently, it increased the strength of the connection by 17%. These investigators recommended the use of 0.5d spacing between the shear band legs

instead of the 0.75d used in their tests and also a maximum strain of 0.0045 for calculating the shear capacity of the CFRP shear band reinforcement.

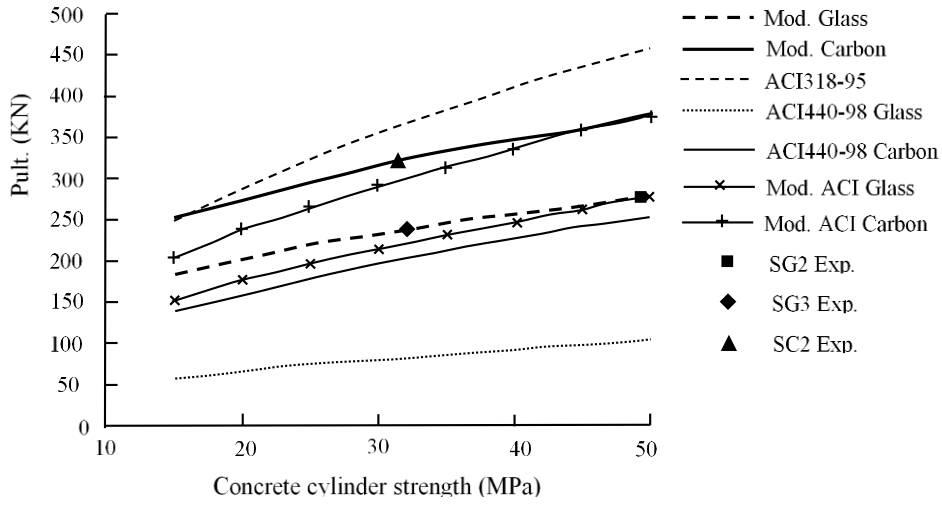

Figure 2.6 Normalized experimental and predicted capacities of Slabs SG2, SG3, and SC2.

Moreover, the analysis involved modifications to the punching–shear design equations used for steel–reinforced slabs in ACI–318–95 (1995) and BS–8110 (1997) to predict the punching shear capacity of tested specimens accurately as shown **Figure 2.6**. They suggested modifying the ACI 318–95 (1995) equation by multiplying it in a stiffness correction factor $(E_f/E_s)^{1/3}$ while a strain limit of 0.0045 was proposed for FRP reinforcement in BS 8110 (1997) equation, yielding these equations for FRP slabs, as shown in Eqns. (2.2 and 2.3), respectively.

$$V_c = 0.33\sqrt[3]{\frac{E_f}{E_s}}\sqrt{f_c'}\,b_{0.15d}\,d \qquad (2.2)$$

$$V_c = 0.79\sqrt[3]{100\rho_f\frac{E_f}{E_s}\left(\frac{0.0045}{\varepsilon_y}\right)}\sqrt{\frac{f_c'}{25}}\left(\frac{400}{d}\right)^{\frac{1}{4}}b_{0.15d}\,d \qquad (2.3)$$

Ospina et al. (2003) examine the punching shear behavior of four isolated full–scale slab-column reinforced with GFRP bars and subjected to concentric gravity loading. The main variables were the slab reinforcement material (steel or GFRP); the type of reinforcing mat (individual bars or two–dimensional grid); and the slab reinforcement ratio (0.73 to 1.46%). Two slabs, GFR–1 and GFR–2, were reinforced with GFRP reinforcing bars (commonly referred to as C–bars). One slab, NEF–1, was reinforced with a GFRP two–dimensional (2–D) grid and one slab, SR–1, with deformed steel bars.

The experimental results of this study showed that the punching failure in FRP–reinforced specimens is affected by the elastic stiffness of the FRP mat as well as its bond characteristics. Whereas, as shown in **Figure 2.7**, the FRP grids in two–way flat slabs might not provide the same punching–shear capacity as FRP bars due to the difference in bond behaviour and concentration of stresses in the grids where the orthogonal reinforcement intersected.

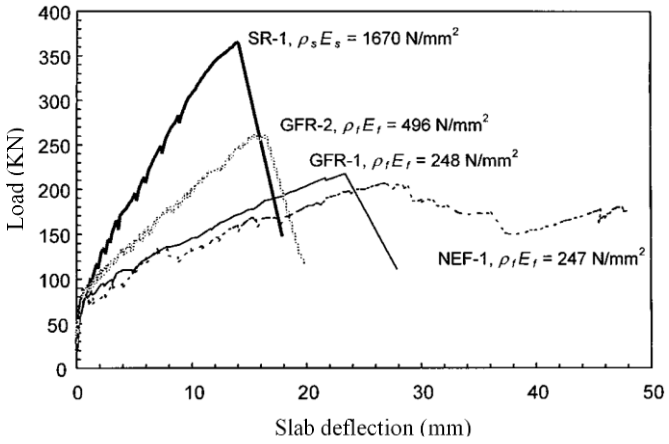

Figure 2.7 Load-deflection behavior.

Furthermore, it would be improbable for a punching shear failure in the FRP–reinforced slab to be triggered by FRP rupture. Even in the most lightly reinforced test specimens, the FRP did not rupture. The results also suggested that concrete crushing did not necessarily trigger punching shear failure in steel or FRP reinforced concrete slabs. On the other hand, the purposes of calculating the ultimate shear strength of their test specimens, they adopted the expression recommended by Matthys and Taerwe (2000 II), as shown in the following Eqn.

$$V_c = 2.77 \sqrt[3]{\rho_f f_c'} \sqrt{\frac{E_f}{E_s}} b_{0.15d} d \qquad (2.4)$$

Zaghloul et al. (2004 and 2007) tested a total of thirteen half–scale specimens to investigate the punching–shear behaviour of CFRP grids interior slab-column connections reinforced with and without special fabricated CFRP shear rail used as shear reinforcement. Ten specimens were reinforced with CFRP grids in flexural only and one specimen with traditional steel reinforcement without shear reinforcement while the remaining two specimens were reinforced with CFRP grids in flexural and CFRP shear reinforcement in shear. The test specimens comprised a 1760×1760 mm slab and a 250×250 mm or 250×350 mm column stub extending

above and below the slab and were made of 35 MPa concrete strength. The specimens were loaded via the cantilever that was a part of the upper column stub (see **Figure 2.8**), and by adjusting the eccentricity of the axial load P, the desired moment to shear (M/V) was achieved.

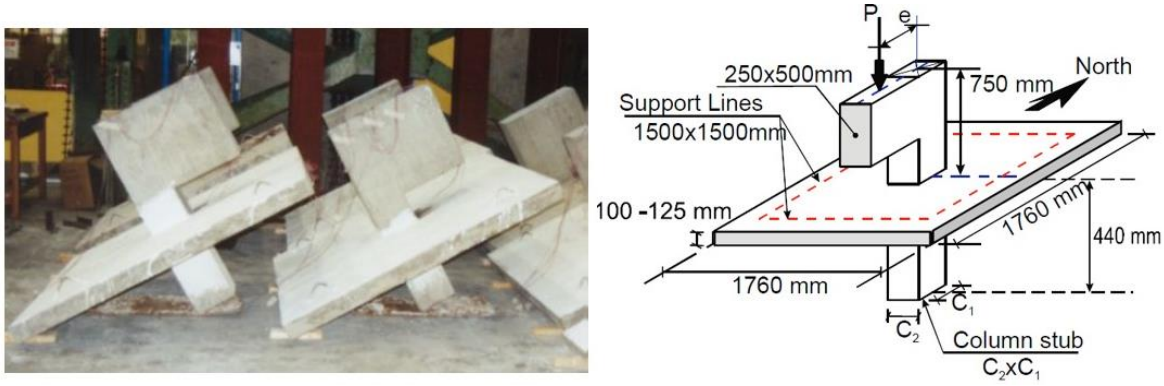

Figure 2.8 Typical test specimen dimensions.

During the tests, the slabs were supported on four sides and were prevented from lifting. Due to the constant eccentricity of the axial load from the column centre, the ratio of the moment to the shear was held constant throughout the test. The investigated parameters were; the ratio of the applied moment to shear (M/V = 0.22 or 0.30); reinforcement ratios (ρ = 0.87%, 1.33%, and 1.48%); reinforcement type (steel or CFRP grids); slab thickness (100 mm or 125 mm); column aspect ratio (1.0 or 1.4); and CFRP shear reinforcement.

Based on their study they reported the following:

i. The basic punching shear behavior of CFRP–reinforced slab-column connections is the same as that of steel–reinforced connections.
ii. The punching shear strength of slabs without shear reinforcement is proportional to the cubic root of their flexural reinforcement rigidity.
iii. The column aspect ratio has an effect on the punching shear capacity of the slabs. Doubling the column aspect ratio caused a 15 % reduction in the punching strength.
iv. The proposed shear reinforcement increased the punching shear strength of the specimens by 24.6% and 30.4%, when the first leg of the shear reinforcement was located 0.5d and 0.85d from the column face, respectively. This increase in punching capacity is comparable to the increase that can be achieved when using steel–headed studs.

v. A 25% increase in the slab thickness would cancel the negative effects of the lower elastic modulus of CFRP reinforcement on the stiffness and strength of the interior slab-column connections.

Lee et al. (2009) examine the behavior of steel and GFRP–reinforced slab-column connections and investigate the effects of the banded distribution of flexural reinforcement and steel fiber reinforced concrete (SF–RC) in a slab on the behavior of two–way slabs reinforced with GFRP bars. A total of six slabs had a side dimension of 2300 mm square and a thickness of 150 mm were loaded with either equal concentrated loads around the perimeter to simulate a uniformly distributed load on the test specimen. The main variables were the reinforcement material; the concentration of reinforcement around the column; and the presence of steel fibers in the concrete. Four specimens were reinforced with uniform and banded distribution (within a distance 1.5h from the column faces, where h is the slab thickness) GFRP bars while two control steel specimens for comparisons as shown in **Figure 2.9**. The flexural reinforcement ratios of the specimens were varied between1.18% and 3%.

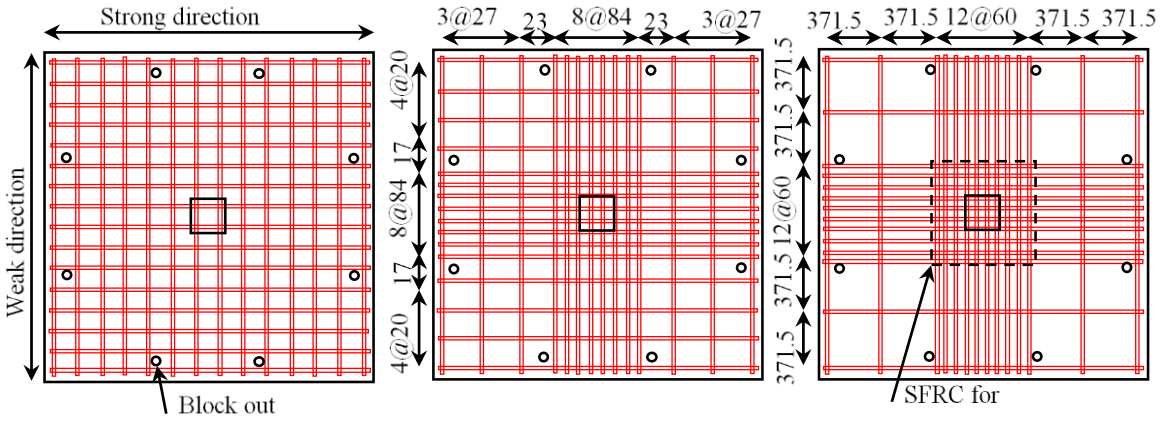

Figure 2.9 Typical reinforcement details for tested specimens.

The test results indicated that concentrating the top mat of flexural reinforcement within a distance 1.5 times the slab thickness from the column faces resulted in slightly higher punching shear strength, more uniform distribution of strains in the top flexural bars and better crack control compared to the companion slab with a uniform distribution of the same amount of reinforcement. Moreover, as shown in **Figure 2.10,** the increase in punching shear strength due to the banded distribution of top reinforcement was 5% and 11% for the steel and GFRP

specimens, respectively. In addition, the punching shear failure plane for the slabs with banded reinforcement surfaced at a greater distance from the column faces. However, excessive concentrations of the reinforcement (ρ = 3%) seems to be ineffective in increasing the punching resistance of GFRP–reinforced concrete slabs.

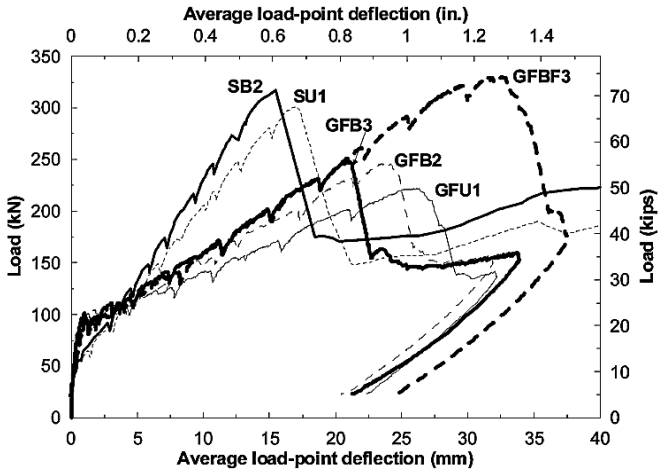

Figure 2.10 Load versus average load–point deflection responses.

They also compared the results in the study including other experimental results performed by various researchers with the nominal punching–shear strength predicted using the design equations in ACI 440.1R–06 (2006) and JSCE (1997). It was concluded that the predictions using the equations of ACI 440.1R–06 (2006) were very conservative, while JSCE (1997) equations gave better predictions. The predictions using JSCE (1997) equations were un–conservative for specimens with reinforcement ratios ranged between 2% to 3%.

Hassan et al. (2013 a & b) investigated the punching–shear behavior of two–way concrete slabs reinforced with glass fiber reinforced polymer (GFRP) bars of different grades. A total of 10 full–scale interior slab-column specimens measuring 2500×2500 mm with thicknesses of either 200 or 350 mm and 300 × 300 mm square column stubs were fabricated with normal and high–strength concretes. The specimens were tested under monotonic concentric loading until failure. The main variables were the slab reinforcement material (steel or GFRP); the GFRP bars grades (Grades I, II, and III according to CSA S807 (CSA 2012)); the slab reinforcement ratio (0.34–1.61%); and concrete compressive strengths (35–75 MPa). The specimens were simply supported on all four sides and tested under monotonic concentrated load, acting on the column stub from the bottom side of the slabs until failure (see **Figure 2.11**).

The specimens were categorized into two series. Series I (200 mm thick) comprised four GFRP–RC specimens with a reinforcement ratio ranging from 0.71–1.56% and reference steel–reinforced one. Series II (350 mm thick) comprised four GFRP–RC specimens with a reinforcement ratio (ρ) ranging from 0.34–1.61% and a reference steel–RC slab. Four slabs in each series were fabricated using a concrete strength of 35 MPa (NSC), while the fifth one was fabricated with a concrete compressive strength of 65 MPa (HSC) to investigate the effects of concrete type and strength. In addition, one slab in Series I was reinforced with Grade–III GFRP bars which had the same axial reinforcement stiffness.

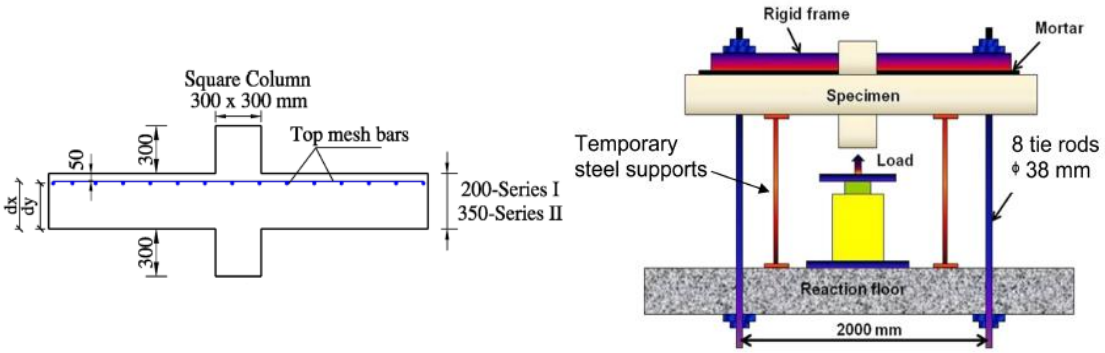

Figure 2.11 Test specimens' geometry, reinforcement configuration and test setup.

The experimental results of this study showed that increasing the GFRP reinforcement ratio yielded higher punching–shear capacities, lower strains in the reinforcement, and smaller slab deflections as shown in **Figure 2.12**. Increasing the reinforcement ratio from 0.71% to 1.56% in Series I and from 0.34% to 1.62% in Series II increased punching–shear stress at the failure by 35% and 81%, respectively. On the other hand, using high compressive strength concrete (HSC) for the GFRP–RC specimens improved the punching– shear capacity and enhanced the load–deflection relationships (see **Figure 2.12**). Furthermore, concrete compressive strength had a significant effect on the initial stiffness (uncracked stiffness) of the GFRP–RC specimens where the initial stiffness increased by 22 and 51%. On the other hand, the punching–shear stress at failure was proportional to the effective reinforcement ratio ($\rho_f E_f = E_s$) to the power of 0.34.

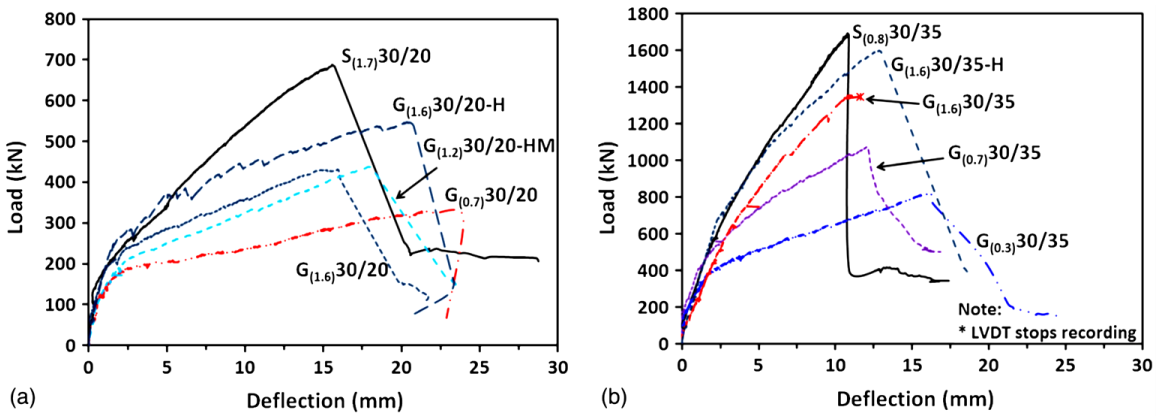

Figure 2.12 Load–deflection relationships: (a) series I (200mm); (b) series II (300 mm).

Nguyen–Minh and Rovňák (2013) studied the punching shear behavior of concrete two–way slabs reinforced with GFRP bars. A total of six full–scale slab-column connections (2200× 2200×150 mm), consisting of three GFRP–reinforced slabs and three control steel–reinforced slabs, were tested. To ensure sufficiently high punching shear stresses in the slabs, the column cross sections were 200×200 mm. Geometric reinforcement ratios A_f (or A_s) = A_c of tested slabs were 0.4%, 0.6%, and 0.8%. No compression reinforcement was used in the slabs. All specimens simply supported on all four sides and tested under a concentrated load, acting on the column stub in the middle of each slab.

Based on the results obtained from the study they concluded that, the increase of the GFRP reinforcement ratio in tested slabs subjected to punching shear loads have proven to have the following benefits; (i) increase in punching shear resistances (up to 36%); (ii) reduction of deflections (up to 35%). In comparison with steel–reinforced slabs, the GFRP–reinforced ones have smaller resistance (up to 38%); higher displacement (up to 2.6 times); and larger crack width (up to 34%). Future, the size factor and the effect of the span to effective depth ratio L=d should be taken into account in calculations of the punching shear resistance of the FRP–reinforced slab-column connections. Furthermore, in comparison with the existing formulas, the proposed semi-empirical (Eq. 2.5) provided more stable predictions of the punching shear resistance of interior FRP reinforced slab-column connections within the entire range of parameters investigated (see **Figure 2.13**).

$$V_u = \sqrt{\frac{400}{d}}\left(\frac{0.8}{\left(\frac{L_1}{d}-\frac{c_1}{d}\right)}\right)\left(\frac{\rho_f}{100}\right)^{0.33}(E_f)^{0.33} f_c' b_{cr;1} d \qquad (2.5)$$

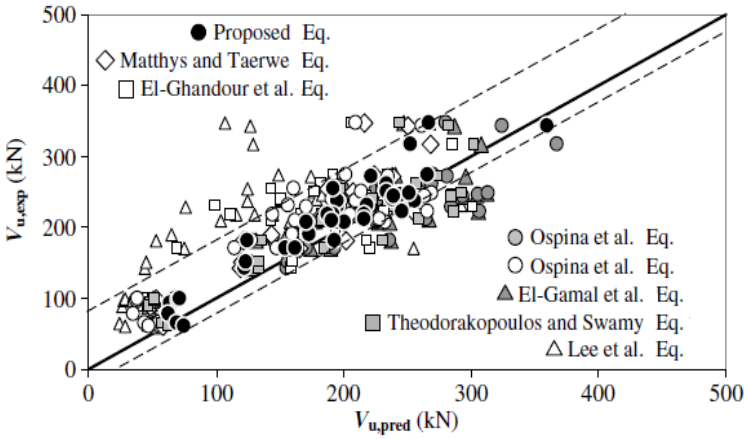

Figure 2.13 Comparison of predicted and experimental punching shear resistance.

Hassan et al. (2014 a & b) investigated the punching–shear behavior of two–way GFRP–RC slabs reinforced with carbon and glass (CFRP and GFRP) stirrups, as shear reinforcement, as shown in **Figure 2.14**. A total of ten full–scale interior slab-column specimens measuring 2500×2500 mm, with thicknesses of either 200 mm (Series I) or 350 mm (Series II), and a square column stub measuring 300×300 mm, the column extended 300 mm beyond the top and bottom surfaces of the slabs. The test specimens were provided with GFRP flexural reinforcement ratios (ρ_f) ranged from 0.34% to 1.61%. This range was chosen to evaluate the efficiency of the FRP stirrups in relatively low and high flexural reinforcement ratios.

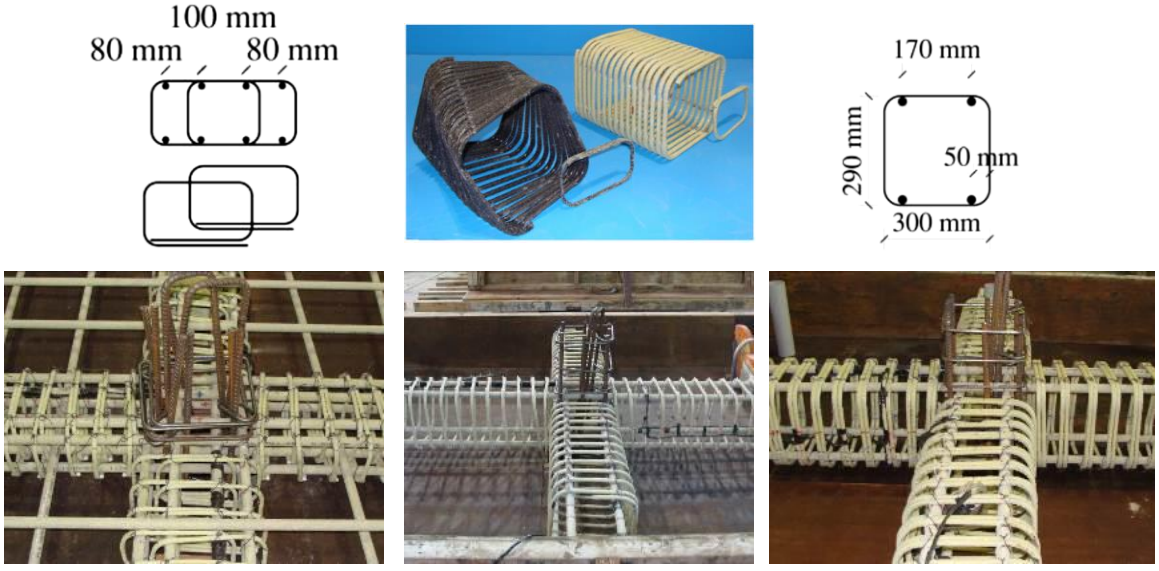

Figure 2.14 Details and configurations of investigated stirrups.

Series I (200 mm thick) comprised three specimens with GFRP bars as flexural reinforcement at a ratio (ρ_f) of 1.21%. Two specimens were reinforced with discrete GFRP and CFRP closed stirrups, while the third one served as the reference slab without shear reinforcement. Series II (350 mm thick) comprised seven specimens with GFRP bars as flexural reinforcement at a ratio of 0.34% or 1.61%. Five specimens were fabricated with GFRP and CFRP spiral stirrups. Spiral stirrups were used because of their fast and easy installation during construction in comparison to discrete closed ones. The shear reinforcement ratio (ρ_{fv}) was calculated with the cross-sectional area of the FRP stirrups on a concentric line parallel to the perimeter of the column at 0.5d from the column face as specified by ACI 318 (2008) and CSA 23.4 (2004).

Based on the experimental results Hassan concluded that

i. The test specimens showed similar crack propagation in the top surface of the slab (tension side). Nevertheless, the single critical shear crack in the specimens without FRP stirrups changed to extensive inclined cracks when FRP stirrups were used as shear reinforcement.
ii. The test specimens without shear reinforcement showed a sudden and brittle punching shear failure, especially when the flexural–reinforcement ratio was high. The use of FRP stirrups in the test specimens, however, yielded to a softer punching–shear failure than the slabs without stirrups.
iii. The use of FRP stirrups not only enhanced the punching–shear strength but also the specimen deformation capacity, which was more pronounced in the slabs reinforced with higher flexural reinforcement ratios. The average increase in the punching–shear capacity was 29% and 23% in Series I and II, respectively. In addition, the average increase in the deflection at the failure of Series I specimens was 107%.
iv. The strain measurements confirmed that the FRP stirrups contributed to the punching shear strength were located within a distance of 2.5d from the column face, which is in agreement with CSA A23.4 (2004), which states the shear reinforcement should extend to at least 2d of the column face.
v. The FRP stirrups with more legs resulted in a better performance than those with fewer legs (even with a higher modulus of elasticity).

Gouda et al. (2015 and 2016) assessed the performance of ten full–scale interior slab-column specimens reinforced with GFRP bars subjected to shear forces and unbalanced moments. A

total of ten full–scale isolated GFRP–RC interior slab-column connections with a side length of 2800 mm and thickness of 200 mm, the column had a 300 mm square section and was extended above and below the slabs for a length of 1000 mm. The specimens were categorized into two series. Series I comprised six slabs were reinforced with sand–coated GFRP bars, Series II comprised three slabs were reinforced with ribbed–deformed GFRP bars, two slabs had been provided with shear reinforcement (shear studs) as shown in **Figure 2.15**.

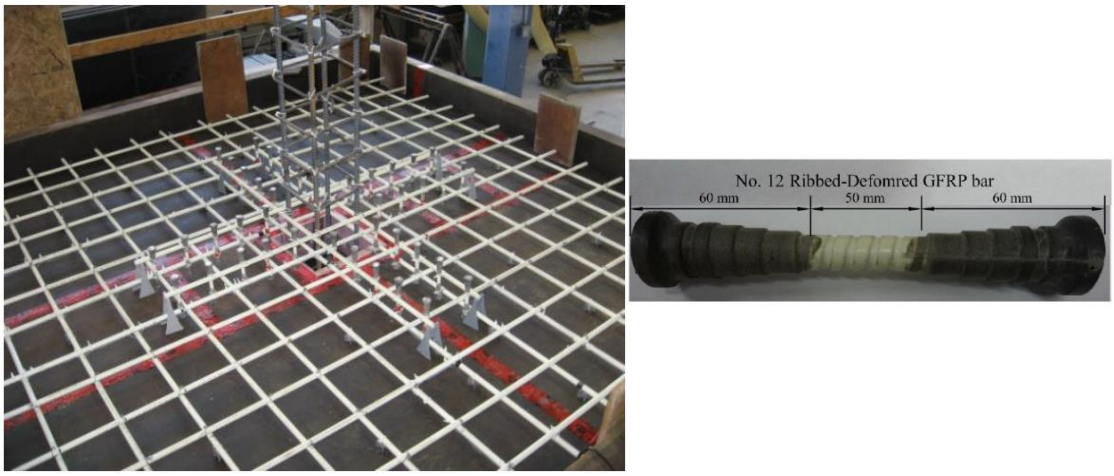

Figure 2.15 Photo for the reinforcement configurations for the specimen.

As shown in **Figure 2.16,** the slabs were supported on four sides and subjected to a vertical shear force (V) simultaneously with the unbalanced moment (M) with a constant M/V ratio of 0.15. To prevent the uplift of the slab sides due to the unbalanced moment, another frame was used on the top of the slab while the corners of the slabs were left free to move in an upward direction only. The parameters investigated in the experimental study were flexural reinforcement ratio (0.65, 0.98 and 1.30%); concrete compressive strength (NSC and HSC), and type of the reinforcement (Steel and GFRP); moment–to–shear ratio (0.15 and 0.3); and the spacing between the shear stud reinforcement (0.5 d and 0.75d).

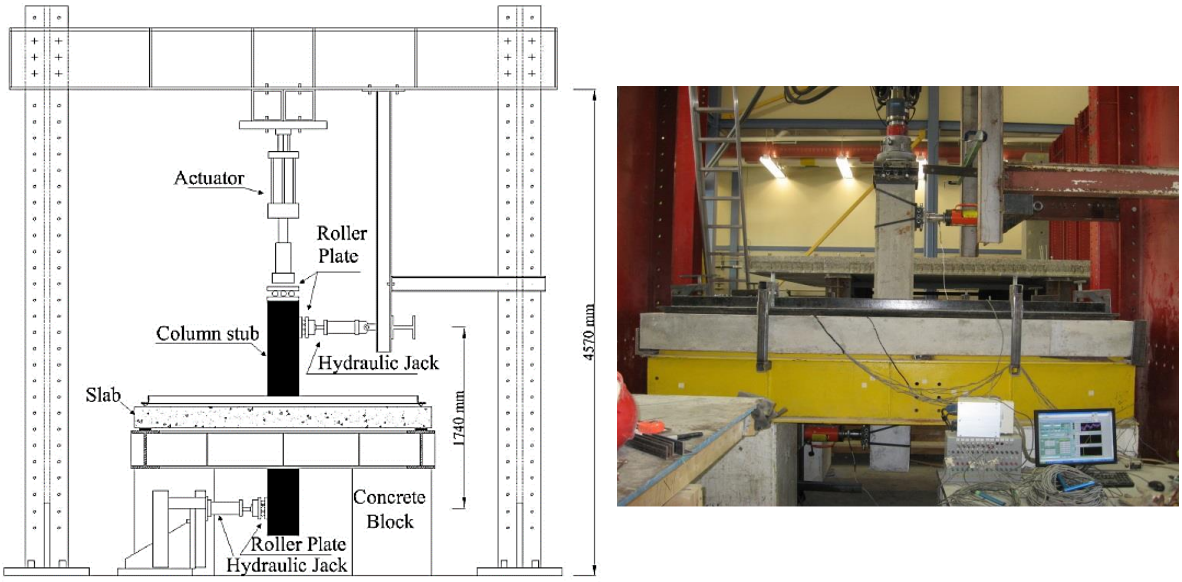

Figure 2.16 Test set up.

Based on the results obtained from the study they concluded that the unbalanced moment increased the deflection and strain in the reinforcing bars. Increasing concrete compressive strength slightly enhanced the punching shear capacity on another hand it enhanced the initial stiffness of the connections and decreased the strains in the GFRP bars in the uncracked stage. Increasing the moment–to–shear ratio increased the deflection and reinforcement strain. Furthermore, increasing the moment–to–shear ratio resulted in a reduction in the vertical load capacity. The presence of GFRP shear studs increased the post-cracking stiffness, deflection at failure, and the load carrying capacity. The punching load capacity increased by approximately 18 and 23% in slabs with 0.75 d and 0.5 d stud spacing, respectively, compared to the slab without shear studs. However, the GFRP shear studs did not prevent punching shear failure.

Hussein et al. (2018) recently tested six full–scale FRP–RC slab-column interior connections under a combination of shear force and unbalanced moment. The experiments aimed to investigate the effect of flexural reinforcement ratio on connections made of HSC and shear reinforcement (see **Figure 2.17**) on connections made of NSC. All slabs were 2800×2800 mm with 200 mm thickness, simply supported along all four edges with the corners free to lift. The connections were isolated from a parking structure to simulate an interior supporting column of a flat plate system consisting of three 6.5 m long bays in both directions and bounded by the lines of contra–flexure.

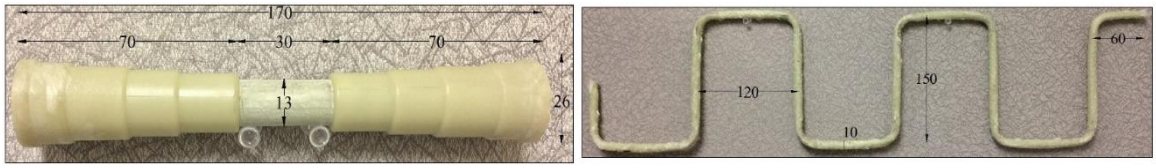

Figure 2.17 Details of shear reinforcement a) GFRP headed studs b) SC–GFRP corrugated bars.

The experimental results showed that increasing the flexural reinforcement ratio significantly enhanced the punching capacity and post-cracking stiffness while decreased the deflection of connections as shown in **Figure 2.18**. It also increased the failure cone angle and consequently decreased the punching shear radius. Regardless of the mode of failure and the provided shear reinforcement type and ratio, both types of shear reinforcement controlled the widening and propagation of shear cracks, which enhanced the post-cracking stiffness and decreased the deflection at the same load level of the shear–reinforced connections. The use of well-anchored shear reinforcement significantly increased the carrying capacity and deflection at failure.

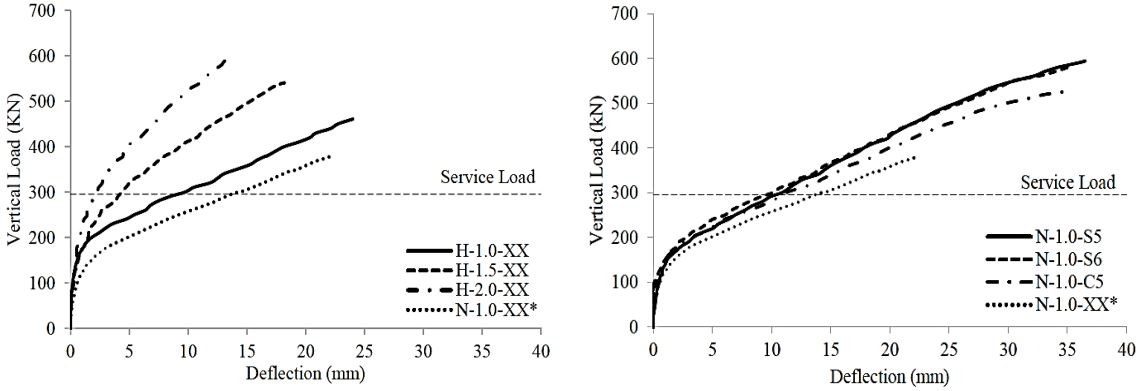

Figure 2.18 Vertical load-deflection relationship.

2.3. Punching Shear Strength of Slab-Column Connections Reinforced with Steel Bars under Lateral Cyclic Load.

There has been extensive research work done on the punching shear behavior of slab-column structures in seismic zones. Most of the previous experiments were done using interior or edge connection subassemblies isolated from prototype structures consisting of a slab with columns extending from the top and bottom of the slab. These subassemblies are subjected to vertical loading from either the top of columns or slab surface and cyclic loading on the column ends

or slab edges. This method is easy to carry out and the test results have been utilized in design codes. There is also some research was done using continuous slab-column specimens. Other experimental methods include testing model structures on shaking tables. Simulation of lateral displacements have been simulated primarily in two different ways: i) a lateral force applied to a free end of one column stub, with the other end supported in a pinned condition, or ii) equal and opposite displacements applied at the edges of the slab, with both column ends supported with a pinned connection.

Robertson et al. (1992) studied the effect of superimposed slab loading on the behavior of interior slab-column connections by testing two–bay slab-column subassemblies. Each subassembly consisted of one interior and two exterior connections. Three identical slab-column subassemblies were subjected to the same cyclic lateral displacement routine while each supported a different superimposed slab load. For true half–scale modelling of the chosen prototype, the specimens would have a span of 10 ft (3.05 m) and a slab width of 9 ft (2.74 m). Due to constraints of the testing frame, these dimensions were reduced to 9.5 ft (2.90 m) and 6.5 ft (2.00 m) as shown in **Figure 2.19**, respectively. The specimen A, B and C were subjected to the vertical load of 140, 285, 420 lb/ft2 (6.7kPa, 13.6kPa, 20.1 kPa), respectively. As reported **Table 2.1**, specimen A reached a peak lateral load of 19.8 kips (88.0 kN) at 3.5% drift, while the peak load on specimens B and C were 13.1 kip (58.3kN) and 9.6 kips (42.7kN), respectively. Specimen A reached maximum drift of 5% at failure, while specimen B and C reached 1.5% and 1%, respectively.

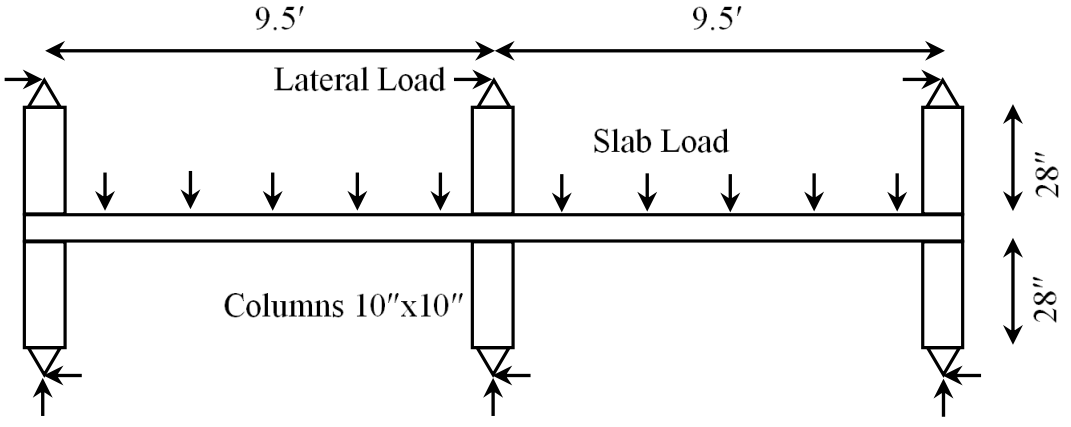

Figure 2.19 Test specimen details.

This work demonstrates that when the gravity load level (gravity shear level) increased, the capacity for moment transfer and ductility of the connection decreased. The hysteresis curves of unbalanced moment versus drift for three specimens A, B and C (with increasing gravity loading) show that the capacity of lateral drift, stiffness, and energy dissipation decreased as the gravity loading increased. Robertson suggested also a design limit $\frac{V_u}{V_o} \leq 0.35$, where V_u is the direct shear force at peak lateral load, and V_o is the nominal shear capacity of the slab in the absence of moment transfer.

Table 2.1 Vertical load influence on peak load and drift [Robertson (1992)].

Specimens	Superimpose slab load (Ib/ft^2)	Peak load and the corresponding drift	The drift of the first failure
A	140	19.8 kip at 3.5 % drift	5% at one extrior connection
B	285	13.1kip at 1.5 %	1.5 % at interior connection
C	420	9.6 kip at 1 %	1 % at interior connection

Emam et al. (1997) tested four interior slab-column connections under simulated earthquake–type loads to investigate the effect of using high strength concrete in connections. Two slabs were made with high compressive strength concrete of 75 MPa and two were made with normal compressive strength concrete of 35 MPa. The columns for all specimens were made with high compressive strength concrete. Two slabs were reinforced with a reinforcement ratio of 0.5% and the other two with 1%. The tested specimens represented a full–scale interior column connected to a slab part–bound by the line of contra flexure around the column. Slabs were 150 mm thick and 1900 mm square, and columns in cross section were 250 mm square and 850 mm length above and below the slab. The test specimens were subjected initially to a portion of the gravity load equal to 125 kN to represent the dead load and 30 % of the live load typically in place in an actual structure. This part of the gravity load was kept constant during testing. Subsequently, each test specimen was subjected to the same lateral loading history.

From observed behavior of the tested specimens, he concluded that HSC-RC slabs could accommodate higher lateral displacement demand during an earthquake (see **Figure 2.20**). Hence, the integrity of the structure may be enhanced by the use of HSC-RC slabs for structures located in moderate to high seismic zones. Shear strength and moment capacity increased by

20 and 31%, respectively, when the HSC-RC slabs of 75 MPa was used, compared to an NSC-RC slab of 35 MPa. For specimens constructed with HSC, cracks were fewer and the observed crack width is smaller; also the failure modes were more gradual compared with those of specimens constructed with NSC. In general, the use of HSC for slab construction may be advantageous for structures located in moderate to high seismic zones.

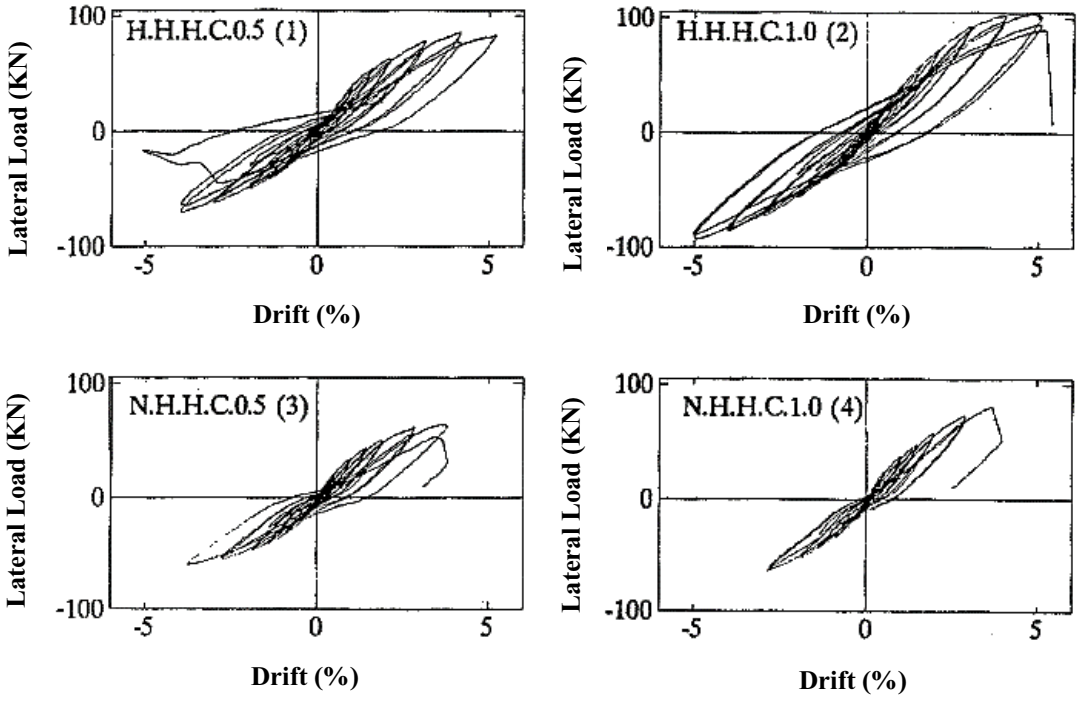

Figure 2.20 Load–drift relationship for test specimens.

Megally and Ghali (2000) investigated the behavior of slab-column connections transferring shearing forces combined with a monotonic or cyclic reversed unbalanced moment between slabs and columns. Eleven full–scale slab-column connection specimens, without and with stud shear reinforcement (SSR) were tested. Five of the test specimens are provided with stud shear reinforcement, the remaining specimens do not have any shear reinforcement. One of the slabs with no shear reinforcement was cast using high strength concrete to study the effects of concrete compressive strength on the seismic behavior of slab-column connections, the slab thickness was 150 mm. The column was square with 250 mm side width. The column stubs were flush with the slab free edge and protruded 700 mm on each side of the slab.

The test variables were the level of gravity load applied when cyclic moment transfer takes place; provision of SSR; the spacing between shear studs; concrete strength; and the amount of slab flexural reinforcement. Slab–column connection specimens divided into 4 series, the first test series (a) included 7 specimens to study the effect of the level of gravity load, transferred at the instant of earthquake occurrence, on seismic behavior of slab-column connections. Series (b) included 7 specimens, some of them were included in test series (a), to study the effect of the provision of shear studs. The third test series (c) was intended to find out what would be more effective for construction of flat plates in seismic zones: use of high strength concrete (HSC) or shear reinforcement (SSR). This series included three specimens only one cast of HSC. The fourth test series (d) included four specimens to study the effect of slab flexural reinforcement ratio.

Based on the experimental results he concluded that:

i. Without shear reinforcement, slab-column connections cast of NSC may fail during earthquakes in brittle punching shear mode at relatively low drift ratios. Slab–column connections must be sufficiently ductile to undergo 2.0% inter-storey drift ratio without punching failure. This can be achieved for connections with no shear reinforcement only if V_u does not exceed $0.3V_c$. No limit on V_u is required for connections with stud shear reinforcement in order to achieve a minimum interstory drift ratio of 2.0% on condition that a minimum amount of stud shear reinforcement is provided (see **Figure 2.21**).
ii. Increasing slab flexural reinforcement in slabs with no SSR reduces the lateral drift capacity substantially. Thus, designers should be careful in detailing of slab-column connections in seismic zones. With SSR, additional slab flexural reinforcement did not have any adverse effects on lateral drift capacity; in fact, the ultimate drift ratio of heavily reinforced slab was higher than the ultimate drift ratio of specimen with less slab flexural reinforcement this observation agrees with earlier experimental results of interior slab-column connections (Brown and Dilger, 1994).
iii. Use of HSC in the slab increases its resistance to punching but does not prevent its brittle punching failure in a severe earthquake.
iv. Provision of stud shear reinforcement, spaced at 0.75d, increases the punching resistance and prevents brittle failure even in a severe earthquake. With SSR, the slab-column

connections can undergo ductile deformations associated with up to 5% inter-storey drift ratios without punching failure. The punching resistance to gravity loads is maintained even after such large interstorey drift. Reduction of the stud spacing from 0.75d to 0.44d slightly improves the ductility.

v. The lateral inter-story drift capacity of slab-column connections, with no shear reinforcement, is restricted by the level of acting gravity loads at the instant of earthquake occurrence, concrete strength and the amount of slab flexural reinforcement. If the amount of flexural reinforcement affects the drift capacity, the yield strength of steel will also affect the drift capacity of slab-column connections. For slab-column connections, Robertson and Durrani (1991) suggest limiting (V_u /V_c) to 0.50 to achieve at least a 1.5% drift ratio.

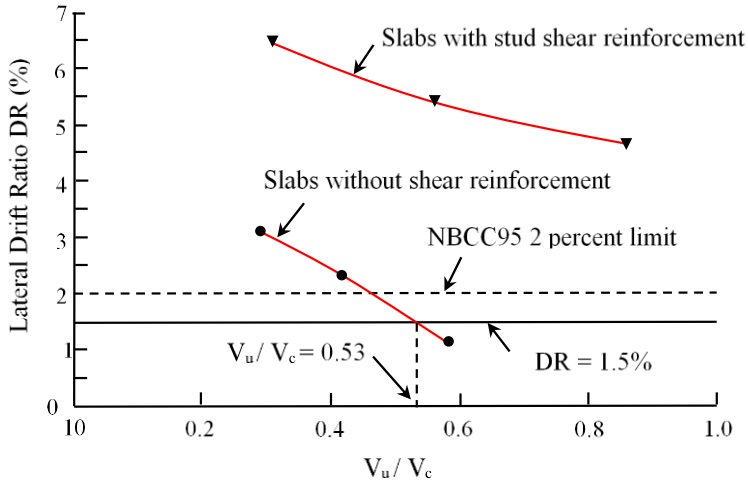

Figure 2.21 Drift ratio after a 20% loss of moment transfer capacity.

Robertson et al. (2002) studied the response of slab-column connections containing different types of shear reinforcement when subjected to combined gravity and cyclic lateral loading, four large–scale flat–plate interior slab-column connections with three different types of slab shear reinforcement were subjected to gravity and cyclic lateral loading, The control specimen had no shear reinforcement, while the other specimens had closed–hoop stirrups, single–leg stirrups, and welded–head studs as shear reinforcement (see **Figure 2.22**). The slabs were subjected to a gravity load equivalent to the dead load plus 30% of the live load in the prototype structure then the specimens were subjected to an incrementally increasing cyclic displacement routine. The intent of this displacement routine was to study the connection behavior under increasing levels of lateral drift and determine the failure drift level for a connection using a

particular type of shear reinforcement. Due to limits in the loading apparatus used, after reversing cyclic loading to approximately 5 % drift, the specimens were unloaded, resulted in the test frame, and then testing was continued in unidirectional cyclic loading. It is not clear how applicable the resulting data are to reverse cyclic loading.

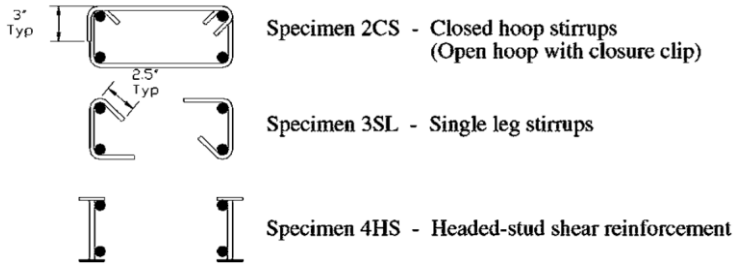

Figure 2.22 Types of slab shear reinforcement.

Based on the results of these tests, Robertson concluded the following: all three types of slab shear reinforcement–namely, open–hoop stirrups with clip closure, single–leg stirrups, and welded–head studs—proved equally effective in resisting punching shear failure of the slab-column connections under relatively low levels of gravity shear. The control specimen without shear reinforcement failed as a result of punching shear failure around the slab-column connection during the 3.5% drift cycle. This failure occurred prior to the load level predicted by the ACI 318–99 Building Code. None of the specimens with slab shear reinforcement experienced punching failure although they were tested to 8% lateral drift as shown in **Figure 2.23**. The specimens with slab shear reinforcement experienced peak lateral loads up to 22% greater than that of the control specimen while displaying superior ductility. These connections failed in flexure without reaching the full capacity of the shear reinforcement.

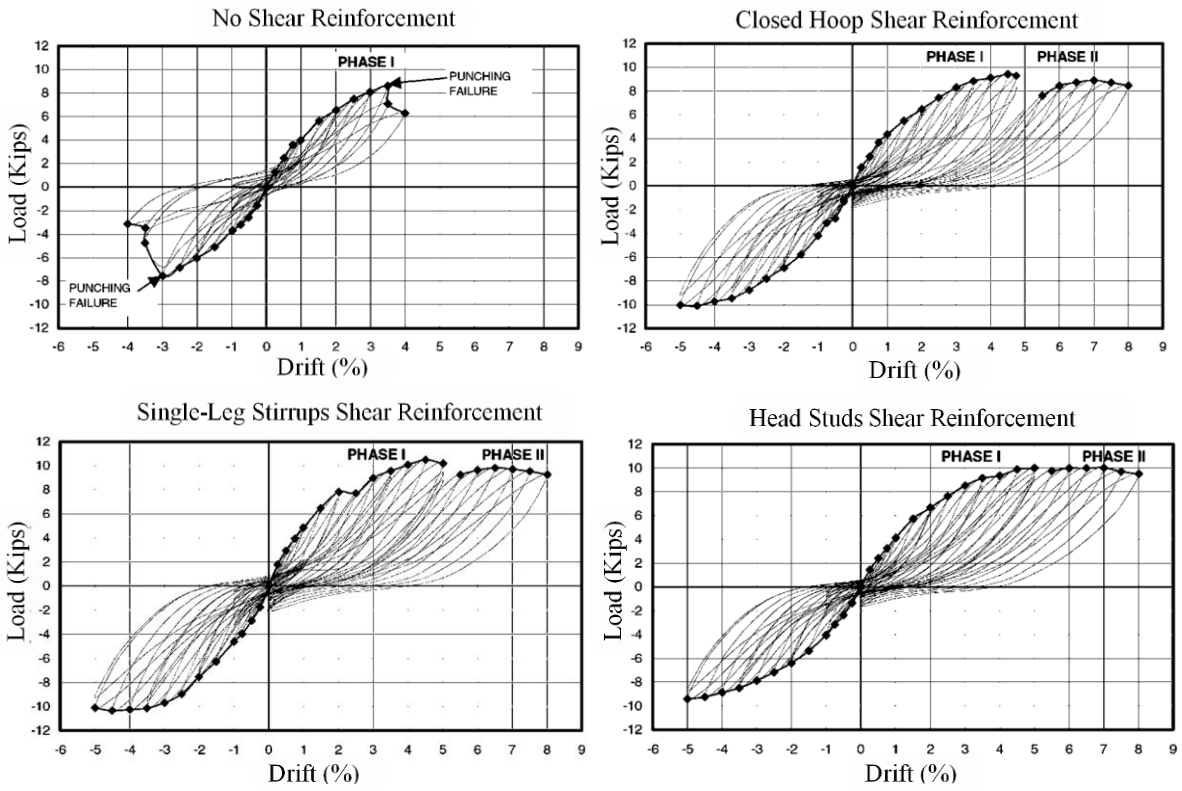

Figure 2.23 Hysteretic response and backbone curve for all Specimen.

Robertson et al. (2006) tested six isolated slab-column connections with varying reinforcing ratios; detailing, and slab gravity loads under monotonic lateral loading(see **Figure 2.24**). The slab reinforcement details used in the six half–scale specimens were typical of older flat slab construction in moderate and high seismic regions. In all specimens, the top slab reinforcement extended to 1/3 of the span and was not continuous through midspan. The bottom slab reinforcement was continuous at midspan, but discontinuous through the column, extending only 152 mm (3 in.) into the column support. The lack of continuous bottom reinforcement passing through the column may result in the total collapse of the slab after punching failure. To prevent this condition in the laboratory tests, two continuous slab bottom bars were added transverse to the loading direction in all specimens.

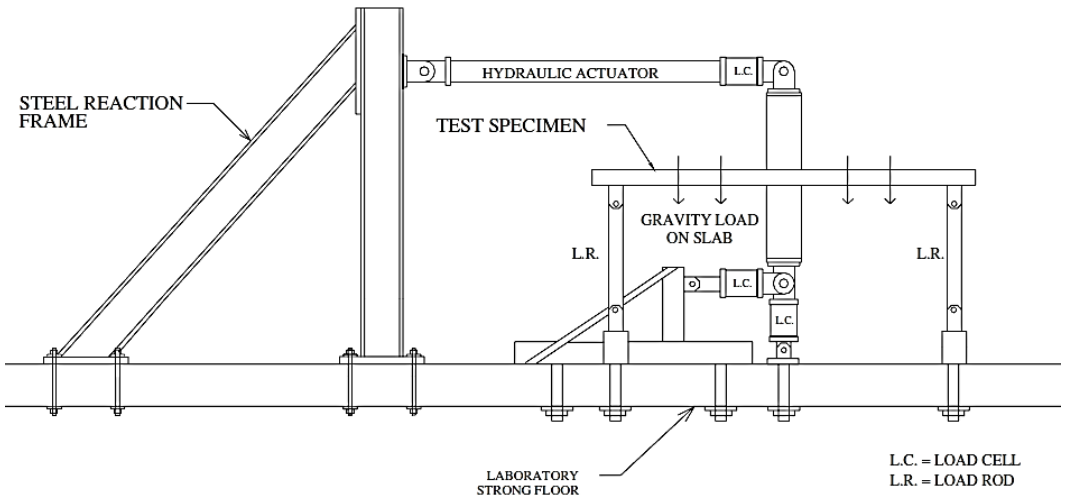

Figure 2.24 Test Frame Configuration.

Based on the results of this cyclic lateral loading test program on the interior slab-column connections with discontinuous slab reinforcement detailing, the following conclusions were drawn:

i. Slab–column connections with discontinuous slab reinforcement perform similarly to those with continuous reinforcement until punching shear failure. After punching failure, connections without adequate continuous bottom reinforcement passing through the column will suffer a complete collapse, which may lead to the progressive collapse of the floors below the initial failure. The exception to this observation is that bent–up bars passing through the column as top reinforcement, but anchored as bottom reinforcement in the slab, were able to prevent collapse after punching failure.

ii. Increased gravity load on the slab during cyclic lateral loading results in a significant reduction in lateral drift capacity before punching failure as shown in **Figure 2.25**. For heavy slab loading conditions, punching failure can occur before reaching the lateral load capacity of the connection.

iii. Connections with increased slab flexural reinforcement will support greater lateral loads (see **Figure 2.25**), but the increased eccentric shear transfer may result in premature punching shear failure.

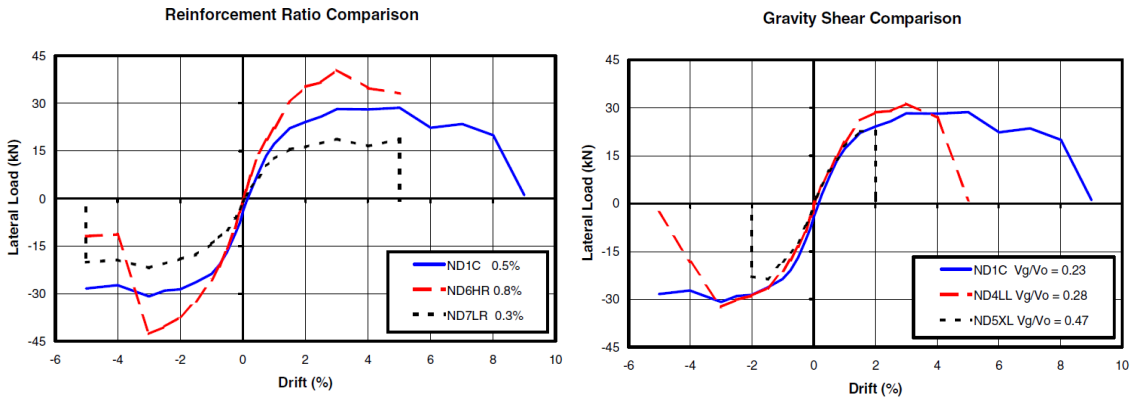

Figure 2.25 Effect of flexural reinforcement ratio and gravity shear ratio.

Carl Broms. (2007) tested four full–scale flat–plate specimens, two with shear studs and two with ductility reinforcement as shown in **Figure 2.26,** under cyclic lateral displacement to simulate the behavior of an interior slab-column connection in a flat–plate with the factored gravity load 10.5 kN/m2 (220 lb/ft2) during a major earthquake. The experiments aim to cover loads up to the upper range of possible factored gravity loading for flat plates in office buildings with span width on the order of 7.5 m (25 ft) or less. The chosen amount of flexural reinforcement is intended to reflect normal design.

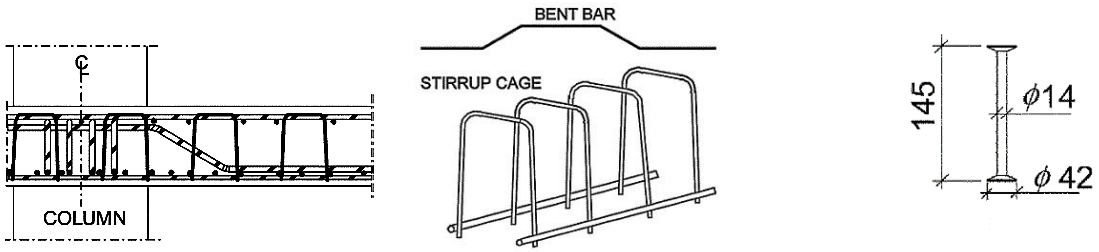

Figure 2.26 Ductility reinforcement and Shear studs details.

The specimens were geometrically identical to the ones used for gravity load testing. They simulated the conditions at an interior 300 mm (12 in.) square column in a continuous flat plate with a span width 5.8 m (19.0 ft) and a slab thickness of 180 mm (7.1 in.). The columns above and below the slabs were pin–supported at their ends to simulate the points of contra flexure for the bending moment in the columns due to imposed lateral displacement of the building during an earthquake. The test setup and specimens geometry is depicted in **Figure 2.27.**

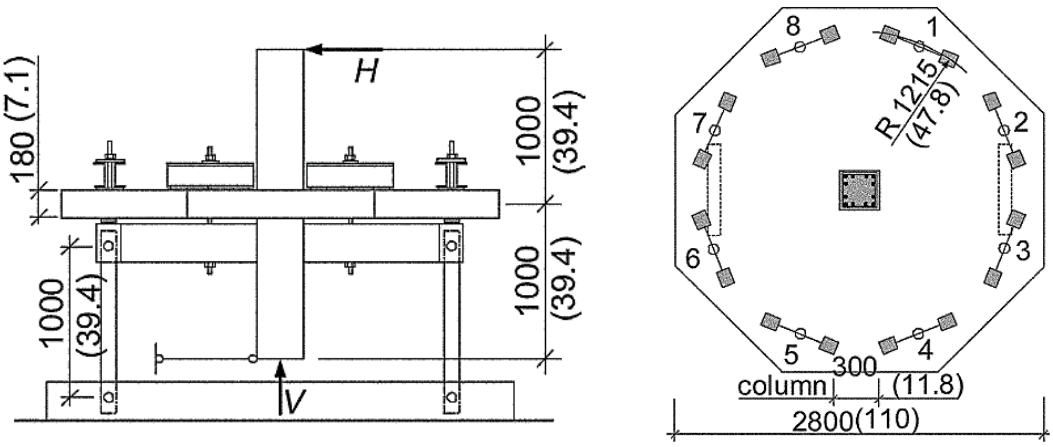

Figure 2.27 Test setup and typical geometry of tested specimens.

Broms concluded that the specimens with shear studs displayed stiffness degradation already at 0.5% drift ratio and failed in punching with low residual capacity for gravity loading after the cyclic lateral loading. The specimens with ductility reinforcement behaved elastically to approximately 1.5% drift ratio (corresponding to approximately 2% drift ratio for the prototype structure). Their residual gravity load capacity was not impaired by the cyclic lateral loading, but neither shear studs nor ductility reinforcement can prevent deterioration of the concrete at the column. A form of punching is therefore ultimately bound to occur with ductility reinforcement as well, but the bent bars act as reliable suspension reinforcement that can bridge over the failure zone in a ductile manner due to the presence of stirrup cages that provide uniform shear toughness to the concrete outside the local failure zone, which explains the very collapse–safe behavior.

Thomas H.K. et al. (2008) reported reversed cyclic tests on four, two–thirds scale specimens with both thin plate stirrups and headed stud–rails to evaluate the effectiveness of thin plate stirrups as shear reinforcement for reinforced concrete slab-column connections. The isolated slab-column connection specimens with both thin–plate stirrups and headed studs were tested under combined gravity and reversed cyclic lateral loading as shown in **Figure 2.28**. Slab shear reinforcement satisfying ACI 318–05, Section 21.11.5, except only extending 1.7h, 0.9h, and 1.7h away from the column face, instead of the required 4h, was provided in specimens PS2.5, PS3.5, and HS2.5 as shown in **Figure 2.29**, respectively.

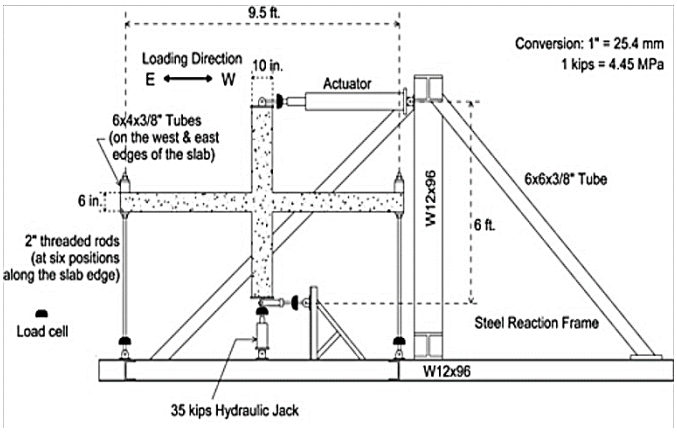

Figure 2.28 Test setup.

Based on the results of these tests, Thomas concluded that, for specimens PS2.5 (with thin plate stirrups) and HS2.5 (with headed stud–rails), lateral–drift ratios of approximately ±5% were reached when the lateral load capacity dropped to 80% of the peak lateral loads as explained in **Figure 2.29**. Both specimens PS2.5 and HS2.5 achieved a higher degree of ductility and hysteretic energy dissipation than specimen C0 (without shear reinforcement). Specimen C0 failed in brittle punching shear manner (that is, stress-induced punching failure) at –1.85% drift. Also the measured drift ratio at punching for Specimen C0 was close to the ACI 318–051 drift limit for nonparticipating frames (2%), whereas the drift ratios at punching for specimens PS2.5 and HS2.5 were substantially higher than the ACI 318–05 limit (2%) or the mean value (3.25%) based on previous tests.

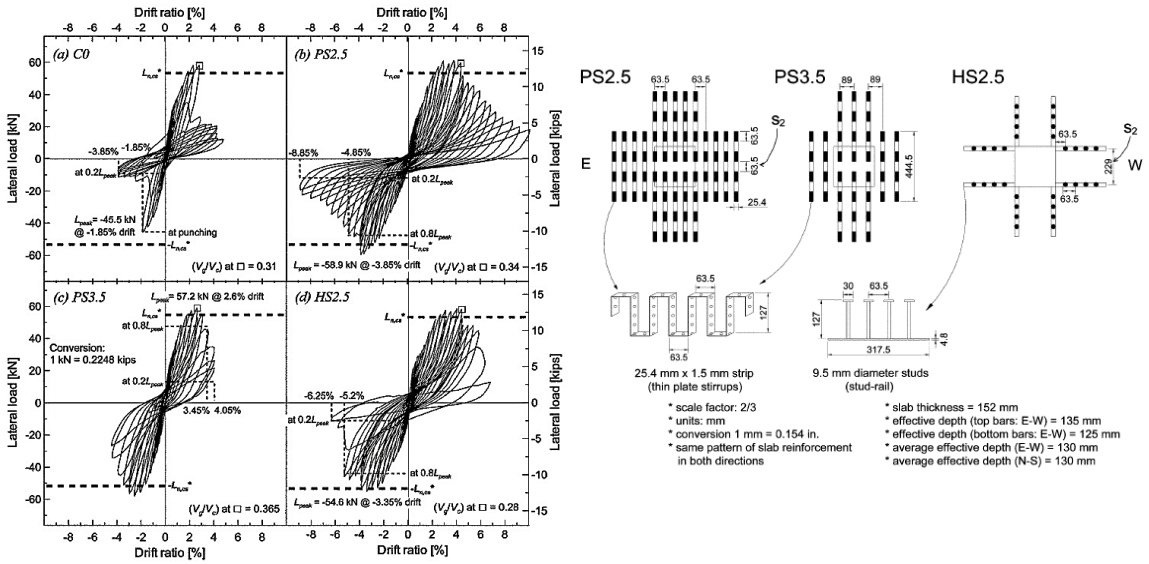

Figure 2.29 Relations for lateral load versus lateral drift ratio.

Jin–Kyu Song et al. (2012) examined three isolated interior flat slab-column connections that include three types of shear reinforcement details; stirrup, shear stud and the shear band under reversed cyclic lateral loading to observe the capacity of slab-column connections. All specimens had the same configurations except shear reinforcement details at the slab-column connections: control specimen with no shear reinforcement (which is denoted as RC1); stirrups (SR1); headed shear stud (SR2); and shear bands (SR3). The slabs (135mm thick) were approximately two–thirds scale with a bay size of 3000 mm × 3000 mm supported by a square column of 300mm x300mm, the details of shear reinforcement are explained in **Figure 2.30**. The slabs were subjected to a gravity load equivalent to 40% of the nominal punching strength (=1/3$\sqrt{f'_c}\ b_o\ d$) of slabs then the specimens were subjected to repeated lateral loads using the displacement control method according to the displacement ratio between stories of a load acting point by using an actuator connected to the upper part of the columns. While repeated lateral load experiments are operating, the gravity load ratio kept on the joints at a certain level by controlling the camber load.

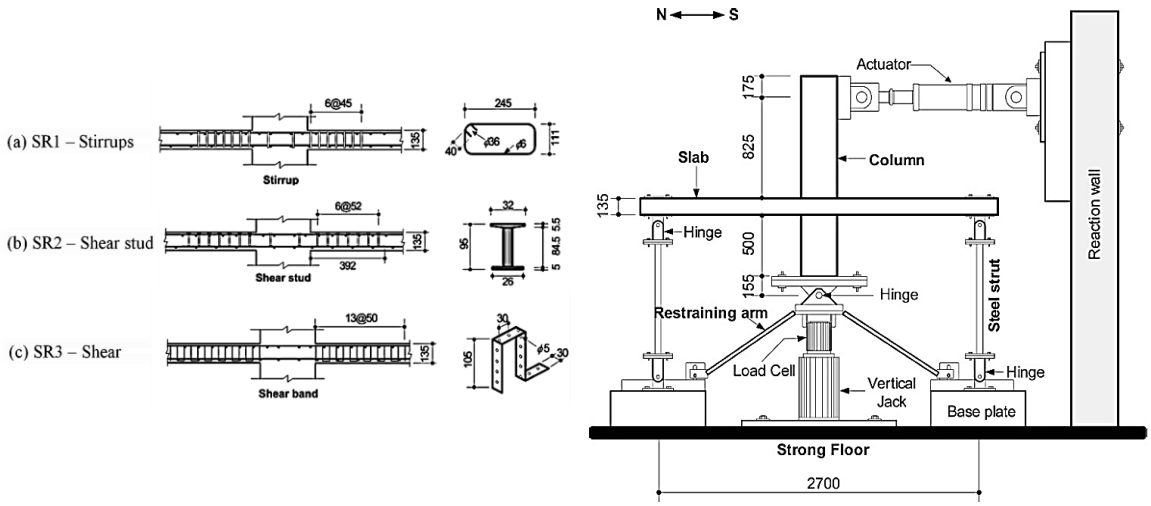

Figure 2.30 Details of the shear reinforcements (unit: mm), and test setup.

Song concluded that installing the correct shear reinforcement may improve the seismic capacity of flat plate connections, the unbalanced moment strength as well as punching shear strength increase by the shear reinforcement for joint of the slab. This is caused by the expanded range resistant to the unbalanced moment, which is due to the plastic redistribution of flexural stress by the shear reinforcement. The experimental results showed that the unreinforced specimen, RC1, reaches the greatest strength of 50 kN at a 1.4% lateral displacement ratio and

sudden punching destruction occurs at a 1.8% lateral displacement ratio, with a joint strength of 38 kN. After punching, the lateral load strength in the joints reduces to about 20% of the maximum strength. The strength reduces and is maintained at the strength greater than 40 kN of the 4.1% lateral displacement ratio.

Unlike RC1, the SR2 and SR3 specimens, in which the stud and shear band are used, do not show brittle punching after maximum strength is reached. The maximum lateral load strength appears to be 50 kN at a 2.3 lateral displacement ratio and 61 kN at a 2.7% lateral displacement ratio. SR2 and SR3 maintain the strength of over 40 kN for 4.5% of the lateral displacement ratio and 8% of the lateral displacement ratio, respectively. These 3–types of shear reinforcements which have designed to have identical punching shear capacities showed different influences for deformation capacity as shown in **Figure 2.31**. The strength and displacement capacity of specimens using shear reinforcement increases significantly compared to that of the unreinforced specimen. SR3, where the shear band was used, showed high lateral displacement compared to other reinforced joints.

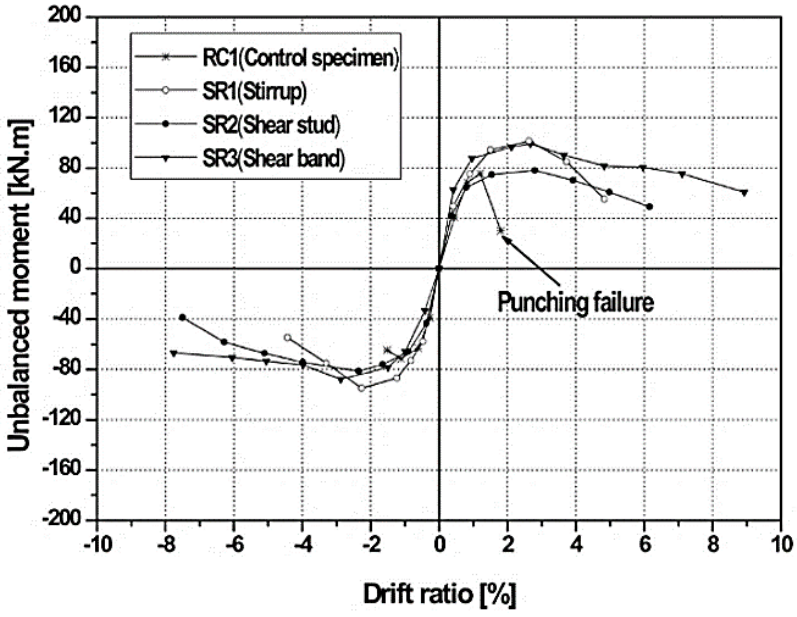

Figure 2.31 Envelope curve of the specimens.

Ioannis Drakatos et el. (2016) tested thirteen full–scale internal slab-column connections without transverse reinforcement. The objective of the test was to assess the influence of the loading history (monotonic vs. reversed cyclically) for different gravity loads and reinforcement

ratios. The dimensions of the specimens were 3000×3000 mm and the slab thickness was 250 mm. The column size was equal to 390×390 mm for all tested slabs. Three different types of loading are distinguished: V stands for the application of symmetrical vertical loads, whereas M and C represent the introduction of monotonically and cyclically increasing unbalanced moments, respectively. The vertical load was applied using four hydraulic jacks, these vertical loads modelled all superimposed loads and the gravity loads of the slab part that was not included in the test setup (0.22–0.50L) as shown in **Figure 2.32**. The effects of seismically induced drifts were simulated by applying two equal and opposite vertical forces by means of two servo-hydraulic actuators. The slab edges were reinforced with additional bars to account for the part of the slab that is not represented by the test setup and to connect the slab to the steel beams for the moment application.

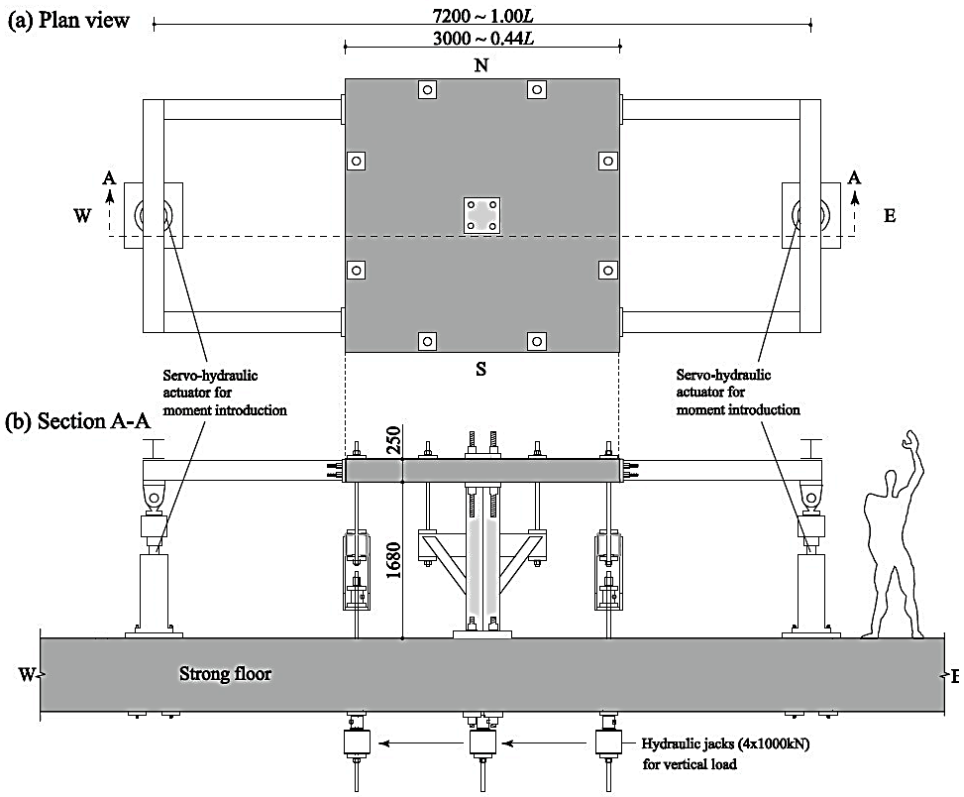

Figure 2.32 Test setup.

Drakatos concluded that reversed cyclic loading reduces the moment capacity and the deformation capacity of slab-column connections. This effect is more pronounced for smaller gravity loads and smaller reinforcement ratios. Moreover, increasing gravity loads reduces the

stiffness and the moment capacity of slab-column connections as observed by others. Further, increasing reinforcement content resulted in general in higher stiffness and lower deformation capacity, as has been noted by previous studies. For low gravity loads, increasing the reinforcement ratio had however little influence on the moment capacity. For high gravity loads, increasing the reinforcement ratio had little influence on the deformation capacity, ACI–318 and fib–MC2010 provide the most conservative estimates of the moment capacity, followed by EC2 with respect to both accuracy and precision.

Thomas H.K. Kang, et al. (2017) recently tested three half–scale specimens of RC interior slab-column connection subassemblies the combined effects of constant gravity and reversed cyclic lateral loads. The slab-column connections were constructed with the same flexural reinforcing ratio but with different shear reinforcing methods as present in **Figure 2.33**. One specimen with no shear reinforcement relied on the punching shear capacity of the concrete only (SN). The other two specimens were shear–reinforced with closed stirrups and shear bands, respectively (SST and SSB). The shear reinforcement was extended to 2.2h (330 mm) and 2.6h (390 mm) away from the column face for the specimens with stirrups and shear bands (SST and SSB), respectively.

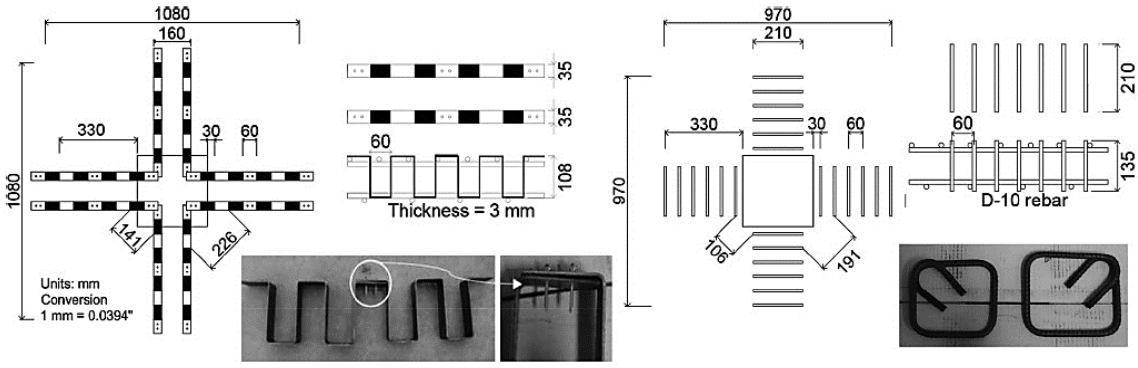

Figure 2.33 Details of the shear reinforcements.

Based on his test results Thomas concluded that seismic behavior of reinforced concrete interior slab-column connections with a relatively large tension reinforcing ratio was significantly improved by the use of either closed stirrups or shear bands. The ductile failure mode was characterized by larger drift capacity (over 4% drift), energy dissipating capacity, and gradual strength degradation and degree of flexural yielding due to enhanced connection integrity. In comparison to closed stirrups, the performance of shear bands was equally excellent as shown

in **Figure 2.34**. The shear band had the same degree of bond strength as the closed stirrups. The drift capacity of approximately 4% or larger was obtained with a gravity shear ratio of approximately 0.5.

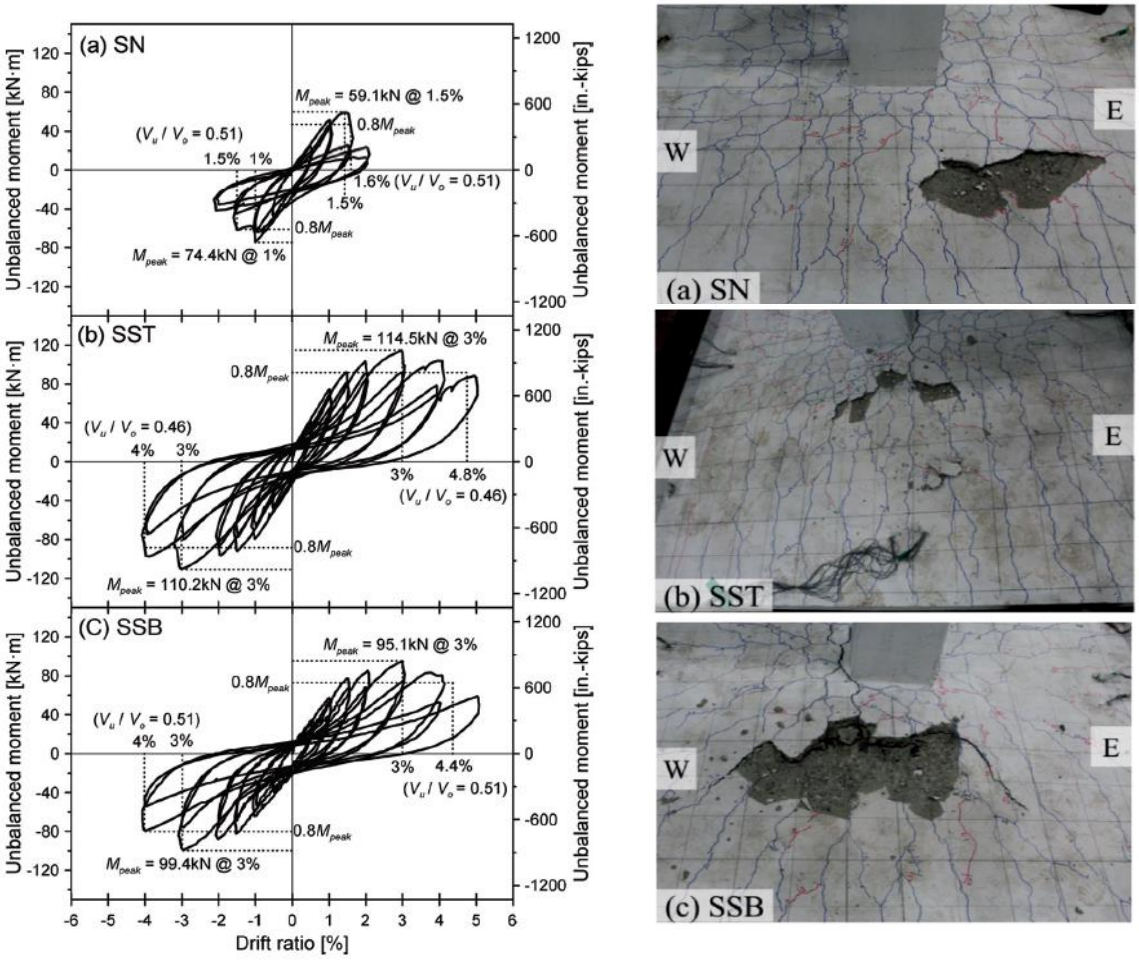

Figure 2.34 Relations of lateral load versus lateral drift ratio and observed damage after seismic tests.

CHAPTER 3. EXPERIMENTAL PROGRAM

3.1. Introduction

Through the Natural Sciences and Engineering Research Council of Canada (NSERC) industrial research chair, an extensive research project has been conducted at University of Sherbrooke to develop and implement GFRP reinforcement bars for RC two–way slabs parking garages. The first phase of this project has completed [Dulude et al. (2013) and Hassan et al. (2013)]. A total of thirty GFRP–reinforced two–way slabs with and without shear reinforcement under concentric punching shear failure were tested. The test results gave a complete understanding of the punching behavior of two–way flat slab reinforced with FRP bars under concentric loading. Also, this study highlighted the significant contribution of FRP stirrups as shear reinforcement in FRP two–way slabs.

The second phase on this project is to investigate the punching shear behvaior of FRP–reinforced two–way slabs under lateral cyclic loading. This chapter presents the details of the experimental; material properties of GFRP, steel reinforcing bars and concrete will be used in this study. Detailed descriptions of the prototypical structure and test specimens, specimen notation and different tests, specimen construction, test instrumentation, test procedure and details of the test setup will be highlighted.

3.2. Material Properties

3.2.1. Reinforcement Properties

Two types of reinforcing bars were used in this study; CSA grade 400 deformed steel bars and sand–coated GFRP V–RODTM (Pultrall Inc.). Two types of reinforcement stirrups were also used; CSA grade 400 deformed steel stirrups and sand–coated GFRP closed and spiral continuous stirrups (Pultrall Inc. 2007). The GFRP bars are classified according to their modulus of elasticity (E_f): Grade *I* (E_f <50 GPa), Grade *II* (50 GPa ≤ E_f < 60 GPa), and Grade

III ($E_f \geq 60$ GPa) as shown in **Figure 3.1**. Sand–coated GFRP bars (V–ROD) Grade *III* of sizes No. 15 and No. 20 designated according to the CSA S807 (2010) were used as flexural reinforcement for all test specimens. **Figure 3.1** shows the steel and GFRP bars with different diameters used in this research project. The GFRP bars were manufactured by combining the pultrusion process with an in-line sand coating to enhance the bond between the bars and the surrounding concrete.

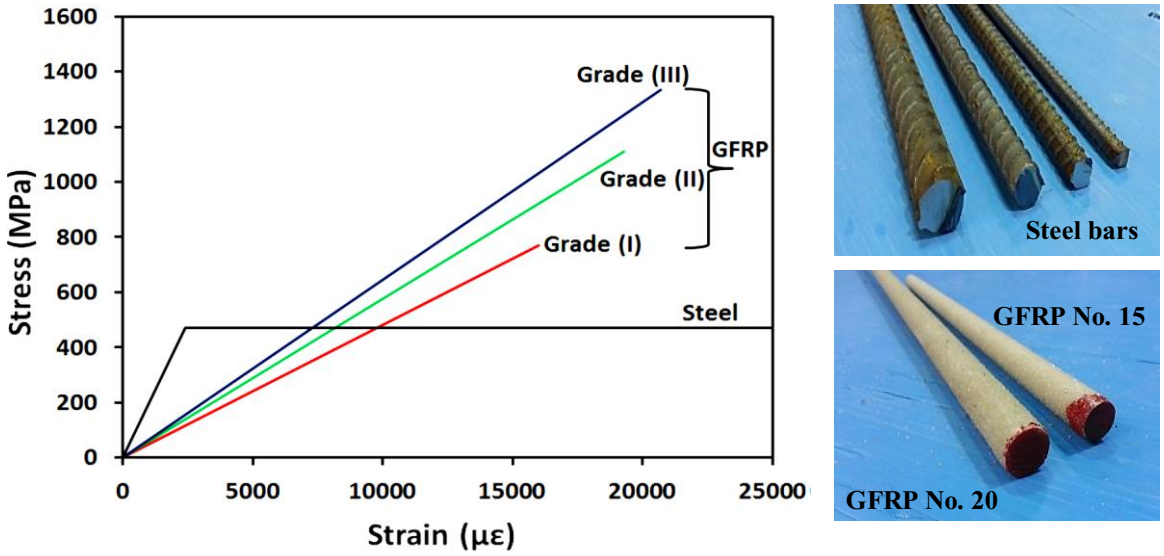

Figure 3.1 Typical stress-strain relationships for the reinforcing bars.

The tensile properties of the GFRP bars were determined by testing five representative bars for each diameter in accordance with ASTM D7205M (2011). All the test samples were prepared by anchorage steel tubes at both ends as anchorages using commercially available cement grout Brister 10. Then, the samples were tested in tension using BALDWIN machine up to failure. **Figure 3.2** Shows a typical tensile test and bars rupture. Table 3.1 summarizes the mechanical properties of the GFRP and steel bars. Two types of deformed steel bars were used to reinforce the control specimens (15M and 20M) and deformed steel bars (25M) were used as a longitudinal bar to reinforce all slabs column's with a yield stress of 470 MPa and modulus of elasticity of 200 GPa, while (10M) as stirrups.

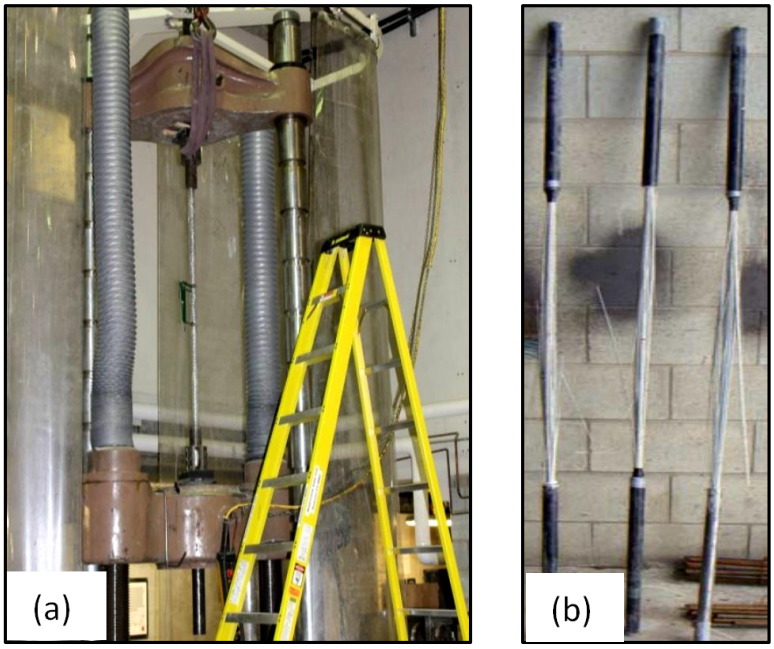

Figure 3.2 Typical tension testing of GFRP bar: (a) Test setup; (b) GFRP bar rupture.

Table 3.1 Properties of the reinforcing bars.

RFT Type	Grade [a]	Bar Size	Area mm^2	Elastic Tensile Modulus, E_f, GPa	Ultimate Tensile Strength, MPa	Characteristic Tensile Strength [b], MPa	Ultimate Tensile elongation, %
GFFRP	III	No.15	199	62.6±2.5	1239	1184	1.89
		No.20	285	63.7±2.5	1196	1105	1.89
Steel	44 W	No.20	300	200	fu=620	Fy=470	εy=0.24
		No.15	175	200	fu=620	Fy=470	εy=0.24
		No.25	490	200	fu=620	Fy=470	εy=0.24
		No.10	79	200	fu=620	Fy=470	εy=0.24

The tensile strength and tensile modulus of the GFRP bars were determined with Eqns. (3.1) and (3.2), respectively. Where f_u is the tensile strength (MPa), F_u is the tensile capacity (N), A is the nominal cross-sectional area of the GFRP bar (mm^2), E is the tensile modulus of elasticity (MPa), F_1 and ε_1 are the load and corresponding strain, respectively, at approximately 50% of

the ultimate tensile capacity; and F_2 and ε_2 are the load and corresponding strain, respectively, at approximately 25% of the ultimate tensile capacity.

$$f_u = \frac{F_u}{A} \qquad (3.1)$$

$$E = \frac{F_1 - F_2}{(\varepsilon_1 - \varepsilon_2)A} \qquad (3.2)$$

Two types of reinforcement stirrups were also used; CSA grade 400 deformed steel stirrups and sand–coated GFRP closed and spiral continuous stirrups No. 10, All the FRP stirrups were delivered prefabricated and produced by (Pultrall Inc.). **Figure 3.3** shows the configurations of the investigated stirrups. Five straight samples of FRP stirrups were tested in accordance with ASTM D7205M (2011). The mechanical properties of the GFRP stirrup are reported in Table 3.2.

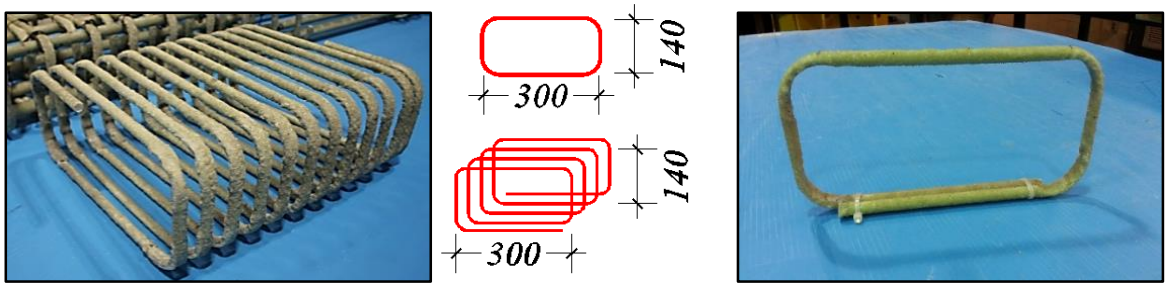

Figure 3.3 Sand–coated GFRP stirrups.

Table 3.2 Test results of the tension characteristics of GFRP No. 10 (9.5 mm)

Specimen	f_{fv} (MPa)	E_{fv} (GPa)	ε_{fu} (%)
1	971	45	2.13
2	968	44	2.18
3	973	45	2.16
4	881	44	1.98
5	946	45	2.11
Average	948	45	2.11
SD	39	0.45	0.08
COV%	4.08	1.00	3.66

The bend strengths of the GFRP stirrups was determined by testing five specimens using the B.5 test method in accordance with ACI 440.3R–04 (2004). The B.5 test method evaluates the bending strength of C–shaped FRP stirrups through embedment in two concrete blocks, which are pushed apart until the rupture of the FRP stirrups. **Figure 3.4** shows the dimensions of the

C–shaped specimens for the B.5 test method. **Figure 3.5** shows the preparation of the specimens. The C–shaped FRP specimens were prepared to keep the two sides of the stirrups as a continuous end in the concrete block. One side of the stirrups was provided with debonding tubes. These debonding tubes were secure into the desired position with silicone and duct tape. The dimensions of the concrete blocks were 500×300×200 mm. The free length of the stirrup between the two blocks was kept constant at 400 mm. Each block was reinforced transversally with 10 mm–diameter steel stirrups spaced 65 mm to prevent any premature splitting prior to rupture of the FRP stirrups. The test specimens were cast using ready–mixed normal weight concrete (Type V, MTQ with a target compressive strength of 35 MPa after 28 days).

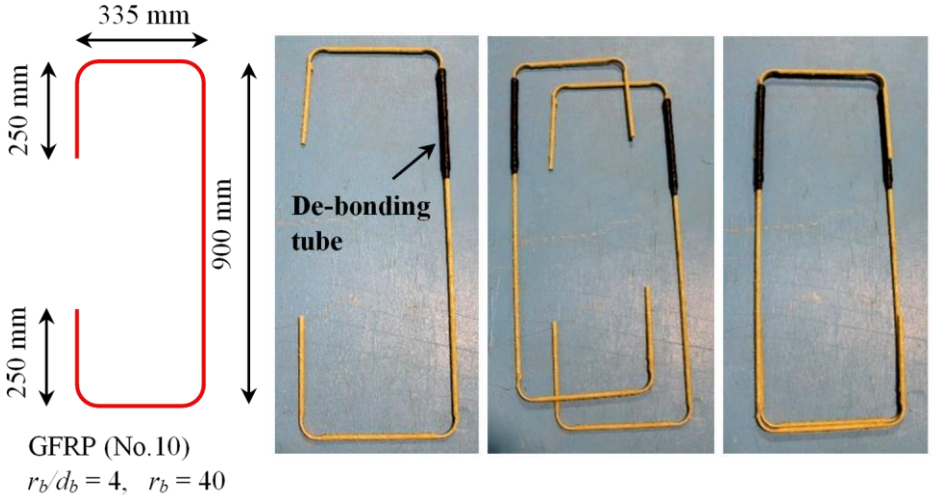

Figure 3.4 Dimensions of the C–shaped specimens for the B.5 test method.

Figure 3.5 Preparation of the test specimens.

After casting, all concrete blocks were cured and stored indoors for 28 days before testing. **Figure 3.6** shows the setup during testing of FRP stirrup in concrete blocks (B.5). The two blocks (for each test) were adjusted on the horizontal testing bed and the inner concrete surface of each block was cleaned. One of two blocks was placed over a moving roller (the moving side) to allow for the horizontal movement and minimize the friction between the block and the testing bed. Following the preparation and placing the moving side block on the roller, two steel plates were placed in front of the inner faces of the concrete blocks to distribute the hydraulic jack loading. The load was applied by pushing the two concrete blocks apart until the failure of the bent specimen. The test specimens failed due to the rupture of FRP bars at the bend, which was followed by slippage of FRP bars out of the concrete blocks as shown in **Figure3.6**. The failure load was recorded and the bending strength was calculated from Eq. (3.3).

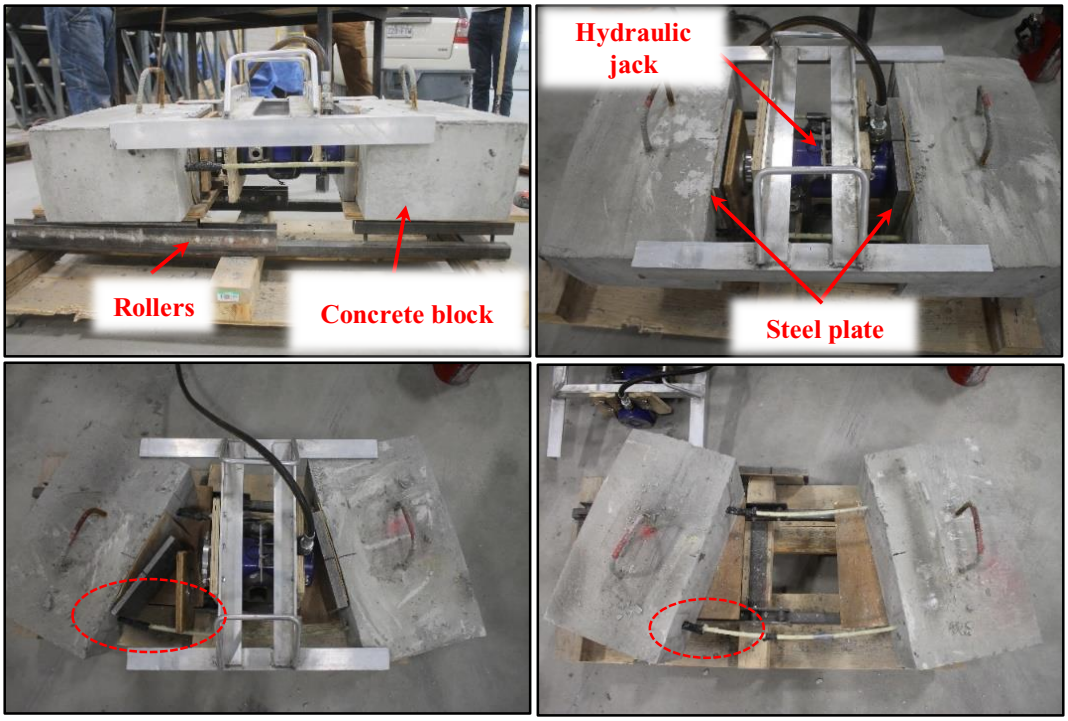

Figure 3.6 B.5 method test setup and rupture of the FRP stirrups.

The measured strengths of the GFRP stirrups at the bend location were reported in Table 3.3. Where f_{bend} is the bending strength (MPa), P_u is the failure load (N), and A is the FRP bar cross-sectional area (mm^2).

$$f_{bend} = \frac{P_u}{2A} \qquad (3.3)$$

Table 3.3 Test results of the bending strength of FRP C–shaped stirrups

Specimen	1	2	3	4	5	Average	SD	COV %	f_{fub}/f_{fv}
P_u (kN)	74	68	82	72	62	72	3.7	5.17	——
f_{fub}	521	479	577	507	437	504	26	5.14	0.53

3.2.2. Concrete Properties

The slab-column connections were designed and constructed using a ready–mixed, normal–strength concrete (NSC) and high strength concrete (HSC). The target compressive strengths of NSC and HSC were 35 MPa and 60 MPa respectively. The slump of the fresh concrete was measured before casting as shown in **Figure 3.7** and was between 80 mm to 100 mm. Twelve concrete cylinders 100×200 mm were cast from used concrete and cured under the same conditions as the test slabs as shown in **Figure 3.7**. The actual concrete compressive and tensile strengths were determined based on the average value of six cylinders for the compressive test and three for the tensile splitting test carried out at the day of slab testing.

Figure 3.7 Slump test before casting and preparation of concrete cylinders.

3.3. Specimen Configurations

The prototype structure for this investigation was a parking garage flat–plate building with 5000×5000 mm panels, the columns were typicality 300×300 mm in cross-section and story height 2800 mm **Figure 3.8**. The live load was assumed to be 2.4 kN/m^2 and superimposed dead load of 1.0 kN/m2. The total gravity load on the floor, including the slab weight, was estimated according to NBCC (2015). A total of eight full–scale interior slab-column connections were reinforced with GFRP bars and one specimen was reinforced with steel bars for comparisons. All test specimens were measured 2500×2500 mm with thicknesses of 200 mm, while the square column stub measured 300×300 mm. The column stub extended 700 mm beyond the top and bottom surfaces of the slabs.

The test specimens were designed to simulate real thicknesses flat slabs being used in the field applications "*La Chancelière parking garage*" (Benmokrane et al. (2012). The structural system of this parking is a two-way flat slab supported on columns and retaining walls. This design was made according to the CAN/CSA-S413-07 for parking structures and CAN/CSA-S806-12 for design and construction of building components with fibre reinforced polymers. The dimensions of the slabs were chosen to represent the locations of contra–flexure lines for the case of gravity loads and were in agreement with the past tests conducted at the University of Sherbrooke [Dulude et al. (2013) and Hassan et al. (2013)]. In the case of gravity plus horizontal cycling loads (as in the case of the presented tests), the locations of contra–flexure lines normal to horizontal loading direction change depending on the direction of the horizontal loading. Therefore, thick neoprene pads were provided on top and bottom of the slab to allow rotations.

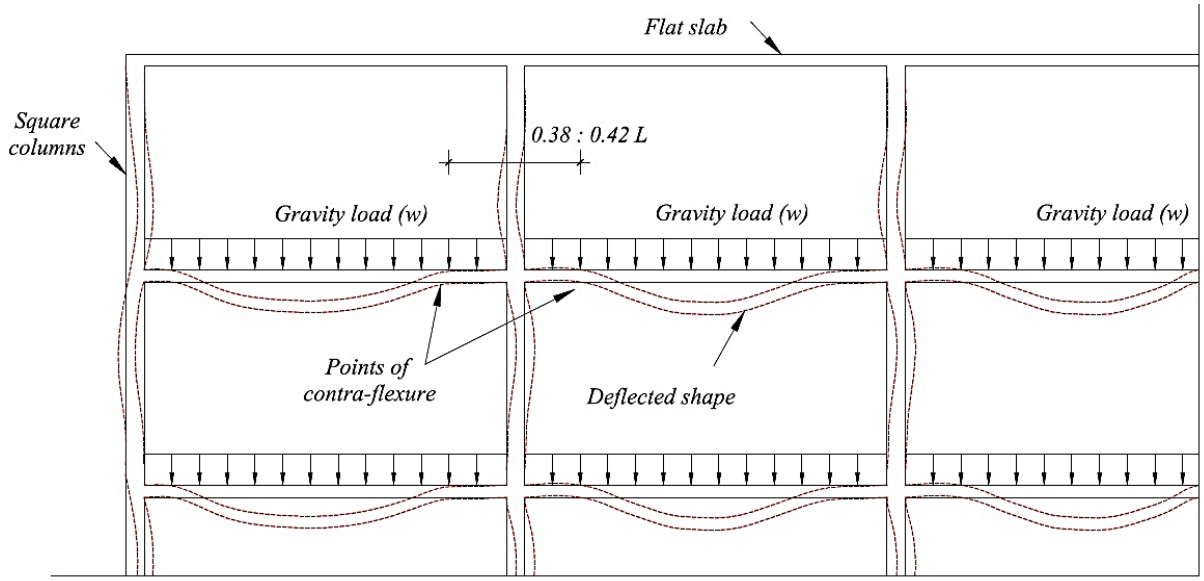

Figure 3.8 Elevation view of the prototype structure. [Yitzhaki (1966) and Schaefers (1984)]

The slabs were simply supported on a 2000×2000 mm perimeter on the bottom face of the slab **Figure 3.9**. All specimens had a typical bottom and top reinforcement configuration in each orthogonal direction.

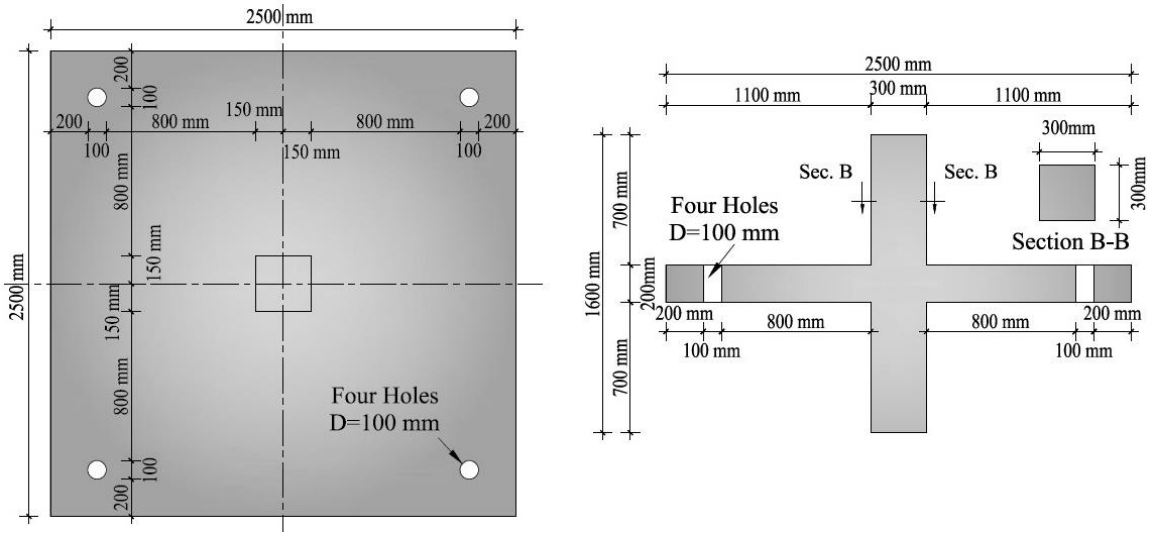

Figure 3.9 Typical geometry for tested specimens.

The specimens were designed to have a flexural–reinforcement ratio such that punching–shear failure would be expected to occur prior to flexural failure. The specimens were labelled with a letter denoting the tension reinforcement type: “S” for steel and “G” for GFRP. The subscripts 1.12%, 1.06%, and 1.51% stand for the flexural–reinforcement ratio, while the subscript “SL”

indicates the intensity of the gravity service load applied. Also "GCS" indicates the stirrups configuration [CS and SS denotes closed stirrups and bundle spiral stirrups, respectively]; "x*d*" the extension of the stirrups from the column faces relative to the effective depth. Table 3.4 and 3.5 presents the configuration and characteristics of each specimen.

The bottom flexural–reinforcement (tension side)—placed symmetrically in each orthogonal direction—consisted of 14 No. 20 or 20M bars **Figure 3.10 and 3.11**. The top flexural reinforcement (compression side)—symmetrically placed in each orthogonal direction—consisted of 10 No. 15 or 15M bars. The bottom flexural–reinforcement in specimen G2 was 20 No. 20 bars (tension side) and the top flexural reinforcement (compression side) was 10 No. 20 bars. The reinforcing ratio on the compression side of all the slabs was half that of the tension reinforcement. Two bars ran through the column core on the compression side to satisfy the requirements for structural integrity reinforcement in CSA A23.3 (2014). The clear concrete cover in the direction of the lateral cycling loads was 30 mm. The average effective depth of the slabs *d* was 151 mm. The column was heavily reinforced with steel bars (reinforcement ratio of 3.0%) to make the column strong enough to transfer shear force and cyclic moments to the slab and to avoid column failure during testing. The column was reinforced with six longitudinal deformed 25M steel bars. In addition, closed deformed 10M steel ties were used spaced at 100 mm.

Specimens $G5_{GCS–4.5d}$, $G6_{GCS–2d}$ and $G8_{GCS–4.5d–SL}$, were reinforced with discrete four branches of GFRP closed–stirrups No. 10. Specimen $G7_{GSS–4.5d}$ was reinforced with four branches GFRP spiral–stirrups No. 10. For all GFRP shear–reinforced specimens the stirrups were extended to 4.5*d* away from the column face. In order to evaluate the effect of the stirrup extension on the punching behaviour, in specimen $G6_{GCS–2d}$ the stirrups extended to 2*d* away from the column face (see **Figure 3.10, 3.11** and **3.12**). The shear reinforcement stirrups were arranged in a cruciform pattern according to ACI 318 (2014) and CSA A23.3 (2014). The spacing between the consecutive lines were 0.5*d*. The first perimeter was offset 0.4*d* from the column face for all slabs with shear reinforcement. For all shear reinforced specimens, the number of peripheral lines of shear–reinforcement was nine in both directions and was four lines in specimen $G6_{GCS–2d}$.

Table 3.4 Details of test specimens: Phase I: Slabs without shear reinforcement.

Phase	Specimen	Tens. Reinf.	Comp. Reinf.	ρ_T, %	$\rho_{bott.}$ %	ρ_b, %	f'_c MPa	f_t *MPa*	Test parameters	Gravity–Load Intensity V_u (KN)
I	**S1$_{(1.12)}$**	14–20M	10–15M	1.12	$0.5\rho_f$	4.29	52	3.93	RFT type	(D.L+0.3 L.L)
	G1$_{(1.06)}$	14 No.20	10 No.15	1.06		0.37	52	3.93	RFT type	(D.L+0.3 L.L)
	G2$_{(1.51)}$	20 No.20	10 No.20	1.51		0.33	46	3.36	RFT ratio	(D.L+0.3 L.L)
	G3$_{(1.06)}$–SL	14 No.20	10 No.15	1.06		0.33	46	3.36	Gravity load intensity	(D.L+L.L)
	G4$_{(1.06)}$–H	14 No.20	10 No.15	1.06		0.53	92	6.20	Concrete compressive strength	(D.L+0.3 L.L)

Table 3.5 Details of test specimens: Phase II: Slabs with shear reinforcement.

Phase	Specimen	Tens. Reinf.	Comp. Reinf.	ρ_T, %	$\rho_{bott.}$ %	ρ_b, %	f'_c MPa	f_t *MPa*	Shear RFT type	Test parameters	Gravity–Load Intensity V_u (KN)
II	**G5$_{GCS–4.5d}$**	14 No.20	10 No.15	1.06	$0.5\rho_f$	0.33	45	3.75	4–GC stirrups (No.10)–4.5d	Glass Stir. distribution	(D.L+0.3 L.L)
	G6$_{GCS–2d}$	14 No.20	10 No.15			0.33	45	3.75	4–GC stirrups (No.10)–2.0d	Glass Stir. distribution	(D.L+0.3 L.L)
	G7$_{GSS–4.5d}$	14 No.20	10 No.15			0.36	51	3.86	4–GS stirrups (No.10)–4.5d	Stir. Shape closed or spiral	(D.L+0.3 L.L)
	G8$_{GCS–4.5d–SL}$	14 No.20	10 No.15			0.36	51	3.86	4–GC stirrups (No.10)–4.5d	Gravity load intensity	(D.L+L.L)

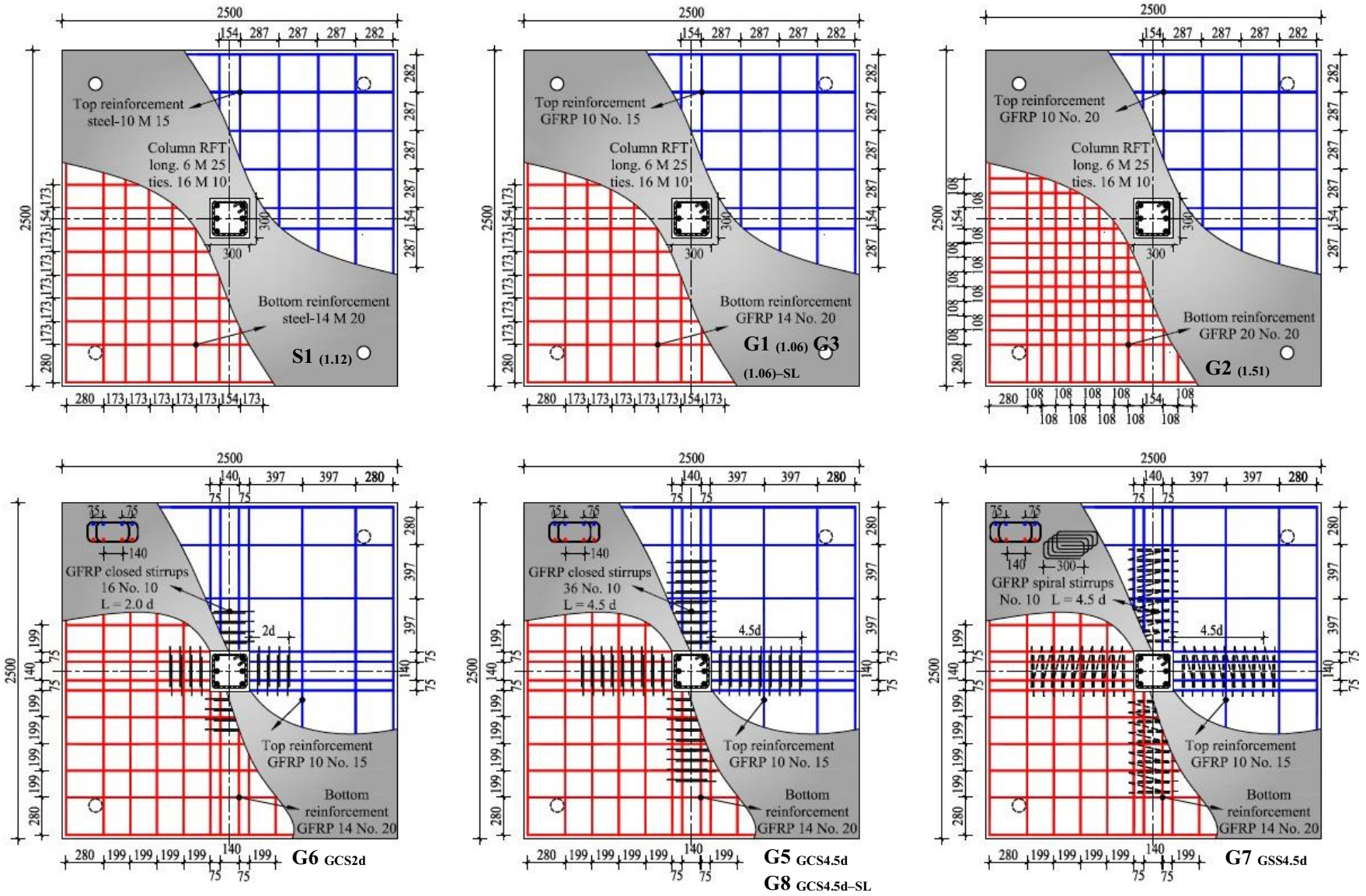

Figure 3.10 Reinforcement details for all specimens (plan).

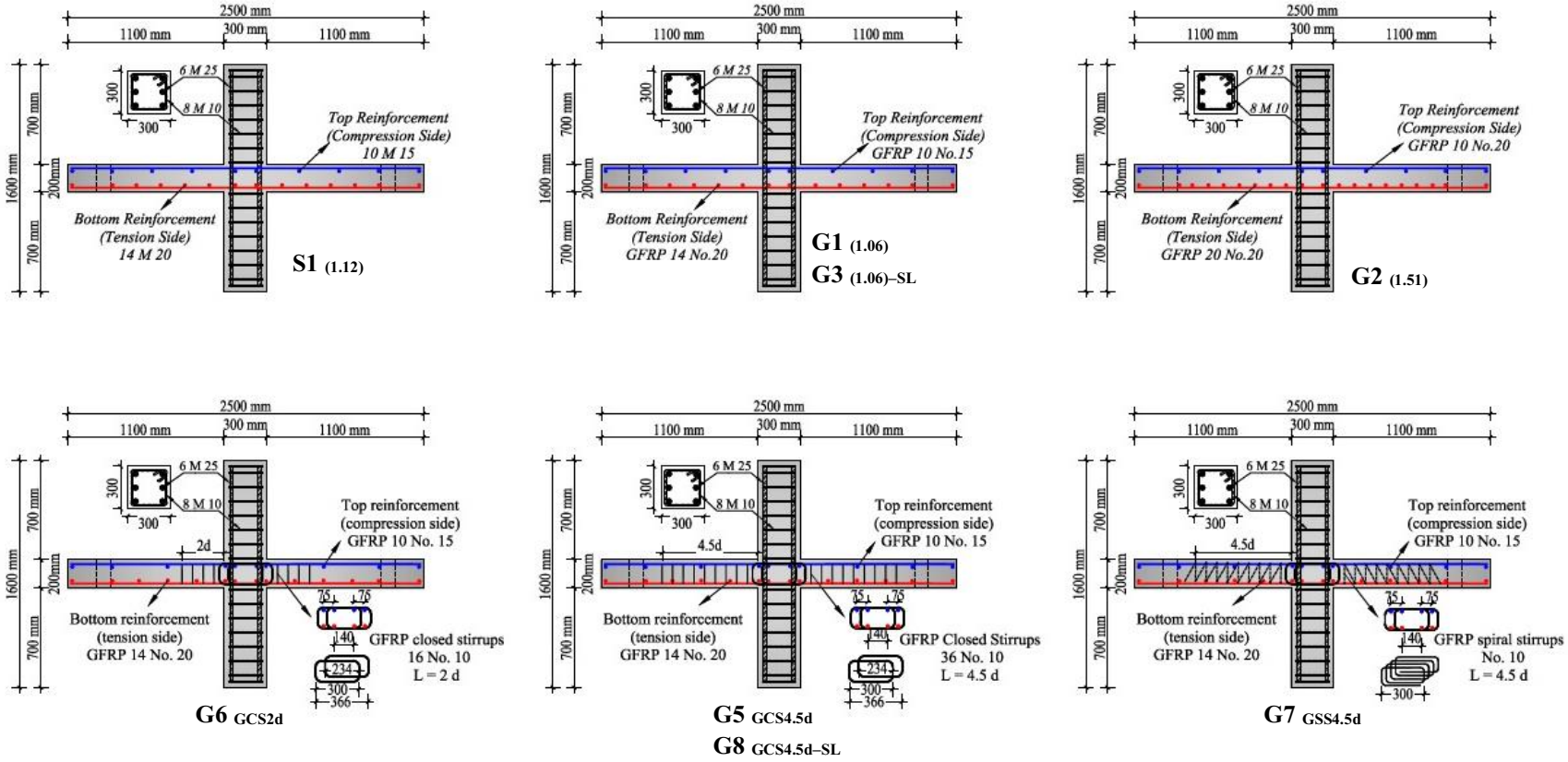

Figure 3.11 Reinforcement details for all specimens (Elevation).

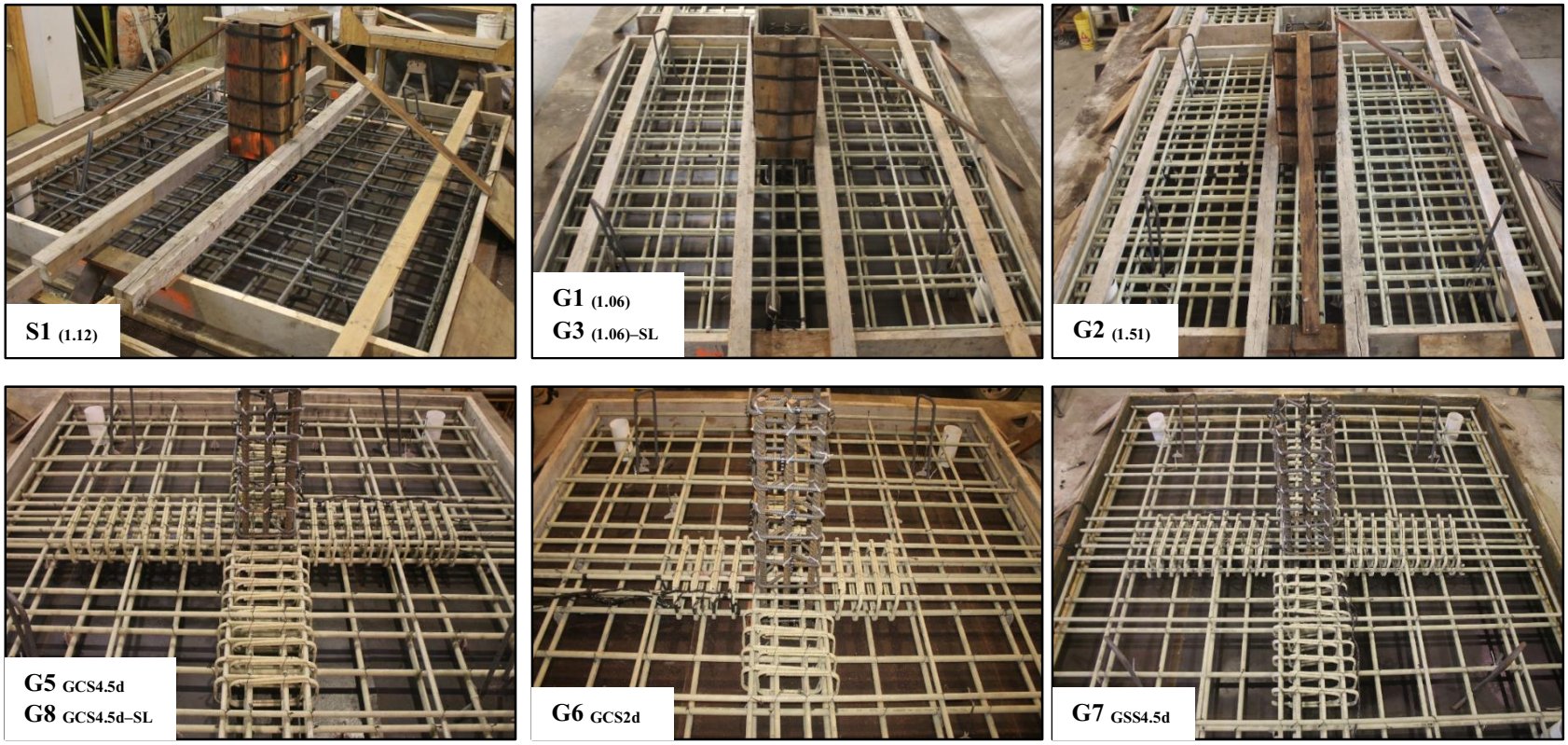

Figure 3.12 Reinforcement configuration for all specimens.

3.4. Fabrication of the Specimens

Construction of tested specimens consisted of the following steps: preparation of the formwork, assembled the slabs reinforcements and column cages, installation of steel column cage thereafter the slab reinforcements, casting the specimens and curing. All specimens were cast in a wood formwork designed to cast two specimens each time. **Figure 3.13** represents the wood formwork which was built using 3/4 in thick plywood as a slab platform and as part of the column forms. Steel I–beams were used to supporting the elevated slab platform. Before assembling the reinforcing cage, the formwork was lubricated with thick oil to provide ease in formwork removal. Four PVC pipe with 10 mm diameter were placed inside the slab before casting at each slab's corner to enable anchorage the specimen through them during testing.

Figure 3.13 Wooden formwork.

All steel columns cages, steel and FRP slab reinforcement cages were assembled first separately then the steel cage for the column was placed inside the formwork first thereafter the tension and compression reinforcement were placed on plastic chairs to get the required concrete cover and finally a vertical steel hooks were placed at each slab corner to carry the slabs after removing from the formwork as shown in **Figure 3.14**. While the specimens with shear reinforcement, the GFRP stirrups shear reinforcement were assembled together first in each direction separately then collecting the reinforcement cage together. **Figure 3.15** shows the shutting and fabrication of the specimens.

Figure 3.14 Shuttering and fabrication of specimens without shear reinforcement.

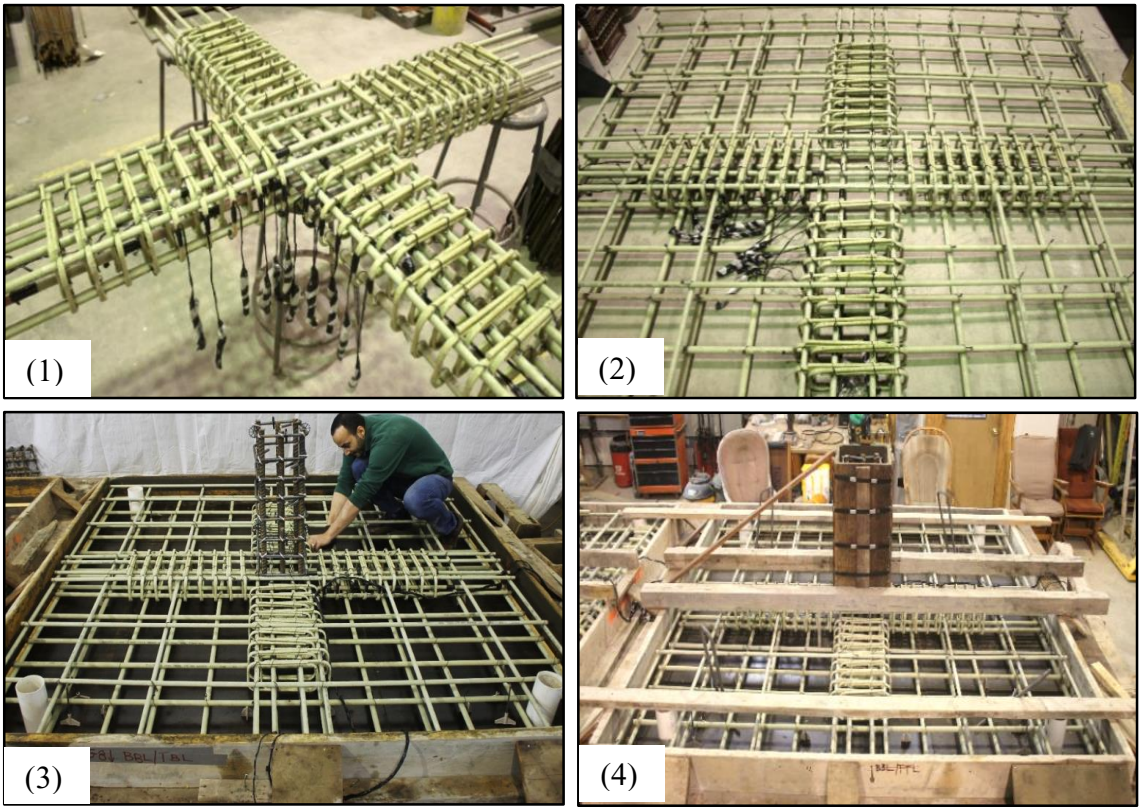

Figure 3.15 Shuttering and fabrication of specimens with shear reinforcement.

A normal–weight ready–mix concrete was used, once the concrete was poured the slabs was internally vibrated by electrical vibrators, and when casting was completed, the surface of the concrete slab was adjusted manually. The bottom and top column stub were cast with the slab on the same day, superplasticizers were used to increase the concrete workability. **Figure 3.16** shows the concrete casting of the test specimens. Standard concrete cylinders (100×200 mm) were cast simultaneously with the slabs. After casting by twenty–four hours, the cylinders and the external sides of the formworks were stripped and then the slabs and the concrete cylinders were covered with wet burlap for 7 days. After one week of curing, the specimens were moved out from the formwork and placed outdoor until the day of testing as shown in **Figure 3.17**. Before testing, each slab was coated with whitewash to facilitate the observation of cracking during testing. The average compressive concrete strength at the day of slab testing was determined based on testing three standard cylinders as given in Table 3.4 and 3.5 for each specimen.

Figure 3.16 Concrete casting procedure of the test specimens.

Figure 3.17 Curing method and storage of the test specimens.

3.5. Instrumentation

The specimens were extensively instrumented for testing. **Figure 3.18** shows the positions of the external and internal instrumentation. Each specimen had a group of displacement transducers (potentiometers or pots) to monitor the vertical displacement and column lateral displacement. On the top slab face, nine pots were aligned vertically along two perpendicular directions at 100, 300, and 600 mm from the column face. Additional two vertical pots were installed on the bottom slab face along two perpendicular directions at 100 mm from the column face. The diagonal shear–crack widths inside the slab were estimated using the vertical–displacement differences. One pot was installed on the centerline of the bottom column to record vertical deflection. One pot was attached horizontally to both ends of the column to measure lateral drift. Lastly, two horizontal pots were installed on the centerline of the slab thickness and the lower supporting frame to detect any movement in the lateral–loading direction. To prevent any frame deformations from affecting the measurements, all pots were attached to a rigidly independent steel rod directly fastened to the laboratory floor. The flexural

cracks width were measured with two LVDTs on the slab tension face. The LVDTs were installed at the locations of the first flexural crack in each direction.

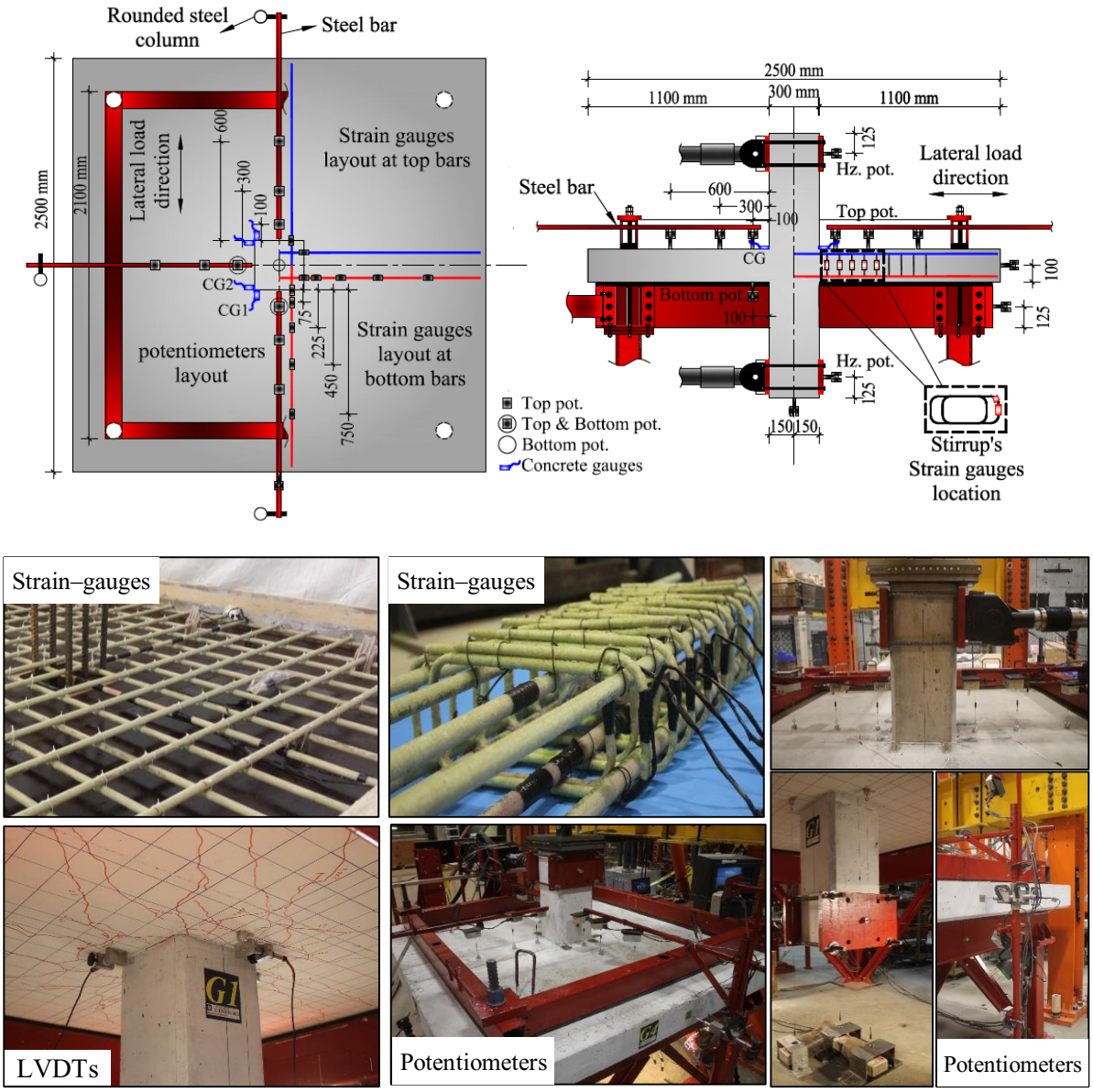

Figure 3.18 Positioning of internal and external instrumentation.

Two instrumented bars were installed in both orthogonal directions on the bottom flexural–reinforcement (tension side). Five electrical strain gauges [6 mm with gauge factor 2.07] were attached to each bar at 0, 75, 225, 450, and 750 mm from the column face (see **Figure 3.18**). In addition, one strain gauge was attached to the top reinforcing bar (compression side) at the column face in both orthogonal directions. Six concrete electrical strain gauges [60 mm with

gauge factor 2.08]—labelled CG1 to CG6—were glued to the compression face of the slab to monitor concrete strains: four at the comers of the column in the direction of the lateral loads and two in the transverse direction. The strain gauges, pots, and LVDTs were connected to a data acquisition system to record all values. In each orthogonal direction at d/2, d, 1.5d, 2d and 2.5d from the column face, the strain in the vertical legs of GFRP stirrups were measured. One electrical strain gauges also were glued at the bend portion of the stirrups at distance d/2.

3.6. Test Setup and Loading Procedures

A new test setup was designed and fabricated at the University of Sherbrooke's laboratory to test all specimens under combined gravity load and lateral reversed cyclic loading. The gravity load was acting on the column stub from the top side of the slabs. While the lateral cyclic loads acting on the column stub from both sides of the slabs simulating the lateral seismic load until failure. **Figure 3.19** and **3.20** shows the test setup used to test all specimens. The setup had two main supporting frames. The first supporting frame, which had two parts, was intended to carry the applied vertical load. The first part—the lower supporting bed—consisted of steel bottom reaction (box) beams [HSS: 250×150×8 mm], tied to four supporting steel (box) columns [HSS: 152×152×6 mm]. It was also laterally stiffened with back–to–back steel angles [102×102×7.9 mm]. The lower steel bed was prestressed directly on the laboratory floor with four vertical Dywidag bars [38 mm diameter]. The second part consisted of the steel upper reaction (box) beams [HSS: 152×100×6 mm]. It served to restrain the specimen from overturning due to lateral loads. Thick neoprene pads [20 mm thickness] were placed between the specimen and the lower and upper reaction beams. The upper steel box beams with the specimen and the lower supporting bed were fastened to the floor using four steel nuts and plates attached to the vertical Dywidag bars.

The second supporting frame consisted of two lateral steel frames. The frames were firmly fastened to the laboratory floor with four vertical Dywidag bars [38 mm diameter]. To restrain any possible frame lateral sway, two steel box beams [HSS: 152×152×6 mm] were installed between the lateral steel frames and the lower supporting bed (see **Figure 3.19** and **3.20**). A hydraulic Enerpac jack [1000 kN capacity] was attached to a stiff steel reaction I–beam to apply the gravity load at the top of the column. The I–beam was connected to the main steel frames

of the structural laboratory. To maintain the vertical load on the column during its lateral reversed movements, a rectangular steel plate with a crosshead was connected to the Enerpac jack. On the other hand, to reduce the friction between the column and the head of the Enerpac jack, a steel plate with 11 steel rollers was fabricated and installed on the top of the upper column, as shown in **Figure 3.19** and **3.20**. In addition, two horizontal hydraulic actuators [capacity of 250kN] were attached to the lateral frames and connected to the column ends to apply cyclic lateral–drift load.

Figure 3.21 shows the details of the lower supporting bed; the four supporting box steel column (HSS.152x152x6 mm) with length 1000mm; bottom reaction box steel beams (HSS.250x150x8 mm). The strength and the stiffness of the base beams are designed high enough to sustain the loading during in the experiments, the bottom supporting frame were installed on the strong floor and were fixed by two Dywidage bars diameter 38 mm. The bottom reaction beams were contact with the four supporting columns with 6 bolts A325–dim3/4 inch, the four bottom reaction beams were contact to gather with 6 bolts A325–dim1inch. Note: *The upper reaction beams should be instrumented in the future testing and observing the behavior of the beams in the lateral load direction*.

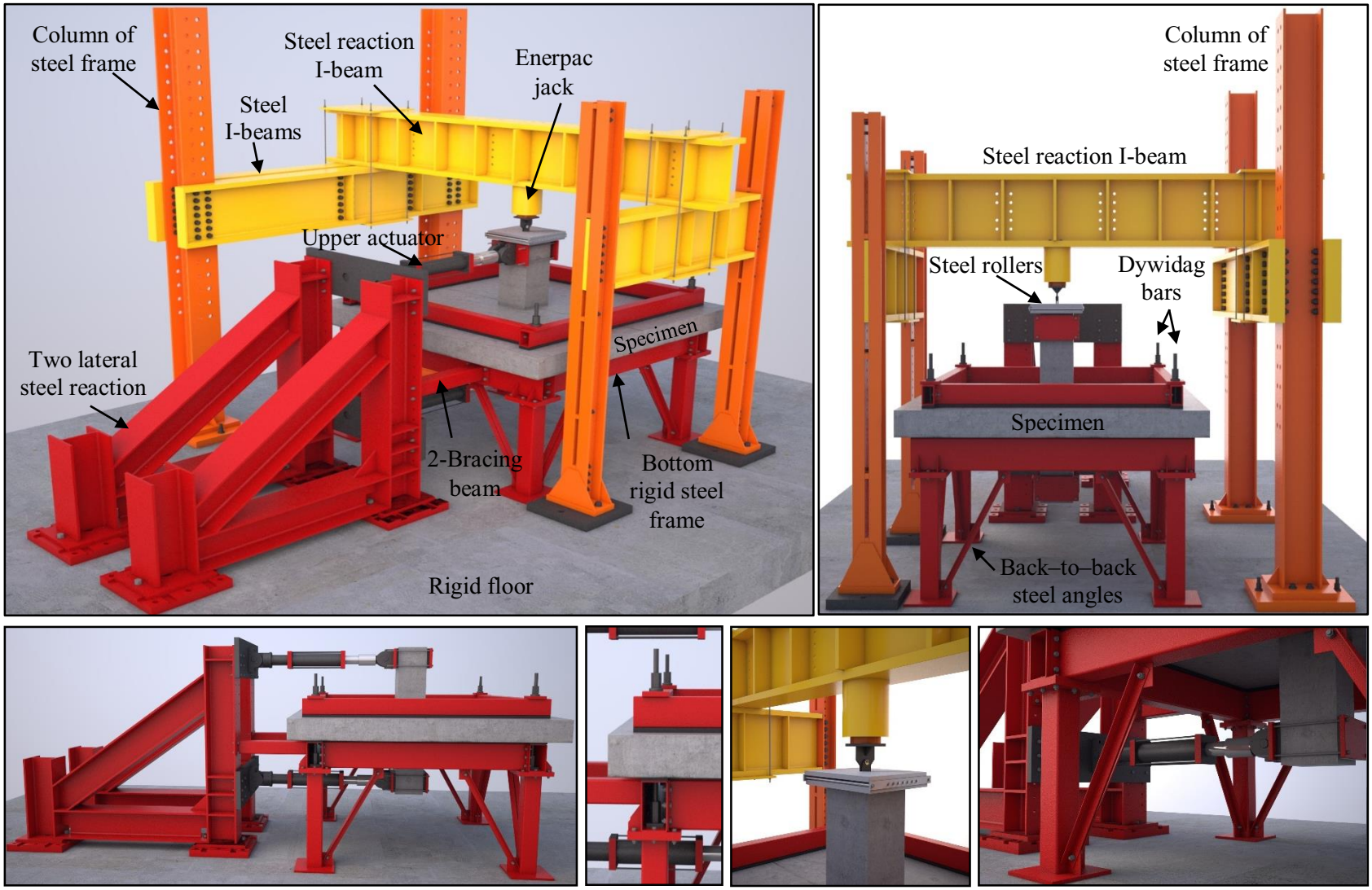

Figure 3.19 Test setup schematic.

Figure 3.20 Overview of the test setup.

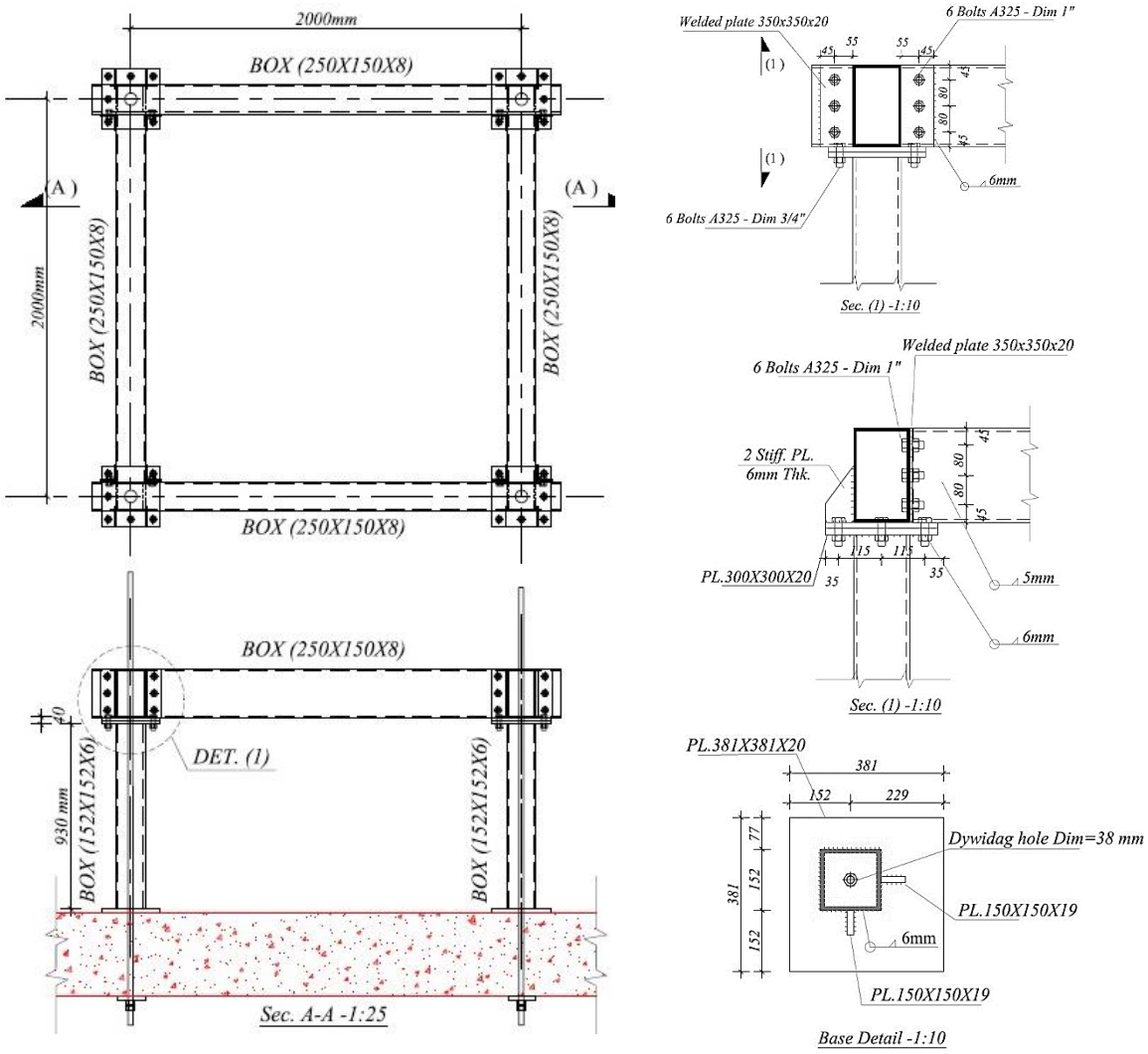

Figure 3.21 Details of lower supporting bed.

At the outset of testing, a concentric load was applied to the top of the upper column in a load–control mode and at a loading rate of 20 kN/min. The desired load was approximately 140 kN. This value represented the dead load plus 30% of the live load on a typical floor–system prototype. This gravity load produced an effective shear stress on the critical perimeter equal to 25% of the direct punching shear capacity of the concrete–defined by the ACI 318 Building Code. The load was maintained in the column throughout testing by continuously adjusting the jack. The oil pressure was applied and regulated throughout the test with a hand pump. In the case of specimen G3 and G8, the desired load was increased to 180 kN, representing the combined dead and live loads. The horizontal actuators were then activated to apply the lateral reversed loads on the column ends. The actuators operated in displacement–control mode.

The actuators pushed and pulled the column ends simultaneously at the same rate according to a planned cyclic–loading pattern but in different directions (**Figure 3.22**). The positive drift in the routine corresponds to the actuator pushing the column, whereas the negative drift corresponds to the actuator pulling the column. Each increment represents an approximate increase in the lateral interstory–drift ratio of 0.25%. Each cycle at a new drift level was performed twice to evaluate the loss of specimen strength and stiffness during the repeated cycles. The design of the horizontal loading path followed the main idea of the ASTM E2126–11: "Standard Test Methods for Cyclic (Reversed) Load Test for Shear Resistance of Vertical Elements of the Lateral Force Resisting Systems for Building". Many similar cyclic testing procedures have been widely used by other researchers and their testing results have been incorporated into structural codes.

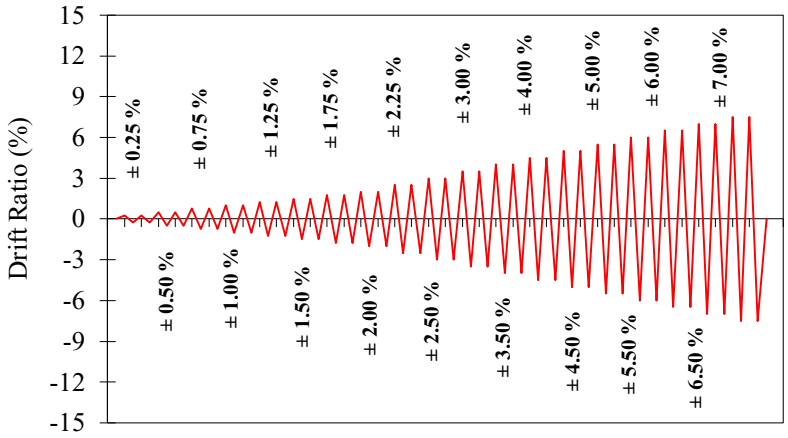

Figure 3.22 Lateral–displacement routine.

CHAPTER 4. EXPERIMENTAL STUDY OF INTERIOR GFRP–RC SLAB–COLUMN CONNECTIONS UNDER LATERAL CYCLIC LOAD

Foreword

Title: Experimental Study of Interior GFRP–RC Slab-Column Connections under Lateral Cyclic Load.

Authors and Affiliation:

- Mohamed Eladawy, PhD candidate, Department of Civil Engineering, University of Sherbrooke, Sherbrooke, QC, Canada.
- Mohamed Hassan, Postdoctoral fellow, Department of Civil Engineering, University of Sherbrooke, Sherbrooke, QC, Canada.
- Brahim Benmokrane, Professor of Civil Engineering and NSERC Research Chair in FRP Reinforcement for Concrete Infrastructure and Tier 1 Canada Research Chair in Advanced Composite Materials for Civil Structures, Department of Civil Engineering, University of Sherbrooke, Sherbrooke, QC, Canada.

Journal: ACI Structural Journal.

Journal: Accepted March 2019

4.1. Abstract

The feasibility of using fiber-reinforced polymers (FRP) as internal reinforcement for a totally reinforced-concrete (RC) structure immune to corrosion essentially pertains to strength, stiffness, and deformation capacity in resisting seismic loads has become questionable. Nevertheless, no experiments have yet been conducted on the punching-shear behavior of FRP-reinforced concrete (FRP-RC) slab–column connections subjected to lateral reversal cyclic loading. Consequently, current FRP-RC design guidelines and codes in North America contain no seismic provisions. This has been the main impetus to conduct the first-ever experimental study on the punching-shear behavior of glass-FRP (GFRP) slab–column connections under the combination of gravity and lateral reversed cyclic loading. Four full-scale interior slab–column connections were constructed and tested to investigate the influence of flexural-reinforcement type (GFRP and steel bars), reinforcement ratio, and gravity-load intensity on the punching-shear performance. All test specimens were identical and measured 2500×2500 mm with a thickness of 200 mm. A column measuring 300×300 mm extended 700 mm at its centre above and below the slab surfaces. The results revealed that the GFRP-RC specimens possessed adequate strength and deformation capacity against punching-shear failure during and after reserved lateral cyclic-load conditions. The GFRP-RC specimens achieved lateral interstory-drift capacities over 1.50% satisfying the limits in CSA A23.3 and ACI 421.3R. The GFRP-RC specimens also had adequate drift-ductility indices, dissipated energy, and connection stiffness. Moreover, the GFRP-bar strains at the ultimate lateral-drift ratio were less than the guaranteed tensile strength by 42%. No rupture of the GFRP bars and bond failure or slip were observed during the test.

Keywords: Concrete; GFRP bars; RC slab-column connection; punching shear; drift capacity; cyclic loading; ductility; dissipated energy; design codes.

4.2. INTRODUCTION

In North America, numerous parking garages, high rise buildings, and bridges, in which flat plates are customarily used, are deficient due to the corrosion of steel reinforcement and consequent failure in concrete occurs. The fiber-reinforced polymers (FRP) reinforcing bars have emerged in concrete structures as an innovative solution to overcome the corrosion problem. Most of the previous investigations was mainly focused on the behavior under static-loading condition omitting the seismic design. Therefore, the feasibility of using FRP as internal reinforcement for a totally reinforced concrete structure immune to corrosion essentially pertains to strength, stiffness, and deformation capacity to resist seismic loads has become questionable.

Limited experimental research has been conducted to address this issue by investigating the seismic performance of FRP-RC elements resisting seismic loading. GFRP-RC beam–column connections subjected to seismic loading were conducted (Mady et. al 2011; and Ghomi et. al 2015). The test results of these studies indicated that the GFRP-RC beam–column connections satisfied both flexural or shear strength and ductility (deformability) requirements as earthquake-resistant structures according to ACI 318-14 (2014) and CSA A23.3-14 (2014). The GFRP-RC beam–column specimens also reached more than 4.0% lateral drift. In addition, the residual strains in the GFRP flexural reinforcement at the 4.0% drift ratio were much lower than in the steel-RC specimens. FRP-RC columns subjected to lateral reversed cyclic loading have been studied by a number of researchers (Ali et al. 2016; and Elshamandy et al. 2017). The results revealed more stable performance of the GFRP-RC column specimens than their companion steel-RC specimens due to the higher stiffness of GFRP bars beyond yielding.

To the authors' knowledge, no tests have been conducted yet on FRP-RC slab–column connections subjected to a combination of gravity and lateral cyclic loads. It should, however, be pointed out that the current North American codes and guidelines (CSA S806-12 and ACI 440.1R-15) do not include any requirements concerning the nominal punching-shear strength, stiffness, or drift capacity of flat-plate structures reinforced with FRP bars under cyclic lateral loading, which is one of the primary motivations of this research. The previous tests conducted on two-way FRP-RC slabs focused on the punching-shear behavior under monotonic concentric

loading only (Matthys and Taerwe 2000; Ospina et al. 2003; Lee et al. 2009; and Hassan et al. 2013). Few studies have been investigated the punching-shear behavior of interior FRP slab-column connections subjected to shear load and static unbalanced moment (Zaghloul et al. 2004; Gouda and El-Salakawy 2015; and Hussein et al. 2018).

The experimental results revealed that, the punching-shear behavior of the FRP-RC slab–column connections was similar to that of their steel counterparts. They also noted that the slab-reinforcement rigidity significantly contributed to the punching-shear strength of the slab–column connections. The results also showed that the unbalanced moment increased deflection and strain in the FRP bars. Moreover, increasing the concrete compressive-strength enhanced the punching-shear capacity, the initial stiffness of the connections, and the strains in the FRP bars decreased. In addition, increasing the moment-to-shear ratio reduced the vertical-load capacity. Furthermore, increasing the flexural-reinforcement ratio significantly enhanced the punching capacity and post-cracking stiffness, while decreasing connection deflection.

Most of the past experiments on steel-RC slab–column connections under seismic conditions were done using interior or edge-connection subassemblies isolated from prototype structures. These subassemblies consisted of a slab with columns extending from the top and bottom faces. The vertical loading was applied from either the top of the columns or slab surface while the cyclic loading was applied to the column ends or slab edges. This technique is simple and yielded reliable test results for the design codes. To assess the seismic behavior of two way slab-column connections, many experiments were conducted on the behavior of steel slab–column connections transferring gravity loads combined with lateral monotonic or reversed cyclic loading between slabs and columns (Robertson 1992; Marzouk et al. 2000; Megally and Ghali 2000; Robertson et al. 2006 and Drakatos et el. 2016).

The researchers reported, the slab–column connections made with normal-strength concrete and without shear reinforcement failed in brittle punching-shear mode at relatively low drift ratios. A 1.5% is a frequently recommended minimum interstory-drift ratio that the multistory structure should withstand in low seismic zone without failure. Moreover, the capacity for moment transfer, lateral drift, stiffness, and ductility of the connection decreased when the gravity-load level increased. On the other hand, increasing slab flexural-reinforcement

substantially reduced lateral-drift capacity. Furthermore, the lateral reversed cyclic loading reduced the moment capacity, further the deformation capacity of slab–column connections under lateral cyclic loading was more than the lateral monotonic loading. The diagonal shear cracks at failure were also much steeper for slabs under lateral cyclic loading than lateral monotonic loading.

4.3. Research Significance

This paper presents pioneer test results of four full-scale GFRP-RC slab–column interior connections under combined gravity loading and lateral reversed cyclic loading. This study aimed at understanding and assessing the punching-shear behavior of two-way GFRP specimens under quasi-static reversed cyclic loading to simulate seismic loading. Based on the laboratory testing results, the punching-shear performances were evaluated in terms of failure modes, cracking patterns, hysteretic response, reinforcement and concrete strains, connection stiffness, energy dissipation, and drift-ductility index with taking into consideration the effects of reinforcing-bar type (GFRP and steel); GFRP flexural-reinforcement ratio, and gravity-load intensity. The findings of this study will support the work of the North American technical committees engaged in developing standards and design provisions for GFRP-RC slab–column connections subjected to lateral reversal cyclic loading.

4.4. EXPERIMENTAL INVESTIGATION

4.4.1. Specimen Configurations

In this study, a total of four full-scale interior slab–column connections were constructed and tested under a combination of constant vertical loading and lateral reversed cyclic loading. The specimens are identified as $S1_{(1.12)}$, $G1_{(1.06)}$, $G2_{(1.51)}$, and $G3_{(1.06)\text{-SL}}$. Table 4.1 presents the configuration and characteristics of each specimens. The specimens were labelled with a letter denoting the tension reinforcement type: S for steel and G for GFRP. The subscripts 1.12%, 1.06% ($2.8\rho_b$), and 1.51% ($1.5\rho_f$) stand for the flexural-reinforcement ratio, while the subscript SL indicates the intensity of the gravity service load applied to specimen G3. **Figure 4.1** shows the typical geometry of the test specimens and reinforcement details.

Table 4.1 Configuration of specimens.

Specimen[1]	*C*, mm (in.)	*ts*, mm (in.)	*d*, mm (in.)	Tension RFT.	Comp. RFT.	ρ_t[2], %	ρ_{bott}, %	ρ_b, %	f'_c[3] MPa (ksi)	f_t[3] MPa (ksi)	Gravity–Load Intensity V_g kN (kip)
S1$_{(1.12)}$	300 (11.8)	200 (7.9)	151 (5.9)	14–20M	10–15M	1.12	$0.5\rho_t$	4.29	52 (7.54)	3.93 (0.57)	140 (31.5)
G1$_{(1.06)}$				14 No.20	10 No.15	1.06		0.37	52 (7.54)	3.93 (0.57)	140 (31.5)
G2$_{(1.51)}$				20 No.20	10 No.20	1.51		0.33	46 (6.67)	3.36 (0.48)	140 (31.5)
G3$_{(1.06)–SL}$				14 No.20	10 No.15	1.06		0.33	46 (6.67)	3.36 (0.48)	180 (40.5)

[1] G denotes GFRP and S for steel bars, with a subscript indicating the reinforcement ratio; specimen G3 followed by the gravity–load intensity.
[2] ρ_t calculated according to CSA/S806–14 and CAN/CSA A23.3–14 for GFRP– and steel–reinforced concrete slabs, respectively.
[3] Compression and splitting testing on 100 × 200 mm concrete cylinders

The prototype structure for this investigation was a parking garage flat-plate building with 5000×5000 mm (196.9×196.9 in) panels. The columns were identical 300×300 mm [11.8×11.8 in.] in cross section and with a story height of 2800 mm [110.23 in.]. The live load was assumed to be 2.4 kN/m^2 (50.1 lb/ft^2), and super-imposed dead load of 1.0 kN/m^2 (20.9 lb/ft^2). The total gravity load on the floor, including the slab weight, was estimated according to NBCC (2015) ($V_g = D.L+0.3L.L \times l_1 l_2$).The test specimens were designed in accordance with CSA A23.3-14 and CSA S806-12. All test specimens were identical and measured 2500×2500 mm [98.4×98.4 in.] with a thickness of 200 mm [7.9 in.]. A column measuring 300 mm×300 mm [11.8×11.8 in.] measuring extended 700 mm [27.56 in.] at its centre above and below the slab surfaces. The slabs were simply supported on a 2000×2000 mm [78.74×78.74 in.] perimeter on the bottom face of the slab. These dimensions were chosen to represent the locations of lines of contra-flexure. On the other hand, the dimensions were consistent with an extensive research project conducted at the University of Sherbrooke to evaluate the punching-shear performance of GFRP-RC slab–column connections (Dulude et al. 2013; and Hassan et al. 2013).

All specimens had a typical bottom- and top-reinforcement configuration in each orthogonal direction, as shown in **Fig. 4.1**. The specimens were designed to have a flexural-reinforcement ratio such that punching-shear failure would be expected to occur prior to flexural failure. The bottom flexural-reinforcement (tension side)—placed symmetrically in each orthogonal direction—consisted of 14 No. 20 or 20M bars. The top flexural-reinforcement (compression side)—symmetrically placed in each orthogonal direction—consisted of 10 No. 15 or 15M bars. The bottom flexural-reinforcement in specimen G2 was 20 No. 20 bars (tension side) and the top flexural-reinforcement (compression side) was 10 No. 20 bars. The reinforcing ratio on the

compression side of all slabs was half that of the tension reinforcement. Two bars ran through the column core on the compression side to satisfy the requirements for structural-integrity reinforcement in CSA A23.3-14. The clear concrete cover in the direction of the lateral cycling loads was 30 mm (1.18 in.). The average effective depth of the slabs d was 151 mm (5.94 in.).

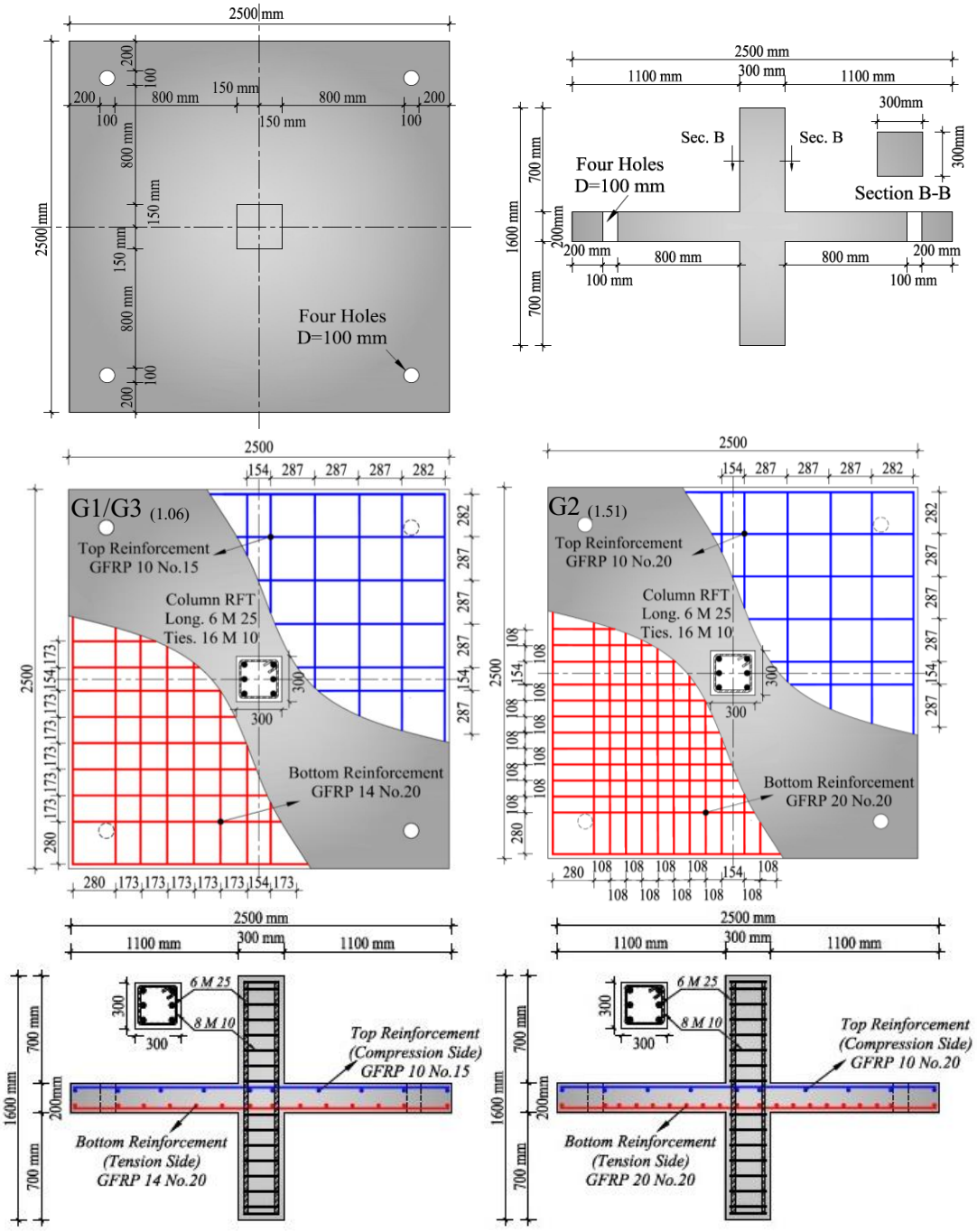

Figure 4.1 Typical geometry and reinforcement details for all tested specimens.

The column was heavily reinforced with steel bars (reinforcement ratio of 3.0%) to make the column strong enough to transfer shear force and cyclic moments to the slab and to avoid column failure during testing. The column was reinforced with six longitudinal deformed 25M steel bars. In addition, closed deformed 10M steel ties were used spaced at 100 mm (3.93 in).

4.4.2. Test Procedure

At the outset of testing, a concentric load was applied to the top of the upper column in a load-control mode and at a loading rate of 20 kN/min (4.5 kip /min). The desired load was approximately 140 kN (31.5 kip). This value represented the dead load plus 30% of the live load on a typical floor-system prototype. The load was maintained in the column throughout testing by continuously adjusting the jack. The oil pressure was applied and regulated throughout the test with a hand pump. In the case of specimen G3, the desired load was increased to 180 kN (40.5 kip), representing the combined dead and live loads. The horizontal actuators were then activated to apply the lateral reversed loads on the column ends. The actuators operated in displacement-control mode. The actuators pushed and pulled the column ends simultaneously at the same rate according to a planned cyclic-loading pattern but in different directions (see **Figure 4.2**). The positive drift in the routine corresponds to the actuator pushing the column, whereas the negative drift corresponds to the actuator pulling the column. Each increment represents an approximate increase in the lateral inter-story drift ratio of 0.25%. Each cycle at a new drift level was performed twice to evaluate the loss of specimen strength and stiffness during the repeated cycles.

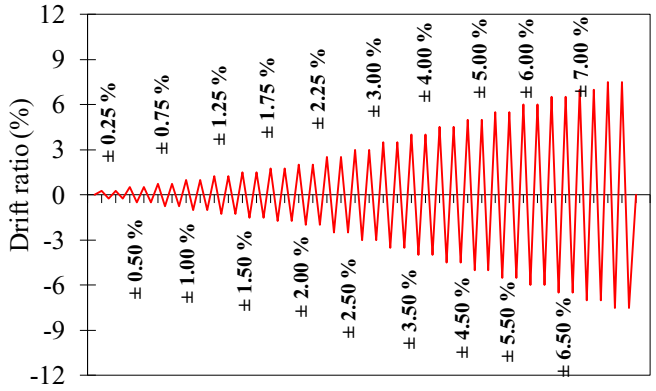

Figure 4.2 Lateral–displacement routine.

4.5. Experimental Results and Observations

4.5.1. Cracking Pattern and Modes of Failure

Figure 4.3 shows typical crack patterns and failure sequence of the tested specimens. Moreover, **Fig. 4.4** presents the final crack patterns on the slab bottom surface at the end of the test. In general, during the application of the gravity load, the initial flexural cracks appeared at the column faces and corners and extended toward the slab edges. Applying the lateral reversed cyclic loads caused the initial flexural cracks to propagate, and additional flexural cracks appeared on the slab bottom surface. Radial and tangential cracks also formed and propagated. Moreover, a crack around the column perimeter was observed on each side of slab surfaces. Increasing the lateral-drift ratio caused the cracks to extend and open throughout. Moreover, new cracks formed and developed at higher drift levels, and the concrete cover began to spall from the bottom surface (see Fig. 5). Due to moment transferred between the column and the connected slab, diagonal torsional cracks were observed and developed adjacent to the column side faces in the transverse lateral-load direction. The cracks on the slab top surface were mainly concentrated at the slab–column intersection. The failure for all specimens was sudden brittle shear mode. Punching-shear failure was evidenced by a sudden drop in applied gravity and lateral-loads. At this point, an attempt was made to reload the specimen to attain the target gravity load until returning the specimen to zero lateral displacements, followed by test termination. It should be pointed out that none of the flexural bars ruptured in the GFRP-reinforced specimens.

In general, the crack patterns and punching-shear failure surface for steel-reinforced specimen S1 and GFRP-reinforced specimen G1 was comparable. The initial visible flexural cracks for S1 and G1 arose in the column faces at gravity load intensity of 120 and 85 kN (26.9 and 19.1 kip), respectively. At a lateral-drift ratio of 2.00 %, the crack pattern for both specimens generally stabilized. For specimens S1 and G1, the first crack associated with punching developed during the first cycle of lateral-drift ratio of 2.0 and 2.25%, respectively. By the end of the second cycle, damage related to punching-shear had propagated and the punching cone was fully formed. Further increasing of the lateral-drift ratio only widened the existing cracks

and a few new cracks appeared. In addition, the concrete cover began to spall from the bottom surface.

For steel-reinforced specimen S1 and GFRP-reinforced specimen G1, the maximum width of the flexural-cracks obtained prior to failure were 0.62 and 1.15 mm (0.024 and 0.045 in.), respectively. On the other hand, in each orthogonal direction, the average distances between the column face and the perimeter of the failure cone varied. For specimens S1 and G1, the corresponding average distance along the lateral-load direction was 3.6d and 4.0d, respectively. While along the transverse direction was 4.8d for both specimens, where d is the effective depth of the slab.

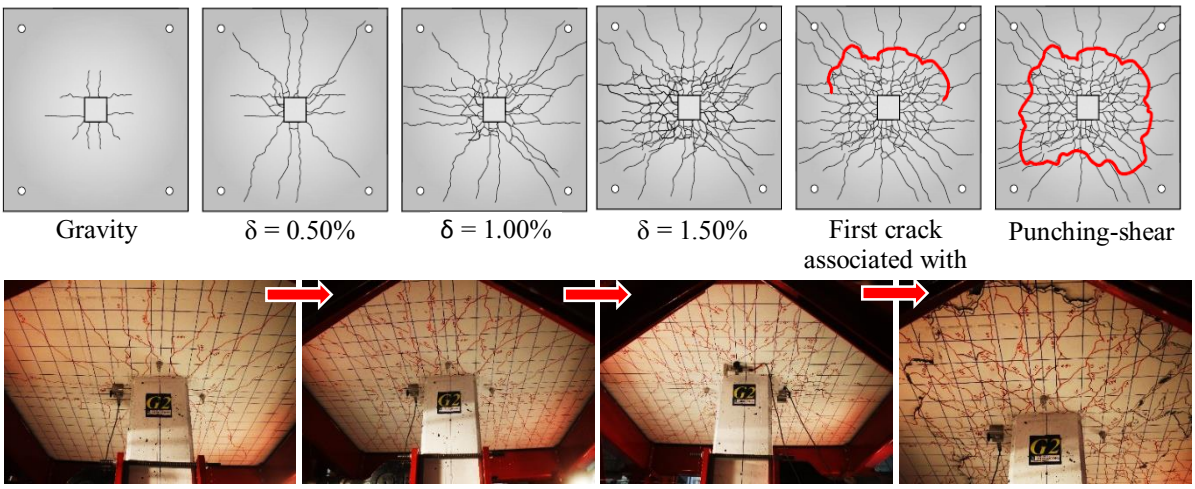

Figure 4.3 Typical crack patterns and failure sequence of the tested specimens.

Unlike specimen G1, highly reinforced specimen G2 and higher gravity-load specimen G3 evidenced more tangential and radial cracks on the tension side of the slab. In addition, more circumferential cracks were observed near the column and connecting the radial cracks. For specimens G2 and G3, at gravity-load intensities of 135 and 140 kN (30.3 and 31.4 kip), the initial flexural cracks formed out from the column faces, respectively. The crack pattern for both specimens generally stabilized at a lateral-drift ratio of 1.50%. The first damage resulting from punching-shear cracking appeared during the first cycle at a lateral-drift ratio of 1.75%. Moreover, the complete punching cone formed during the second cycle at a lateral-drift ratio of 1.75%. The maximum recorded flexural-cracks for specimens G2 and G3 before the failure were 0.84 and 0.98 mm (0.033 and 0.038 in.), respectively. The average distances between the

column face and the perimeter of the failure cone along the lateral-load direction were 2.8d and 2.9d, compared to 4.3d along the transverse direction.

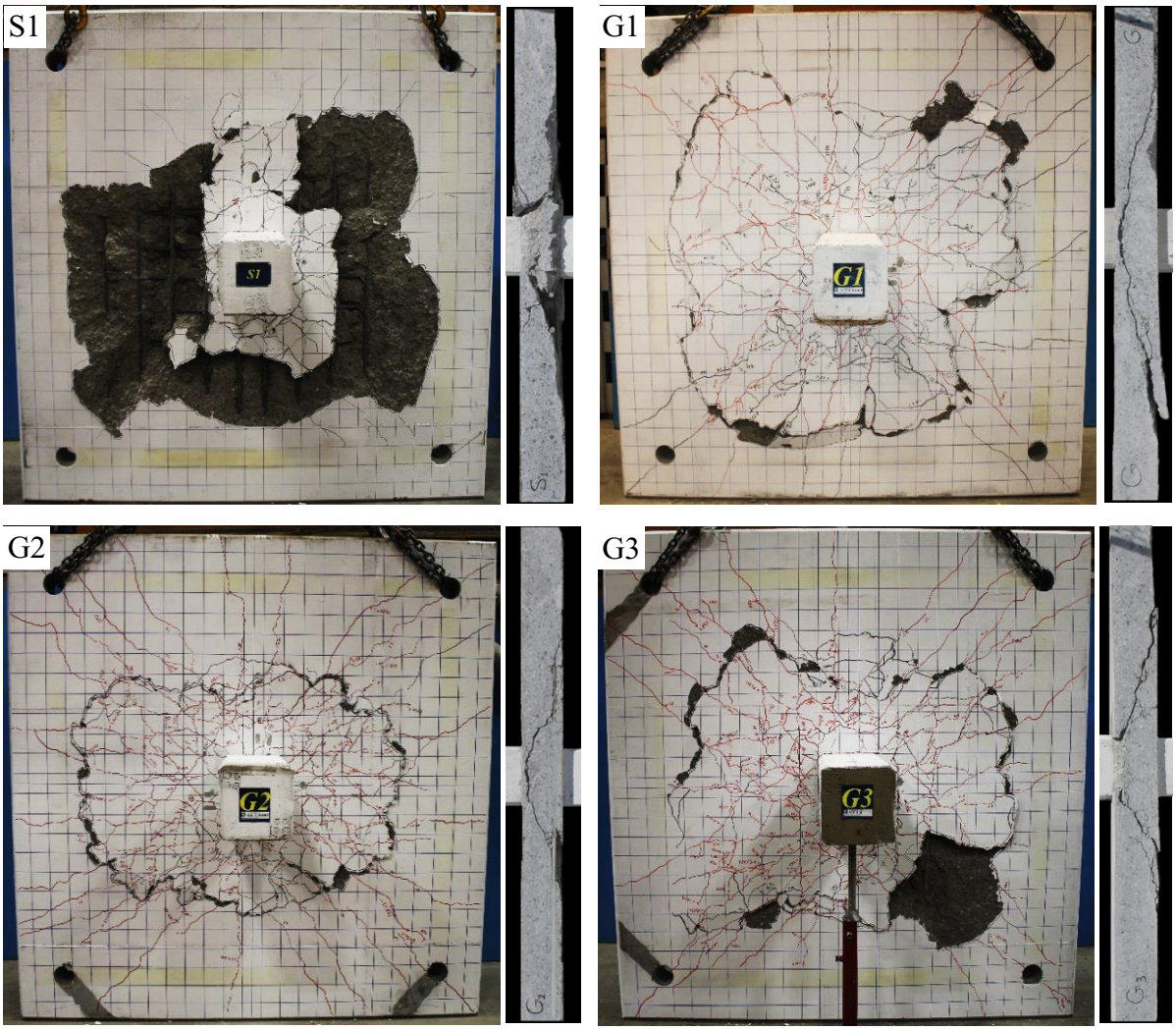

Figure 4.4 Final crack patterns and saw–cut of all tested specimens along the load direction.

To observe the inclination of the diagonal cracks, all specimens were cut along a line close to the column face in the lateral-load direction. **Figure 4.4** shows the sawn cross sections for all specimens along the lateral-load direction. The main diagonal shear crack started at the column face with different inclination angles. The range of the inclination angle for steel-reinforced specimen S1 was 27° to 30°, compared to 23° to 25°, 33° to 37°, and 33° to 35°, respectively, for GFRP-reinforced specimens G1, G2, and G3. It should be pointed out that the diagonal shear crack at failure was significantly steeper for the cyclic test than for the slab-column connections subjected to a concentric vertical load or to vertical shear forces and unbalanced

moments. This confirms the early observation of (Drakatos et al. 2016). Steep shear cracks due to lateral-load reversals indicate severe concrete degradation that limits the deformation capacity of the connection.

4.5.2. Hysteretic Response

Figure 4.5 provides the unbalanced moment versus lateral-drift-ratio relationships for all specimens. The unbalanced moment is defined as the moment transferred between the column and the connected slab. The unbalanced moment generated through reversed lateral quasi-static loading at the column ends. The unbalanced moment was obtained at each load step by multiplying each jack load by the effective height. The effective height is the distance from the application point to the slab center, that is, 675 mm (26.57 in.). The lateral-drift ratio was calculated by dividing the lateral-drift between the top and bottom of the column by the effective height. Table 4.2 provides the peak lateral load, maximum unbalanced moment, and corresponding lateral-drift ratio in each direction.

Table 4.2 Test results.

Specimen	ρ_t (E_r/E_s) %	Gravity Load KN (kip)	Peak Lateral Load KN (kip)		Max. Unbalanced Moment KN.m (kip.in)		Max. Unbalanced Moment KN.m (kip.in)		Drift Ratio (%)		Max Reinforcement Strain at *d/2* (μs)	Max Concrete Strain (μs)
		Vg	H_+	H_-	M_+	M_-	*ACI*	*CSA*	δ_+	δ_-	$\varepsilon_{s/G-max}$	ε_{c-max}
S1$_{(1.12)}$	1.12	140 (31.5)	168.4 (37.8)	165.6 (37.2)	223.7 (1981.3)	220.4 (1952)	196.2 (1737.6)	231.2 (2047.7)	2.0	–2.0	2350	–1048
G1$_{(1.06)}$	0.36	140 (31.5)	136.6 (30.8)	136.7 (30.7)	179.8 (1592.7)	180.9 (1600.4)	58.2 (515.2)	139.1 (1232.1)	2.25	–2.25	5239	–1040
G2$_{(1.51)}$	0.52	140 (31.5)	146.1 (32.8)	129.4 (29.1)	185.9 (1646.7)	171.2 (1516.4)	73.0 (646.3)	154.8 (1370.9)	1.75	–1.50	6211	–1445
G3$_{(1.06)-SL}$	0.36	180 (40.5)	125.1 (28.1)	117.9 (26.5)	156.6 (1387)	148.2 (1312.9)	39.0 (345.4)	115.9 (1026.9)	1.75	–1.50	5715	–2593

Note: *d* = is the effective depth of the slab; *(+)* refers to the positive direction and *(–)* to the negative direction; 1 MPa = 145 psi; 1 KN = 0.225 kips; 1 mm = 0.0394 in.

Figure 4.6 presents the envelope of unbalanced moment–drift-ratio relationship to aid in comparison. The relationship indicates that, at the early stages in which the lateral-drift ratio ranged from 0.25% to 0.50%, all specimens achieved almost the same unbalanced moment-carrying capacity. The maximum unbalanced moment-carrying capacities were varied at higher lateral-drift ratios. All specimens achieved lateral-drift ratios ranging from 1.75% to 2.25%, which is compatible with the recommended allowable design drift. It should be pointed out that

all specimens exhibited punching-shear failure resulting from a sudden drop in the gravity and lateral loads. On the other hand, the peak lateral loads in the negative direction were always smaller than those in the positive direction. This was attributed to the effect of cyclic loading on propagating the cracks and damaging the concrete at the first path of the first cycle.

For steel-reinforced specimen S1 and GFRP-reinforced specimen G1, the maximum unbalanced moment-carrying capacity in the positive direction ($M_{Max\text{-}P}$) was 223.7 and 179.8 kN.m (1981.3 and 1592.7 kip.in.), achieved during the first cycle at a lateral-drift ratio of 2.00 and 2.25%, respectively. While, the maximum unbalanced moment-carrying capacity in the negative direction ($M_{Max\text{-}N}$) was 220.4 and 180.9 kN.m (1952 and 1600.4 kip.in.), respectively. For the steel-reinforced specimen the lateral load dropped to 49% of the peak value during the second repeated cycle at a lateral-drift ratio of 2.00%, while a significant loss of lateral-load resistance was observed at lateral-drift ratio of 2.25%.

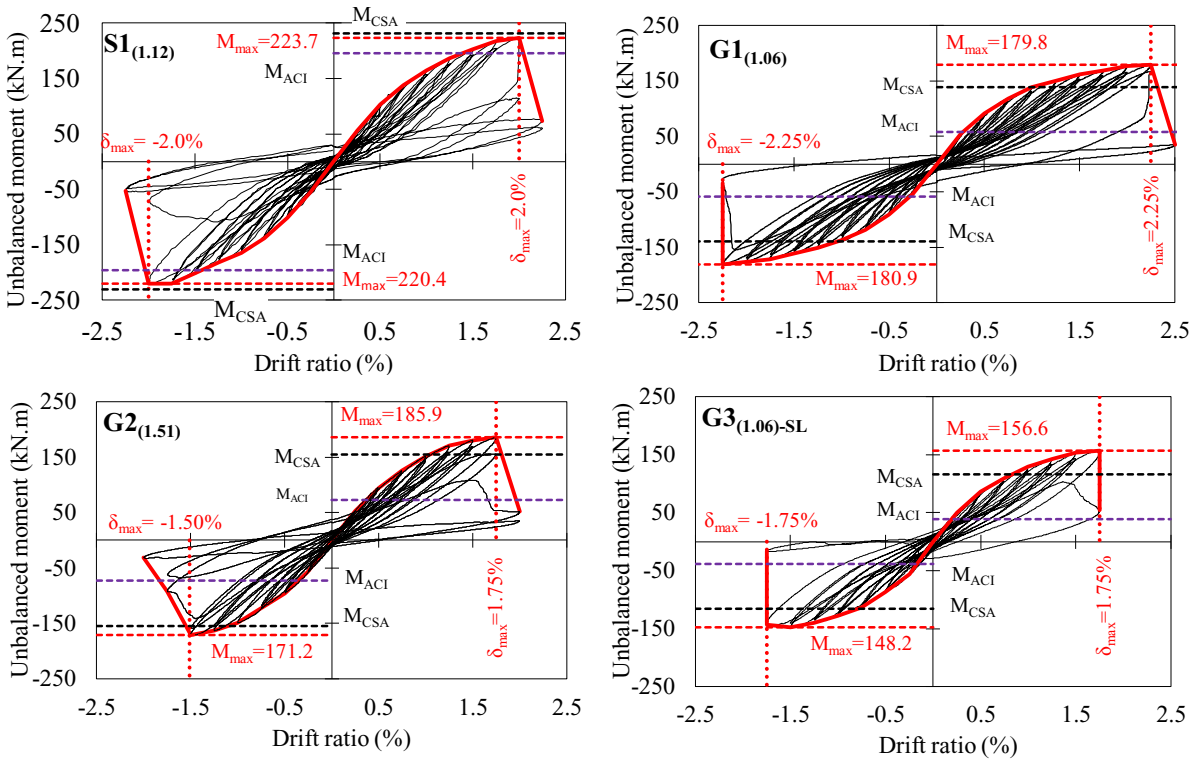

Figure 4.5 Unbalanced moment–lateral–drift ratio relationship of test specimens.

The effectiveness of increasing the GFRP flexural-reinforcement ratio in specimen G2 clearly enhanced the unbalanced moment-carrying capacity. At the first path of the first cycle at a lateral-drift ratio of 1.75% (positive direction), the specimen achieved $M_{Max\text{-}P}$ of 185.9 kN.m

(1646.7 kip.in.). The punching failure occurred during the second path of the first cycle before reaching a lateral-drift ratio of 1.75% (negative direction), therefore the $M_{Max\text{-}N}$ dropped by 24% to 141 kN.m (1248.8 kip.in.). During the second repeated cycle of 1.75%, the M_{Max} dropped by 16% and 53% in the positive and negative directions, respectively. On the other hand, increasing the gravity-load intensity to 180 kN (40.5 kip) for specimen G3 effectively contributed to the unbalanced moment-carrying capacity and lateral-deformation capacity. The M Max-P was 156.6 kN.m (1387 kip.in.) or 0.86 times that of specimen G1. This value was achieved during a lateral-drift ratio of 1.75%. The $M_{Max\text{-}N}$ was 148.2 kN.m (1312.9 kip.in.) at a lateral-drift ratio of 1.75%. A significant loss of lateral-load resistance was observed during the second repeated cycle of 1.75%.

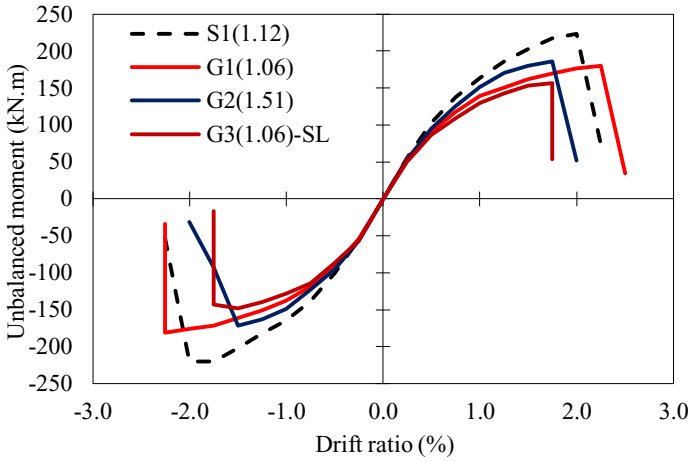

Figure 4.6 Backbone curves for test specimens.

4.5.3. Flexural Reinforcement and Concrete Strains

The flexural-reinforcement strains were measured in each orthogonal direction at 0, 75, 225, 450, and 750 mm (0, 3.0, 8.9, 17.7 and 29.5 in.) from the column face. **Figure 4.7(a)** illustrates the strain profile along the lateral-load direction for all specimens at each level of lateral-drift ratio. **Figure 4.7(b)** plots reinforcement strain versus lateral-drift ratio relationships in each orthogonal direction at distance (d/2) from the column face. Generally, the reinforcement strains decreased as the distance from the column edges increased. At 750 mm (29.52 in.) from the column edges, very low reinforcement strains were recorded. In addition, none of the GFRP-reinforced specimens experienced bars rupturing, slippage or bond failure during testing. This implies that the GFRP bars adequately transferred loads with no signs of bar slippage or bond

failure during the tests. Further, the reinforcement strains in the compression side, for all specimens, were very low compared with the flexural-reinforcement strains. The concrete strain also were measured at column faces during the testing and reported in Table 4.3.

In the case of steel–reinforced specimen S1, an evident yielding of the steel bars at a lateral–drift ratio equal to 1.25% was observed. The maximum recorded flexural–reinforcement strain (ε_{s-max}), at the column face, was 3204 μs during lateral–drift ratio of 2.00% and along the lateral–loading direction. On the other hand, the ε_{s-max} was 2350 μs at distance (d/2) from the column face. The maximum concrete strains ($\varepsilon_{c-max.}$) at the column face (point CG1) was –1048 μs, which is below the theoretical crushing strain of –3500 μs in CSA S806 (2012). No signs of concrete crushing were observed on the compression side of the slab during testing.

All the GFRP–reinforced specimens had comparable strain profiles and less than the characteristic tensile strength. Moreover, no signs of concrete crushing were observed on the compression side of the slab. The ε_{G-max} along the lateral–loading direction for GFRP–reinforced specimen G1 was 5641, representing 32% of the guaranteed tensile strength. The ε_{G-max} along the transverse direction was 0.39 times those recorded along the lateral–loading direction. On the other hand, the ε_{c-max} at the column face (point CG1) was –1040 μs.

In contrast, increasing the GFRP flexural–reinforcement ratio and the gravity–load intensity for specimens G2 and G3 effectively contributed to the flexural–reinforcement strains and concrete strains. For specimens G2 and G3, the ε_{G-max} increased to 6898 and 7420 μs, respectively, along the lateral–loading direction, representing 39% and 42% of the guaranteed tensile strength. While, the ε_{G-max} along the transverse direction were 0.17 and 0.42 times that recorded along the lateral–loading direction for specimens G2 and G3, respectively. As well, the ε_{c-max} increased to –1445 and –2593 μs, respectively. For specimen G2, the data from the reinforcement strain gauge (at the column edge) was lost for the first two cycles.

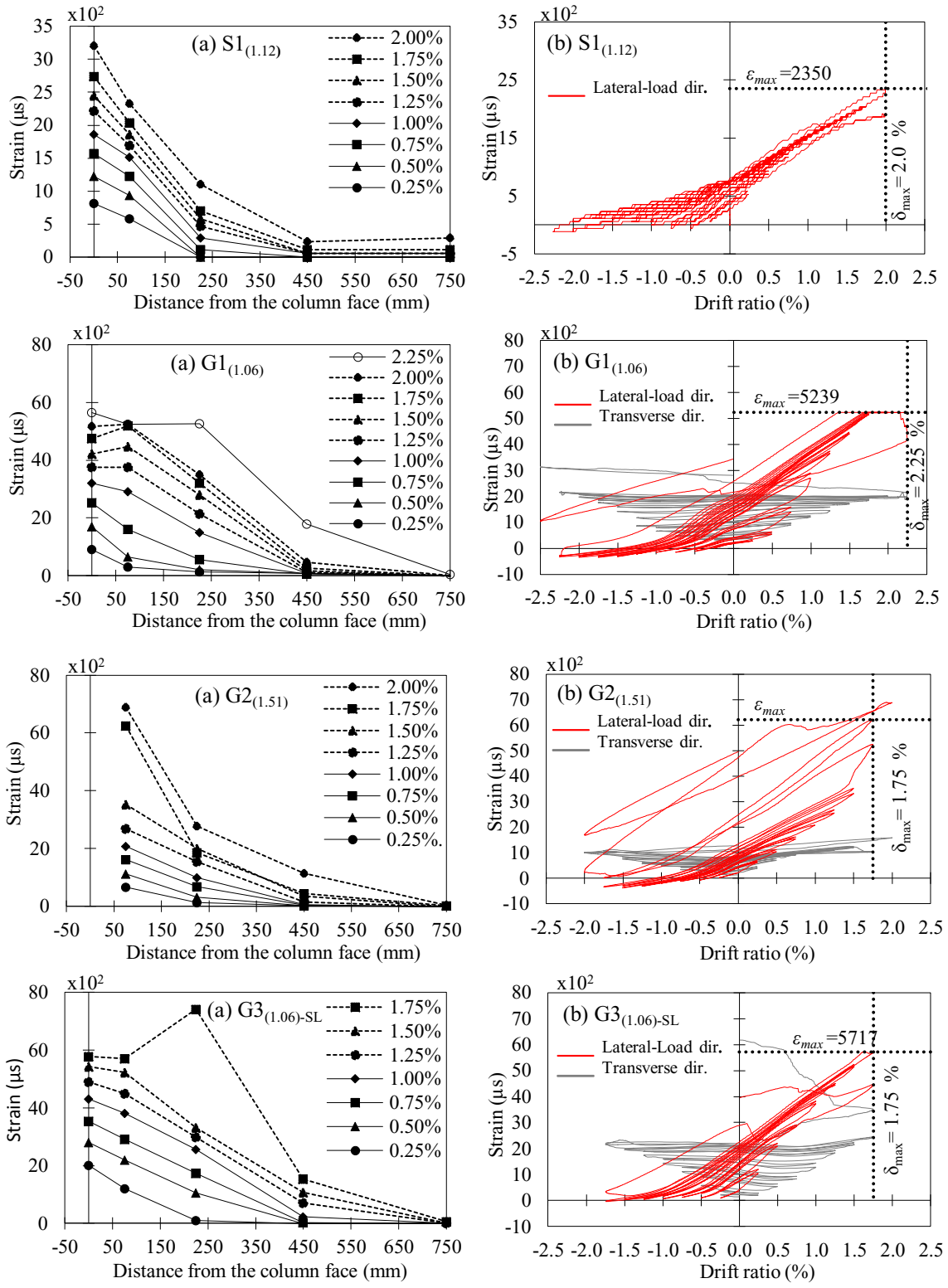

Figure 4.7 (a) Strain profile along the lateral load direction and (b) Reinforcement strain versus lateral–drift ratio at d/2.

4.5.4. Connection Stiffness

One of the major considerations in seismic design for slab–column connections is lateral stiffness. The peak-to-peak stiffness is defined as the slope of the line connecting the maximum achieved unbalanced moments in a given cycle (see **Fig. 4.8**) (Robertson et al. 1992; Megally et al. 1998; and Emam et al. 1997). **Figure 9 (a)** plots the average peak-to-peak stiffness versus lateral-drift ratio. In general, the reduction in connection stiffness occurred during the successive cycles of increasing lateral displacement. The initial connection stiffness (S_i) is defined as the slope of the line connecting the maximum unbalanced moments of the first cycle at a lateral-drift ratio of 0.25%. Table 4.3 provides the connection stiffness for all specimens; (S_i) at the initial, 1.5%, and (S_u) at ultimate lateral-drift ratios. It should be pointed out that the Si for all specimens was approximately the same.

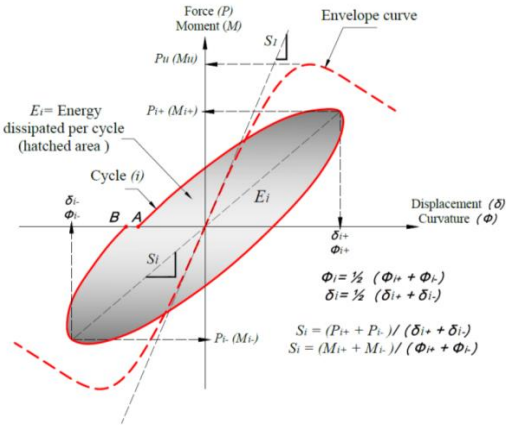

Figure 4.8 Normalization of energy–dissipation capacity and stiffness calculation according to ACI T1.1–01.

Table 4.3 Connection stiffness.

Specimen	M_{max} kN.m (Kip.in)	Initial Stiffness S_i kN.m (kip.in)		Stiffness at 1.50% S kN.m (kip.in)		Stiffness at Ultimate Drift S_i kN.m (kip.in)	
		First cycle	Second cycle	First cycle	Second cycle	First cycle	Second cycle
S1$_{(1.12)}$	223.7 (1981.3)	218.0 (1930.4)	215.0 (1903.8)	125.1 (1107.8)	120.0 (1062.6)	103.8 (919.2)	51.9 (459.6)
G1$_{(1.06)}$	180.9 (1600.4)	214.5 (1899.4)	213.7 (1892.3)	107.7 (953.9)	102.8 (910.5)	80.2 (710.2)	71.5 (633.1)
G2$_{(1.51)}$	185.9 (1646.7)	216.8 (1919.8)	216.1 (1913.6)	117.2 (1038.1)	109.5 (969.9)	93.4 (827.1)	63.2 (559.6)
G3$_{(1.06)-SL}$	156.6 (1387)	212.6 (1882.6)	207.8 (1840.1)	100.4 (889.6)	94.6 (838.2)	85.7 (758.9)	58.9 (521.6)

Note: 1 MPa = 145 psi; 1 kN = 0.225 kips; 1 mm = 0.0394 in.

The S_i for both specimens S1 and G1 were approximately equal. Nevertheless, the steel-reinforced specimen behaved stiffer than the GFRP-reinforced specimens and showed a moderate degradation of connection stiffness. This was attributed to the lower axial-stiffness of the GFRP bars. Therefore the connection stiffness degradation of specimen G1 was higher than the steel-reinforced specimen. The losses in the connection stiffness at the ultimate lateral-drift ratio was 47% and 37% compared to the initial stiffness for specimens S1 and G1, respectively. About 4 to 5 % reduction in (S) observed during the second reputed cycle at each lateral-drift level.

The connection stiffness for highly reinforced specimen G2 was higher than in specimen G1. This was attributed to increasing the GFRP reinforcement ratio from 1.06% to 1.51%. In comparison, specimen G3, which was subjected to a higher gravity load, had less connection stiffness than the other specimens. This was attributed to the accelerated slab cracking around the connection as a result of the increased gravity-load intensity. The effect of repeated load cycles was also evident. The reduction in connection stiffness during the second cycle for specimen G2 and G3 was approximately 5%, and the losses in the connection stiffness at the ultimate lateral-drift ratio were 43% and 40%, respectively.

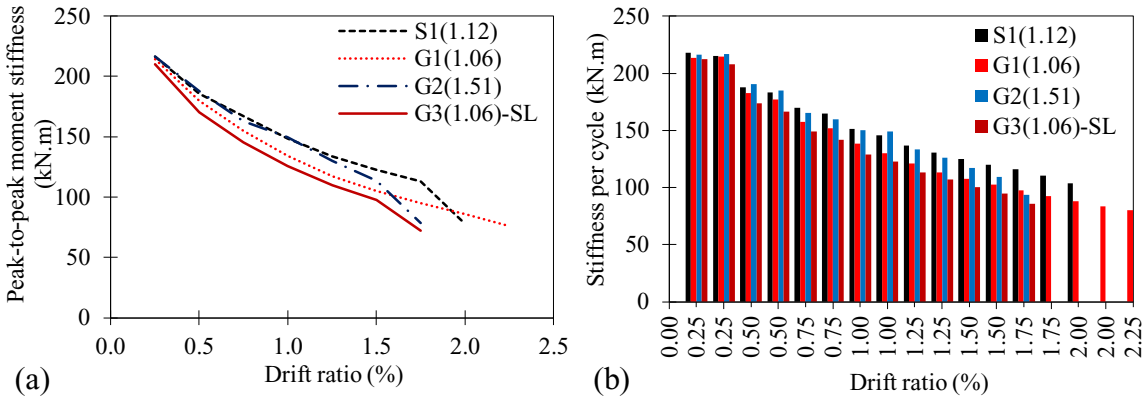

Figure 4.9 (a) Peak–to–peak stiffness for test specimens, (b) Peak–to–peak stiffness per cycle.

4.5.5. Energy Dissipation

Energy dissipation (E_D) is a significant indicator of RC elements being able to absorb energy before failure. Accordingly, it is one of the most important criteria used to assess the seismic performance of RC elements. Higher E_D capacity points to better post-peak behavior and ductile failure. The normalization of E_D capacity was determined according to ACI T1.1-01 by

calculating the area within the corresponding moment–drift-ratio hysteresis loop at each drift cycle (see **Fig. 4.8**). The average energy dissipated versus lateral-drift ratio shows in **Fig. 4.10 (b)**. Table 4.4 presents the energy dissipation at maximum lateral drift ratio.

Table 4.4 Ductility index and dissipated energy.

Specimen	M_{max} kN.m (kip.in)	$\delta_{0.8u}$ (%)	Method (I)		Method (II)		Dissipated Energy E_D kN.m (Kip.in)	
			$\delta_{(y),\,e}$ (%)	μ_δ	$\delta_{(y),\,e}$ (%)	μ_δ	First cycle	Second cycle
S1(1.12)	223.7 (1981.3)	2.00	1.50	1.33	1.42	1.41	243.3 (2154.9)	220.3 (1951.0)
G1(1.06)	180.9 (1600.4)	2.05	1.30	1.57	1.24	1.65	125.7 (1113.3)	349.8 (3098.4)
G2(1.51)	185.9 (1646.7)	1.73	1.34	1.29	1.19	1.45	166.2 (1471.9)	128.9 (1142.3)
G3(1.06)–SL	156.6 (1387)	1.69	1.07	1.58	1.16	1.46	120.8 (1069.6)	120.1 (1063.4)

Note: $\delta_{0.8u}$ = slab lateral–drift ratio at 20% loss of ultimate lateral strength; δ_y = slab lateral–drift ratio based on steel yield; δ_e = virtual slab lateral–drift ratio; μ_δ= lateral drift –based ductility factor; 1 MPa = 145 psi; 1 kN = 0.225 kips; 1 mm = 0.0394 in.

The responses clearly show that steel-reinforced specimen S1 exhibited higher E_D. This was due to the yielding of the steel reinforcement, which produces a wide loop in its hysteresis response. In addition, a reduction in E_D of about 24% was observed during the second cycle. Unlike steel bars, GFRP bars do not exhibit a yielding plateau. Consequently, GFRP-reinforced specimen G1 dissipated less energy than the steel-reinforced specimen. Moreover, the effect of repeated load cycles was evident, where the average reduction in the ED at each drift cycle was about 25%. In case of GFRP specimens G2 and G3, the energy dissipation behavior was comparable to that of specimen G1 at early lateral drifts (0.25% to 1.25%). Then, a considerable progress was observed in energy dissipation until failure. This sudden increase was due to the significant concrete damage that occurred due to high punching-shear stress, which resulted in wider loops in the hysteresis responses of the specimens. Moreover, the average reduction in the E_D at each drift cycle increased by 30%.

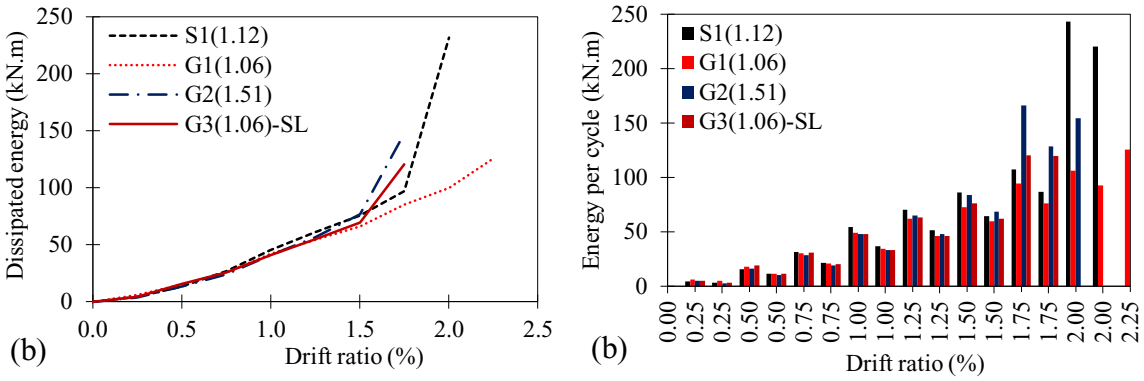

Figure 4.10 (a) Dissipated energy versus drift ratio, (b) Dissipated energy per cycle.

4.5.6. Ductility Index

Ductility of flat–plate structures located in seismic zones is deemed a very important design consideration. The ductility can be defined as an element's ability to sustain inelastic deformations prior to collapse without substantial loss of strength. The ductility factor is the ratio of the ultimate lateral displacement (deflection or drift) of the element to its corresponding displacement at an equivalent yielding of the steel reinforcement. This definition cannot be directly applied to FRPs or FRP–reinforced concrete members given the fact that FRP bars do not yield. Accordingly, the transition point between the elastic and inelastic regions in GFRP–reinforced concrete members is defined herein as the virtual deflection (Δ_e) or drift point (δ_e). ACI 440.1R (2015) and CSA S806 (2012) design codes offer no unified method for assessing the ductility index of FRP–reinforced concrete members. When calculating ductility capacity, the definition of yield displacement often causes difficulty because the force-displacement response of RC components may not have a well–defined yield point. This may occur due to the nonlinear behavior of the materials (steel reinforcement and concrete) or due to yielding in different parts of a RC structure or subassembly initiating at different load levels. Consequently, the general practice has been to define the ductility parameters of RC components based on an idealized bilinear force-displacement response (Park R. 1989).

Various alternative definitions have been proposed for estimating yield displacement. **Figure 4.11** illustrates tow–ideal curve definition proposed by (Park R. 1989) and adopted herein. Two methods were used to estimate the ductility index. In Method, I, the virtual limit, was evaluated based on the equivalent elastic–plastic energy absorption, where the secant line was chosen so as to have identical hatched areas and ensure equal energy criteria [see **Figure 4.11** (I)]. The

relative displacement or drifts corresponding to the intersection point of the secant line and a line of the tangent to the maximum unbalanced moment was defined as the virtual deflection (Δ_e) or drift–ratio point (δ_e). In Method II, the virtual limit was evaluated based on the reduced stiffness equivalent elastic–plastic system.

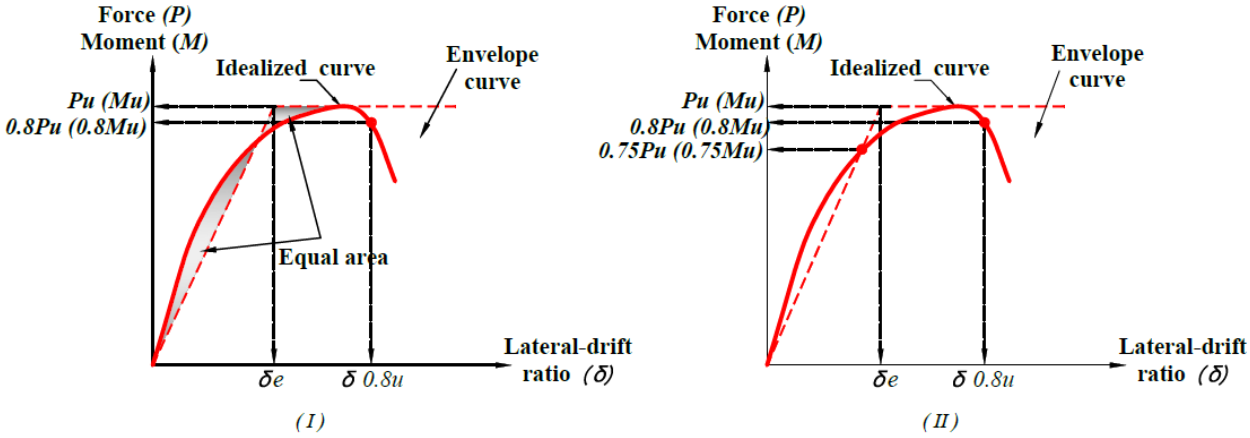

Figure 4.11 Ideal curve definition.

The initial slope of the idealized relation is a secant through the measured relation at 75% of the maximum unbalanced moment [see **Figure 4.11** (II)]. The plastic portion of the idealized relation passes through the maximum unbalanced moment. The intersection between these two lines indicates the virtual deflection (Δ_e) or drift–ratio point (δ_e). Table 4.4 provides the lateral–drift ratio at a 20% loss of ultimate lateral strength ($\delta_{0.8u}$), the lateral–drift ratio based on steel yield (δ_y), the virtual lateral–drift ratio (δ_e), and the lateral drift–based ductility index (μ_δ). The ultimate deflection or drift ratio is well recognized as a 20% loss of ultimate lateral strength (NBCC 2015). The drift ductility index (μ_δ) is determined with Eqns. (4.1) and (4.2).

$$(\mu_\delta = \frac{\delta_{0.8u}}{\delta_y}) \quad \text{or} \quad (\mu_\delta = \frac{\Delta_{0.8u}}{\Delta_y}) \qquad \text{(steel)} \quad (4.1)$$

$$(\mu_\delta = \frac{\delta_{0.8u}}{\delta_e}) \text{ or } (\mu_\delta = \frac{\Delta_{0.8u}}{\Delta_e}) \qquad \text{(FRP)} \quad (4.2)$$

As reported values in Table 4.4, all tested specimens showed reasonable predicated ductility indexes and consistent with the minimum required ductility factor of 1.2 for steel slab-column connections in a seismic zone, as reported by Moehle (1988) and Megally (1994). In steel–reinforced specimen S1, the μ_δ were 1.33 and 1.41 according to Methods I and II, respectively.

All of the GFRP–reinforced specimens had adequate ductility indices compared to the steel–reinforced specimen. According to method I, GFRP–reinforced specimens G1, G2 and G3, had adequate μ_δ of 1.57, 1.29 and 1.58, which are 31, 8 and 32% higher than the minimum ductility index–1.2–required for slab-column connection in a seismic zone of building combined with sufficiently stiff shear walls. While based on method II, the μ_δ were 1.65, 1.45 and 1.46, which are 38, 21 and 22% higher than the minimum ductility index.

4.5.7. Crack Opening

Figure 4.12 (a) & **(b)** illustrates the diagonal shear–crack width through the slab thickness versus lateral–drift ratio relationships along the lateral–load direction and the transverse direction. The diagonal shear–crack width was estimated by monitoring the vertical–displacement difference of the slab faces during testing. It should be noted that, in all the tested specimens, there was an abrupt increase in crack width at the ultimate drift ratio. This was attributed to large slab deformations and rotations.

The test results indicate that steel–reinforced specimen S1 had narrower cracks than all the GFRP specimens. This is due to the high effective reinforcement ratio ($\rho E_r/E_s$, where E_r is the modulus of elasticity of the reinforcing bars), which ranged from 3.1 to 2.1 times that of the GFRP specimens. The maximum recorded crack widths prior punching failures were 9.98 and 5.4 mm (0.39 and 0.21 in.) along the lateral–load and transverse directions, respectively. Contrariwise, GFRP–reinforced specimen G1 had greater diagonal shear and the maximum width of the diagonal shear cracks along the lateral–loading direction was 19.3 mm (0.76 in.), compared to 8.1 mm (0.32 in.) in the transverse direction.

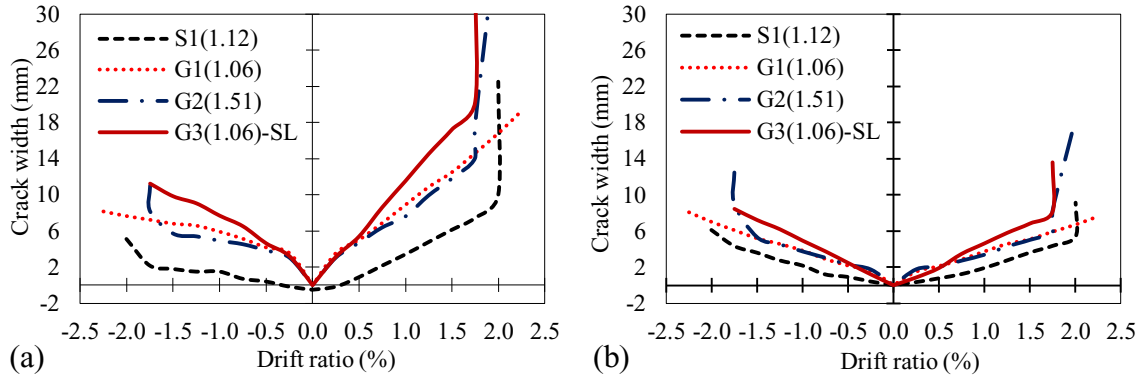

Figure 4.12 Opening of cracks versus drift ratio (a) along the lateral–load direction, (b) along the transverse direction.

The flexural–reinforcement strains were lower in specimen G2 due to increased slab flexural reinforcement. Consequently, the crack openings were moderate narrower than in specimen G1. On the other hand for specimen G3, the effect of increasing the gravity–load intensity on crack openings was clear. At the same lateral–drift levels, specimen G3 had a wider diagonal shear crack than specimen G1. As shown in **Figure 4.12 (a)** & **(b)**, the crack openings in all the GFRP–reinforced specimens were smaller in the transverse direction than in the lateral–loading direction.

4.5.8. Comparison of Predictions and Experimental Results

The North American codes [ACI 318 (2014), ACI 440.1R (2015), CSA A23.3 (2014) and CSA S806 (2012)] are assessed in this section by comparing their predictions with the experimental results. Table 4.5 provides the punching–shear predictions, peak lateral loads (H_{ACI}/H_{CSA}), and maximum unbalanced moments (M_{ACI}/M_{CSA})] as well as the ratio of the ultimate punching–shear capacity and applied gravity load (V_g/V_c).

The predicated ultimate unbalanced moment capacity (M_{ACI}/M_{CSA}) was calculated using the eccentric shear–stress model with a fraction (Υ_v) and resisted by the shear at the perimeter of $d/2$ from the column face using Eqns. (4.3).

$$M_n = \frac{J_x}{\Upsilon_v e}\left[v_{max} - \frac{V_n}{b_o d_v} \right] \qquad (4.3)$$

$$J_x = \frac{d\,(c_1+d)^3}{6} + \frac{d^3\,(c_1+d)}{6} + \frac{d^3\,(c_2+d)\,(c_2+d)^2}{2} \qquad (4.3.1)$$

$$\Upsilon_v = 1 - \frac{1}{1+\frac{2}{3}\sqrt{\frac{b_1}{b_2}}} \qquad (4.3.2)$$

where M_n is the unbalanced moment; J_x is the polar moment of inertia of the critical shear perimeter in Eq. (4.3.1); Υ_v is the fraction of unbalanced moment transferred from Eq. (4.3.2); e is the distance from column centerline to the edge of the critical section; c_1 and b_1 are the column length and the length of the critical section in the direction perpendicular to the moment axis, respectively; and c_2 and b_2 are the column length and the length of the critical section in the direction parallel to the moment axis, respectively. All safety factors and partial material factors in the equations were taken as equal to 1.0.

The available punching–shear equations provided by FRP design codes and guides [ACI 440.1R (2015) and CSA S806 (2012)] are summarized as follows. In ACI 440.1R (2015), the punching–shear capacity provided by V_c for FRP–reinforced slabs is simply a modified punching–shear equation for steel–reinforced slabs. On the other hand, it was modified by the factor 5/2 *k* to account for FRP axial stiffness in FRP–reinforced concrete elements through the term *kd*, as shown in Eqns. (4.4). The punching–shear strength provided by CSA–S806–2012 is calculated as the smallest of Eqns. (4.5) to (4.7). The critical perimeter nearest a column equal to 0.5 times the effective depth of 0.5*d* was taken, where λ is the concrete density factor; ϕ_c is the concrete resistance factor; β_c is the ratio of the long side to the short side of the column (α_s=4); and $f_c^{'}$ shall not exceed 60 MPa.

ACI 440.1R (2015):

$$V_c = \frac{4}{5}\sqrt{f_c^{'}}\, b_{0.5d}\, kd \qquad (4.4)$$

$$k = \sqrt{2\rho n + (\rho n)^2} - \rho n \qquad (4.4.1)$$

$$n = E_f / E_c \qquad (4.4.2)$$

CSA S806 (2012):

$$V_c = 0.056\,\lambda\,\phi_c \left(E_f\ \rho_f\ f_c^{'}\right)^{1/3} b_{0.5d} d \qquad (4.5)$$

$$V_c = 0.147\,\lambda\,\phi_c \left(0.19 + \frac{\alpha_c d}{\beta_c}\right)\left(E_f\ \rho_f\ f_c^{'}\right)^{1/3} b_{0.5d} d \qquad (4.6)$$

$$V_c = 0.028\,\lambda\,\phi_c \left(1 + \frac{2}{\beta_c}\right)\left(E_f\ \rho_f\ f_c^{'}\right)^{1/3} b_{0.5d} d \qquad (4.7)$$

The test results reported in table 4.5 indicate that the ACI 318 (2014) and CSA A23.3 (2014) gave conservative predications of the ultimate capacity for specimen S1 and the ratio of $M_{Exp.}/M_{The}$. was of 1.14 and 0.97, respectively. The ACI 440.1R (2015) equations were very conservative, giving average $M_{Exp.}/M_{The.}$ of 3.11, 2.55, and 4.02 for GFRP–reinforced specimens G1, G2, and G3, respectively. Contrariwise, the CSA s806 (2012) equations yielded reasonable and conservative predictions with average $M_{Exp.}/M_{The}$ of 1.30, 1.20, and 1.35 for GFRP–

reinforced specimens G1, G2, and G3, respectively. It should be pointed out that the ACI 440.1R (2015) equations were adopted from the same concept as the beam–shear model. This approach leads to very conservative estimates of punching–shear capacity for FRP–reinforced concrete slabs. The reason for this is that the contribution of the compression area is dependent on the reinforcement axial stiffness. Thus, the lack of this axial stiffness in the equations may make them excessively conservative. In contrast, the CSA S806 (2012) equations account for FRP axial stiffness and therefore gave better predictions.

Table 4.5 Code comparison.

Specimen	Gravity Load *kN(Kip)*	V_u / V_c		Peak Lateral Load KN (kip)		Peak Lateral Load KN (kip)		$H_{Exp.} / H_{The.}$		Max. Unbalanced Moment KN.m (kip.in)		Max. Unbalanced Moment KN.m (kip.in)		$M_{Exp.} M_{The.}$	
	Vu	ACI	CSA	H_+	H_-	*ACI*	*CSA*	*ACI*	*CSA*	M_+	M_-	ACI	CSA	ACI	CSA
S1(1.12)	140 (31.5)	0.22	0.19	168.4 (37.8)	165.6 (37.2)	145.3 (32.7)	171.3 (38.5)	1.16	0.98	223.7 (1981.3)	220.4 (1952)	196.2 (1737.6)	231.2 (2047.7)	1.14	0.97
G1(1.06)	140 (31.5)	0.48	0.28	136.6 (30.8)	136.7 (30.7)	43.1 (9.7)	103.0 (23.2)	3.17	1.33	179.8 (1592.7)	180.9 (1600.4)	58.2 (515.2)	139.1 (1232.1)	3.11	1.30
G2(1.51)	140 (31.5)	0.43	0.26	146.1 (32.8)	129.4 (29.1)	54.1 (12.2)	114.7 (25.8)	2.70	1.27	185.9 (1646.7)	171.2 (1516.4)	73.0 (646.3)	154.8 (1370.9)	2.55	1.20
G3(1.06)–SL	180 (40.5)	0.64	0.37	125.1 (28.1)	117.9 (26.5)	28.9 (6.5)	85.9 (19.3)	4.33	1.46	156.6 (1387)	148.2 (1312.9)	39.0 (345.4)	115.9 (1026.9)	4.02	1.35

Note: *(+)* refers to the positive direction and *(–)* to the negative direction; 1 MPa = 145 psi; 1 KN = 0.225 kips; 1 mm = 0.0394 in.

4.6. Discussion

4.6.1. Influence of Reinforcement Type

The reported test results and measures clearly show that the steel–reinforced specimen and GFRP specimen G1 had comparable punching–shear performance. Regardless of reinforcement type, the crack patterns, punching–shear failure surface, and failure mode of GFRP specimen G1 was comparable to that of the steel–reinforced specimen. The punching-shear stresses at failure were normalized to the cubic root of the concrete strength to account for the variation in the concrete strengths. Besides, the effective reinforcement ratios ($\rho E_r/E_s$) of the specimens were used to account for the difference between the moduli of elasticity of the GFRP and steel bars. The results in Table 4.3 showed that the GFRP-RC specimens evidenced lower punching-shear stress at failure. This was related to the smaller dowel action and the lower modulus of elasticity of GFRP reinforcing bars compared to that of steel (~0.25). Using a GFRP reinforcement ratio approximately equal to the steel reinforcement ratio yielded smaller neutral-axis depth as well as higher strains and deeper and wider cracks at the same load level. Thus, both the

contributions of the uncracked concrete zone (compression side), and the aggregate interlock decreased, which, in turn, yielded lower punching-shear capacity.

GFRP specimen G1 had a higher rate of stiffness degradation than the steel–reinforced specimen. This was attributed to the GFRP bars having lower axial stiffness than the steel bars. It should be pointed out that GFRP specimen G1 had drift–ductility indices of 1.57 and 1.65, which exceed the minimum required slab-column connection ductility factor of 1.2 reported by Moehle (1988) and Megally (1994). Due to the yielding of steel reinforcement, which produces a wide loop in its hysteresis response, the steel–reinforced specimen dissipated more energy than GFRP specimen G1. The steel–reinforced specimen had narrower diagonal shear cracks than the GFRP specimen due to the high effective reinforcement ratio ($\rho E_r/E_s$).

4.6.2. Influence of Reinforcement Ratio

The effectiveness of increasing the GFRP flexural–reinforcement ratio in specimen G2 was clear in the crack patterns and punching–shear failure surface. Increasing the number of FRP bars decreased the spacing between bars, which distributed stresses. As a consequence, there were more tangential and radial cracks on the tension side than in specimen G1. In addition, the distance between the column face and the perimeter of the failure cone was lower by 30% and 10% along the lateral–load and transverse directions, respectively. This confirms the findings of Osman et al. (2000), Gouda et al. (2015), and Hussein et al. (2018). Moreover, the unbalanced moment–carrying capacity was slightly enhanced by 12%, whereas the lateral–drift capacity was reduced by 22%. This is in agreement with the findings of Megally et al. (2000), Marzouk et al. (2000), and Robertson et al. (2006). Consequently, it should be mentioned that the lateral inter-story drift capacity of the GFRP slab-column connections was controlled by the amount of flexural reinforcement in the slab.

On the other hand, the maximum flexural–reinforcement strains increased. Nevertheless, the maximum recorded strain in the GFRP reinforcement was 39% of the guaranteed tensile strength. Increasing the amount of slab flexural reinforcement efficiently enhanced the stiffness of the slab-column connection. In addition, a slight effect on dissipated energy was observed. It is very important to mention that the draft–ductility index was influenced by increasing the GFRP flexural–reinforcement ratio, reducing it by 20%. This confirms the early observation made by Marzouk et al. (2001).

4.6.3. Influence of Gravity–Load Intensity

Increasing the slab gravity–load intensity and subsequent punching shear level at the interior connection had a considerable effect on punching–shear performance. The applied gravity–load intensity was increased to simulate combined dead and live loads. Consequently, higher joint shear stress and lower shear stiffness were exhibited. In specimens G3, the initial flexural, tangential, and radial cracks were considerably wider than counterpart specimen G1. In addition, the diagonal shear crack was steeper. Furthermore, the unbalanced moment–carrying capacity and the lateral–drift capacity dropped by 20% and 22%, respectively. A 30% increase in the flexural–reinforcement strains was, however, observed. Nevertheless, the maximum recorded strain in the GFRP reinforcement was 42% of the guaranteed tensile strength.

On the other hand, one consequence of increasing the punching–shear stress in specimens G3 is that the concrete strain was 2.5 times that's recorded in the counterpart specimen G1 (1.06). Moreover, the slab-column connection stiffness, dissipated energy, and diagonal shear–crack width were influenced by concrete damage around the connection. Consequently, 6% dropped of the slab-column connection stiffness was observed at the same drift ratio levels, while at the ultimate load, the drift ratio dropped by 24%. On the other hand, the dissipated energy increased at all drift ratios.

4.7. CONCLUSIONS

This paper presented the test results of an experimental study that was undertaken to investigate the punching–shear performance of full–scale interior slab-column connections reinforced with GFRP bars and subjected to gravity and reversed lateral cyclic loads. Based on the findings, the following conclusions can be drawn:

1. All GFRP specimens can be designed to satisfy punching shear strength and lateral–deformation requirements during and after the reversed lateral cyclic load conditions. Consequently, GFRP reinforcing bars could be used as reinforcement in slab–column connections subjected to seismic load conditions.
2. All GFRP-RC specimens experienced a typical sudden and brittle punching-shear failure without much warning. All GFRP-RC specimens, however, evidenced stable hysteretic

behavior and achieved lateral-drift ratio ranging from 1.75% to 2.25%, which is over 1.50% as recommended in guidelines and codes used for seismic analysis.

3. The GFRP-RC slab-column connections showed that punching-shear failure was not triggered by the GFRP bars rupturing; no bond failure nor slip occurred during the tests. Therefore, a minimum amount of repair after surviving a seismic-loading event would be required, which is considered an advantage for GFRP-reinforced concrete structures.
4. Reduction of slab–column connection stiffness was observed in all GFRP-RC specimens during successive cycles of increasing displacement. The GFRP specimens demonstrated a moderately higher rate of degradation compared to the steel-RC specimen, although they followed a similar trend. Further, the effect of repeated loading cycles was obvious with the average reduction in stiffness in each drift cycle ranging from 2% to 5%.
5. The GFRP-RC slab-column connections dissipated less energy than the steel-RC specimen. Reduction in dissipated energy in each drift cycle was observed, due to the excessive damage induced in the slab–column connections during the second repeated loading cycle. All GFRP-RC specimens evidenced adequate drift-ductility indices for slab–column connections subjected to reversed lateral cyclic loads.
6. All GFRP-RC specimens showed wider diagonal shear cracks than the steel-RC specimen. This is due to the high effective reinforcement ratio ($\rho E_r/E_s$). The widths of the diagonal shear cracks in all GFRP specimens were narrower in the transverse direction than in the lateral-loading direction.
7. The punching shear strength and associated eccentric shear due to unbalanced moment is well predicated by CSA S806-12, with an average $M_{Exp.}/M_{Theo}$ values of 1.28 ± 0.08. However, the ACI 440.1R-15 equations were very conservative with an average $M_{Exp.}/M_{Theo}$ of 3.32 ± 0.74.
8. The test results indicate that all the GFRP specimens had wider diagonal shear cracks than the steel–reinforced specimen. This is due to the high effective reinforcement ratio ($\rho E_r/E_s$), which ranged from 3.1 to 2.1 times that of the GFRP specimens. The widths of the diagonal shear cracks in all the GFRP specimens were narrower in the transverse direction than in the lateral–loading direction.

9. Increasing the slab flexural reinforcement contributed to diminishing the lateral inter-story drift capacity; lateral-drift ductility index; and strains in reinforcing bars. Further, the GFRP-RC slab–column connection stiffness, energy dissipation, and capacity of moment transfer were enhanced.
10. The slab-column connections seismic performance significantly affected with the increase of gravity-load intensity. Moreover, the lateral-drift and moment transfer capacities; connection stiffness; and drift-ductility index were reduced. On the other hand, dissipated energy, reinforcement strain, and concrete strain were increased.

CHAPTER 5. CYCLIC TESTING OF INTERIOR TWO–WAY SLAB–COLUMN CONNECTIONS REINFORCED WITH GFRP BARS

Foreword

Title: Cyclic Testing Of Interior Two–Way Slab-Column Connections Reinforced With GFRP Bars.

Authors and Affiliation:

- Mohamed Eladawy, PhD candidate, Department of Civil Engineering, University of Sherbrooke, Sherbrooke, QC, Canada.
- Mohamed Hassan, Postdoctoral fellow, Department of Civil Engineering, University of Sherbrooke, Sherbrooke, QC, Canada.
- Brahim Benmokrane, Professor of Civil Engineering and NSERC Research Chair in FRP Reinforcement for Concrete Infrastructure and Tier 1 Canada Research Chair in Advanced Composite Materials for Civil Structures, Department of Civil Engineering, University of Sherbrooke, Sherbrooke, QC, Canada.

Journal: ASCE Journal of Composites for Construction.

Journal: Submitted February 2019

5.1. Abstract

In flat plates, the use of high-strength concrete (HSC) in the slabs, and the presence of shear reinforcement in the vicinity of columns are considered effective, economical, and practical solutions for enhancing the punching shear performance of slabs. This paper presents the first-ever experimental results for interior concrete slab–column connections reinforced with glass-fiber-reinforced-polymer (GFRP) bars subjected to a combination of gravity and lateral reversed cyclic loads. Four full-scale slabs measured 2500×2500mm with a thickness of 200mm, and 300mm square column extending 700 mm above and below the slab surfaces specimens were constructed and tested until failure. The main test variables were (1) flexural-reinforcement type (GFRP and steel bars); (2) slab's concrete compressive strength (NSC and HSC); and (3) the use of GFRP shear reinforcement. All the tested specimens demonstrated adequate strength, deformation capacity, drift ductility indices, dissipated energy, and connection stiffness. The GFRP-reinforced NSC specimen without shear reinforcement showed adequate ability to withstand interstory drift up to 2.25% without punching failure. The GFRP-reinforced HSC specimen without shear reinforcement had a 33% higher lateral deformation and moment-transfer capacities compared to the GFRP-reinforced NSC specimen. The provision of GFRP-stirrups in the slab–column connection significantly influenced slab overall performance. The shear-reinforced specimen was able to sustain lateral drifts as high as 5% with no more than a 20% decrease in the moment carrying capacity. Moreover, the shear-reinforced slab was able to sustain the gravity load until the end of testing and only exhibited softer punching-shear failure with a gradual decrease in lateral loads.

Keywords: Punching–shear; GFRP–reinforced concrete; slab-column connection; stirrups; shear reinforcement; high–strength concrete; drift capacity; cyclic loading; ductility.

5.2. Introduction

In North America, structures in which flat plates/slabs are customarily used—such as numerous parking garages and bridges—are deficient due to the corrosion of steel reinforcement, which leads to concrete failure. Fiber-reinforced-polymer (FRP) reinforcing bars have emerged as an innovative solution to overcome the steel reinforcement corrosion problem in concrete structures. Most experimental researches in the past have focused mainly on the behavior of FRP-RC elements under static-loading conditions, omitting seismic design. Therefore, the feasibility of using FRP as internal reinforcement in reinforced-concrete (RC) members immune to corrosion essentially pertains to its strength, stiffness, and deformation capacity to resist seismic loads, which has been called into question.

Recently, several experimental research has been conducted to investigate the seismic performance of FRP-RC structural elements, such as beam–column connections, columns, and shear walls. Mady et al. (2011) and Ghomi and El-Salakawy (2015) tested and addressed the seismic performance of FRP-RC beam–column connections. Their test results indicated that, the FRP-RC beam–column connections satisfied flexural or shear strength and ductility (deformability) requirements as earthquake-resistant structures according to ACI 318-14 and CSA A23.3-14. The FRP-RC beam–column specimens reached more than 4.0% lateral drift. In addition, the residual strains in the FRP flexural reinforcement at the 4.0% drift ratio were much lower than in steel-reinforced concrete specimens. A number of researchers [Ali and El-Salakawy (2016) and Elshamandy et al. (2017)] have studied the seismic behavior of FRP-RC columns. Their results revealed that the FRP-RC column specimens evidenced stable performance, and achieved lateral drift capacity more than the 2.5 and 4% required by the National Building Code of Canada NBCC (2015) and CSA S806 (2012), respectively.

To the authors' knowledge, no tests have been conducted yet on FRP-RC interior slab–column connections subjected to a combination of reversed lateral cyclic loading and gravity load. It should, however, be pointed out that the current North American codes and guidelines [CSA S806 (2012) and ACI 440.1R (2015)] do not include any requirements concerning the nominal punching-shear strength, stiffness, and drift capacity of flat-plate structures reinforced with FRP bars under cyclic lateral loading. El-Gendy and El-Salakawy (2018) examined two full-scale edge slab-column connections under gravity and reversed-cyclic lateral loading. El-

Gendy concluded that GFRP bars could be used as longitudinal slab reinforcement in slab-column edge connections subjected to simulated seismic loading conditions. On the other hand, GFRP-RC connection achieved lateral drift ratio higher than the 1.5% minimum drift ratio before punching failure. Moreover, GFRP-RC connection exhibited a lateral displacement deformability/ductility factor of 2.0 due to the lower gravity load applied to the GFRP-RC connection and the lower modulus of elasticity of the GFRP bars. These factors are higher than the minimum 1.2 factor suggested by Pan and Moehle (1989).

Few studies have investigated the punching-shear behavior of interior FRP slab–column connections subjected to shear load and static unbalanced moment [Zaghloul et al. (2004); Gouda et al. (2015); and Hussein et al. (2018)]. The researchers reported that the punching-shear behavior of the FRP-RC slab–column connections was comparable to steel-RC connections. In addition, the column aspect ratio, slab thickness, shear reinforcement, and use of high-strength concrete (HSC) significantly affected the punching-shear capacity and deformation capacity of the slabs. Furthermore, using FRP shear reinforcement (stirrups; headed studs, and corrugated bars) in the slab–column connection zone significantly increased the punching-shear strength, deformation capacity, post-cracking stiffness of the slabs and increased their safety. Moreover, the experimental results revealed that the slab–column connection with shear reinforcement exhibited a softer punching-shear failure mechanism.

Most of the past experiments on steel-reinforced concrete slab–column connections under seismic conditions involved interior or edge-connection subassemblies isolated from prototype structures. These subassemblies consisted of a slab with columns extending from the top and bottom faces. The vertical loading was applied from either the top of the column or slab surface, while the cyclic loading was applied to column ends or slab edges. This technique is simple and yielded reliable test results for the design codes. Other techniques—such as using shaking tables—were rarely used due to complexity and costs. To assess the seismic behavior of two-way slab–column connections, many experiments were conducted on the behavior of steel slab–column connections transferring gravity load combined with lateral monotonic or reversed cyclic loading between slabs and columns [Emam et al. (1997); Megally and Ghali (1998); Marzouk et al. (2000); Robertson et al. (2002) and Kang, T. H.-K. et al. (2017)].

The experimental results revealed that slab–column connections made with normal-strength concrete but without shear reinforcement failed in a brittle punching-shear mode at relatively low drift ratios. A minimum interstory-drift ratio of 1.5% is frequently recommended for multistory structures to perform well in low seismic zones without failure. Emam et al. (1997) reported that high-strength-concrete (HSC) slabs could accommodate higher lateral-displacement demands during an earthquake. Hence, using HSC might enhance the integrity of structures located in moderate-to-high seismic zones Moreover, HSC slabs appear to enhance structure ductility. Kang, T. et al. (2017) also demonstrated that the use of shear reinforcement [closed stirrups or shear bands and studs] significantly improved a connection's capacity for moment transfer, lateral drift, stiffness, and ductility. As well, the punching resistance to gravity loads was maintained even after such large values of interstory drift.

5.3. Research Significance

Our study aimed at understanding and assessing the punching-shear behavior of two-way GFRP-reinforced specimens under quasi-static reversed cyclic loading to simulate seismic loading. Based on the laboratory results, the punching-shear performances were evaluated in terms of failure mode, cracking patterns, hysteretic response, reinforcement and concrete strains, connection stiffness, dissipation energy, and drift ductility index taking into consideration the effects of the reinforcing-bar type (GFRP or steel), concrete compressive strength, and using GFRP closed stirrups as shear reinforcement. The experimental evidence from this study provides experimental data for including design provisions that allows for the design and use of GFRP reinforcement in interior two way concrete slab-column connections subjected to shear load and unbalanced moment in a future edition of the ACI 440.1R Code for Structural Concrete Reinforced with GFRP Bars and CSA S806 Canadian Standard Association Code on Design and Construction of Building Structures with Fiber Reinforced Polymers for the use of GFRP bars and stirrups in interior reinforced- two way concrete slab-column connections.

5.4. Experimental Investigation

5.4.1. Specimen Configurations

All test specimens were geometrically identical and measured 2500×2500×200 mm with a square column 300×300 mm, extending 700 mm above and below the slab center. The slabs were simply supported on a 2000×2000 mm perimeter on the bottom face of the slab. **Figure 5.1** shows the typical geometry of the test specimens and reinforcement details. These dimensions were chosen to represent the interior slab–column connection in a flat-plate parking garage built with 5×5 m bays. The columns were identical in cross section and had a story height of 2800 mm. The live load was assumed to be 2.4 KN/m^2 and the superimposed dead load 1.0 kN/m^2. The total gravity load on the floor, including slab weight, was estimated according to the NBCC (2015) [$V_g = deal\ load + 0.3 live\ load \times l_1 l_2$]. The test specimens were designed in accordance with CSA A23.3 (2014) and CSA S806 (2012). On the other hand, the dimensions of the slab were consistent with an extensive research project conducted at the University of Sherbrooke to evaluate the punching-shear performance of GFRP-reinforced slab–column connections [Dulude et al. (2013) and Hassan et al. (2013 & 2014)]. In case of gravity plus horizontal cycling loads the locations of contra flexure lines normal to horizontal loading direction change depending on the direction of the horizontal loading. Therefore, since in the setup the location of supports remain the same (in-between the actual locations of the lines of contra flexure), thick neoprene pads were provided on top and bottom of the slab to allow rotations along the contra flexure lines. The neoprene pads were 20 mm thick and 100 mm wide, and installed along the lines of support. That's is in agreement with the previous experimental researches [Emam et al. (1997); Megally (1998); Marzouk et al. (2000); Wensheng et. al (2008); Gouda and El Salakawy (2015); and Genikomsou and Polak (2015 & 2017)].

The specimens herein are identified as $S1_{(1.12)}$, $G1_{(1.06)}$, $G4_{(1.06)–H,}$ and $G5_{GCS–4.5d}$. The specimen labelling includes a letter denoting the tension–reinforcement type: S for steel and G for GFRP. This is followed by the subscript 1.12% or 1.06%, representing the flexural–reinforcement ratio, and possibly H, indicating HSC. GCS gives the stirrup configuration and *xd* the stirrup

extension beyond the column faces relative to the effective depth. Table 5.1 presents the configuration and characteristics of each test specimen.

Table 5.1 Configuration of specimens.

Specimen[1]	c, mm	h, mm	d, mm	Flexural Reinforcement		ρ_t, %	ρ_{bott}, %	ρ_b, %	f'^{3}_{c} MPa	f^{3}_{t} MPa	Gravity–Load Intensity V_g, KN	Stirrup Parameters		
				Bottom	Top.							S_o	S_{fv}	Extent
S1$_{(1.12)}$	300	200	151	14 No. 20	10 No. 15	1.12	$0.5\rho_t$	4.29	52	3.93	140	—	—	—
G1$_{(1.06)}$						1.06		0.37	52	3.93		—	—	—
G4$_{(1.06)–H}$								0.53	92	6.20		—	—	—
G5 $_{GCS–4.5d}$								0.33	45	3.75		0.4d	0.5d	4.5 d

[1] "S" denotes steel and "G" GFRP bar and stirrups, with a subscript (x%) indicating flexural–reinforcement ratio; (H) denotes high–strength concrete; (GCS) stands for stirrup configuration; and (xd) is the extension of the stirrups from the column faces relative to the effective depth.
[2] ρ_t calculated according to CSA/S806–14 and CAN/CSA A23.3–14 for GFRP– and steel–reinforced concrete slabs, respectively.
[3] Compression and splitting testing on 100 × 200 mm concrete cylinders

The specimens were designed to have a flexural-reinforcement ratio and transverse reinforcement such that punching-shear failure would be expected to occur prior to flexural failure. The bottom flexural reinforcement (tension side)—placed symmetrically in each orthogonal direction—consisted of 14 No. 20 or 20M bars (nominal diameter of 20 mm). The top reinforcement (compression side)—placed symmetrically in each orthogonal direction—consisted of 10 No. 15 or 15M bars (nominal diameter of 15 mm). The reinforcing ratio on the compression side of all slabs was half the tension reinforcement. Because the unbalanced moment may reverse sign, producing tensile concrete strains in the slab top surface. Also compression reinforcements increase the dowel force after punching failure (acted as hanger bars), which can prevent progressive collapse of a structure. Two bars ran through the column core on the compression side to satisfy the requirements for structural integrity reinforcement in CSA A23.3 (2014). The clear concrete cover in the direction of the lateral cyclic loads was 30 mm, and the average effective depth of the slabs d was 151 mm.

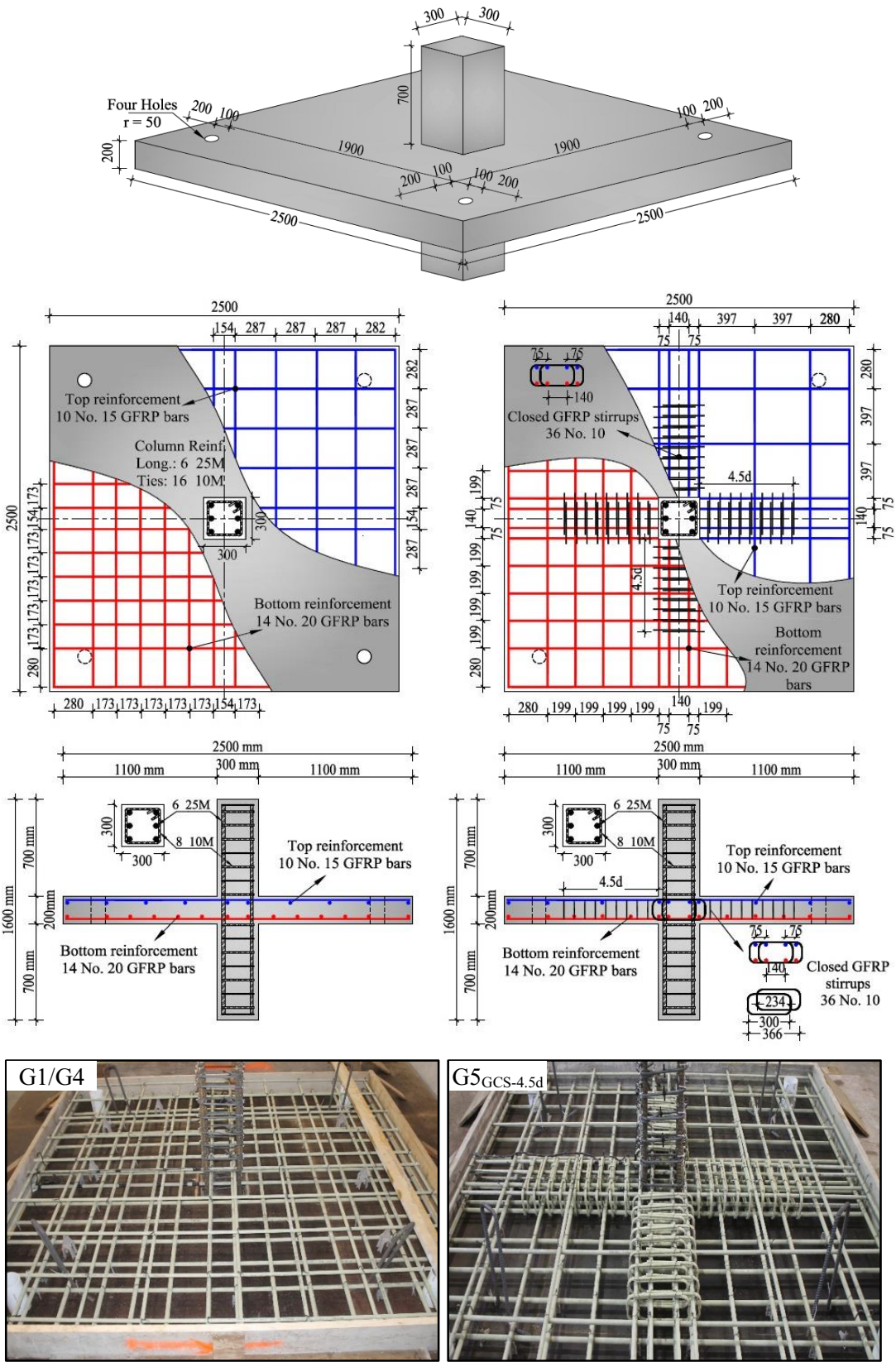

Figure 5.1 Typical geometry and reinforcement details for the tested specimens.

Specimen G5 $_{GCS\text{-}4.5d}$ was reinforced with discrete four branches of No. 10 closed GFRP stirrups, (nominal diameter of 10 mm). The GFRP stirrups extended 4.5*d* from the column face. The shear-reinforcement stirrups were arranged in a cruciform pattern according to ACI 318-14 and CSA A23.3-14. The spacing between the stirrups was 0.*5d*. The first perimeter was offset 0.*4d* from the column face for all slabs with shear reinforcement. The number of peripheral lines of shear reinforcement was nine in both directions, as shown in **Figure 5.1**. The column was heavily reinforced with six longitudinal deformed 25M steel bars (nominal diameter of 25.2 mm) to make the column strong enough to transfer shear force and cyclic moments to the slab and to avoid column failure during the test. In addition, deformed closed 10M steel ties were (nominal diameter of 11.3 mm) used with a closer spacing of 100 mm.

5.4.2. Test Procedure

At the outset of testing, a concentric load was applied to the top of the upper column in a load-control mode and at a loading rate of 20 kN/minute. The desired load was approximately 140 kN. This value represents the dead load plus 30% of the live load on a typical flat-plate system prototype. This gravity load produced an effective shear stress on the critical perimeter equal to 25% of the direct punching shear capacity of the concrete defined by the ACI 318-14. The load was maintained on the column throughout testing by continuously adjusting the jack. The oil pressure was applied and regulated throughout the test with a hand pump. The actuators were then activated to apply the lateral reversed loads on the column ends. The actuators operated in the displacement-control mode. The actuators pushed and pulled the column ends at the same rate according to a planned cyclic-loading pattern but in opposite directions (see **Figure 5.2**). The positive drift in the routine corresponded to the actuator pushing the upper column, whereas the negative drift corresponded to the actuator pulling the upper column. Each increment represents an approximate increase in the lateral interstory-drift ratio of 0.25%. The horizontal-loading path was designed along the lines of ASTM E2126.3 (2011) "*method B-ISO 16670 protocol*". Each cycle at a new drift level was performed twice to evaluate specimen loss of strength and stiffness during the repeated cycles

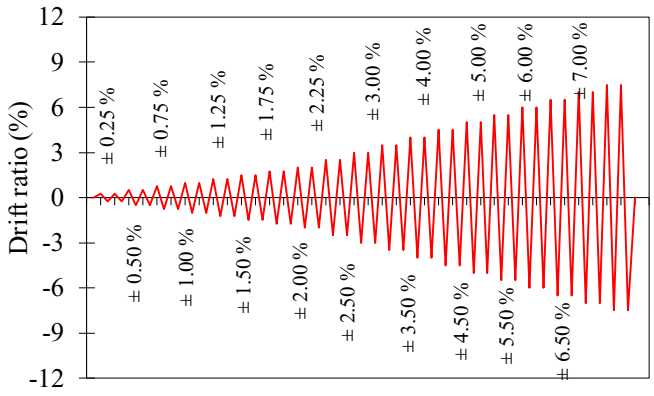

Figure 5.2 Lateral–displacement routine.

5.5. Experimental Results and Observations

5.5.1. Cracking Pattern

Figure 5.3 presents the final cracking and damage patterns on the slab bottom surface (tension side). In general, during the application of gravity load, the initial flexural cracks were generated at column faces and corners and extended toward the slab edges. Applying the reversed lateral cyclic loads caused the initial flexural cracks to extend and new flexural cracks formed on the slab bottom surface. Radial and tangential cracks also formed and propagated. Moreover, a crack around the column perimeter was observed on each side of the slab surfaces. Increasing the lateral–drift ratio caused the cracks to extend and open throughout. Moreover, new cracks formed and developed at higher drift levels, and the concrete cover began to spall from the bottom surface. Due to the moment transferred between the column and the connected slab, diagonal torsional cracks were observed and developed adjacent to the side faces of the column in the transverse lateral–load direction.

In general, the crack patterns and punching–shear failure surface were comparable in both specimen S1 (steel reinforced) and specimen G1 (GFRP–reinforced NSC) without shear reinforcement. The initial visible flexural cracks in S1 and G1 arose in the column faces at gravity–load intensities of 120 and 85 KN, respectively. At a lateral–drift ratio of 2.00%, the crack pattern for both specimens generally stabilized. The first crack associated with punching in specimens S1 and G1 developed during the first cycle at lateral–drift ratios of 2.0% and 2.25%, respectively. By the end of the second cycle, damage related to punching shear had

propagated, and the punching cone was fully formed. Further increasing the lateral–drift ratio widened the existing cracks, and a few new cracks appeared. In addition, the concrete cover began to spall from the bottom surface. Note: slab S1 was subjected to additional one lateral cycle load, for that's the reason, the concrete cover totally destroyed at the bottom surface**.**

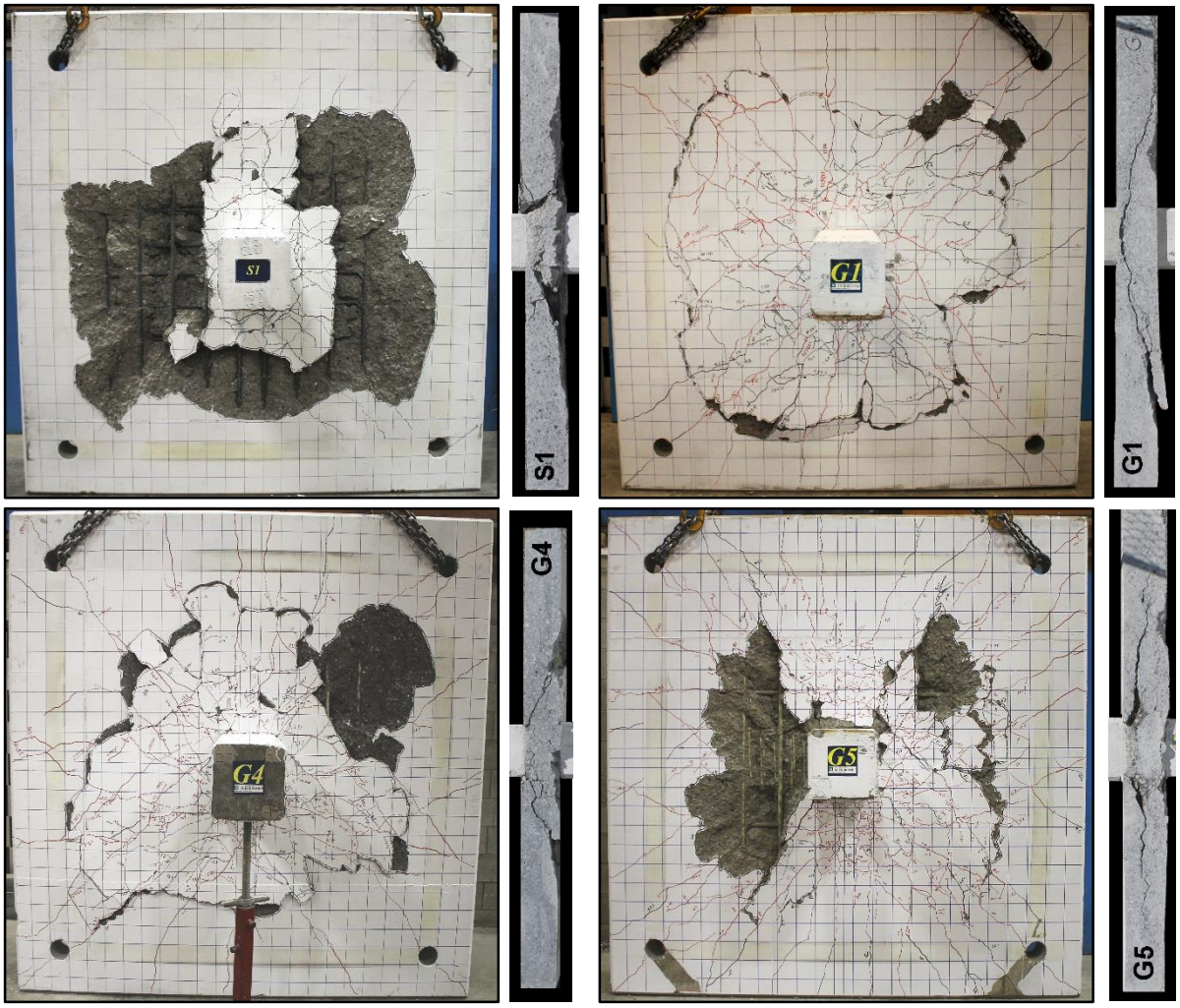

Figure 5.3 Final crack patterns and saw–cut of all tested specimens along the load direction.

The effect of using HSC with GFRP reinforcement and CSSR in specimens G4 and G5 was clear. At gravity-load intensities of 140 and 135 KN, the initial flexural cracks formed out from the column faces and extended toward the slab edges. The crack patterns in specimens G4 and G5 were fully formed at lateral-drift ratios of 2.50 and 3.50%, respectively. At higher lateral-drift ratios, the existing cracks become extensive, and few new cracks appeared. The first crack associated with punching for both specimens developed at a lateral-drift level of 3.0%. A complete punching cone formed in the HSC specimen during the first path of the first cycle at

a lateral-drift ratio of 3.50%, while the punching-shear failure crack had totally formed in the GFRP-reinforced specimen with CSSR at lateral-drift levels of 4.0% and 4.5%. Flexural cracks were observed along the transverse lateral-load direction at lateral-drift levels of 1.5% to 2%. A few flexural cracks formed as the lateral-drift level increased. The GFRP closed stirrups were more efficient in enhancing the specimen G5 performance than G1. This is due to the stirrup configuration, where the stirrups had four legs, which contributed to the shear-resistance mechanism. Also, the number of flexural reinforcement bars enclosed inside the stirrups. Nielsen (1999) and Braestrup et al. (1976) reported that the concrete stresses have to be transferred to the longitudinal bars supported by stirrups and the number of enclosed bars and their distribution along the concrete section may increase the effective concrete strength. Consequently, the stress concentrations around the supported bars led to a highly complicated state of micro cracking.

The average distances between the column face and the perimeter of the failure cone varied in each orthogonal direction. For specimens S1, G1, and G4 (without shear reinforcement) the corresponding average distance along the lateral–load direction was 3.6*d*, 4.0*d* and 3.6*d*, respectively, compared to 4.8*d*, 4.8*d* and 4.3*d*, respectively, in the transverse direction, where d is the effective depth of the slab. On the other hand, the average distances between the column face and the failure crack were 3.8*d* in specimen G5.

5.5.2. Failure Modes

Specimens S1, G1, and G4 (without shear reinforcement) experienced typically abrupt and brittle punching-shear failure without much warning. Punching-shear failure was evidenced by a sudden drop in applied loads. At this point, an attempt was made to reload the specimen to attain the target gravity load before returning the specimen to zero lateral displacement, followed by test termination. In contrast, specimen G5 (with shear reinforced) exhibited a softer punching-shear failure with a gradual decrease in the lateral loads. It should be pointed out that no signs of GFRP-bar rupture, slippage, or bond failure were observed, whereas a clear yielding of the steel bars was observed in the steel-reinforced specimen.

Figure 5.3 shows the sawn cross sections for all the specimens. To reveal the inclination of the diagonal cracks, all the specimens were cut along a line close to the column face in the lateral-

load direction. The punching failure was characterized by a single diagonal shear crack extending from the column face to the slab tension side at different inclination angles. The inclination angle for the specimens without shear reinforcement (S1, G1, and G4) ranged from 27° to 30°, 23° to 25°, and 23° to 26°, respectively. For specimen G5, the inclination of the main diagonal shear cracks was significantly affected by GFRP stirrups. The sawn surface of specimen G5 shows a horizontal splitting crack located above the upper ends of the shear stirrups. This splitting crack did not become inclined until it had extended to the outermost peripheral line of the shear reinforcement, thereby confirming that the punching shear occurred outside the shear-reinforced zone. It should be pointed out that no rupturing of the GFRP stirrups was observed

5.5.3. Hysteretic Response

Figure 5.4 provides the unbalanced moment versus the lateral-drift-ratio relationships for all the specimens. The unbalanced moment is defined as the moment transferred between the column and the slab. The unbalanced moment is generated through reversed lateral cyclic loading at the column ends. The unbalanced moment was obtained at each load step by multiplying each jack load by the effective height. The effective height is the distance from the application point to the center of the slab, that is, 675 mm. The lateral-drift ratio was calculated by dividing the lateral drift between the top and bottom of the column by the total effective height. Table 5.2 provides the peak lateral load (H_{max}), maximum unbalanced moment (M_{max}), and the corresponding lateral-drift ratio (δ) in each direction; the ultimate lateral-drift ratio (δ_{ult}); and the lateral-drift ratio corresponding to 80% of the peak unbalanced moment ($\delta_{0.8\,Mmax}$). **Figure 5.5** presents the envelope of unbalanced moment versus the lateral-drift-ratio relationship to aid in comparison.

Table 5.2 Test results.

Specimen	Gravity Load, KN	Peak Lateral Load, KN		Max. Unbalanced Moment, KN.m		Drift Ratio *(%)*				Max. Reinforcement Strain at *d/2* *(με)*	Max. Concrete Strain *(με)*
	Vg	H_+	H_-	M_+	M_-	δ_+	δ_-	δ_{ult}	$\delta_{0.8\,Mmax}$	ε_{max}	$\varepsilon_{c\,max}$
S1$_{(1.12)}$	140	168.4	165.6	223.7	220.4	2.00	–2.00	2.00	2.00	2350	–1048
G1$_{(1.06)}$		136.6	136.7	179.8	180.9	2.25	–2.25	2.25	2.25	5239	–1040

G4$_{(1.06)-H}$	183.5	173.0	240.7	228.2	3.00	–3.00	3.50	3.50	6750	–1473
G5 $_{GCS-4.5d}$	154.4	152.1	202.1	206.4	2.25	–2.25	6.50	5.00	5579	–2311

Note: d = slab effective depth; + refers to the positive direction and – to the negative direction

The relationships indicate that both specimens S1 and G1 (without shear reinforcement) displayed good ability to withstand interstory drift up to a level of 1.5% minimum drift capacity without punching failure. The maximum unbalanced moment carrying capacities varied at higher lateral-drift ratios. The maximum lateral-drift ratios for specimens S1 and G1 were 2.0% and 2.25%, respectively. On the other hand, the peak lateral loads during the first loading cycle were always higher than those recorded during the second repeated cycle load. This was attributed to the effect of cyclic loading on propagating the cracks and damaging the concrete at the first cycle. The GFRP-reinforced specimen G1 achieved a maximum unbalanced moment carrying capacity of 180.9 kN.m, which is 81% that of the steel-reinforced specimen.

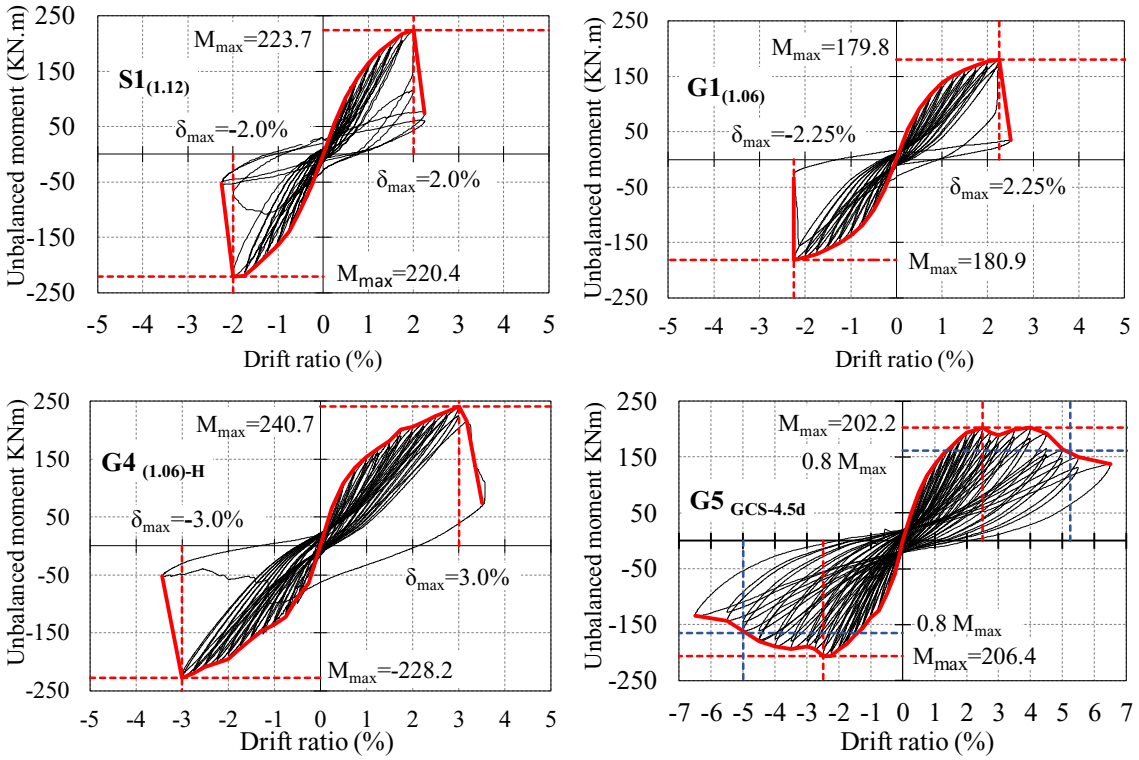

Figure 5.4 Unbalanced moment–lateral–drift ratio relationship of test specimens.

Using HSC in specimen G4 without shear reinforcement clearly enhanced the slab's performance. The lateral-drift ratio increased to 3.0% and the maximum unbalanced moment carrying capacity reached 240.7 kN.m. The lateral-drift ratio and the unbalanced moment capacity was 33% higher than that of specimen G1. During the second repeated cycle of 3.0%,

a gradual decrease in load occurred. The punching failure occurred during the first path of the first cyclic of lateral-drift ratio of 3.50% (positive direction). It should be pointed out that specimen G4 exhibited punching-shear failure that resulted in a sudden drop in gravity and lateral loads.

On the other hand, using the GFRP stirrups around the column area effectively contributed to the lateral-deformation and unbalanced moment carrying capacities. The maximum unbalanced moment carrying capacity was 206.4 kN.m, whereas the corresponding lateral-drift ratio was 2.25%. The unbalanced moment carrying capacity decreased slightly with increasing lateral-drift ratio. The shear-reinforced specimen was able to sustain lateral drifts as high as 5% with no more than a 20% decrease in the maximum unbalanced moment carrying capacity. The lateral-drift ratio and unbalanced moment capacity of G5 were 2.22 and 1.14 times of specimen G1 without shear reinforcement, respectively.

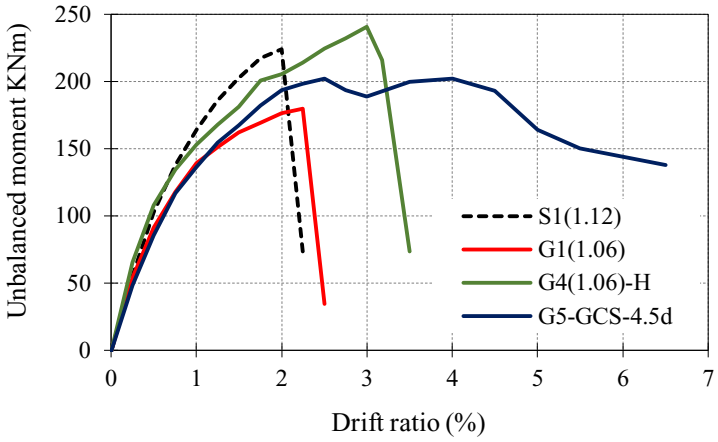

Figure 5.5 Backbone curves for the test specimens.

5.5.4. Flexural Reinforcement and Concrete Strains

The flexural-reinforcement strains were measured in each orthogonal direction at 0, 75, 225, 450, and 750 mm from the column face. **Figure 5.6** illustrates the strain profiles of all the specimens at each lateral-drift ratio along the lateral-loading direction. **Figure 5.7** illustrates the reinforcement strain versus at lateral-drift-ratio relationships in each orthogonal direction at a distance d/2 (75 mm) from the column face. For the specimens without shear reinforcement, the flexural-reinforcement strains generally decreased as the distance from the column face increased. At a distance of 750 mm from the column edges, very low reinforcement strains

values were recorded. In addition, none of the GFRP-reinforced specimens experienced bar rupturing, slippage, or bond failure during testing. This implies that the GFRP bars adequately transferred loads with no signs of bar slippage or bond failure during the tests. Further, the reinforcement strains in the compression side were very low compared to the flexural-reinforcement strains. The concrete strains also were measured at column faces during testing (see Table 5.2).

An evident yielding of the steel bars was observed at a lateral-drift ratio of 1.25% in specimen S1. At the column faces, a maximum flexural-reinforcement strain of 3204 μs was recorded at a lateral-drift ratio of 2.00%. At 75 mm from the column face, the maximum reinforcement strain was 2350 $\mu\varepsilon$. The maximum concrete strain at the column face was -1048 $\mu\varepsilon$, which is below the theoretical crushing strain of 3500 and 3000 $\mu\varepsilon$ as per CSA S806 (2012) and ACI 440.1R (2015), respectively. Upon punching-shear failure, however, no signs of concrete crushing were observed on the compression side of the slab during testing.

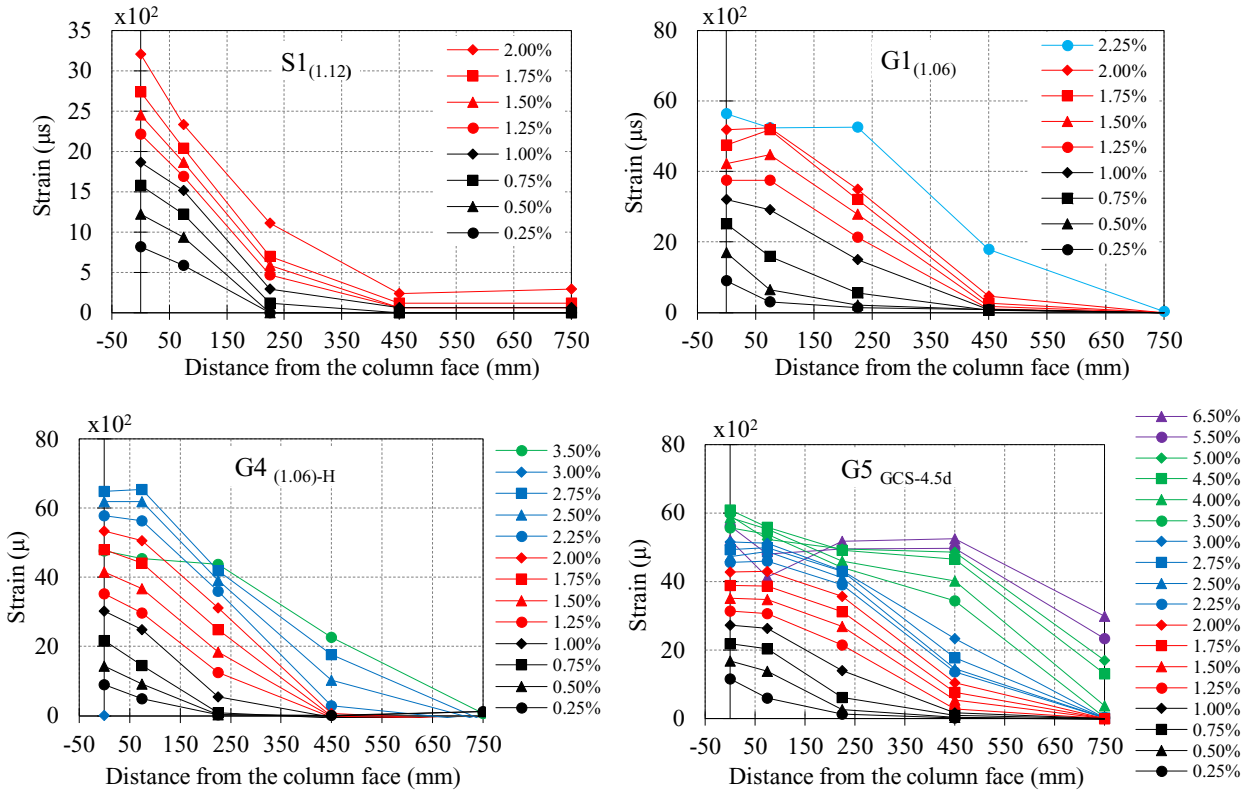

Figure 5.6 Strain profile along the lateral–load direction.

In all the GFRP-reinforced specimens, the maximum flexural-reinforcement strains were less than the characteristic tensile strength. Along the lateral-loading direction, the maximum

flexural-reinforcement strains were 5641, 6533, and 6078 $\mu\varepsilon$ for specimens G1, G4, and G5, respectively, representing 32%, 38%, and 35% of the guaranteed tensile strength. In the transverse direction, the maximum flexural-reinforcement strains were 2715, 2646 and 4681 $\mu\varepsilon$, respectively, representing 0.48, 0.39, and 0.77 times those recorded along the lateral-loading direction, respectively. On the other hand, the maximum concrete strains at the column face were also lower than the theoretical crushing strain and equal to -1040, -1473 and -2311 $\mu\varepsilon$, respectively. No signs of concrete crushing were observed on the compression side. For shear-reinforced specimen G5, at higher lateral drift levels a moderate increase in the flexural-reinforcement strain was observed as the distance from the column face increased. No signs of GFRP-bar rupture, slippage, or bond failure were observed.

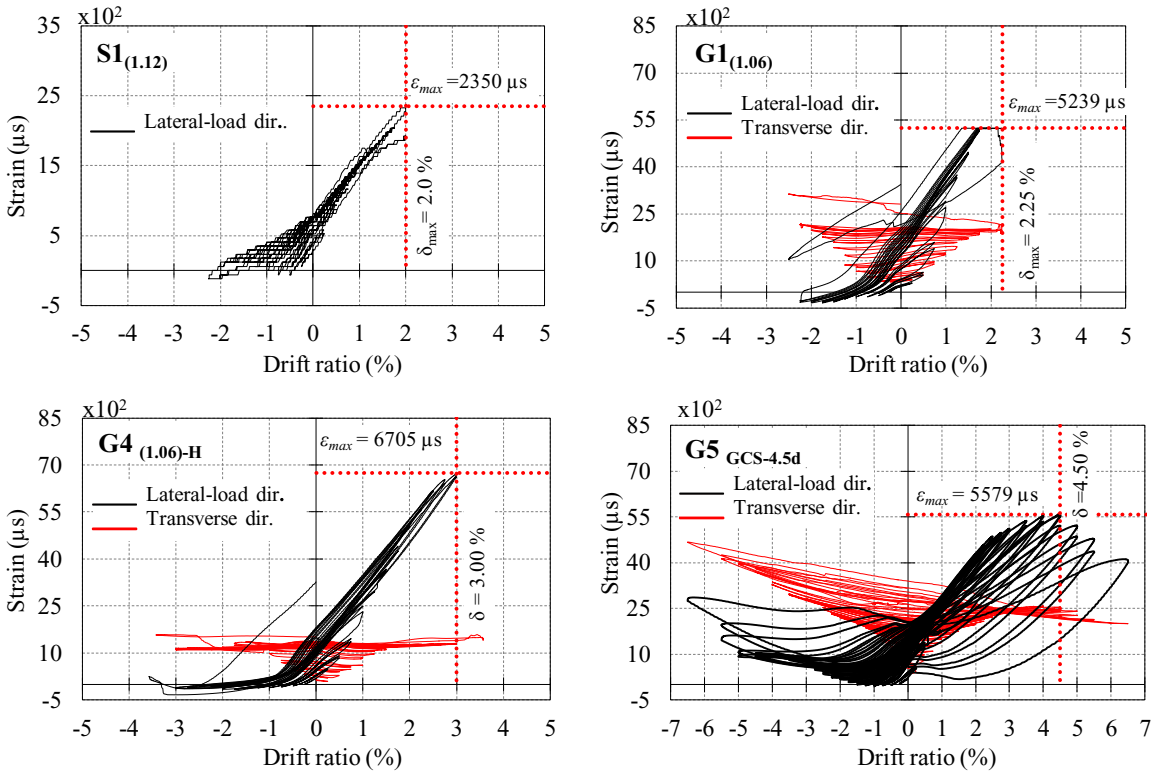

Figure 5.7 Reinforcement strain versus lateral–drift ratio at d/2.

5.5.5. Connection Stiffness

Figure 5.8 (a) plots the average peak-to-peak stiffness versus the lateral-drift ratio and the peak-to-peak stiffness per each drift cycle of loading. The peak-to-peak stiffness is defined as the slope of the line connecting the maximum achieved unbalanced moments in a given cycle (see

Figure 5.9 [Robertson et al. (1992), Megally et al. (1998) and Emam et al. (1997)]. In general, the reduction in connection stiffness occurred during the successive cycles of increasing lateral displacement. The initial connection stiffness (S_i) is defined as the slope of the line connecting the maximum unbalanced moments of the first cycle at a lateral-drift ratio of 0.25%. Table 5.3 compares the connection stiffness for all specimens; (S_i) at the initial, 1.5%, and (S_u) at ultimate lateral-drift ratios.

Table 5.3 Connection stiffness.

Specimen	M_{max} KN.m	Initial Stiffness S_i KN.mm		Stiffness at 1.50% S KN.mm		Stiffness at Ultimate Drift S_u KN.mm	
		1st cycle	2nd cycle	1st cycle	2nd cycle	1st cycle	2nd cycle
S1$_{(1.12)}$	223.7	218.0	215.0	125.1	120.0	103.8	51.9
G1$_{(1.06)}$	180.9	214.5	213.7	107.7	102.8	80.2	71.5
G4$_{(1.06)-H}$	240.7	260.0	255.8	114.2	109.3	78.1	74.2
G5 $_{GCS-4.5d}$	206.4	214.2	213.4	112.1	107.3	32.6	29.2

The initial connection stiffness for both specimens S1 and G1 was approximately equal. Nevertheless, the steel-reinforced specimen behaved stiffer than the GFRP-reinforced specimens and showed a moderate degradation of connection stiffness. This is attributed to the lower axial stiffness of the GFRP bars. Therefore, the degradation in the connection stiffness of specimen G1 was higher than that of the steel-reinforced specimen. The connection stiffness at the ultimate lateral-drift ratio were 47% and 37%, of the initial stiffness of specimens S1 and G1, respectively. A reduction of about 4% to 5% in connection stiffness was observed during the second cycle at each lateral-drift level.

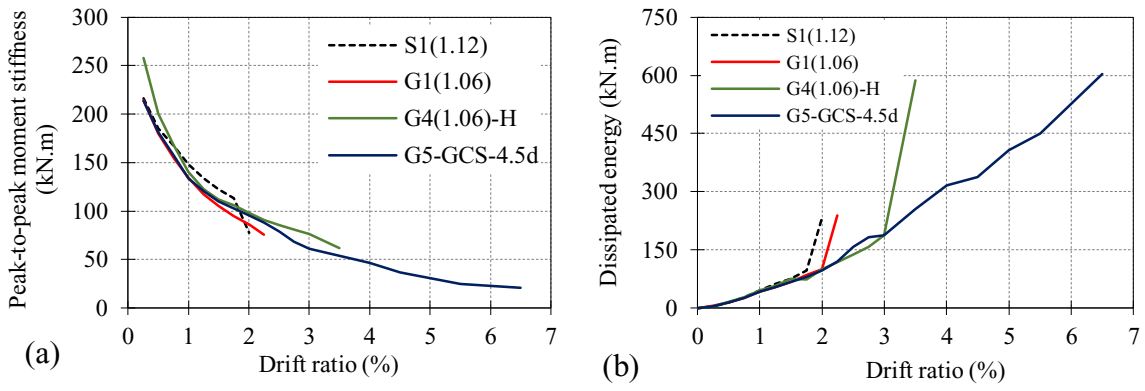

Figure 5.8 (a) Average peak-to-peak stiffness for test specimens, (b) Average dissipated energy versus drift ratio.

The effectiveness of using HSC in specimen G4 was evident: the initial connection stiffness was 21% higher than in NSC-specimen G1, because of the HSC's higher compressive strength and modulus of elasticity compared to the NSC. This confirms the findings of Hassan et al. (2013). The connection-stiffness values of the HSC specimen at all lateral drift levels were higher than the NSC specimen. This observation is in agreement with the findings of Marzouk et al. (2001). For HSC-specimen G4, the connection stiffness at the ultimate lateral-drift ratio was 30% of the initial stiffness. During the second cycle at each lateral-drift level, a 5% reduction in connection stiffness was observed in HSC-specimen. As shown in **Figure 5.8 (a)**, the shear reinforcement specimen had a little effect on the connection-stiffness at the early lateral-drift levels up to a drift ratio of 1.50%. As the lateral-drift levels increased, the shear-reinforced specimen exhibited higher connection stiffness compared to specimen G1. Shear-reinforced specimen G5 showed a god ability to undergone far more deformation without abruptly losing stiffness. Moreover the shear-reinforced specimen didn't degrade as rapidly at higher drift levels. This is attributed to controlling the crack development and associated damage in the slab–column connection with GFRP stirrups. Also, at early lateral drifts of 0.25% to 2.50%, about 4% reduction in connection stiffness was observed during the second reputed cycle. While, the reduction in connection stiffness increased to 11% at higher drift levels during the second repeated cycle.

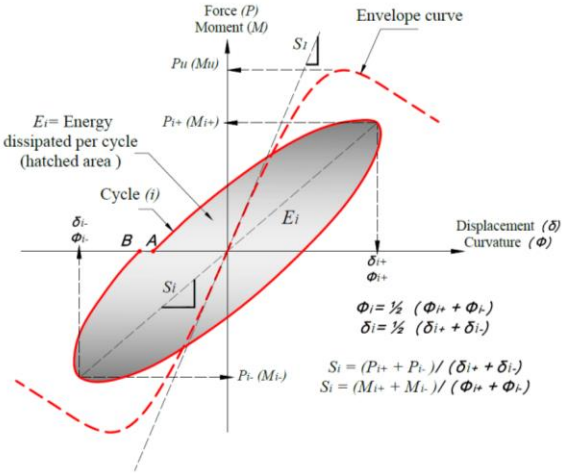

Figure 5.9 Normalization of energy-dissipation capacity and stiffness calculation according to ACI T1.1-01.

5.5.6. Energy Dissipation

Energy dissipation (E_D) is a significant indicator of RC elements being able to absorb energy before failure. Accordingly, it is one of the most important criteria used to assess the seismic performance of RC elements. A higher capacity for energy dissipation points to better post-peak behavior and ductile failure. The normalization of E_D capacity was determined according to ACI T1.1-01 by calculating the area within the corresponding moment–drift-ratio hysteresis loop at each drift cycle (see **Figure 5.9**). The average energy dissipated versus lateral-drift ratio shows in **Figures 5.8 (b)**. Table 5.4 lists the energy dissipation at maximum lateral drift ratio.

The responses clearly show that the steel–reinforced specimen exhibited slightly higher energy dissipation compared to GFRP–reinforced specimen G1. This was due to yielding of the steel reinforcement, which produced a wide loop in its hysteresis response. On the other hand, the effect of repeated load cycles was evident, where the average reduction in the dissipated energy at each drift cycle was about 24% for both specimens.

Table 5.4 Ductility index and dissipated energy.

Specimen	M_{max} KN.m	$\delta_{0.8u}$ (%)	Method (I)		Method (II)		Dissipated Energy E_D, KN.mm	
			$\delta_{(y),\,e}$ (%)	μ_δ	$\delta_{(y),\,e}$ (%)	μ_δ	1st cycle	2nd cycle
S1(1.12)	223.7	2.00	1.50	1.33	1.42	1.41	243.3	220.3
G1(1.06)	180.9	2.05	1.30	1.57	1.24	1.65	125.7	349.8
G4(1.06)–H	240.7	3.27	1.79	1.82	1.97	1.66	192.4	181.9
G5 GCS–4.5d	206.4	5.00	1.57	3.20	1.64	3.05	419.8	393.0

Note: $\delta_{0.8u}$ = slab lateral–drift ratio at 20% loss of ultimate lateral strength; δ_y = slab lateral–drift ratio based on steel yielding; δ_e = virtual slab lateral–drift ratio; μ_δ= lateral–drift–based ductility factor

Due to the higher concrete strength and, consequently, the higher concrete tensile strength, the HSC specimen G4 recorded a relative increase in dissipated energy compared to NSC specimen G1. This confirms the early observation by Megally and Ghali (2000) "*the use of high strength concrete slightly increases the energy dissipation capacity*". It is worth mentioning that all of the specimens without shear reinforcement experienced an abrupt increase in energy dissipation at the ultimate drift ratio. This sudden increase was due to significant concrete damage that occurred at the connection, which resulted in wider loops in the hysteresis responses of the specimens. On the other hand, providing GFRP stirrups in the shear-reinforced specimen

effectively contributed to its energy-dissipation capacity. The shear-reinforced specimen exhibited the ability to dissipate energy during high lateral-drift levels. This observation coincides with experimental findings reported by Megally et al. (1998) and Kang, T. H.-K. et al. (2017).

5.5.7. Ductility Index

The ductility of flat–plate structures in seismic zones is deemed a very important design consideration. In seismic zones, slab-column connections are expected to undergo inelastic deformations, so connections must be designed with adequate strength and ductility. In addition, such connections must be able to withstand a specific limit of inter-story drift without punching–shear failure. Ductility can be defined as an element's ability to sustain inelastic deformations prior to collapse without substantial loss of strength. The ductility factor is the ratio of the ultimate lateral displacement (deflection or drift) of the element to its corresponding displacement at an equivalent yielding of the steel reinforcement. This definition cannot be directly applied to FRPs or FRP–reinforced concrete members given the fact that FRP bars do not yield. Accordingly, the transition point between the elastic and inelastic regions in GFRP–reinforced concrete members is defined herein as the virtual deflection Δ_e or drift point δ_e. ACI 440.1R (2015) and CSA S806 (2012) design codes offer no unified method for assessing the ductility index of FRP–reinforced concrete members. When calculating ductility capacity, the definition of yield displacement often causes difficulty because the force-displacement response of RC components might not have a well–defined yield point. This can occur due to the nonlinear behavior of the materials (steel reinforcement and concrete) or due to yielding in different parts of the RC structure or subassembly initiating at different load levels. Consequently, the general practice has been to define the ductility parameters of RC components based on an idealized bilinear force-displacement response (Park R. 1989).

Various definitions have been proposed for the estimation of yield displacement. **Figure 5.10** illustrates the procedure proposed by Park (1989) and adopted herein. Two methods were used to estimate the ductility index. In Method 1, the virtual limit was evaluated based on the equivalent elastic–plastic energy absorption where the secant line was chosen so as to have identical hatched areas and ensure equal energy criteria (see **Figure 5.10** (1)). The relative displacement or drift ratio corresponding to the intersection point of the secant line from the

origin to the tangent line of the maximum unbalanced moment (M_{max}) is defined as a virtual deflection (Δ_e) or lateral–drift ratio point (δ_e). In Method 2, the virtual limit was evaluated based on the reduced stiffness equivalent elastic–plastic system. The reduced stiffness found as the secant stiffness at 75% of the maximum unbalanced moment (M_{max}) (see **Figure 5.10** (2)). The plastic portion of the idealized relation passes through the maximum unbalanced moment. The intersection between these two lines is the virtual deflection (Δ_e) or lateral–drift–ratio point (δ_e). Table 5.4 provides the lateral–drift ratio at a 20% loss of ultimate lateral strength (δ0.8u); the lateral–drift ratio based on steel yield (δ_y); the virtual lateral–drift ratio (δ_e), and the lateral–drift ductility index (μ_δ). The ultimate deflection or lateral–drift ratio is well recognized as a 20% loss of ultimate lateral strength (NBCC 2005). The drift ductility index (μ_δ) is determined using Eqns. (5.1) and (5.2).

$$(\mu_\delta = \frac{\delta_{0.8u}}{\delta_y}) \text{ or } (\mu_\delta = \frac{\Delta_{0.8u}}{\Delta_y}) \qquad \text{(steel)} \quad (5.1)$$

$$(\mu_\delta = \frac{\delta_{0.8u}}{\delta_e}) \text{ or } (\mu_\delta = \frac{\Delta_{0.8u}}{\Delta_e}) \qquad \text{(FRP)} \quad (5.2)$$

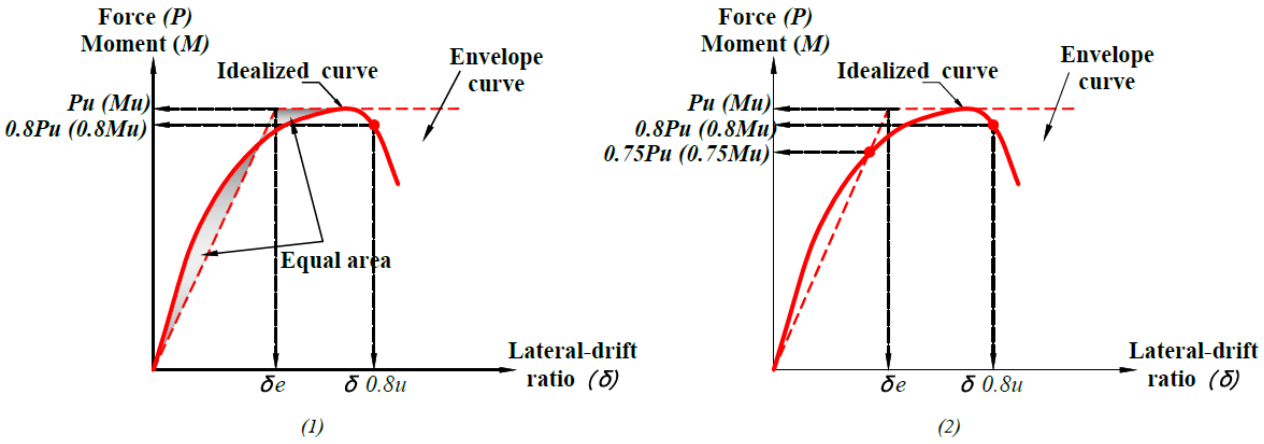

Figure 5.10 Ideal–curve definition.

As reported in Table 5.4, all of the GFRP-RC specimens demonstrated reasonable predicated ductility indexes and consistent with the minimum required ductility factor of 1.2 for steel slab–column connections in a seismic zone, as reported by Pan and Moehle (1988); and Megally & Ghali (1994). Methods 1 and 2 gave ductility factors of 1.33 and 1.41, respectively, for the steel-reinforced specimen. Specimen G1 (NSC with GFRP reinforcement) had adequate drift

ductility indices ranging between 1.57 and 1.65, that is, 30% and 37% higher than the minimum ductility index of 1.2 required for slab–column connections for a building in a seismic zone, combined with sufficiently stiff shear walls [Pan and Moehle (1988)]. On the other hand, using HSC or GFRP CSSR in the GFRP-reinforced specimens generally yielded higher ductility indexes than specimens S1 and G1. According to Method 1, the drift ductility index for HSC specimen G4 was 1.82, and 1.66 according to Method 2. The specimen with GFRP shear reinforcement displayed higher drift ductility indexes (3.20 and 3.05), which are around twice that of specimen G1. This was attributed to the ability of the specimen to sustain lateral–drifts as high as 5% with no more than a 20% decrease in the maximum carrying capacity. This observation coincides with previous observation *"the ductility factor for the shear–reinforced specimens always exceeded 3"* [S.U. Pillai et al. (1982) and Megally and Ghali (1998)].

5.5.8. Crack Opening

The diagonal shear–crack width was estimated by monitoring the vertical–displacement difference of the slab faces during testing. Two potentiometers were installed on the top and bottom slab faces at 100 mm from the column faces in each orthogonal direction. **Figure 5.11** (a–b) illustrates the diagonal shear–crack width through the slab thickness versus drift–ratio relationships in both orthogonal directions. All the specimens without shear reinforcement demonstrated an abrupt increase in crack–width opening at the ultimate drift ratio, confirming punching–shear failure occurred. Crack widths in the direction of lateral loading were larger than those in the direction perpendicular to lateral loading. The test results indicate that steel–reinforced specimen S1 had narrower cracks than all the GFRP–reinforced specimens. This is due to the high effective reinforcement ratio ($\rho E_r/E_s$, where E_r is the modulus of elasticity of the reinforcing bars), which was 3.1 times that of the GFRP specimens. The maximum recorded crack widths prior to punching failure were 9.98 and 5.4 mm along the lateral–load and transverse directions, respectively. Contrariwise, GFRP–reinforced specimen G1 had greater diagonal shear, and the maximum width of the diagonal shear cracks along the lateral–loading direction was 19.3 mm, compared to 8.1 mm in the transverse direction.

In the case of the HSC specimen without shear reinforcement (G4), the concrete strength significantly affected crack openings. At the same lateral–drift levels, specimen G4 had a narrower diagonal shear crack than NSC specimen G1. This is attributed to the higher concrete

strength and, consequently, the higher concrete tensile strength. On the other hand, the crack openings in the GFRP shear–reinforced specimen were moderately narrower than in specimen G1 without shear reinforcement. Moreover, the crack openings in the GFRP shear–reinforced specimen increased with increasing lateral–drift ratio. It should be mentioned that in the GFRP shear–reinforced specimen, horizontal splitting cracks near the columns above the shear stirrups appeared and, due to the growth of the splitting cracks above the shear stirrups, increases in the crack openings were observed [Dam et al. (2017)].

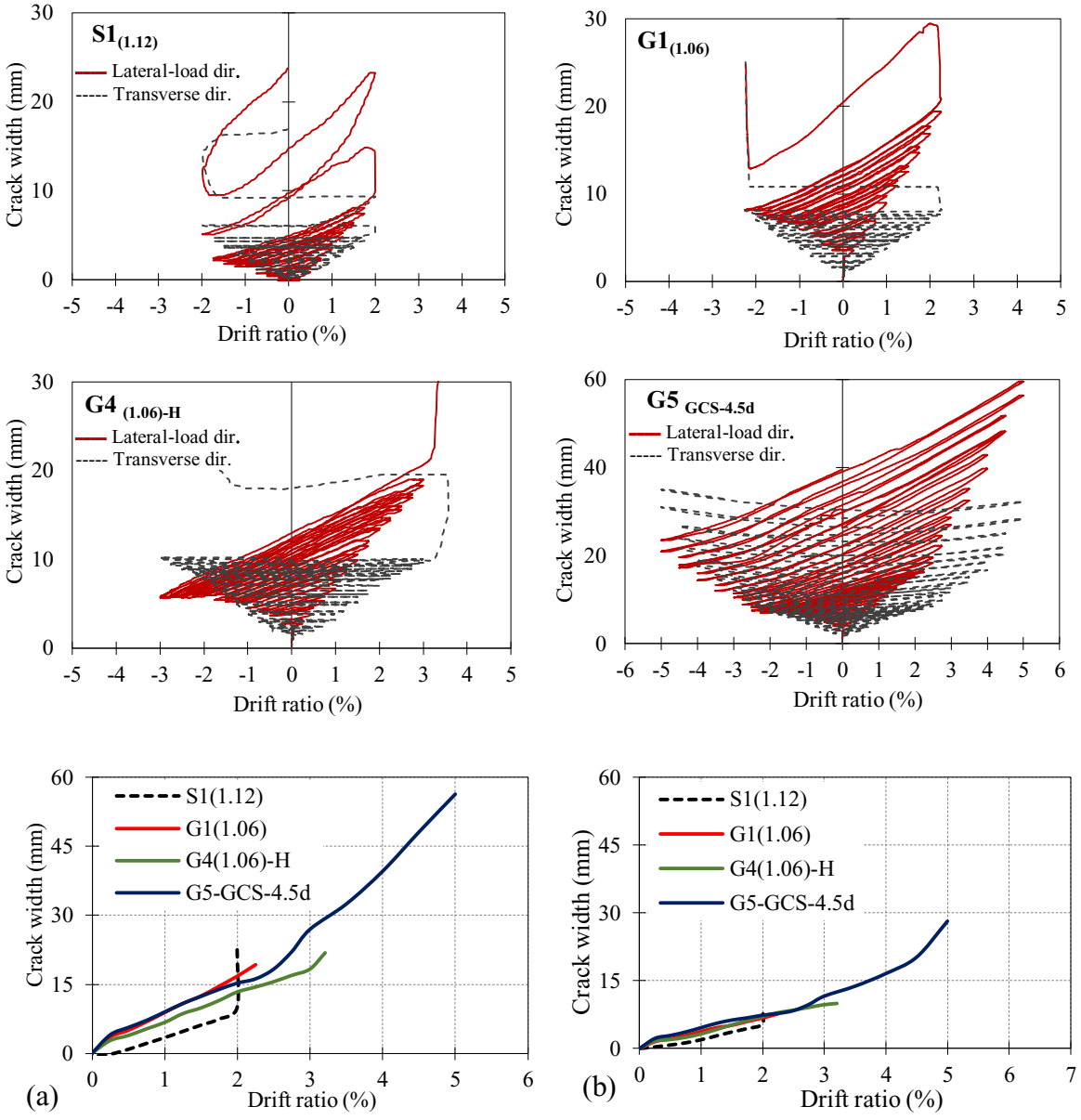

Figure 5.11 (a) Opening of cracks versus drift ratio in the direction of the lateral–cyclic loads and (b) In the transverse direction.

5.6. Discussion

5.6.1. Effect of Reinforcement Type

Through the reported test results and measures, it was clear that the steel-reinforced specimen S1 and NSC specimen G1 with GRFP reinforcement had comparable punching-shear response. Regardless of reinforcement type, the crack patterns, punching-shear failure surface, and failure of the GFRP-reinforced specimens was comparable to that of the steel-reinforced specimen. The punching-shear stresses at failure were normalized to the cubic root of the concrete strength to account for the variation in the concrete strengths. Besides, the effective reinforcement ratios ($\rho E_r/E_s$) of the specimens were used to account for the difference between the moduli of elasticity of the GFRP and steel bars. The results in Table 3 showed that the GFRP-RC specimens evidenced lower punching-shear stress at failure. This was related to the smaller dowel action and the lower modulus of elasticity of GFRP reinforcing bars compared to that of steel (~0.25). Using a GFRP reinforcement ratio approximately equal to the steel reinforcement ratio yielded smaller neutral-axis depth as well as higher strains and deeper and wider cracks at the same load level. Thus, both the contributions of the uncracked concrete zone (compression side), and the aggregate interlock decreased, which, in turn, yielded lower punching-shear capacity. Yielding of the steel bars was clearly evident and there were no signs of GFRP-bar rupture, slippage, or bond failure in the GFRP-reinforced specimen. Moreover, the maximum recorded strain of the GFRP reinforcement was 32% of the guaranteed tensile strength. Consequently, a minimum amount of slab repair would be required after a seismic-loading event, which is considered an advantage for GFRP-reinforced concrete structures. Due to the steel reinforcement yielding, which produces a wide loop in the hysteresis response, the steel-reinforced specimen dissipated more energy than GFRP-reinforced specimen G1. The steel-reinforced specimen had narrower diagonal shear cracks than specimen G1 due to the high effective reinforcement ratio ($\rho E_r/E_s$). Specimen G1 had a higher rate of stiffness degradation than the steel-reinforced specimen. This is attributed to the GFRP bars having lower axial stiffness than the steel bars. Specimen G1 had drift-ductility indexes of 1.57 and 1.65, which exceed the minimum required slab–column connection ductility factor of 1.2 reported by Moehle (1989) and Megally (1994).

5.6.2. Effect of Concrete Strength

Increasing the concrete compressive strength and subsequent punching-shear level in the flat-plate floor system had a considerable effect on punching-shear performance. Increasing the concrete strength by 77%, from 52 to 92 MPa, resulted in a 33% increase in the lateral-drift ratio and the maximum unbalanced moment carrying capacities. An increase in failure cone angle was also observed in the GFRP-reinforced HSC specimen, therefore the punching-shear radius was smaller. The use of HSC GFRP reinforcement enhanced specimen G4's punching resistance, but the punching-shear failure was not gradual, but rather brittle and abrupt. On the other hand the maximum flexural-reinforcement strain was 38% of the guaranteed tensile strength, and no signs of concrete crushing were observed on the compression side. The impact of concrete strength on the slab–column connection stiffness, the energy dissipated, and drift ductility index was evident. Because of the HSC's higher compressive strength and modulus of elasticity compared to the NSC, a 21% improvement in the initial connection stiffness was evidence. Moreover, the GFRP-HSC specimen had more moderate degradation of connection stiffness degradation than the NSC specimen with GFRP reinforcement. The connection stiffness of the HSC specimen with GFRP reinforcement (G4) was 10% higher than that of the NSC specimen. The HSC specimen with GFRP reinforcement dissipated relatively more energy than the NSC specimen with GFRP reinforcement. The lateral-drift ductility indexes for the HSC specimen with GFRP reinforcement were also slightly enhanced. This agree with the previous findings Megally et al. (1998) "*Specimen made of high strength concrete is a little more ductile than the similar specimen cast of normal strength concrete*".

5.6.3. Effect of GFRP–Stirrup Shear Reinforcement

The impact of using GFRP CSSR in the vicinity of the slab–column connections was obvious in the seismic response in terms of lateral-drift ratio, unbalanced moment carrying capacity, energy dissipation, connection stiffness, and lateral-drift ductility indices. The GFRP shear-reinforced specimen exhibited a softer punching-shear failure with only a gradual decrease in the lateral loads. The GFRP shear-reinforced specimen achieved a lateral-drift ratio of 5.0% with no more than a 20% decrease in the maximum unbalanced moment carrying capacity. Moreover, a gradual decrease in the lateral loads alone was evidenced at higher drift ratio levels. The specimen was also able to sustain the gravity load until the end of testing. No signs of bar

or stirrup rupture, slippage, or bond failure were observed, and the specimen with GFRP shear reinforcement maintained its integrity. The lateral-drift ratio and the unbalanced moment carrying capacity were improved by 122% and 14%, respectively. The use of GFRP CSSR effectively contributed to controlling crack development and the associated damage in the slab–column connection. Consequently, at higher drift levels, the specimen revealed higher connection stiffness and didn't degrade as rapidly as the specimen without shear reinforcement. Furthermore, the specimen with shear reinforcement exhibited the ability to dissipate energy a high levels of lateral drift. A significant increase (85% to 103%) in drift ductility indices was observed, and this observation coincides with the experimental findings reported by Megally (1998).

5.7. Summary and Conclusions

This paper presented the test results of an experimental study undertaken to investigate the punching–shear performance of full–scale interior slab-column connections reinforced with steel or GFRP bars and subjected to a combination of gravity and quasi-static reversed lateral cyclic loading. The tests primarily explored the effect of reinforcement type, the use of high–strength concrete, and the feasibility of using closed GFRP stirrups as shear reinforcement on slab seismic performance. Based on the findings, the following conclusions can be drawn:

1. The GFRP-reinforced specimens showed adequate punching strength and deformation capacity against punching-shear failure during and after reversed lateral cyclic-loading conditions. Accordingly, GFRP reinforcing bars could be used as reinforcement in slab–column connections subjected to a combination of gravity and reversed lateral cyclic loads.
2. The specimens without shear reinforcement experienced a typically sudden and brittle punching-shear failure without much warning. The failure manifested as a sudden drop in both the applied gravity and lateral loads. The specimen with GFRP-stirrups exhibited softer punching-shear failure with a gradual decrease in the lateral loads and maintained its integrity.
3. The GFRP specimens without shear reinforcement achieved level of lateral drift of 2.25% and 3.00%, which is in agreement with the recommended minimum design lateral drift in

codes used for seismic analysis. The specimen with GFRP-stirrups recorded a high lateral drift of 6.50% with the ability to sustain the gravity load.

4. A reduction in slab–column connection stiffness was observed in all the specimens tested during successive cycles of increasing displacement. Moreover, the effect of repeated loading cycles was evident. All the GFRP-RC specimens showed a moderately higher rate of degradation than the steel-reinforced specimen, although they followed a similar trend.
5. All GFRP-RC specimens exhibited reasonable levels of energy dissipation upon punching-shear failure. Moreover, specimen with GFRP shear reinforcement displayed the ability to dissipate energy during high lateral-drift levels. On the other hand, all GFRP-RC slab–column connections yielded sufficient drift ductility indexes when subjected to reversed lateral cyclic loads compared to the minimum required ductility factor of 1.2 for the steel-RC connections.
6. The use of HSC had a significant effect on the GFRP-reinforced slab–column connection. A 33% enhancement in the lateral-deformation and moment capacities were observed. Nevertheless, the HSC specimen with GFRP reinforcement failed suddenly in a brittle punching-shear failure. The degradation of the connection stiffness was enhanced. Moreover, a 21% improvement in the initial connection stiffness was observed as well as a 10% increase in connection stiffness.
7. The presence of the GFRP stirrups in the slab–column connection zone significantly enhanced the punching-shear performance. The lateral- deformation and carrying capacities increased by 122% and 14%, respectively. The punching-shear failure was softer and the specimen's integrity maintained. Furthermore, the specimen with shear reinforcement exhibited the ability to dissipate energy during high lateral drift levels. On the other hand a clear increase (85 to 103%) in drift ductility indices were observed in specimen with stirrups.

On the basis of the test results, slab-column connections reinforced with GFRP flexural and shear reinforcement achieved high levels of strength and lateral drift capacity. Consequently, GFRP shear reinforcement could be used effectively as shear reinforcement in the two–way slab in the seismic zone. However, further research efforts are needed to assess the effectiveness

of the GFRP stirrups, taking into account the effects of GFRP–stirrup type and extension. Further, develop adequate design guideline and recommendations for such structural elements.

CHAPTER 6. EFFECT OF GFRP STIRRUPS ON PUNCHING SHEAR BEHAVIOR OF GFRP–RC SLAB–COLUMN CONNECTIONS UNDER LATERAL CYCLIC LOAD

Foreword

Title: Effect of GFRP Stirrups Shear Reinforcement on Punching Behavior of GFRP–RC Slab-Column Connections under Lateral Cyclic Load.

Authors and Affiliation:

- Mohamed Eladawy, PhD candidate, Department of Civil Engineering, University of Sherbrooke, Sherbrooke, QC, Canada.
- Mohamed Hassan, Postdoctoral fellow, Department of Civil Engineering, University of Sherbrooke, Sherbrooke, QC, Canada and Queen's University, Kingston, ON, Canada.
- Brahim Benmokrane, Professor of Civil Engineering and NSERC Research Chair in FRP Reinforcement for Concrete Infrastructure and Tier 1 Canada Research Chair in Advanced Composite Materials for Civil Structures, Department of Civil Engineering, University of Sherbrooke, Sherbrooke, QC, Canada.
- Amir Fam, Associate Dean and Donald and Sarah Munro Chair Professor in Engineering and Applied Science in the Department of Civil Engineering, Queen's University, Kingston, Ontario, Canada.

Journal: ASCE Journal of Structural Engineering.

Journal: Submitted March 2019.

6.1. Abstract

Providing shear reinforcement around slab–column connections in flat-plate structures located in seismic zones has proved to be effective in enhancing their seismic performance. It results in increased strength, lateral-drift capacity, and ductility, while reducing stiffness deterioration. This paper presents experimental work involving five full-scale concrete slab–column connections reinforced with glass-fiber-reinforced-polymer (GFRP) bars and stirrups. Each test specimen was a 2500 × 2500 × 200 mm slab with a 300 mm square column extending 700 mm from the top and bottom at the center of the slab. All specimens were tested to failure under combined constant gravity and reversed lateral cyclic loads. The objectives of this experimental study was to evaluate the effects of GFRP-stirrup type (closed and spiral) as shear reinforcement, stirrup extension, and gravity-load intensity on the behavior of the connections. The test results clearly show that using GFRP stirrups around the slab–column connection significantly enhanced performance. The specimens with GFRP stirrup exhibited flexible punching-shear failure with a gradual decrease in lateral load and maintained their integrity. All specimens achieved lateral inter-story-drift capacities exceeding 2.5%, satisfying the limits in CSA A23.3 and ACI 421.3R. Moreover, the tested specimens demonstrated highly predictable lateral-ductility indexes over the minimum required ductility factor of 1.2. In addition, the GFRP shear reinforcement (closed or spiral) enabled adequate connection stiffness and ability to dissipate energy during high lateral-drift levels. The promising results can provide impetus for constructing two-way concrete slabs reinforced with GFRP for buildings in low-to-moderate seismic zones.

Keywords: Concrete slab-column connection; Glass FRP (GFRP) reinforcement, Seismic loading; Lateral reversed cyclic loading, GFRP shear reinforcement; Punching shear; Connection stiffness; Energy dissipation; Drift–ductility index; Design codes.

6.2. Introduction

Flat-plate construction is common throughout North America and much of the world. It can be made even more economical by using the simplest form of flat slab, namely a flat-plate system with no variations in slab depth. Punching-shear strength at the slab–column connection is a critical design criterion for flat plates subjected to seismic activity. Various types of shear reinforcement (SR) can be used in the slab around the column connection to increase the slab's shear, lateral-drift and ductility capacities. Moreover, provision SR around the column zone effectively contributed to preventing premature punching-shear failure of slab–column connections.

In the slab–column connections, various types of SR have been investigated including stirrups; stud rails; shear bands or heads; and lattice bars (Pillai et al. 1982; Megally 1998; Robertson et al. 2002; Broms 2007 and Kang et al. 2017). The researchers reported that, the SR effectively improves the overall behavior of slab–column connections. Furthermore, the failure mode was characterized by a larger drift capacity (over 4% drift), energy-dissipating capacity and gradual strength degradation. Consequently improving the lateral-load resistance of the reinforced concrete structure system. Further, the residual gravity-load capacity is not impaired by cyclic lateral loading, the SR, however, cannot prevent concrete deterioration at the column. On the other hand, slab–column connections with SR exhibited lateral inter-story-drift ratios much higher than 1.5% without limiting of V_u/V_c (where, V_u is applied shearing force at failure and V_c is the ultimate punching shear capacity provided by the concrete). Subsequently, shear reinforcements are recommended in flat plate-structures located in seismic zones.

Current North American codes and guidelines—CSA S806 (2012) and ACI 440.1R (2015)—contain no requirements concerning the nominal punching-shear strength, stiffness, and drift capacity of flat-plate structures under lateral cyclic loading. No tests, however, have yet been conducted on FRP-RC slab–column connections with FRP-SR under a combination of gravity loading and reversed lateral cyclic loading. Few studies have investigated the punching-shear behavior of interior FRP-RC slab–column connections with various types of FRP-SR (Hassan et al. 2014; Gouda et al. 2016; and Hussein et al. 2018). The effectiveness and contribution of FRP stirrups as shear reinforcement were examined in two-way GFRP-RC slabs (Hassan et al. 2014). The results indicated that using the GFRP-SR yielded a more flexible punching-shear

failure mechanism. Furthermore, the amount of GFRP-SR played a significant role in enhancing the punching-shear strength and deformation capacity of the slabs, thus increasing their safety.

GFRP double-headed bars (studs) and corrugated bars were investigated as SR on the punching-shear behavior of GFRP-RC interior slab–column connections (Gouda and El-Salakawy 2016 and Hussein and El-Salakawy 2018). The experimental results revealed that, the presence of GFRP shear studs and corrugated bars as SR significantly increased the post-cracking stiffness, deflection at failure, and load-carrying capacity. Further, the GFRP shear studs and corrugated bars did not, however, prevent punching-shear failure. They recommended also extending the GFRP-SR in FRP-RC two-way slabs to distance not less than 2.0d from the column face (d is the effective depth of the slab), as specified by CSA A23.3-14.

6.3. Research Objective

The shear reinforcements customized for use according to the North American standards and design provisions include single-leg, multiple-leg, single U, multiple U, and closed stirrups. This experimental study was intended to be the first-ever on the punching-shear behavior of GFRP-RC slab–column connections with FRP-SR under a combination of gravity and reversed lateral cyclic loading. The performance of such connections was evaluated in terms of moment–lateral drift response, connection stiffness, energy dissipation, and drift–ductility index. The study took into consideration the effect of the type of stirrups (closed and spiral), stirrup extension, and the gravity-load intensity. This pioneering study will enable the development of new design provisions in the future edition of the ACI 440 Code for Structural Concrete Reinforced with GFRP Bars and the Canadian Standard Association's Design and Construction of Building Structures with Fibre-Reinforced Polymers.

6.4. Experimental Program

6.4.1. Specimen Configurations

All test specimens were geometrically identical and measured 2500×2500 mm with a thickness of 200 mm and a square column measuring 300 mm extending 700 mm at the slab's center above and below the slab surfaces. The slabs were simply supported on a 2000×2000 mm perimeter on the bottom face of the slab. **Figure 6.1** shows the geometry and reinforcement

details of the specimens. These dimensions were chosen to represent the interior slab–column connection of a flat-plate parking-garage building with 5000×5000 mm square panels. The live load was assumed to be 2.4 kN/m^2 and superimposed dead load to be 1.0 kN/m^2. The total gravity load on the floor, including the slab weight, was estimated according to NBCC (2015). Moreover, the dimensions were consistent with an extensive research project conducted at the University of Sherbrooke to evaluate the punching-shear performance of GFRP-RC slab–column connections (Dulude et al. 2013 and Hassan et al. 2013 & 2014).

The specimens have been identified as G1, G5$_{GCS–4.5d}$, G6$_{GCS–2d}$, G7$_{GSS–4.5d}$, and G8$_{GCS–4.5d–SL}$. The nomenclature can be explained as follows. The letter G indicates the reinforcement type: GFRP tension reinforcement or stirrup shear reinforcement. The subscripts CS and SS indicate the stirrup configuration: CS for closed stirrups and SS for spiral stirrups, respectively. The notation *x*d is the extension of the stirrups from the column faces relative to the effective depth and SL indicates a specimen with higher gravity-load intensity (if any). Table 6.1 presents the configuration and characteristics of each specimen.

Table 6.1 Specimen configuration

Specimen[1]	*C*, mm	*ts*, *mm*	*d*, *mm*	Flexural reinforcement		ρ_t, %	ρ_{bott}, %	ρ_b, %	f'_c[3] MPa	f_t[3] MPa	Gravity load intensity V_u KN	Stirrups parameters			
				Tension	Comp.							S_o	S_{fv}	Type	Extent
G1									52	3.93		—	—	—	—
G5 $_{GCS–4.5d}$									45	3.75	140	0.4d	0.5d	closed stirrups	4.5 d
G6 $_{GCS–2d}$	300	200	151	14 No.20	10 No.15	1.06	$0.5\rho_t$	0.30	45	3.75		0.4d	0.5d	closed stirrups	2.0 d
G7 $_{GSS–4.5d}$									51	3.86		0.4d	0.5d	spiral stirrups	4.5 d
G8 $_{GCS–4.5d–SL}$									51	3.86	180	0.4d	0.5d	closed stirrups	4.5 d

[1] "G" denotes for GFRP bars and stirrups, with a subscript indicating the stirrups configuration; (CS denotes closed stirrups and SS denotes bundle spiral stirrups), also, the extension of the stirrups from the column faces relative to the effective depth, specimen G8 followed by the gravity load intensity.
[2] ρ_t calculated according to CSA/S806–14.
[3] Compression and splitting testing on 100 × 200 mm concrete cylinders.

The specimens were designed to have a flexural-reinforcement ratio such that punching-shear failure would be expected to occur prior to flexural failure. The bottom and top reinforcement placed symmetrically in each orthogonal direction and consisted of 14 No. 20 and 10 No. 15 bars, respectively. The reinforcing ratio on the compression side of all slabs was half the tension reinforcement. Two bars ran through the column core on the compression side to satisfy the

requirements for structural integrity reinforcement in CSA A23.3-14. The clear concrete cover in the direction of the cyclic lateral loads was 30 mm and the average effective depth of the slabs d was 151 mm. The central column was heavily reinforced with six longitudinal deformed steel bars (25M) to make the column strong enough to transfer shear forces and cyclic moments to the slab and to avoid columns failure during the test. In addition, deformed closed ties (10M) were used with a closer spacing of 100 mm.

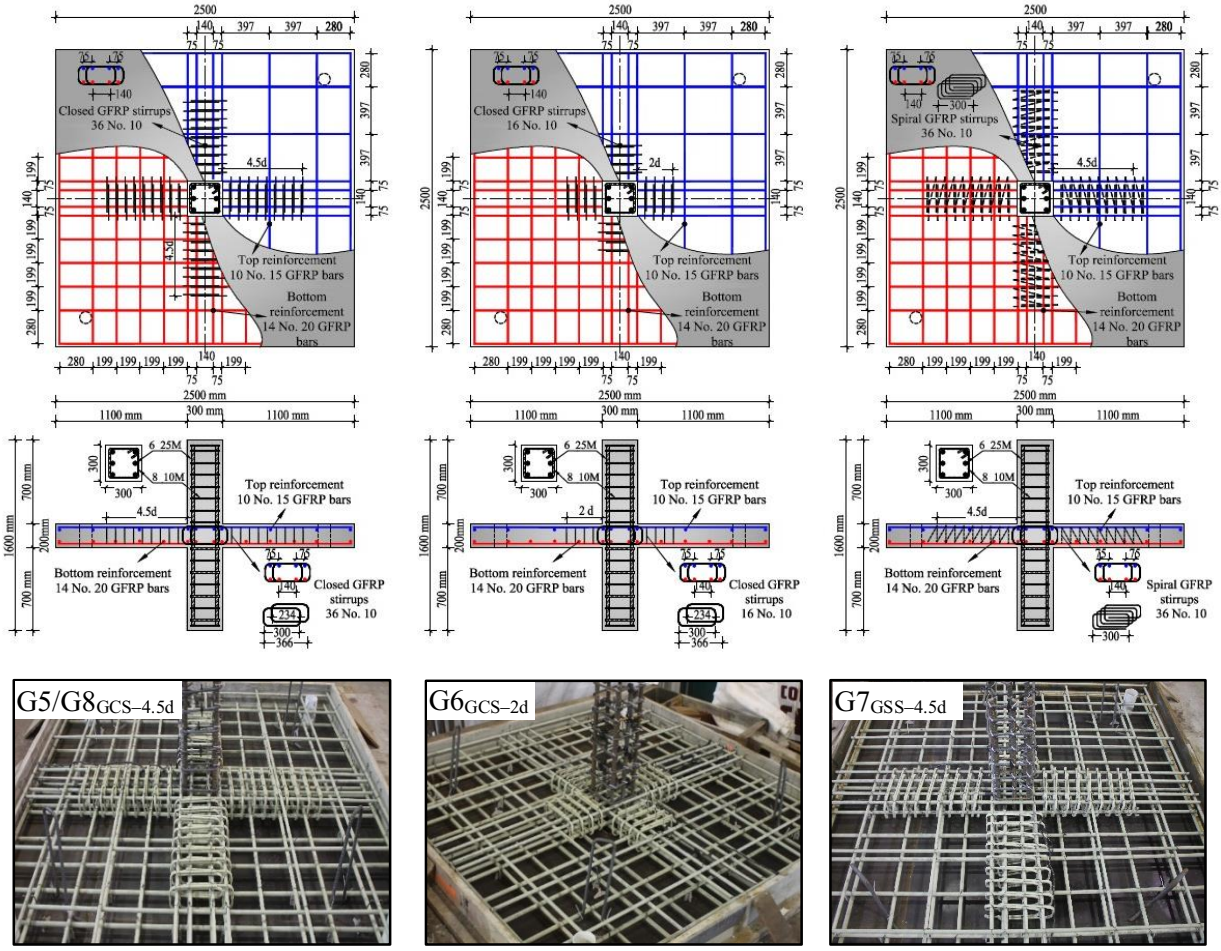

Figure 6.1 Typical geometry and reinforcement details for tested specimens.

Specimens $G5_{GCS–4.5d}$, $G6_{GCS–2d}$, and $G8_{GCS–4.5d–SL}$ were reinforced with four discrete branches of No. 10 GFRP closed stirrups. Specimen $G7_{GSS–4.5d}$ was reinforced with four branches of No. 10 GFRP spiral stirrups. The stirrups were extended 4.5*d* from the column face in all the shear-reinforced specimens. In order to evaluate how the stirrup extension affected the punching behavior, the stirrups specimen $G6_{GCS–2d}$ extended 2*d* from the column face. The shear-reinforcement stirrups were arranged in a cruciform pattern according to ACI 318 (2014) and

CSA A23.3 (2014). The spacing between the consecutive lines was 0.*5d*. The first perimeter was offset 0.*4d* from the column face for all slabs with shear reinforcement, as specified in CSA A23.3 (2014). There were nine peripheral lines of shear reinforcement (SR) in both directions and four lines in specimen $G6_{GCS–2d}$, as shown in **Figure 6.1**.

6.4.2. Test Procedure

At the outset of testing, a concentric load was applied to the top of the upper part of the column in a load-control mode at a loading rate of 20 kN/min. The desired load was approximately 140 kN. This value represents the dead load plus 30% of the live load on a typical flat-plate system prototype. In the case of specimen $G8_{GCS–4.5d\text{-}SL}$, the desired load was increased to 180 kN, representing the combined dead and live loads. The load was maintained on the column throughout testing by continuously adjusting the jack. The oil pressure was applied and regulated throughout the test with a hand pump. The horizontal actuators were then activated to apply the reversed lateral loads to the column ends. The horizontal actuators operated in displacement-control mode. The actuators pushed and pulled the column ends simultaneously at the same rate according to a planned cyclic-loading pattern but in different directions (see **Figure 6.2**). The positive drift in the routine corresponded to the actuator pushing the column, while the negative drift corresponded to the actuator pulling the column. Each increment represents an approximate increase in the lateral interstory-drift ratio of 0.25%. The design of the horizontal loading path was generally consistent with ASTM E2126.3 (2011). Each cycle at a new drift level was performed twice to evaluate the specimen's loss of strength and stiffness during the repeated cycles.

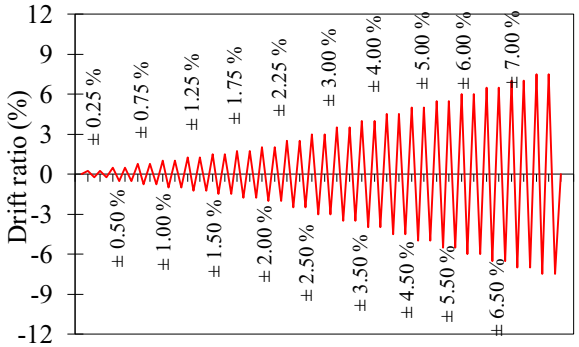

Figure 6.2 Lateral–displacement routine.

6.5. Experimental Results and Observations

6.5.1. Cracking Behavior and Modes of Failure

Figure 6.3 presents the final crack and damage patterns on the slab bottom surface (tension side). During the application of the gravity load, the initial flexural cracks were generated at the column faces and corners, extending toward the slab edges. Applying the reversed lateral cyclic loads extended the initial flexural cracks further, and new flexural cracks formed on the slab's bottom surface. Radial and tangential cracks also formed and propagated. Moreover, a crack around the column perimeter was observed on each side of the slab surfaces. Increasing the lateral-drift ratio caused the cracks to extend and open throughout. New cracks also formed and developed at higher drift levels, and the concrete cover began to spall from the bottom surface. The moment transferred between the column and slab caused diagonal torsional cracks develop adjacent to the side faces of the column in the transverse lateral-load direction.

The specimen without SR experienced a typical abrupt, brittle punching-shear failure without much warning. The punching-shear failure was evidenced by a sudden drop in applied gravity and lateral loads. At this point, an attempt was made to reload the specimen to attain the target gravity load before returning the specimen to zero lateral displacements, followed by test termination. In contrast, the specimens with SR exhibited substantial differences in damage. The mode of failure for all specimens with SR was a softer punching-shear failure with a gradual decrease in the lateral loads and integrity maintenance. It should be pointed out that there were no signs of GFRP-bar rupture or slippage or of bond failure.

In the case of specimen G1, the flexural cracks initially visible arose at the column faces at a gravity-load intensity of 85 kN. At a lateral-drift ratio of 2.00%, the crack pattern generally stabilized. The first crack associated with punching developed during the first cycle at a lateral-drift ratio of 2.25%. By the end of the second repeated cycle, damage related to punching shear had propagated, and the punching cone was fully formed. Further increasing of the lateral-drift ratio widened the existing cracks, and a few new cracks appeared. In addition, the concrete cover began to spall from the bottom surface. In each orthogonal direction, the average distances between the column face and the perimeter of the failure cone varied. The

corresponding average distance along the lateral-load direction and the transverse direction was 4.0*d* and 4.8*d*, respectively, where *d* is the effective depth of the slab.

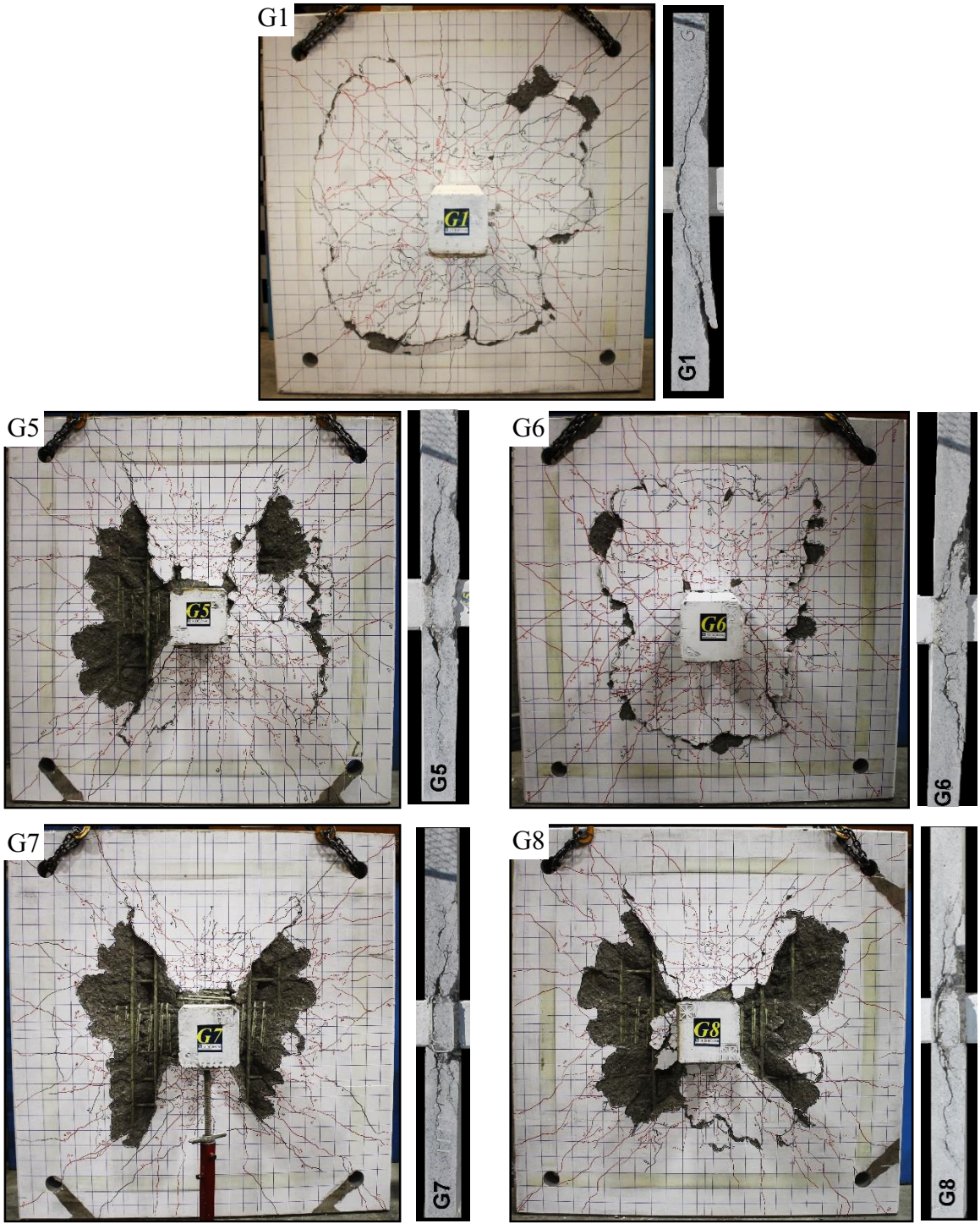

Figure 6.3 Final crack patterns and saw–cut of all tested specimens along the load direction.

In the case of the specimens with SR, using GFRP stirrups had a clear impact. For specimen $G6_{CS–2d}$, which had a relatively short extension of closed-stirrup (CSSR), the flexural cracks initially visible arose at the column faces at a gravity-load intensity of 125 kN. The first crack associated with punching developed at a lateral-drift level of 2.75%, while a complete punching cone was formed during the first cycle at a lateral-drift ratio of 3.50%. The corresponding average distance along the lateral-load direction was 4.3d, compared to 3.3d in the transverse direction.

On the other hand, extending the stirrups to 4.5d from the column face was effective in specimens $G5_{CS–4.5d}$, $G7_{SS–4.5d}$, and $G8_{CS–4.5d–SL}$. The flexural cracks initially visible arose at the column faces at gravity-load intensities of 135, 140, and 180 kN, respectively. The first crack associated with punching developed at a lateral-drift level of 3.50%, while the punching-shear failure crack was formed on at least three sides of the slab tension side at lateral-drift levels of 4.0% and 4.50%. At the higher lateral-drift levels, the concrete cover began to spall from the bottom surface, and the cracks widened. The average distance between the column face and the perimeter of the failure cone was approximately 3.8*d*.

To observe the inclination of the diagonal cracks, all specimens were cut along a line close to the column face in the lateral-load direction (see **Figure 6.3**). The punching failure in specimen G1 was characterized by a single diagonal shear crack that extended from the column face to the slab tension side at an inclination of 23° to 25°. While, the main diagonal shear crack, in all shear-reinforced specimens, was clearly affected by the provision of the stirrups around the column zone. The sawn surface of the shear-reinforced specimens showed several inclined shear cracks within the regions reinforced with shear stirrups as well as horizontal splitting cracks located above the upper ends of the stirrups. Lastly, these inclined and splitting cracks created the failure surfaces. It should be pointed out that no rupture of stirrups was observed, except in specimen $G7_{SS–4.5d}$. The outer bent portion of the spiral stirrup had ruptured along the lateral-load direction at a distance of 0.4*d* and at the higher levels of lateral drift levels.

6.5.2. Moment–Lateral Drift Response

Figure 6.4 provides the unbalanced moment–lateral-drift ratio relationships for all specimens. Table 6.2 summarizes the peak lateral load, maximum unbalanced moment (M_{max}), and

corresponding lateral-drift ratio in each direction (δ_{Mmax}), the ultimate lateral-drift ratio (δ_{max}), and the drift ratio corresponding to 80% of the peak unbalanced moment ($\delta_{0.8Mmax}$). The unbalanced moment (M_{max}) is defined as the moment transferred between the column and the slab generated through reversed lateral quasi-static loading at the column ends. The unbalanced moment was obtained at each load step by multiplying each jack load by the effective height. The effective height is the distance from the application point to the slab center, that is, 675 mm. The lateral-drift ratio was calculated by dividing the lateral drift between the top and bottom of the column by the total effective height.

Table 6.2 Test results

Specimen	Gravity load KN	Peak lateral Load KN		Max. unbalanced moment KN.m		Drift ratio (%)				Max reinforcement strain at $d/2$ (μs)	Max concrete strain (μs)
	V_u	H_+	H_-	M_+	M_-	δ_+	δ_-	δ_{ult}	$\delta_{0.8Mmax}$	ε_{max}	$\varepsilon_{c\,max}$
G1$_{(1.06)}$	140	136.6	136.7	179.8	180.9	2.25	–2.25	2.25	——	5239	–1040
G5 $_{GCS–4.5d}$		154.4	152.1	202.1	206.4	2.25	–2.25	6.50	5.00	5576	–2311
G6 $_{GCS–2d}$		150.9	139.8	198.6	184.0	2.25	–2.25	4.50	3.00	4787	–1477
G7 $_{GSS–4.5d}$		166.5	163.0	219.7	217.5	2.50	–2.50	7.50	5.00	6436	–1452
G8 $_{GCS–4.5d–SL}$	180	155.7	146.5	200.4	189.9	2.25	–2.25	6.50	5.00	7905	–1860

Note: d = is the effective depth of the slab; *(+)* refer to a positive direction and *(–)* to the negative direction.

As shown in **Fig. 6.4**, specimen G1 displayed good ability to withstand inter-story drift up to the level of 1.5% minimum drift capacity without punching failure. The δ_{Mmax} for specimen G1 was 2.25%, while the M_{max} was 180.9 kN.m. A gradual decrease in load occurred during the second repeated cycle at 2.25%. The punching-shear failure then occurred suddenly and was accompanied by a sudden drop in gravity and lateral loads. The peak lateral loads in the first lateral cycle load were always smaller than those in the second repeated cycle load. This is attributed to the effect of cyclic loading on crack propagation and damaging the concrete on the positive path in the first cycle.

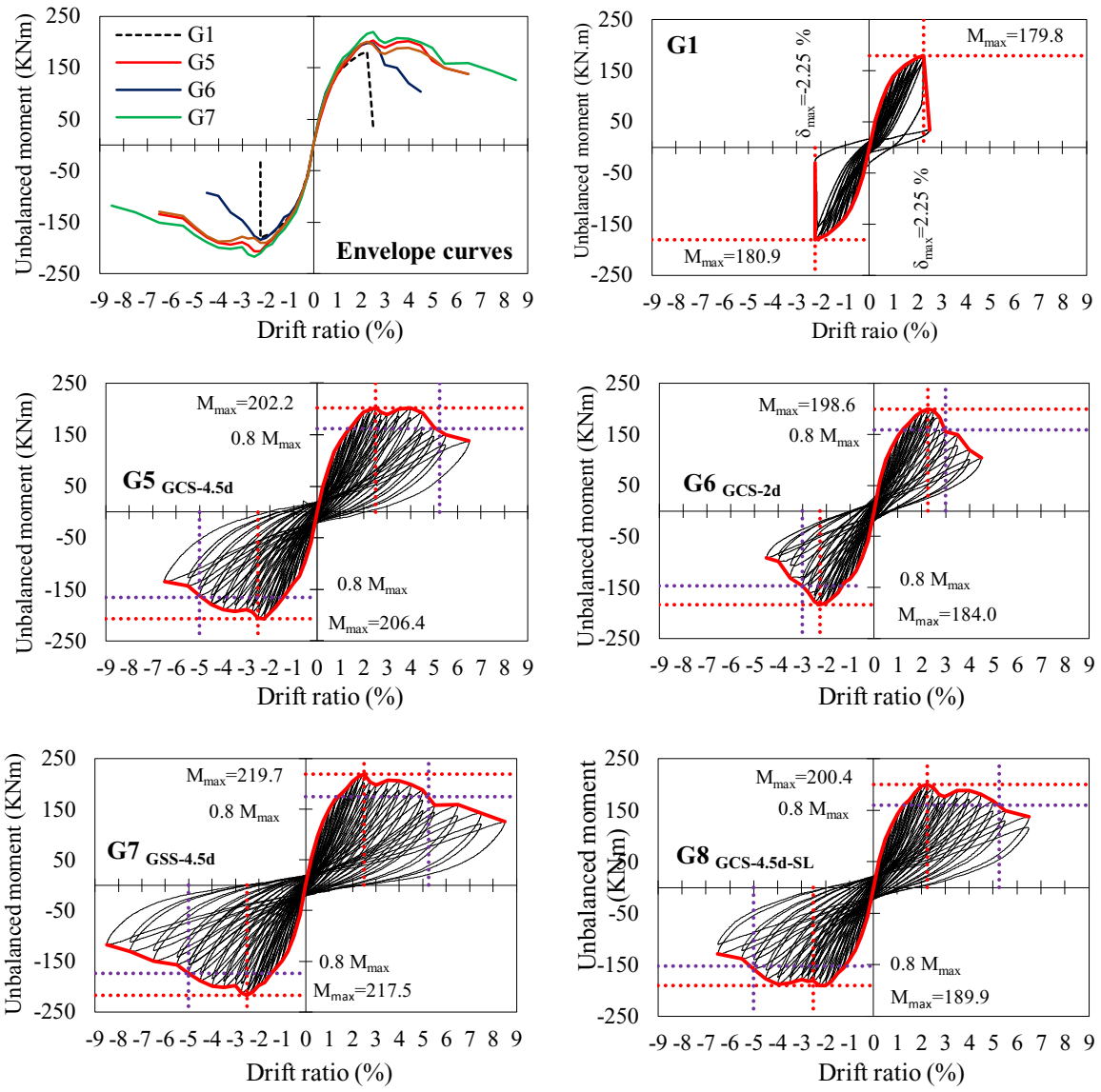

Figure 6.4 Unbalanced moment–lateral drift ratio relationship of test specimens.

For all shear-reinforced specimens, the GFRP-SR effectively contributed to the unbalanced moment-carrying and lateral-deformation capacities. The unbalanced moment–lateral drift ratio relationships for all specimens with SR were approximately similar. The performance of specimen $G5_{CS–4.5d}$ was obviously influenced by CSSR around the column area. The M_{max} was 206.4 kN.m, while the δ_{Mmax} was 2.25%. The unbalanced moment-carrying capacity decreased slightly with increasing lateral-drift ratio. Specimen $G5_{CS–4.5d}$ was able to sustain lateral drifts as high as 5% with no more than a 20% decrease in its M_{max}. A gradual decrease in the moment-transfer capacity was observed up to a lateral-drift ratio of 6.5%. The lateral-drift ratio and

unbalanced-moment capacity of G5 were, respectively, 2.22 and 1.14 times that of specimen G1.

The performance of specimen $G6_{CS-2d}$ was influenced by the relatively short extension of the CSSR. In comparison to the specimen without SR, it had a higher M_{max} of 198.6 kN.m with δ_{Mmax} of 2.25%. A gradual decrease in the unbalanced moment-carrying capacity was evidenced at higher drift-ratio levels. Moreover, specimen $G6_{CS-2d}$ was able to sustain lateral drifts as high as 3% with no more than a 20% decrease in the M_{max}.

Using spiral-stirrup shear reinforcement (SSSR) in specimen G7SS–4.5d clearly affected the slab's performance. Specimen $G7_{SS-4.5d}$ achieved M_{max} of 219.7 kN.m at δ_{Mmax} of 2.5%. Furthermore, with no more than a 20% decrease in the maximum unbalanced moment-carrying capacity, the specimen was able to sustain lateral drifts as high as 5.5%. The decreases in moment-transfer capacity were also gradual up to a lateral-drift ratio of 7.5%. Increasing the gravity-load intensity of specimen $G8_{CS-4.5d-SL}$ to 180 kN slightly affected the unbalanced moment-carrying capacity and lateral-deformation capacity. Specimen $G8_{CS-4.5d-SL}$ achieved M_{max} of 200.4 kN.m at δ_{Mmax} of 2.25%. Slightly decreased unbalanced moment-carrying capacity also appeared with increasing lateral-drift ratio. Moreover, the specimen was able to sustain lateral drifts as high as 5% with no more than a 20% decrease in the maximum unbalanced moment-carrying capacity.

6.5.3. Flexural Reinforcement and Concrete Strains

Figure 6.6 illustrates the reinforcement strain versus the lateral-drift ratio relationships in each orthogonal direction at a distance of *d*/2 (75 mm) from the column face. **Figure 6.7** illustrates also the strain profiles of all specimens at each lateral-drift ratio along the lateral-loading direction. The concrete strains were also measured at the column faces during testing. For all specimens in which the stirrups extended up to 4.5*d* away from the column face, the reinforcement strains decreased as the distance from the column edges increased up to a lateral-drift ratio of 3.00%. Nevertheless, a moderate increase in the flexural-reinforcement strain was observed at 450 and 750 mm from the column edges at higher drift levels. Very low reinforcement-strain values were recorded 750 mm from the column edges for specimen $G6_{CS-2d,}$ which had a relatively short extension of the stirrups. None of specimens, however,

experienced bar rupturing, slippage, or bond failure during testing. This implies that the GFRP bars adequately transferred loads.

It should be pointed out that the maximum flexural-reinforcement strain (εmax) in all specimens with SR was less than the characteristic tensile strength. Along the lateral-loading direction, the εmax were 6078, 4787, 6436, and 7968 μs for specimens $G5_{CS–4.5d}$, $G6_{CS–2d}$, $G7_{SS–4.5d}$, and $G8_{CS–4.5d–SL}$, respectively, representing 35%, 27%, 37%, and 45% of the guaranteed tensile strength. Along the transverse direction, the ε_{max} were 4681, 2356, 5892, and 7672 μs, respectively, representing 0.77, 0.49, 0.91, and 0.96 times those recorded along the lateral-loading direction, respectively. The maximum concrete strain at the column face in all specimens was lower than the theoretical crushing strain and equal to -2311, -1477, -1452, and -1860 μs, respectively. When the punching-shear failure occurred, however, there were no signs of concrete crushing on the slab compression side.

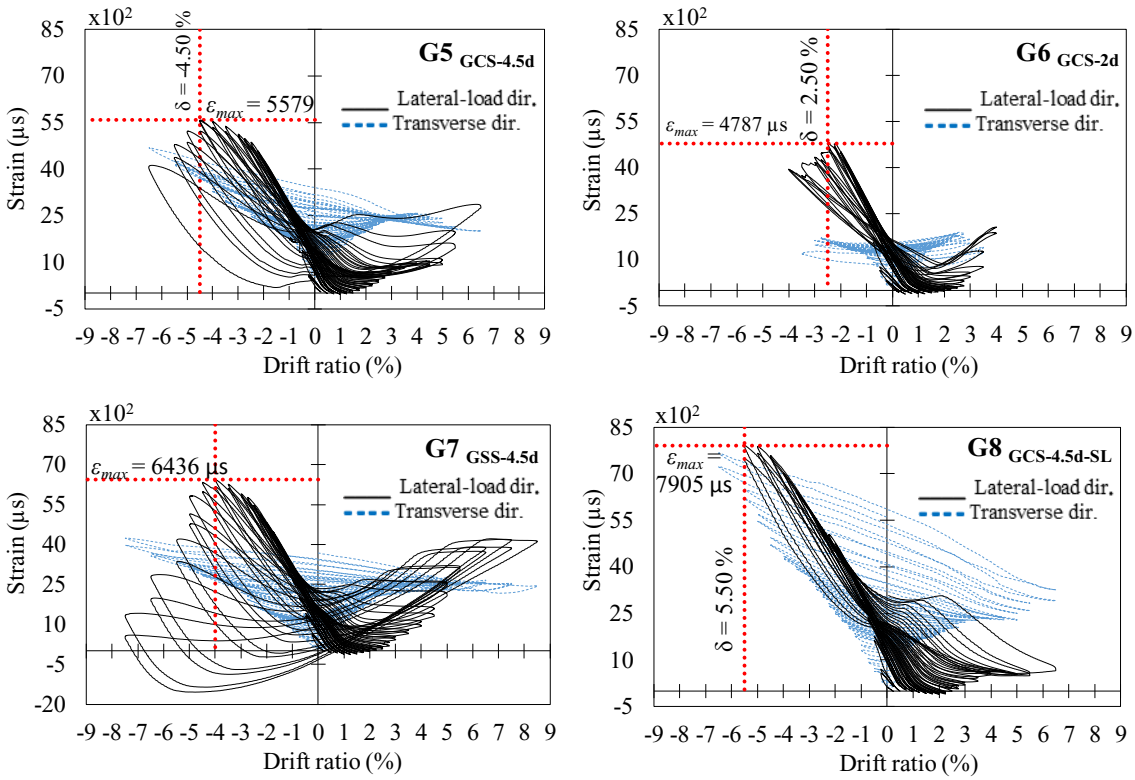

Figure 6.5 Reinforcement strain versus lateral–drift ratio at (d/2).

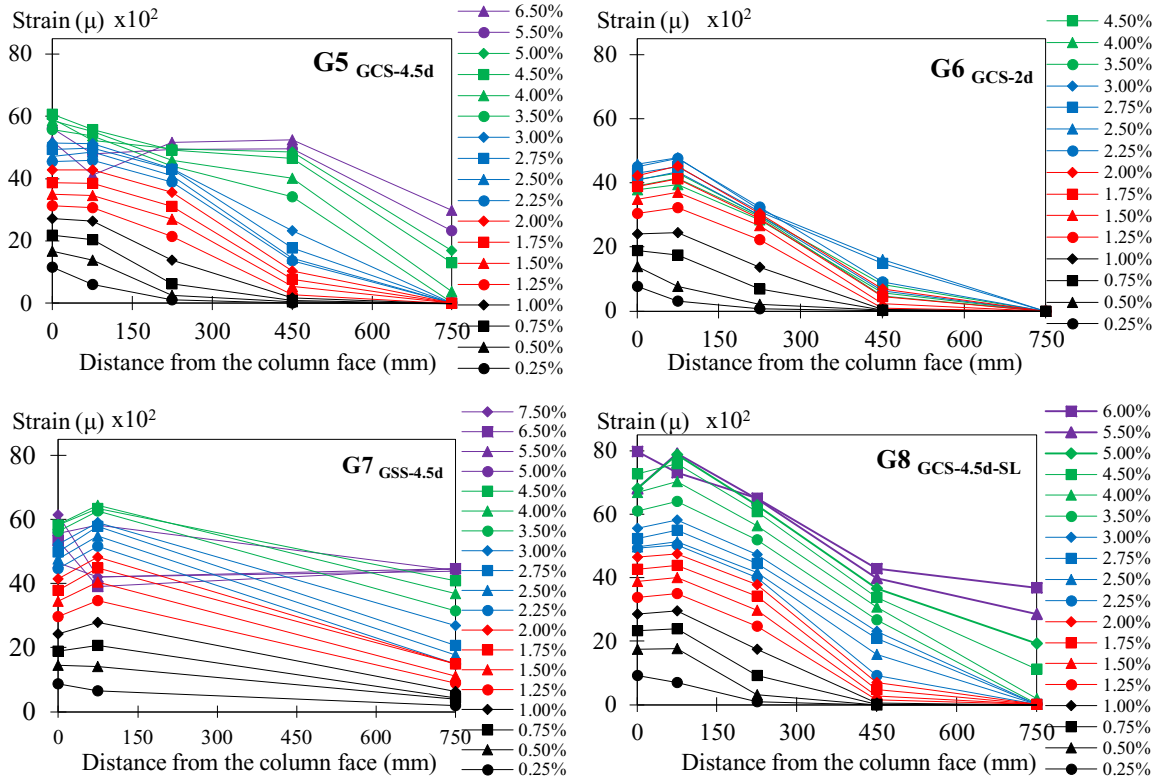

Figure 6.6 Strain profile along the lateral–load direction.

6.5.4. Connection Stiffness

One of the major considerations in seismic design for slab–column connections is lateral stiffness. The peak-to-peak stiffness is defined as the slope of the line connecting the maximum achieved unbalanced moments in a given cycle (see **Fig. 6.7**) (Robertson et al. 1992; Megally 1998; and Emam et al. 1997). Table 6.3 compares the initial connection stiffness (S_i), at 1.5% and at the ultimate lateral-drift ratio (S_u). The initial connection stiffness is defined as the slope of the line connecting the maximum unbalanced moments of the first cycle at a lateral-drift ratio of 0.25%. **Figure 6.8** plots the average peak-to-peak stiffness versus lateral-drift ratio. As seen in **Fig. 6.8**, the connection's reduction in stiffness occurred during successive cycles of increasing lateral displacement. All specimens had nearly the same initial connection stiffness, the initial connection stiffness for specimen $G7_{SS-4.5d}$ was approximately 6% higher than that of all CSSR specimens.

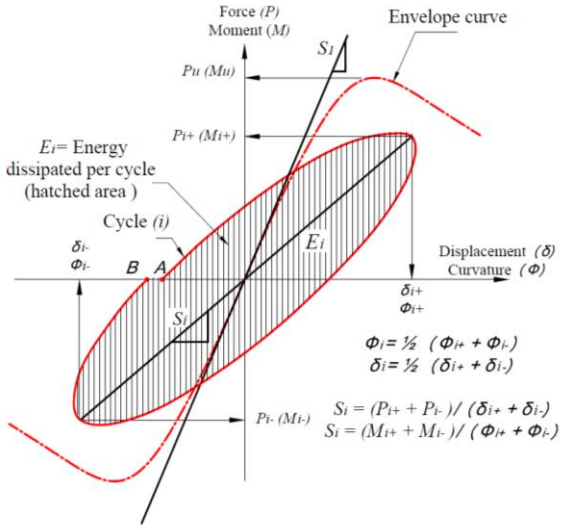

Figure 6.7 Normalization of stiffness and energy–dissipation capacity calculation.

All specimens with SR could clearly undergo far more deformation without abruptly losing stiffness. This is attributed to controlling the crack development and associated damage in the slab–column connection with stirrups. At early lateral drifts (0.25% to 2.50%), a reduction in connection stiffness of about 4% was observed during the second repeated cycle. The connection stiffness at a drift ratio of 2.50% was 37%, 34%, 37%, and 34% of the initial stiffness for specimens $G5_{CS–4.5d}$, $G6_{CS–2d}$, $G7_{SS–4.5d}$, and $G8_{CS–4.5d\text{-}SL}$, respectively. At higher drift levels, the reduction in connection stiffness increased to 11% during the second repeated cycle. Moreover, the connection stiffness at the ultimate drift ratio was 14%, 22%, 12%, and 14% of the initial stiffness, respectively.

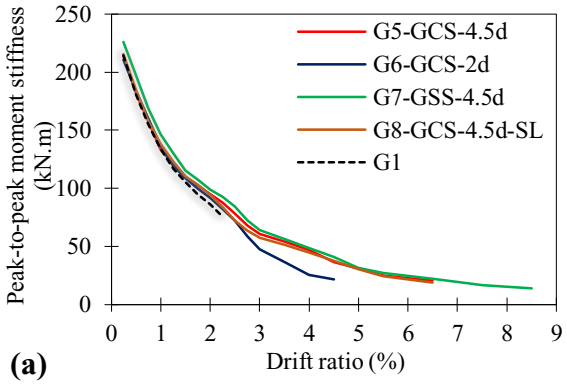

Figure 6.8 Peak–to–peak stiffness for test specimens.

All of the GFRP-CSSR specimens had comparable degradation of the connection stiffness up to a lateral-drift ratio of 2.50%. Specimens $G5_{GCS–4.5d}$ and $G8_{GCS–4.5d–SL}$, however, exhibited higher connection stiffness with increasing lateral-drift ratio compared to specimen $G6_{GCS–2d}$. This is attributed to the 4.5*d* extension of the GFRP stirrups from the column face. On the other hand, using GFRP-SSSR in specimen $G7_{GSS–4.5d}$ had little impact on the degradation of connection stiffness. At the same lateral-drift levels, specimen $G7_{GSS–4.5d}$ exhibited slightly stiffer behavior than the other specimens. On the other hand, specimen $G8_{GCS–4.5d–SL}$, which was subjected to a higher gravity load, exhibited insignificant impact on the connection stiffness compared to its counterpart $G5_{GCS–4.5d}$. This observation coincides with the experimental findings reported by Megally (1998).

Table 6.3 Connection stiffness

Specimen	M_{max} KN.m	Initial stiffness S_i KN.mm		Stiffness at 1.50% S KN.mm		Stiffness at ultimate drift S_u KN.mm	
		1st cycle	2nd cycle	1st cycle	2nd cycle	1st cycle	2nd cycle
G1(1.06)	180.9	214.5	213.7	107.7	102.8	80.2	71.5
G5 GCS–4.5d	206.4	214.2	213.4	112.1	107.3	32.6	29.2
G6 GCS–2d	198.6	213.3	208.1	111.0	106.9	28.6	26.0
G7 GSS–4.5d	219.7	226.7	225.3	118.5	112.6	39.9	33.7
G8 GCS–4.5d–SL	200.4	216.4	214.9	112.7	108.4	32.6	28.8

6.5.5. Energy Dissipation

Energy dissipation (E_D) is a significant indicator of RC elements being able to absorb energy before failure, making it one of the most important criteria used to assess the seismic performance of RC elements. Higher energy-dissipation capacity points to better post-peak behavior and ductile failure. The energy-dissipation capacity was normalized by calculating the area within the corresponding moment–drift-ratio hysteresis loop at each drift cycle (see **Fig. 6.7**). The average energy dissipated versus the lateral-drift ratio plots in Fig. **6.9**. Table 5 provides also the dissipated-energy at maximum lateral drift ratio. The results indicate that all specimens with SR had energy-dissipation behavior comparable to specimen G1 at early lateral drifts. On the other hand, the effect of repeated load cycles was evident. At lateral-drift levels of 0.25% to 2.50%, the average reduction in dissipated energy was about 32%, decreasing to 12% at higher lateral-drift levels.

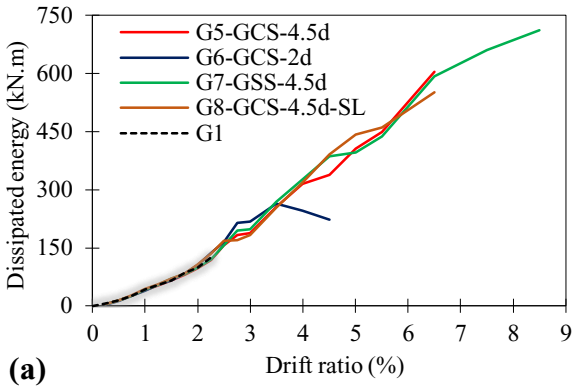

Figure 6.9 Dissipated energy versus drift ratio.

Provision stirrups around the column zone effectively contributed to the energy-dissipation capacity. Specimens with SR were able to dissipate energy at high lateral-drift levels. This observation coincides with the experimental findings reported by Megally (1998) and Kang et al. (2017). Specimen $G6_{CS–2d}$, with a relatively short stirrup extension, exhibited a clear increase in dissipated energy at lateral-drift levels of 2.50% to 3.5%. This state can be considered as the initiation of punching failure and high punching-shear stress. A sudden decrease in the dissipated energy occurred at increased lateral-drift ratios. Specimen $G7_{SS–4.5d}$ dissipated relatively more energy than specimen $G5_{CS–4.5d}$. Specimen $G8_{CS–4.5d–SL}$ with a high gravity-load intensity, exhibited a slight decay in slab-connection strength, resulting in slightly lower energy dissipation, particularly at high lateral-drift levels, compared to its counterpart $G5_{CS–4.5d}$.

Table 6.4 Ductility index and dissipated energy

Specimen	M_{max} KN.m	$\delta_{0.8u}$ (%)	Method (I)		Method (II)		Dissipated energy E_D KN.mm	
			δ_e (%)	μ_δ	δ_e (%)	μ_δ	1st cycle	2nd cycle
G1(1.06)	180.9	2.05	1.30	1.57	1.24	1.65	125.7	349.8
G5 GCS–4.5d	206.4	5.00	1.57	3.20	1.64	3.05	419.8	393.0
G6 GCS–2d	198.6	3.00	1.32	2.27	1.45	2.06	277.7	251.0
G7 GSS–4.5d	219.7	5.00	1.59	3.28	1.58	3.28	451.6	422.3
G8 GCS–4.5d–SL	200.4	5.00	1.50	3.46	1.52	3.42	462.3	422.8

Note: $\delta_{0.8u}$ = slab lateral drift ratio at 20% loss of ultimate lateral strength; δ_e = virtual slab lateral drift ratio; μ_δ= lateral drift –based ductility factor.

6.5.6. Ductility Index

Ductility is a very important design consideration for flat-plate structures in seismic zones. In such areas, slab–column connections are expected to undergo inelastic deformations, making it necessary to design connections with adequate strength and ductility. In addition, such connections must be able to undergo a specific limit of interstory drift without punching-shear failure. Ductility can be defined as an element's ability to sustain inelastic deformations prior to collapse without substantial loss of strength. The ductility factor is the ratio of the ultimate lateral displacement (deflection or drift) of the element to its corresponding displacement at an equivalent yielding of the steel reinforcement. This definition cannot be directly applied to FRPs or FRP-reinforced concrete members given the fact that FRP bars do not yield. Accordingly, the transition point between the elastic and inelastic regions in GFRP-reinforced concrete members is defined herein as the virtual deflection Δ_e or drift point δ_e. ACI 440.1R (2015) and CSA S806 (2012) design codes offer no unified method for assessing the ductility index of FRP-reinforced concrete members. When calculating ductility capacity, the definition of yield displacement often causes difficulty because the force-displacement response of RC components may not have a well-defined yield point. This may occur due to the nonlinear behavior of the materials (steel reinforcement and concrete) or due to yielding in different parts of an RC structure or subassembly initiating at different load levels. Consequently, the general practice has been to define the ductility parameters of RC components based on an idealized bilinear force-displacement response [Park R. (1989)].

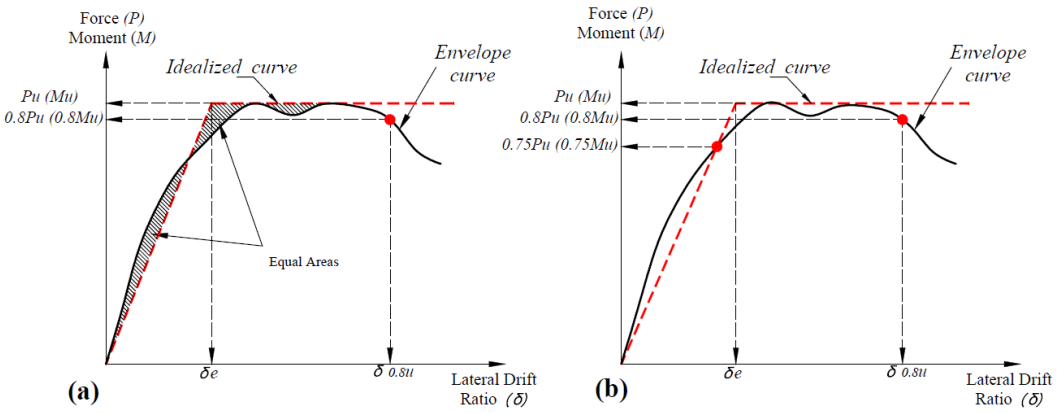

Figure 6.10 Ideal curve definition.

Various alternative definitions have been proposed for estimating yield displacement. **Figure 6.10** illustrates the procedure proposed by Park (1989) and adopted herein. Two methods were used to estimate the ductility index. In Method A, the virtual limit was evaluated based on the equivalent elastic-plastic energy absorption, where the secant line was chosen so as to have identical hatched areas and ensure equal energy criteria (see **Figure 6.10** (a)). The relative displacement or drift ratio corresponding to the intersection point of the secant line from the origin to the tangent line of the maximum unbalanced moment is defined as a virtual deflection (Δ_e) or lateral-drift ratio point (δ_e). In Method B, the virtual limit was evaluated based on the reduced stiffness equivalent elastic-plastic system. The reduced stiffness in this method is computed by taking the secant line from the origin to the 75% of the maximum unbalanced moment (M_{max}) (see **Figure 6.10** (b)). The plastic portion of the idealized relation passes through the maximum unbalanced moment. The intersection of these two lines represents the virtual deflection (Δ_e) or lateral-drift ratio point (δ_e). Table 6.4 provides the lateral-drift ratio at 20% loss of ultimate lateral strength ($\delta_{0.8u}$); the virtual lateral-drift ratio (δ_e), and the lateral-drift ductility index (μ_δ). The ultimate deflection or lateral-drift ratio is accepted as a 20% loss of ultimate lateral strength [NBCC (2015)]. The drift-ductility index (μ_δ) is determined with Eqns. 6.1 & 6.2.

$$(\mu_\delta = \frac{\delta_{0.8u}}{\delta_y}) \text{ or } (\mu_\delta = \frac{\Delta_{0.8u}}{\Delta_y}) \qquad \text{(steel)} \quad (6.1)$$

$$(\mu_\delta = \frac{\delta_{0.8u}}{\delta_e}) \text{ or } (\mu_\delta = \frac{\Delta_{0.8u}}{\Delta_e}) \qquad \text{(FRP)} \quad (6.2)$$

All the GFRP-reinforced specimens had adequate predicted ductility indexes consistent with the minimum required ductility factor of 1.2 for steel slab–column connections in a seismic zone [Moehle (1989) and Megally (1998)]. The specimen without shear reinforcement had adequate drift-ductility indices ranging from 1.57 to 1.65. Specimens $G5_{GCS–4.5d}$, $G7_{GSS–4.5d}$, and $G8_{GCS–4.5d–SL}$ displayed higher drift-ductility indices ranging from 3.2 to 3.46 for Method A and 3.05 to 3.42 for Method B. It is worth mentioning that, as with steel specimens, the ductility factor for the shear-reinforced specimens always exceeded 3 [Pillai et al. (1982) and Megally (1998)]. On the other hand, specimen $G6_{GCS–2d}$, with a relatively short GFRP-CSSR extension, yielded a higher ductility index compared to the specimen without shear reinforcement.

According to Methods A and B, the drift-ductility index for $G6_{GCS–2d}$ was 2.27 and 2.06, which is 45% and 25% higher than in specimen G1.

Along the lateral-loading direction, all the specimens reinforced with closed-stirrup shear reinforcement showed similar trends and comparable widths of the diagonal shear crack up to a lateral-drift ratio of 2.75%. An abrupt increase was observed in specimen $G6_{GCS–2d}$ at higher lateral-drift ratios. This is attributed to large slab deformations and rotations, confirming that punching-shear failure occurred. Specimen $G7_{GSS–4.5d}$ (reinforced with spiral-stirrup shear reinforcement) had the narrowest cracks of all the specimens. This can be attributed to the more effective mechanical anchorage of the spiral stirrups, which offered sufficient resistance and confinement to control the development of large shear cracks. In all the specimens reinforced with closed stirrups, the crack openings along the transverse direction were smaller than along the lateral-loading direction. A moderate increase in the crack openings along the transverse direction was observed in specimen $G7_{GSS–4.5d}$ compared to along the lateral-loading direction.

6.5.7. Comparison of Experimental Results and Available FRP Design Provisions

The North American standards and design provisions [ACI 440.1R (2015) and CSA S806 (2012)] were assessed by comparing their predictions with the experimental results. Table 6.5 provides the punching-shear predictions, maximum unbalanced moments (M_{ACI} and M_{CSA}), and the ratio of the ultimate punching-shear capacity and applied gravity load (V_u/V_c). The available punching-shear equations provided by FRP design codes and guides—ACI 440.1R (2015) and CSA S806 (2012)—are similar to equations for steel-RC slabs—ACI 318 (2014) and CSA A23.3 (2014)—with modifications to account for the effect of FRP-bar axial stiffness.

In ACI 440.1R (2015), the punching-shear capacity provided by V_c for FRP-reinforced slabs is simply a modified punching-shear equation for steel-reinforced slabs. The V_c is modified by the factor 5/2 k to account for FRP axial stiffness in FRP-reinforced concrete elements through the term kd, as shown in Eq. (6.3). CSA S806 (2012) accounts for the effect of both the reinforcement ratio and elastic modulus of the FRP bars to the one-third power and also considers the cubic root of the concrete compressive strength as the punching-shear resistance. The punching-shear strength provided in CSA S806 (2012), in absence of shear reinforcement, is calculated as the smallest of Eqns. (6.4) to (6.6). The critical perimeter nearest a column equal

to 0.5 times the effective depth; (λ) is the concrete density factor; (ϕ_c) is the concrete resistance factor; (β_c) is the ratio of the long side to the short side of the column (α_s=4); and (f_c') shall not exceed 60 MPa.

ACI 440.1R (2015) – without shear reinforcement:

$$v_c = \frac{4}{5} k \sqrt{f_c'} \qquad (6.3)$$

$$k = \sqrt{2\rho n + (\rho n)^2} - \rho n \qquad (6.3.1)$$

$$n = E_f / E_c \qquad (6.3.2)$$

CSA S806 (2012) – without shear reinforcement:

$$v_c = 0.056\ \lambda\ \phi_c \left(E_f\ \rho_f\ f_c'\right)^{1/3} \qquad (6.4)$$

$$v_c = 0.147\ \lambda\ \phi_c \left(0.19 + \frac{\alpha_c d}{\beta_c}\right)\left(E_f\ \rho_f\ f_c'\right)^{1/3} \qquad (6.5)$$

$$v_c = 0.028\ \lambda\ \phi_c \left(1 + \frac{2}{\beta_c}\right)\left(E_f\ \rho_f\ f_c'\right)^{1/3} \qquad (6.6)$$

On the other hand, ACI 440.1R (2015) and CSA S806 (2012) do not yet provide provisions for the design of FRP-RC slab–column connections with shear reinforcement. Equations (6.7) to (6.8) for steel-RC slab–column connections were used to calculate the predicted capacities of the connections. It should be mentioned that yielding strength (f_y) has been replaced with a specific stress (f_{fv}) at a limiting strain value of 4000 in ACI 440.1R (2015) and 5000 μs in CSA S806 (2012). Furthermore, the concrete contribution inside and outside the region reinforced with shear stirrups was calculated as 0.50% of the punching-shear strength of the slabs without shear reinforcement. This is consistent with ACI 318 (2014) and CSA A23.3 (2014) code provisions for steel-reinforced members. The spacing between the consecutive lines was 0.5*d*. The first perimeter was offset S_o = 0.4*d* from the column face for all the slabs with shear reinforcement. The critical section outside the shear-reinforced zone was located at a distance S_o from the outermost peripheral line of stirrups.

ACI 440.1R (2015) – with shear reinforcement:

$$v_r = v_c + v_s \quad (6.7)$$

$$v_c = \frac{2}{5} k \sqrt{f_c'} \quad (6.7.1)$$

$$v_{sf} = \frac{A_f \ \phi_f \ f_{fv}}{b_o \ S_{fv}} \quad (6.7.2)$$

$$f_{fv} = 0.004 \ E_{fv} \quad (6.7.3.1)$$

$$f_{fv} = \frac{(0.05 r_b / d_b + 0.3) f_{fv}}{1.5} \leq f_{fbend} \quad (6.7.3.2)$$

CSA S806 (2012) – with shear reinforcement:

$$v_r = v_c + v_s \quad (6.8)$$

$$v_{c inside} = v_{c outside} = 0.028 \ \lambda \ \phi_c \left(E_f \ \rho_f \ f_c' \right)^{1/3} \quad (6.8.1)$$

$$v_{sf} = \frac{A_f \ \phi_f \ f_{fv}}{b_o \ S_{fv}} \quad (6.8.2)$$

$$f_{fv} = 0.005 \ E_{fv} \quad (6.8.2.1)$$

$$f_{fv} = \frac{(0.05 r_b / d_b + 0.3) f_{fv}}{1.5} \leq f_{fbend} \quad (6.8.2.2)$$

The predicated ultimate unbalanced moment capacity (M_{ACI}/M_{CSA}) was calculated using the eccentric shear–stress model with a fraction (Υ_v), and resisted by the shear at the perimeter of 0.5d from the column face or S_o = 0.4d from the outermost peripheral line of shear reinforcement when failure is inside or outside the shear–reinforced zone, respectively, using Eqns. (6.9).

$$M_n = \frac{J_x}{\Upsilon_v e} \left[v_{max} - \frac{V_n}{b_o d_v} \right] \quad (6.9)$$

$$J_x = \frac{d \ (c_1 + d)^3}{6} + \frac{d^3 \ (c_1 + d)}{6} + \frac{d^3 \ (c_2 + d) \ (c_2 + d)^2}{2} \quad (6.9.1)$$

$$\Upsilon_v = 1 - \frac{1}{1 + \frac{2}{3}\sqrt{\frac{b_1}{b_2}}} \qquad (6.9.2)$$

The ACI 440.1R (2015) gave conservative predictions for the ultimate capacity on an average $M_{Exp.}/M_{The}$ of 1.40 ± 0.07 (a corresponding COV of 5.9%) inside the shear reinforcement zone for slabs (G5, G6, G7 and G8). On the other hand, the CSA S806 (2012) predictions showed reasonable predictions with an average $M_{Exp.}/M_{The}$ value of 1.10 ± 0.05 (a corresponding COV of 2.8%). The CSA S806 (2012) yielded reasonable predictions than the ACI 440.1 with respect to the experimental test results for slabs with shear reinforcement. More experimental results, however, are needed to establish design provisions for FRP–RC two–way slabs with different shapes and types of FRP shear reinforcement.

Table 6.5 Codes predictions

Specimen	Gravity Load kN	V_u/V_c		Max. Unbalanced Moment kN.m		Max. Unbalanced Moment kN.m				$M_{Exp.}/M_{The.}$			
						ACI		CSA		ACI		CSA	
	Vu	ACI	CSA	M_+	M_-	Inner	Outer	Inner	Outer	Inner	Outer	Inner	Outer
G1(1.06)		0.48	0.28	179.8	180.9	58.2	—	139.1	—	3.10	—	1.30	—
G5 GCS–4.5d	140	0.26	0.22	202.1	206.4	150.6	355.3	188.7	734.6	1.37	0.58	1.09	0.28
G6 GCS–2d		0.26	0.22	198.6	184.0	150.6	254.4	188.7	663.5	1.32	0.78	1.05	0.30
G7 GSS–4.5d		0.26	0.22	219.7	217.5	152.5	374.2	192.6	773.7	1.44	0.58	1.14	0.28
G8 GCS–4.5d–SL	180	0.33	0.28	200.4	189.9	137.1	322.4	177.2	721.9	1.46	0.62	1.13	0.28

6.6. Discussion

6.6.1. Influence of GFRP Stirrups Shear Reinforcement

The effectiveness of the presence of the stirrups in the vicinity of the slab–column connections was obvious in the seismic response. The specimens with 2*d* and 4.5*d* stirrup extensions exhibited a softer punching-shear failure with a gradual decrease in lateral loads. Moreover, lateral-drift ratios of 3.0 to 5.0% were achieved with no more than a 20% decrease in the maximum unbalanced moment-carrying capacity. A gradual decrease in lateral load was evidenced during higher drift-ratio levels and was also able to sustain the gravity load until the

end of testing. The lateral-drift capacities of specimens $G5_{CS–4.5d}$ and $G6_{CS–2d}$ were 122% and 33% higher, respectively. Further, the unbalanced moment-carrying capacities were also increased by 14 and 10%, respectively. The use of CSSR effectively contributed to controlling crack development and the associated damage in the slab–column connection. Consequently, at higher drift levels, the specimen experienced higher connection stiffness and did not degrade as rapidly as the specimen without SR. The specimens with SR exhibited the ability to dissipate energy at high levels of lateral drift. A significant increase in the drift ductility indices was also observed in all specimens with SR.

6.6.2. Influence of GFRP Stirrups Extension

The seismic responses were strongly influenced by the characteristics of the shear reinforcing system. Improvements of 66% and 4% were observed in the lateral deformation and unbalanced moment-carrying capacities, respectively, in specimen $G5_{CS–4.5d}$ by extending the stirrups 4.5d from the column face. Specimen $G5_{CS–4.5d}$ displayed a less gradual decrease in the unbalanced moment-carrying capacity at higher levels of drift ratio. Up to a lateral-drift ratio of 2.0%, extending the CSSR 4.5d from the column face had an insignificant effect on connection stiffness, while clear decreases in the connection stiffness were observed at higher drift levels up to failure. This is attributed to an inability to control crack development and the associated damage in the slab–column connection with an extension greater than 2d. Furthermore, up to a lateral-drift level of 2.50%, the stirrup extension had no effect on dissipated energy, while at higher levels of lateral drift, specimen $G5_{CS–4.5d}$ exhibited the ability to dissipate energy without a sudden decrease. The specimen with a relatively short stirrup extension, had drift-ductility indices of 29% and 32% lower than for specimen $G5_{CS–4.5d}$.

6.6.3. Influence of GFRP Stirrups Type

Regardless of the stirrups type (closed or spiral), the results showed comparable seismic performance for specimens $G5_{CS–4.5d}$ and $G7_{SS–4.5d}$. Nevertheless, the spiral stirrups contributed an additional confining effect that reduced the concrete softening effect and limited slab cracking and extension. Subsequently, the lateral drift and unbalanced moment-carrying capacities increased by 10% and 6%, respectively. The SSSR specimen was also able to sustain lateral drifts up to a lateral-drift ratio of 7.5%. Since spiral stirrups had sufficient resistance and

confinement to control the development of large shear cracks, specimen $G7_{SS–4.5d}$ exhibited higher initial connection stiffness. Moreover, it had slightly stiffer behavior at higher levels of lateral drift. The specimen with SSSR also dissipated relatively more energy than the specimens with CSSR. Significant increases (109% and 99%) in the drift-ductility index were observed by comparing with the specimen without shear reinforcement.

6.6.4. Influence of Gravity Load Intensity

Unlike the specimen without SR, increasing the slab gravity-load intensity had an insignificant effect on the unbalanced moment-carrying and lateral-deformation capacities. Moreover, the specimen was able to sustain lateral drifts as high as 5% with no more than a 20% decrease in the maximum unbalanced moment-carrying capacity. Specimen $G8_{CS–4.5d–SL}$, however, showed a marginal decrease in the unbalanced moment-carrying capacity at higher levels of drift ratio. Specimen $G8_{CS–4.5d–SL}$ had no impact on the overall stiffness of the connection or energy dissipation compared to specimen $G5_{CS–4.5d}$. This is attributed to the relatively low values of vu/vc for specimen $G8_{CS–4.5d–SL}$. A slight increase was, however, observed in the drift-ductility index compared to specimen $G5_{CS–4.5d}$.

6.7. Conclusions

In this study, the seismic performance of the GFRP reinforced concrete slab-column connections with or without GFRP stirrups shear reinforcement was assessed by testing five full–scale specimens under combined gravity and lateral reversed cyclic loads. The main findings of this study are summarized as follows:

1. All specimens with shear reinforcement demonstrated increase in strength and lateral-deformation capacity against punching shear failure during and after reversed lateral cyclic loading conditions. The tested specimens with GFRP-SR achieved a high lateral drift of 4.0% to 7.50% with the ability to sustain the gravity load. Moreover, flexible punching-shear failure with a gradual decrease in lateral loads while maintaining integrity was observed.
2. The GFRP stirrups offered sufficient resistance and confinement to control the development of wide shear cracks. All specimens with SR displayed the ability to undergo

more deformation without abruptly losing stiffness. Moreover, all specimens with SR showed the ability to dissipate energy at high levels of lateral drift. Further, the presence of the stirrups in the slab–column connection zone yielded higher drift-ductility indexes when subjected to reversed lateral cyclic loads.

3. Extending the stirrups by 4.5*d* instead of 2*d* significantly affected the performance of the slab–column connections. The lateral deformation capacity increased by 66% and the lateral ductility index by 41% and 48%. The addition of stirrups resulted in a softer punching-shear mechanism due to the mobilization of the shear reinforcement before punching-shear failure occurred.
4. The spiral stirrups provided an additional confining effect that reduces the concrete softening and limited cracking and cracking extension in the slabs. The lateral drift and unbalanced moment-carrying capacities also increased by 10% and 6%, respectively. Using spirals stirrups enabled also slightly higher connection stiffness and allowed more energy dissipation at higher levels of lateral drift. In addition, a slight increase of 2.5% and 7.5% in the drift ductility indexes was observed.
5. Increasing the gravity-load intensity in the specimen with SR had a slightly detrimental effect on the lateral drift capacity and the overall punching-shear behavior. Further experimental tests, however, are needed.
6. All slab–column connections with SR attained higher strength and deformation capacity as well as adequate lateral-ductility indexes. The GFRP-SR is recommended for use in RC flat-plate structures in seismic zones, although further research is needed to implement adequate design guidelines for such structural elements.

CHAPTER 7. SUMMARY, CONCLUSIONS AND RECOMMENDATIONS

7.1. Summary

This research study was carried on eight full–scale concrete two–way slab-column connections reinforced with glass fiber–reinforced polymers (GFRP) bars. All tested specimens were identical and measured 2500×2500 mm with a thickness of 200 mm. A column measuring 300 mm×300 mm extended 700 mm at its centre above and below the slab surfaces. All specimens were tested to failure under combined constant gravity and lateral reversed cyclic loads. Based on the laboratory testing results, the punching–shear performances were evaluated in terms of failure modes, cracking patterns, hysteretic response, reinforcement and concrete strains, connection stiffness, energy dissipation, and drift–ductility index with taking into consideration the effects of: (i) flexural–reinforcement type (GFRP and steel bars); (ii) the flexural–reinforcement ratio (1.06% and 1.51%); (iii) service gravity load intensity (dead load plus 30% of the live load or combined dead and live loads); and (iv) concrete compressive strength (NSC and HSC). Moreover, the impact of using GFRP stirrups as shear reinforcement around the slab-column connection on slab seismic performance was assessed. The main investigated variables were: (i) GFRP stirrups type (closed and spiral); (ii) GFRP stirrups distribution; and (iii) service gravity load intensity (dead load plus 30% of the live load or combined dead and live loads). The main findings of this study are summarized as follows.

7.2. Conclusions

7.2.1. GFRP–reinforced slab-column connections without shear reinforcement

- All GFRP–reinforced specimens showed adequate strength and deformation capacity against punching–shear failure during and after reversed lateral cyclic–loading conditions. Accordingly, GFRP reinforcing bars could be used as reinforcement in slab-column connections subjected to a combination of gravity and reversed lateral cyclic loads.

- All tested GFRP–reinforced specimens experienced a typical sudden and brittle punching–shear failure without much warning. The punching–shear failure was evidenced by a sudden drop in the applied gravity and lateral loads. No signs of GFRP–bar rupture, slippage, or bond failure were observed.
- All tested GFRP–reinforced specimens demonstrated stable hysteretic behavior and achieved values of lateral–drift ratio ranging from 1.75% to 3.00%, which is over the 1.50% recommended allowable design drift in the codes used for seismic analysis. Moreover, all the GFRP–reinforced specimens achieved adequate unbalanced moment–carrying capacity.
- The maximum GFRP–reinforcement strains in all the GFRP–reinforced specimens were less than the characteristic tensile strength. This relatively low strain at ultimate load in all the GFRP–RC specimens shows that slab punching was not triggered by GFRP–bar rupture; no bond failure nor slippage occurred during the tests. Therefore, a minimum amount of repair after surviving a seismic–loading event would be required, which is considered an advantage of GFRP–RC structures.
- The maximum concrete strains in all GFRP–reinforced specimens were low and below the theoretical crushing failure of –3500 με. Furthermore, no signs of concrete crushing on the compression side of the slabs were observed during testing.
- Reduction of slab-column connection stiffness was observed in all GFRP–reinforced specimens during successive cycles of increasing displacement. On the other hand, the effect of repeated loading cycles was obvious with the average reduction in stiffness in each drift cycle ranging from 2% to 5%.
- All GFRP–reinforced specimens exhibited reasonable levels of energy dissipation upon punching–shear failure. Further, the reduction in dissipated energy in each drift cycle was about 25% to 30%, due to the excessive damage induced in the slab-column connections during the second loading cycle.
- Compared to the steel–reinforced specimen and the minimum required ductility factor of 1.2, all the GFRP–reinforced specimens offered sufficient drift–ductility indices for slab-column connections subjected to reversed lateral cyclic loads.
- The test results indicate that all the GFRP–reinforced specimens had wider diagonal shear cracks than the steel–reinforced specimen. This is due to the high effective reinforcement

ratio ($\rho E_r/E_s$). The widths of the diagonal shear cracks in all the GFRP–reinforced specimens were narrower in the transverse direction than in the lateral–loading direction.

- Increasing the slab flexural reinforcement contributed to increased crack propagation but smaller crack widths. The lateral inter-story drift capacity, drift–ductility index, and strains in GFRP–reinforcing bars were reduced. In addition, the slab-column connection stiffness, energy dissipation, and capacity of moment transfer were enhanced.
- Increasing the gravity–load intensity significantly affected the performance of the slab-column connection subjected to reversed lateral cyclic loads. The lateral–drift capacity, the capacity of moment transfer, connection stiffness, and drift–ductility index were reduced, while increased dissipated energy, reinforcement strain, and concrete strain were evident.
- The use of high concrete compressive strength (HSC) had a significant effect on the punching–shear performance. The HSC enhanced the GFRP–reinforced specimen punching resistance, but the punching–shear failure was not gradual, but rather brittle and abrupt. Using HSC also enhanced the degradation of the connection stiffness, drift ductility index, and dissipated relatively more energy than the GFR–NSC specimen.

7.2.2. GFRP–reinforced slab-column connections with GFRP stirrups shear reinforcement

- All GFRP–reinforced specimens with GFRP shear reinforcements demonstrated substantial strength and lateral deformation capacity against punching shear failure during and after reversed lateral cyclic–loading conditions. Accordingly, the GFRP stirrups, either closed or spiral, could be used effectively as shear reinforcement in the concrete slab-column connections reinforced with GFRP bars and subjected to gravity and reversed lateral cyclic loads.
- All GFRP–reinforced specimens with GFRP stirrups shear reinforcement displayed flexible punching shear failure with a gradual decrease in the lateral loads and maintained its integrity. Moreover, all specimens achieved a high lateral drift of 4.0% to 7.50% with the ability to sustain the gravity load. The specimens with GFRP shear reinforcement exhibited also stable hysteretic response and achieved adequate unbalanced moment carrying capacities.
- The GFRP stirrups offered sufficient resistance and confinement to control the development of shear cracks of wide opening. Consequently, all tested GFRP–reinforced specimens

demonstrated the capability to undergo far with more deformation without abruptly losing stiffness. Furthermore, all specimens with GFRP shear reinforcement displayed the ability to dissipate energy during high lateral–drift levels.

- All specimens displayed higher drift ductility indices and like steel–reinforced specimens with shear–reinforcement, the ductility factor always exceeded 3.
- Provision of shear reinforcement around the slab-column connections to distance 4.5d had a substantial increase in lateral–drift ratio, unbalanced moment, connection stiffeners and drift ductility indexes compared to its counterpart without shear reinforcement. The lateral–drift ratio increased by 122% and the moment carrying capacity by 14%. At higher drift levels, the specimen with GFRP shear reinforcement revealed higher connection stiffness and didn't degrade as rapidly as the specimen without shear reinforcement. Furthermore, the specimen with shear reinforcement exhibited the ability to dissipate energy during high lateral drift levels.
- Extending the GFRP closed stirrups to distance 4.5d instead of 2d had a significant influence on the performance of the slab-column connection. The lateral deformation capacity was increased by 66%, and lateral ductility index was enhanced by 41 to 48%. Furthermore, the addition of GFRP stirrups resulted in a softer punching shear mechanism due to the mobilization of the shear reinforcement before the punching–shear failure.
- The GFRP spiral, as continuous stirrups, provides an additional confining effect which reduces the concrete softening and limits the cracking and its extension in the slabs. Consequently, the lateral drift and unbalanced moment carrying capacities were increased by 10% and by 6%, respectively. Moreover, the use of GFRP spiral afforded slightly high connection stiffness for the tested specimen and allowed more energy dissipation at the higher lateral drift levels. Also, the specimen with the GFRP spiral has shown a slight increase of 2.5% and 7.5% in the drift ductility indexes in comparison to the specimen with closed GFRP stirrups.
- Increasing the gravity load intensity in the GFRP–tested specimen with GFRP stirrups shear reinforcement had a slightly detrimental effect on the unbalanced moment capacity and the overall punching shear behavior, which coincided with the steel–reinforced slabs in the literature. However, further experimental tests are required.

- The GFRP reinforcement is recommended to be used in concrete flat plate structures located in the seismic zone, although further research is needed to implement adequate design guidelines for such structural element.

7.3. Recommendations for Future Work

The promising results of this research study can provide impetus for constructing concrete two–way slabs reinforced with GFRP for buildings in low–to–moderate seismic zone. Even though the number of test specimens in this research study is limited to understanding the punching behavior of interior to way GFRP slab-column connections under seismic conditions, it is expected to set the direction for further research to investigate other parameters. Based on the findings of the current study, additional researchers are recommended to cover the following points:

- Exterior slab-column connections may influence significantly the stiffness and the strength of flat slab buildings. Therefore, the further experimental investigation could focus on the seismic behavior of corner connections and edge connections with bending parallel to the slab edge.
- Investigate the effects of the banded distribution of flexural reinforcement in the slab on the seismic behavior of two–way slabs reinforced with FRP bars.
- Examining the response of slab-column connections containing various types of FRP shear reinforcement when subjected to combined gravity and cyclic lateral loading. Also evaluating the impacts of the amount and layout of FRP shear reinforcement.
- Study the effects of thickening the slab over different plan dimensions (drop panels or column capital) on the behavior of interior slab-column connections under combined gravity and cyclic lateral loading
- Assess the impacts of openings on the seismic behavior of slab-column connections without and with shear reinforcements. Openings located on different sides of the column and at a distance from the column could be researched by testing appropriate specimens.

These proposed studies would allow better assessment of the FRP–RC flat plates/slabs, as well as establishing the design guidelines required for FRP–RC flat plates/slabs. This facilitates for

wide utilization of FRP bars in many constructing concrete two–way slabs reinforced with GFRP for buildings in the low–to–moderate seismic zone.

7.4. Résumé

Ce projet de recherche a porté sur huit (8) jonctions dalle bidirectionnels-poteau pleine grandeur en béton armé de barres en polymère renforcé de fibres de verre (PRFV). Toutes les dalles avaient une géométrie identique de 2500 × 2500 × 200 mm. Les dalles comportaient également en leur centre, un poteau carré de 300 mm de côté et ayant une saillie de 700 mm au-dessus et au-dessous de la surface de la dalle. Tous les spécimens ont été testés jusqu'à la rupture sous une combinaison de charges de gravité constante et de charges cycliques latérales inversées. Sur la base des résultats des essais effectués en laboratoire, les comportements au poinçonnement ont été évalués suivant les modes de rupture, les patrons de fissuration, la réponse hystérétique, les déformations du béton et des armatures, la rigidité des jonctions, la dissipation d'énergie et l'indice de ductilité du déplacement relatif, en tenant compte des effets suivants: (i) le type d'armature en flexion (PRFV et acier), (ii) le taux d'armature en flexion (1,06% et 1,51%) (iii) l'intensité de la charge de gravité en service (charge morte plus 30% de la charge vive ou une combinaison de charges morte et vive), et (iv) la résistance à la compression du béton (béton de résistance normale et béton à haute résistance). De plus, l'effet de l'utilisation d'étriers en PRFV comme armature de cisaillement autour de la jonction dalle-poteau sur la performance sismique des dalles a été évalué. Les principaux paramètres étudiés étaient: (i) le type d'étriers en PRFV (fermés et en spirale), ii) la distribution des étriers en PRFV, et (iii) l'intensité de la charge de gravité en service (charge morte plus 30% de la charge vive ou une combinaison de charges morte et vive). Les principales conclusions de cette étude sont résumées ci-après.

7.5. Conclusions

7.5.1. Jonctions dalle-poteau en béton armé de PRFV sans armatures de cisaillement

- Tous les spécimens en béton armé de PRFV ont présenté une résistance et une capacité de déformation suffisantes par rapport à la rupture par poinçonnement pendant et après le chargement cyclique latéral inversé. Par conséquent, les barres d'armature en PRFV

pourraient être utilisées dans les jonctions dalle-poteau soumises à une combinaison de charges de gravité et de charges cycliques latérales inversées..

- Tous les spécimens en béton armé de PRFV ont présenté une rupture soudaine et fragile par poinçonnement typique sans trop d'avertissements. La rupture par poinçonnement a été caractérisée par une réduction soudaine de la charge de gravité et de la charge latérale. Aucun signe de rupture de barre en PRFV, de glissement ou de rupture de l'adhérence n'a été observé.
- Tous les spécimens en béton armé de PRFV testés ont présenté un comportement hystérétique stable et ont atteint des déplacements relatifs latéraux allant de 1,75% à 3,00%, ce qui est supérieur au déplacement relatif de conception de 1,50% recommandé dans les codes pour l'analyse sismique. De plus, tous les spécimens en béton armé de PRFV ont atteint une résistance adéquate au moment non équilibré.
- Les déformations maximales des armatures en PRFV de tous les spécimens en béton armé de PRFV étaient inférieures aux déformations ultimes en traction des barres. Cette déformation relativement faible à la charge ultime dans tous les spécimens en béton armé de PRFV montre que le poinçonnement de la dalle n'a pas été causé par une rupture de barre en PRFV, et aucune rupture de l'adhérence ni aucun glissement n'est survenu pendant les essais. Par conséquent, une réparation mineure de la structure après avoir été soumise à un chargement sismique serait nécessaire, ce qui constitue un avantage pour les structures en béton armé de PRFV.
- Les déformations maximales du béton dans tous les spécimens béton armé de PRFV étaient faibles et inférieures à la déformation ultime théorique du béton en compression de -3500 µdef. De plus, aucun signe d'écrasement du béton sur la face en compression des dalles n'a été observé lors des essais.
- Une réduction de la rigidité de la jonction dalle-poteau a été observée sur tous les spécimens en béton armé de PRFV au cours de cycles successifs d'augmentation croissante de déplacement. D'autre part, l'effet de la répétition des cycles de chargement était visible avec une réduction moyenne de la rigidité dans chaque cycle de déplacement relatif allant de 2% à 5%.
- Tous les spécimens en béton armé de PRFV ont présenté des niveaux raisonnables de dissipation d'énergie au moment de la rupture par poinçonnement. En outre, la réduction de

l'énergie dissipée dans chaque cycle de déplacement relatif était d'environ de 25% à 30%, en raison des dommages excessifs induits dans les joints dalle-poteau au cours du deuxième cycle de chargement.

- Par rapport au spécimen avec armature en acier et au facteur de ductilité minimum requis de 1,2, tous les spécimens en béton armé de PRFV présentaient des indices de ductilité de déplacement relatif suffisants pour les jonctions dalle-poteau soumises à des charges cycliques latérales inversées.
- Les résultats des essais indiquent que tous les spécimens en béton armé de PRFV présentaient des fissures de cisaillement diagonal plus larges que les spécimens avec armatures en acier. Cela est dû au taux d'armature effectif élevé (ρEr/Es). Les largeurs des fissures de cisaillement diagonal dans tous les spécimens en béton armé de PRFV étaient plus étroites dans la direction transversale que dans la direction de chargement latéral.
- L'augmentation du taux d'armature en flexion de la dalle a contribué à une propagation accrue des fissures, mais avec des ouvertures de fissure réduites. La capacité de déplacement relatif latérale entre les étages, l'indice de ductilité du déplacement relatif et les déformations des barres d'armature en PRFV ont été réduits. De plus, la rigidité de la jonction dalle-poteau, la dissipation d'énergie et la capacité de transfert de moment ont été améliorées.
- L'augmentation de l'intensité de la charge de gravité a eu une incidence importante sur les performances de la jonction dalle-poteau soumise à des charges cycliques latérales inversées. La capacité de déplacement latéral relatif, la capacité de transfert de moment, la rigidité des jonctions et l'indice de ductilité du déplacement relatif ont été réduits, tandis qu'une augmentation de l'énergie dissipée, des déformations des armatures et du béton était visible.
- L'utilisation d'un béton à haute résistance (BHR) a eu un effet significatif sur les performances de poinçonnement. Le BHR a amélioré la résistance au poinçonnement des spécimens en béton armé de PRFV, mais la rupture par poinçonnement n'était pas progressive, et était plutôt fragile et soudaine. L'utilisation de BHR a également amélioré la dégradation de la rigidité de la jonction et de l'indice de ductilité du déplacement relatif, et a permis de dissiper relativement plus d'énergie que le spécimen avec du béton normal armé de PRFV.

7.5.2. Jonctions dalle-poteau avec des étriers en PRFV comme armatures de cisaillement

- Tous les spécimens en béton armé de PRFV avec armatures de cisaillement en PRFV ont présenté une résistance et une capacité de déformation latérale élevées par rapport à la rupture par poinçonnement, pendant et après le chargement cyclique latéral inversé. Par conséquent, les étriers en PRFV, fermés ou en spirale, pourraient être utilisés efficacement comme armatures de cisaillement dans les jonctions dalle-poteau en béton armé de PRFV soumises aux charges de gravité et aux charges cycliques latérales inversées.
- Tous les spécimens en béton armé de PRFV avec armatures de cisaillement constituées d'étriers en PRFV présentaient une rupture par poinçonnement flexible avec une diminution progressive des charges latérales, tout en préservant leur intégrité. De plus, tous les spécimens ont atteint un déplacement latéral relatif élevé de 4,0% à 7,50% avec la capacité de supporter la charge de gravité. Les spécimens avec armatures de cisaillement en PRFV ont également présenté une réponse hystérétique stable avec des résistances au moment non équilibré adéquates.
- Les étriers en PRFV offraient une résistance et un confinement suffisants pour contrôler le développement de fissures de cisaillement dans le cas de larges ouvertures. Par conséquent, tous les spécimens en béton armé de PRFV testés ont démontré la capacité de subir beaucoup plus de déformations sans perdre brusquement leur rigidité. En outre, tous les spécimens avec des armatures de cisaillement en PRFV montraient la capacité de dissiper de l'énergie pour des niveaux élevés de déplacement latéral relatif.
- Tous les spécimens présentaient des indices de ductilité de déplacement latéral effectif élevés et, comme pour les spécimens avec armatures de cisaillement en acier, le facteur de ductilité était toujours supérieur à 3.
- L'utilisation d'armatures de cisaillement autour des jonctions dalle-poteau à une distance 4,5d a entraîné une augmentation substantielle du déplacement latéral relatif, du moment non équilibré, des rigidités des jonctions et des indices de ductilité du déplacement latéral relatif par rapport au spécimen sans armatures de cisaillement. Le déplacement relatif latéral a augmenté de 122% et la capacité portante de 14%. Pour des déplacements relatifs élevés, le spécimen avec armatures de cisaillement en PRFV a montré une rigidité de jonction plus élevée et n'a pas connu de ruine aussi rapide que le spécimen sans armatures de cisaillement.

De plus, le spécimen avec armatures de cisaillement montrait une capacité de dissipation de l'énergie à des niveaux élevés de déplacement relatif latéral.

- L'extension des étriers fermés en PRFV à une distance de 4,5d au lieu de 2d a eu une influence significative sur les performances de la jonction dalle – poteau. La capacité de déformation latérale a été augmentée de 66% et l'indice de ductilité latérale a augmenté de 41% à 48%. De plus, l'ajout d'étriers en PRFV a permis d'atténuer le mécanisme de poinçonnement du fait de la mobilisation des armatures de cisaillement avant la rupture par poinçonnement.
- La spirale en PRFV, du fait de sa continuité, fournit un effet de confinement supplémentaire qui réduit l'adoucissement du béton et limite la fissuration et sa propagation dans les dalles. Par conséquent, le déplacement relatif latéral et les résistances au moment non équilibré ont été augmentés de 10% et de 6%, respectivement. De plus, l'utilisation de spirale en PRFV a conféré à la jonction une rigidité légèrement élevée pour le spécimen testé et permettait une dissipation d'énergie accrue à des niveaux de déplacement relatif latéral élevés. En outre, le spécimen avec spirale en PRFV a montré une légère augmentation des indices de ductilité du déplacement relatif de 2,5% et 7,5% par rapport au spécimen avec étriers en PRFV fermés.
- L'augmentation de l'intensité de la charge de gravité dans le cas des spécimens en béton armé de PRFV avec armatures de cisaillement en PRFV testés a eu un effet légèrement défavorable sur la résistance au moment non équilibré et le comportement général au poinçonnement, correspondant aux dalles avec armatures en acier dans la littérature. Cependant, d'autres essais expérimentaux sont nécessaires.
- Il est recommandé d'utiliser l'armature en PRFV dans les planchers-dalles en béton situés dans la zone sismique, bien que des recherches supplémentaires soient nécessaires établir des directives de calcul adéquates pour ce type d'élément structural.

7.6. Recommandations pour les travaux futurs

Les résultats prometteurs de ce projet de recherche peuvent donner l'impulsion nécessaire à la construction de dalles bidirectionnelles en béton armé avec armatures de PRFV pour les bâtiments situés dans une zone de risque sismique faible à modéré. Bien que le nombre de spécimens d'essai dans ce projet de recherche se limite à la compréhension du comportement au poinçonnement des jonctions dalle bidirectionnelle-poteau intérieur en béton armé de PRFV, sous sollicitations sismiques, il devrait orienter les recherches futures pour étudier d'autres

paramètres. Sur la base des conclusions de la présente étude, il est recommandé de réaliser des études supplémentaires pour couvrir les points suivants:

- Les jonctions dalle-poteau extérieur peuvent influencer de manière significative la rigidité et la résistance des planchers-dalles de bâtiments. Par conséquent, les études expérimentales supplémentaires pourraient porter sur le comportement sismique des jonctions dalle-poteau de coin et de rive avec des sollicitations flexion dans la direction parallèle au bord de la dalle.
- Étudier les effets de la distribution en bande des armatures en flexion dans la dalle sur le comportement sismique des dalles bidirectionnelles avec des barres d'armature en PRF.
- Étudier la réponse des jonctions dalle-poteau comportant divers types d'armatures de cisaillement en PRF lorsqu'elles sont soumises à une combinaison de charge de gravité et de charge latérale cyclique. Évaluer également les impacts du taux et de la disposition des armatures de cisaillement en PRF.
- Étudier les effets de l'épaisseur de la dalle sur différents plans (panneaux de retombée ou chapiteau) sur le comportement des jonctions dalle-poteau intérieur sous l'effet combiné de la charge de gravité et de la charge latérale cyclique.
- Évaluer les impacts des ouvertures sur le comportement sismique des jonctions dalle-poteau sans et avec des armatures de cisaillement. Des ouvertures situées sur différents côtés du poteau et à une certaine distance de celle-ci pourraient être fixées en testant des spécimens appropriés.

Ces propositions d'études permettraient de mieux évaluer les planchers-dalles et les dalles pleines sur poteaux avec panneaux de retombée et champignons en béton armé de PRFV et d'établir les guides de calcul requis pour ces types de dalles. Cela facilite une large utilisation des barres en PRF dans de nombreuses constructions de dalles bidirectionnelles en béton armé de PRFV pour les bâtiments situés dans une zone de risque sismique faible à modérée.

.

REFERENCES

Ali, M. and El–Salakawy, E., (2016), "Seismic Performance of GFRP–Reinforced Concrete Rectangular Columns." Journal of Composites for Construction, 20(3): 04015074.

American Concrete Institute (ACI Committee 318), (2014), "Building Code Requirements for Structural concrete" (*ACI 318–14*), Farmington Hills, MI.

American Concrete Institute (ACI Committee 421), (2010), "Guide to Seismic Design of Punching Shear Reinforcement in Flat Plates." *(ACI 421.2R–2010)*, ACI, Farmington Hills, Mich.

American Concrete Institute (ACI Committee 440) (2004), "Guide Test Methods for Fiber–Reinforced Polymers (FRPs) for Reinforcing or Strengthening Concrete Structures *(ACI 440.3R–04)*." ACI, Farmington Hills, MI, 40 pp.

American Concrete Institute (ACI Committee 440), (2015), "Guide for the Design and Construction of Structural Concrete Reinforced with Fiber–Reinforced Polymer (FRP) Bars." *(ACI 440.1R–2015)*, Farmington Hills, MI.

American Society for Testing and Materials (ASTM D7205M), (2011), "Standard test method for tensile properties of fiber reinforced polymer matrix composite bars. Conshohocken, USA. p.12.

Benmokrane, B.; Ahmed, E.; Dulude, C.; and Boucher, E., (2012), "Design, Construction, and Monitoring of the First Worldwide Two–Way Flat Slab Parking Garage Reinforced with GFRP Bars.", Proceedings of the 6th International Conference on FRP Composites in Civil Engineering, Rome, Italy, June 13–15, 8 p.

Benmokrane, B.; El–Salakawy, E.; El–Ragaby, A.; and Lackey, T., (2006), "Designing and Testing of Concrete Bridge Decks Reinforced with Glass FRP Bars." ASCE Journal of Bridge Engineering, 11(2): 217–229.

Bompa D.V. and Onet¸ T., (2015), "Punching shear strength of RC flat slabs at interior connections to columns." Magazine of Concrete Research, 24–42, doi.org/10.1680/macr.14.00402.

Canadian Standards Association (CSA), (2012), "Design and Construction of Building Structures with Fiber Reinforced Polymers." *(CAN/CSA S806–12)*, Rexdale, Ontario, Canada, 198 p.

Canadian Standards Association (CSA), (2014), "Design of concrete structures for buildings." (*CSA–A23.3 M–14*), Rexdale, Ontario, Canada, 240 p.

Canadian Standards Association (CSA), (2015), "Specification for Fiber–Reinforced Polymers." (*CAN/CSA S807–15*), Rexdale, Ontario, Canada, 27 p.

Dam, Thai X.; Wight, James K.; and Parra–Montesinos; Gustavo J. (2017). "Behavior of Monotonically Loaded Slab-Column Connections Reinforced with Shear Studs," ACI Structural Journal, V. 114, No. 1, Jan.–Feb., pp. 221 232.

Drakatos IS., Muttoni A., Beyer K., (2015), "Internal slab-column connections under monotonic and cyclic imposed rotations." Engineering Structures V.123–501–516, 15 Sep. 2016.

Dulude, C., Hassan, M., Ahmed, E.A., and Benmokrane, B., (2013), "Punching Shear Behaviour of Two–Way Flat Concrete Slabs Reinforced with GFRP Bars." *ACI Structural Journal*, 110(5): 723–734.

El–Gamal, S.; El–Salakawy, E.; and Benmokrane, B., (2005a), "Behavior of Concrete Bridge Deck Slabs Reinforced with Fiber–Reinforced Polymer Bars under Concentrated Loads." ACI Structural Journal, 102 (5): 727–735.

El–Gamal, S.E.; El–Salakawy, E.F.; and Benmokrane, B., (2005b), "A New Punching Shear Equation for Two–Way Concrete Slabs Reinforced with FRP Bars." Fiber–Reinforced Polymer Reinforcement for Concrete Structures, American Concrete Institute, Farmington Hills, MI, SP–230–50: 877–894.

El–Ghandour, A.W.; Pilakoutas, K.; and Waldron P., (2003), "Punching Shear Behavior of Fiber Reinforced Polymers Reinforced Concrete Flat Slabs: Experimental Study." ASCE Journal of Composites for Construction, 7(3): 258–265.

Elshamandy, M. G., Farghaly, A. S., and Benmokrane, B., (2017), "Experimental Behavior of GFRP–Reinforced Concrete Columns under Lateral Cyclic Load", ACI Structural Journal.

Emam M., Marzouk H., and Hilal S., (1997), "Seismic Response of Slab-Column Connections Constructed With High–Strength Concrete" ACI Structural Journal, V. 94, No. 2, March–April 1997. pp. 94–S19.

Ghomi, Shervin K., and El–Salakawy, E., (2015),"Seismic Behavior of Beam-Column Joints Reinforced with GFRP Bars and Stirrups." Journal of American Society of Civil Engineers, ASCE ISSN 1090–0268/04015019(11).

Gouda, A., and El–Salakawy, E., (2015), "Punching Shear Strength of GFRP–RC Interior Slab-Column Connections Subjected to Moment Transfer." American Society of Civil Engineers, DOI: 10.1061/ (ASCE) CC.1943–5614.0000597.

Gouda, A., and El–Salakawy, E., (2016), "Behavior of GFRP–RC Interior Slab-Column Connections with Shear Studs and High–Moment Transfer." Journal of American Society of Civil Engineers, doi 10.1061/ (ASCE) V.20; No.4; p.04016005.

Hassan, M., Ahmed, E. A., and Benmokrane, B., (2013), "Punch¬ing–Shear Strength of GFRP–Reinforced Concrete Flat Slabs," Canadian Journal of Civil Engineering, V. 40, No. 10, Apr., pp. 951–960.

Hassan, M., Ahmed, E. A., and Benmokrane, B., (2013), "Punching–Shear Strength of Normal– and High–Strength Two–Way Concrete Slabs Rein¬forced with GFRP Bars," Journal of Composites for Construction, ASCE, V. 17, No. 6, Dec., doi: 10.1061/(ASCE)CC.1943–5614.0000424.10.1061/(ASCE)

Hassan, M., Ahmed, E. and Benmokrane, B., (2014), "Punching Shear Behavior of Two–Way Slabs Reinforced with FRP Shear Reinforcement," Journal of Composites for Construction, ASCE, V. 19, No.1, Feb., doi: 10.1061/ (ASCE) CC.1943–5614.0000493.10.1061/ (ASCE)

Hassan, M.; Ahmed, E.; and Benmokrane, B., (2014), "Punching–Shear Design Equation for Two–Way Concrete Slabs Reinforced with FRP Bars and Stirrups," Construction and Building Materials, V. 66, Sept., pp. 522–532.

Hawkins, N.M.; Criswell, M.E.; and Roll, F. (1974), "Shear Strength of Slabs without Shear Reinforcement." ACI Publication, Shear in Reinforced Concrete, 42 (30): 677–720.

Hussein, A., and El–Salakawy, E., (2018), "Punching Shear Behavior of Glass Fiber–Reinforced Polymer–Reinforced Concrete Slab-Column Interior Connections" ACI Structural Journal, V. 115, No. 4, July 2018. MS No. S–2017–264.R1, doi: 10.14359/51702134.

Kang, T. H.–K., Lee JD, BS Lee, Bum, MJ Kim, and KH Kim., (2017). "Punching and Lateral Cyclic Behavior of Slab-Column Connections with Shear Bands," ACI Structural Journal, V. 114, No. 5, pp. 1075–1086. Sept.–Oct 2017

Kinnunen, S. and Nylander, H., (1960). "Punching of concrete slabs without shear reinforcement." Transactions of the Royal Institute of Technology, No. 158, 112 pp., Stockholm, Sweden, 1960.

Komová, E.; Varga, M.; Varga, R.; Vojtan, P.; Torrejon, J.; Provencio, M.; and Vazquez, M., (2008). "Stress Dependence of the Switching Field in Glass Coated Microwires." Acta. Phys. Pol. A, 113(1), 135–138.

Lee, J.H.; Yoon, Y.S.; and Mitchell, D, (2009), "Improving Punching Shear Behavior of Glass Fiber–Reinforced Polymer Reinforced Slabs." ACI Structural Journal, 106(4): 427–434.

Li, R.; Cho, Y.S.; and Zhang, S., (2006), "Punching Shear behavior of Concrete Flat plate Slab Reinforced with Carbon Fiber Reinforced Polymer Rods.", Composites: Part B, 38(5–6): 712–719.

Mady, M., El–Ragaby, A., and El–Salakawy, E., (2011),"Seismic Behavior of Beam-Column Joints Reinforced with GFRP Bars and Stirrups." Journal of Composites for Construction, ASCE, 15(6), 875–886.

Marzouk H., Osman M and Hussein, A., (2001), "Cyclic Loading of High–Strength Lightweight Concrete Slabs" ACI Structural Journal, V. 98, No. 2, March–April 2001. pp. 00–101.

Marzouk, H.; Emam, M.; and Hilal, S., (1996), "Effect of High–Strength Concrete Columns on the Behavior of Slab-Column Connections." ACI Structural Journal, 93(5): 545–555.

Matthys, S.; and Taerwe, L., (2000 a & b), "Concrete Slabs Reinforced with FRP Grids. I: One–Way Bending." ASCE Journal of Composites for Constructions, 4(3): 145–153.

Megally, S., and Ghali, A., (1994), "Design Considerations for Slab-Column Connections in Seismic Zones." ACI Structural Journal, V.91 No. 3 May–June 1994, pp. 303–314.

Megally, S., and Ghali, A., (1998), "Punching Shear Resistance of Concrete Slabs to Gravity and Earthquake Forces." PhD thesis, Department of Civil Engineering, Calgary University, Alberta, Canada, 504 p.

Megally, S., and Ghali, A., (2000), "Seismic Behavior of Edge Column–Slab Connections with Stud Shear Reinforcement." ACI Structural Journal, 97(1), 53–60.

National Research Council of Canada. (2010), "National Building Code of Canada." NBCC 2005, National Research Council of Canada, Ottawa, ON, 1222.

Nguyen–Minh L.; and Rovnak M., (2013), "Punching–Shear Resistance of Interior GFRP Reinforced Slab–Column Connection." ASCE Journal of Composites for Constructions, 17(1): 2–13.

Osman M., Marzouk H., and Helmy S., (2000), "Behavior of High–Strength Lightweight Concrete Slabs under Punching Loads" ACI Structural Journal, V. 97, No. 3. May–June 2000, pp. 99–097.

Ospina, C.E.; Alexander, S.D. B.; and Roger Cheng, J.J., (2003), "Punching of Two–Way Concrete Slabs with Fiber–Reinforced Polymer Reinforcing Bars or Grids." ACI Structural Journal, 100(5): 589–598.

Ospina, C.E.; Alexander, S.D. B.; and Roger Cheng, J.J., (2003), "Punching of Two–Way Concrete Slabs with Fiber–Reinforced Polymer Reinforcing Bars or Grids." ACI Structural Journal, 100(5): 589–598.

Pan, A., and Moehle, J.P., (1988), "Lateral Displacement Ductility of Reinforced Concrete Flat Plates," ACI Structural Journal, V. 86, No. 3, May–June 1989, pp. 250–258.

Park R., (1989), "Evaluation of ductility of structures and structural assemblages from laboratory testing". Bull N Z Natl Soc Earthq Eng 22(3):155–166.

Pillai S.U., Kirk W., and Scavuzzo L., (1982). "Shear Reinforcement at Slab-Column Connections in a Reinforced Concrete Flat Plate Structure." ACI Structural Journal, V. 79, No.1, pp. 36–42.

Park, R.; and Gamble, W., (2000), "Reinforced Concrete Slabs." 2nd Edition, John Wiley & Sons, Inc. 715p.

Regan, P.E., (1981), "Behaviour of Reinforced Concrete Flat Slabs." Technical Report 89, Construction Industry Research and Information Association (CIRIA), London, UK, 89p.

Regan, P.E., and Bræstrup, M.W., (1985), "Punching Shear in Reinforced Concrete.", Comité Euro-International du Béton, Bulletin d'Information, No. 168, Jan. 1985, 232 p.

Rizk, E.; Marzouk, H.; and Hussein, A., (2011), "Punching Shear of Thick Plates with and without Shear Reinforcement." ACI Structural Journal, 108 (5): 581–591.

Robertson I. and Johnson G., (2006), "Cyclic Lateral Loading of Non–ductile Slab-Column Connections" ACI Structural Journal, V. 103, No. 3, May–June 2006. pp. 04–194.

Robertson, I. N.; Kawai, T.; Lee, J.; and Enomoto, B. (2002). "Cyclic Testing of Slab-Column Connections with Shear Reinforcement," ACI Structural Journal, V. 99, No. 5, pp. 605–613. Sept.–Oct 2002.

Robertson NI., and Durrani AJ., (1992), "Gravity Load Effect on Seismic Behavior of Interior Slab–Column Connection" ACI Structural Journal, V. 98, No. 1, Jan–Feb 1992. pp. 89–S5.

Sherif, A., (1996), "Behavior of Reinforced Concrete Flat Slabs." PhD. Thesis, Civil Engineering Department, Calgary University, Canada, 395 p.

Zaghloul A.; and Razaqpur A., (2004), "Punching Shear Strength of Concrete Flat Plates Reinforced with CFRP Grids." Advanced Composite Materials in Bridges and Structures, Proceedings of the 4th International Conference on Advanced Composite Materials in Bridges and Structures, CSCE, Calgary, AB, Canada, 8 p.

Zaghloul, A., (2007), "Punching Shear Strength of Interior and Edge Column–Slab Connections in CFRP Reinforced Flat Plate Structures Transferring Shear and Moment.", PhD thesis, Department of Civil and Environmental Engineering, Carleton University, Ottawa, Ontario, 372 p.

Appendix (A):

Flexural and Shear Capacity of Connections without Shear Reinforcement

Design criteria:

Concrete properties:

Strain before crunching = 0.0035.

Material resistance factor ϕ_c=1.0

Concrete density factor λ=1.0

Clear cover = 30 mm.

Steel bars properties:

Modulus of elasticity = 200 GPa.

Ultimate tensile strength = 470 MPa.

Bar diameter = 200 mm.

Bar area = 300 mm^2

Sand coated GFRP bars properties:

Modulus of elasticity = 64.9 GPa.

Ultimate tensile strength = 1334 MPa.

Bar diameter = 19.5 mm.

Bar area =285 mm^2.

Steel–RC specimen (S1–control slab)

Design for flexure according to CSA/A23.3–14

14 bars 20M were used as flexural reinforcement.

$d_x = h_s$ – cover – d_b / 2 = 200 – 30 – 20/2 = 160mm

$d_y = h_s$ – cover – d_b – d_b / 2 = 200 – 30 – 20 – 20/2 = 140mm.

$d_{av} = (d_x + d_y) / 2 = (160 + 140)/2 = 150$ mm.

$\alpha_1 = 0.85 - 0.0015 f_c' = 0.85 - 0.0015(52) = 0.772 \geq 0.67$ Clause 10.1.7 (A23.3–14)

$\beta_1 = 0.97 - 0.0025 f_c' = 0.97 - 0.0025(52) = 0.840 \geq 0.67$ Clause 10.1.7 (A23.3–14)

$$\rho_s = A_s / A_c = 4200 / (2500 * 150.5) = 0.0112 (1.12\%)$$

According to clause 13.10.4, the spacing between reinforcement shall not be greater than the minimum of three times the slab thickness (600 mm) or 500 mm.

S = 173 mm < 500 mm

Check of the balanced reinforcement ratio ρ_b

$$\rho_b = \alpha_1\beta_1 \frac{\Phi_c f_c^{'}}{\Phi_s f_y}\frac{\varepsilon_{cu}}{\varepsilon_{cu}\varepsilon_s} = 0.772x0.840x\frac{1\ x\ 52}{1\ x\ 470}\frac{0.0035}{0.0035+0.0020} = 4.29\%$$

ρ_b = 4.29 % > ρ_{act} = 1.12 % Under–reinforced

From equilibrium and strain compatibility

$$C_u = T_u = \alpha_1\beta_c\Phi_c f_c^{'}ab = \Phi_s f_y A_s$$
$$= 0.772x1x1x52xax2500 = 1x470x14x300$$
$$a = 19.669mm$$
$$c = \frac{a}{\beta_1} = \frac{19.669}{0.840} = 23.416mm$$

$$M_r = T_u(d - a/2) = \Phi_s f_y A_s(d - a/2)$$
$$= 1x470x14x300x(150 - 19.669/2)$$
$$= 276.687KN.m$$

According to clause 10.5.2, the tension reinforcement can be assumed to reach yielding if

$$\frac{c}{d} \geq \frac{700}{700+f_y} \rightarrow \frac{23.146}{150} = 0.156 \geq \frac{700}{700+470} = 0.598$$ *Reinforcement yielded*

Shear Capacity According to CAN/CSA A23.3–14.

Perimeter of critical section for shear: b_o = 2 (b_1+ b_2) = 2 (450 +450) =1800 mm

Factor to account for low–density concrete λ = 1.0

Factor accounting for shear resistance of cracked concrete: $\beta = b_1 / b_2$ = 1.0

α = 4.0

Shear resistance attributed to the concrete factored by Φ_c:

$$v_c = 0.38\lambda\Phi_c\sqrt{f_c^{'}} = 0.38x1x1x\sqrt{52} = 2.74\text{N/mm}^2$$
$$= 0.19\lambda(1+\frac{2}{\beta_c})\sqrt{f_c^{'}} = 0.19x1x(1+2)\sqrt{52} = 4.11\text{N/mm}^2$$
$$= (0.19+\frac{d\alpha}{b_o})\lambda\Phi_c\sqrt{f_c^{'}} = (0.19+\frac{150x4}{1800})x1x1x\sqrt{52} = 3.774\text{N/mm}^2$$

The minimum shear stresses according to the code equations is 2.74 N/mm^2

Fraction of unbalanced moment transferred:

$$\gamma_V = 1 - \frac{1}{1+\frac{2}{3}\sqrt{\frac{b_1}{b2}}} = 0.4$$

Polar moment of inertia:

$$j = \frac{d(c_1+d)^3}{6} + \frac{d^3(c_1+d)^3}{6} + \frac{d^3(c_2+d)(c_2+d)^3}{2}$$

j = 9365625000.0 mm^4

Distance from center line to edge of critical section:

e = (c+d)/2 = (300+150)/2=225 mm

$$M_n = \frac{j}{\gamma_v e}(v_c - \frac{V_u}{b_o d_{av}})$$
$$= \frac{9365625000}{0.4x225}(2.74 - \frac{140}{1800x150}) = 231.19\text{KN.m}$$

Horizontal force lead to unbalanced moment $V_h = M_n / H$ = 231.19 / 1.35 = 171.3 KN

Shear Capacity According to ACI 318–14.

$$v_c = 0.33\lambda\sqrt{f_c'} = 0.33x1x\sqrt{52} = 2.40\text{N/mm}^2$$
$$= 0.083\lambda(2+\frac{4}{\beta_c})\sqrt{f_c'} = 0.083x1x(1+4)\sqrt{52} = 3.61\text{N/mm}^2$$
$$= 0.083(2+\frac{d\alpha}{b_o})\lambda\sqrt{f_c'} = 0.083(2+\frac{150x4}{1800})x1x\sqrt{52} = 3.21\text{N/mm}^2$$

The minimum shear stresses according to the code equations is 2.404 N/mm^2

$$M_n = \frac{j}{\gamma_v e}(v_c - \frac{V_u}{b_o d_{av}})$$
$$= \frac{9365625000}{0.4x225}(2.404 - \frac{140}{1800x150}) = 196.177\text{KN.m}$$

Horizontal force lead to unbalanced moment $V_h = M_n / H$ = 196.177 / 1.35 = 145.3 KN

GFRP–RC specimen (G1–GFRP control specimen)

Design for flexure according to CSA/S806–14

$d_x = h_s$ – cover – d_b / 2 = 200 – 30 – 19.5/2 = 160.5mm

$d_y = h_s$ – cover – d_b – d_b / 2 = 200 – 30 – 19.5 – 19.5/2 = 140.5mm.

$d_{av} = (d_x + d_y) / 2 = (160.5 + 140.5)/2 = 150.5$ mm.

$\alpha_1 = 0.85 - 0.0015 f_c' = 0.85 - 0.0015(52) = 0.772 \geq 0.67$

$\beta_1 = 0.97 - 0.0025 f_c' = 0.97 - 0.0025(52) = 0.840 \geq 0.67$

According to clause 8.4.2.3, the spacing between reinforcement shall not be greater than the minimum of three times the slab thickness (600 mm) or 300 mm. 14 Bars No.20 with spacing = 173mm were used as flexural reinforcement.

$$A_f = 14x285 = 3990mm^2 \geq A_{f\,\mathrm{Min}} = \frac{400}{E_f} A_g = 3081.66mm^2$$

$$\rho_f = A_f / A_c = 3990/(2500*150.5) = 0.0106(1.06\%)$$

From equilibrium and strain compatibility

$$\frac{\varepsilon_{cu}}{\varepsilon_{cu} + \varepsilon_{fu}} = \frac{c_b}{d} \rightarrow c_b = 21.77\mathrm{mm}$$

$$C_u = T_u = \alpha_1 \beta_1 \Phi_c f_c^{'} c_b b = \Phi_f f_{fu} A_{fb}$$
$$= 0.772x0.840x1x52x21.77x2500 = 1x1334xA_{fb}$$
$$A_{fb} = 1375.76mm^2$$

ρ = 0.0106 (1.06%) > ρ_b = 0.0037 (0.37%) (Compression failure)

According to CAS–S806 its recommend to design FRP members to be over reinforcement, in this case the concrete will crushing without rapture of the reinforcement and that will give a warning.

From equilibrium and strain compatibility

$$f_f = \frac{1}{2} E_f \varepsilon_{cu} \left(\sqrt{1 + \frac{4\alpha_1 \beta_1 \Phi_c f_c^{'}}{\rho_f \beta_1 \Phi_f E_f \varepsilon_{cu}}} - 1\right)$$
$$= 743.86\mathrm{N/mm}^2 \leq f_{fu} = 1334\mathrm{N/mm}^2$$

$$C_{uf} = T_{uf} = \alpha_1 \beta_1 \Phi_c f_c^{'} cb = \Phi_f f_f A_f$$
$$= 0.772x0.840x1x1x52xcx2500 = 1x743.86x3990$$
$$c = 35.207mm$$

According to clause 8.4.1.4 concrete strain shall be assumed to have reached 0.0035 provided that the ratio of c/d satisfies the following equation:

$$\frac{c}{d} \geq \frac{7}{7 + 2000\varepsilon_{fu}} \rightarrow \frac{35.207}{150.5} = 0.233 \geq \frac{7}{7 + 2000x0.0207} = 0.145$$

$$M_r = C_u \left(d - \frac{c\beta_1}{2}\right)$$
$$= 0.772x0.840x1x52x35.207x2500\left(150.5 - \frac{0.840x35.207}{2}\right)$$
$$= 402.798KN.m$$

Shear Capacity According to CSA/S806–14.

Perimeter of critical section for shear: b_o = 2 (b_1+ b_2) = 2 (450.50 +450.50) =1802 mm

Factor to account for low–density concrete $\lambda = 1.0$

Factor accounting for shear resistance of cracked concrete: $\beta = b_1 / b_2 = 1.0$

$\alpha = 4.0$

Shear resistance attributed to the concrete factored by Φ_c:

$$v_c = 0.056\lambda\Phi_c \sqrt[3]{E_f \rho_f f_c'}$$

$$= 0.056x1x1x\sqrt[3]{64900x0.0106x52} = 1.845\text{N/mm}^2$$

$$v_c = (0.19 + \frac{d\alpha}{b_o})[0.147\lambda\Phi_c \sqrt[3]{E_f \rho_f f_c'}]$$

$$= (0.19 + \frac{150.5x4}{1802})[0.147x1x1x\sqrt[3]{64900x0.0106x52}] = 2.539\text{N/mm}^2$$

$$v_c = (1 + \frac{2}{\beta_c})[0.028\lambda\Phi_c \sqrt[3]{E_f \rho_f f_c'}]$$

$$= (1 + \frac{2}{1})[0.028x1x1x\sqrt[3]{64900x0.0106x52}] = 2.768\text{N/mm}^2$$

The minimum shear stresses according to the code equations is 1.845 N/mm2

Fraction of unbalanced moment transferred:

$$\gamma_V = 1 - \frac{1}{1 + \frac{2}{3}\sqrt{\frac{b_1}{b2}}} = 0.4$$

Polar moment of inertia:

$$j = \frac{d(c_1 + d)^3}{6} + \frac{d^3(c_1 + d)^3}{6} + \frac{d^3(c_2 + d)(c_2 + d)^3}{2}$$

$j = 9429333893.8$ mm^4

Distance from center line to edge of critical section:

e = (c+d)/2 = (300+150.5)/2=225.25 mm

$$M_n = \frac{j}{\gamma_v e}(v_c - \frac{V_u}{b_o d_{av}})$$

$$= \frac{9429333893.8}{0.4x225.25}(1.845 - \frac{140}{1802x150.5}) = 139.109\text{KN.m}$$

Horizontal force lead to unbalanced moment $V_h = M_n / H = 139.109 / 1.35 = 103.0$ KN

Shear Capacity According to ACI 440.1 R–15.

$$n = \frac{E_f}{E_c} = \frac{64900}{4500\sqrt{52}} = 2$$

$$k = \sqrt{2\rho n + (\rho n)^2} - \rho n = 0.186$$

$$v_c = \frac{4}{5} kd\sqrt{f_c'} = \frac{4}{5} x0.186x150.5\sqrt{52} = 1.07\text{N/mm}^2$$

$$M_n = \frac{j}{\gamma_v e}(v_c - \frac{V_u}{b_o d_{av}})$$

$$= \frac{9429333893.8}{0.4x225.25}(1.07 - \frac{140}{1802x150.5}) = 58.172\text{KN.m}$$

Horizontal force lead to unbalanced moment $V_h = M_n / H = 58.172 / 1.35 = 43.1$ KN

GFRP–RC specimen (G2–with high reinforcement ratio)

Design for flexure according to CSA/S806–14

$d_x = h_s$ – cover – d_b / 2 = 200 – 30 – 19.5/2 = 160.5mm

$d_y = h_s$ – cover – d_b – d_b / 2 = 200 – 30 – 19.5 – 19.5/2 = 140.5mm.

$d_{av} = (d_x + d_y) / 2 = (160.5 + 140.5)/2 = 150.5$ mm.

$\alpha_1 = 0.85 - 0.0015 f_c' = 0.85 - 0.0015(46) = 0.781 \geq 0.67$

$\beta_1 = 0.97 - 0.0025 f_c' = 0.97 - 0.0025(46) = 0.855 \geq 0.67$

According to clause 8.4.2.3, the spacing between reinforcement shall not be greater than the minimum of three times the slab thickness (600 mm) or 300 mm. 20 Bars No.20 with spacing = 173mm were used as flexural reinforcement.

$$A_f = 20x285 = 5700mm^2 \geq A_{f\,\text{Min}} = \frac{400}{E_f} A_g = 3081.66mm^2$$

$$\rho_f = A_f / A_c = 5700 / (2500*150.5) = 0.0151(1.51\%)$$

From equilibrium and strain compatibility

$$\frac{\varepsilon_{cu}}{\varepsilon_{cu} + \varepsilon_{fu}} = \frac{c_b}{d} \rightarrow c_b = 21.77\text{mm}$$

$$C_u = T_u = \alpha_1 \beta_1 \Phi_c f_c' c_b b = \Phi_f f_{fu} A_{fb}$$

$$= 0.781x0.855x1x46x21.77x2500 = 1x1334xA_{fb}$$

$$A_{fb} = 1253.19mm^2$$

$\rho = 0.0151$ (1.51%) > $\rho_b = 0.0033$ (0.33%) (Compression failure)

According to CAS–S806 its recommend to design FRP members to be over reinforcement, in this case the concrete will crushing without rapture of the reinforcement and that will give a warning.

From equilibrium and strain compatibility

$$f_f = \frac{1}{2} E_f \varepsilon_{cu} \left(\sqrt{1 + \frac{4\alpha_1 \beta_1 \Phi_c f_c^{'}}{\rho_f \beta_1 \Phi_f E_f \varepsilon_{cu}}} - 1\right)$$
$$= 575.61 \text{N/mm}^2 \le f_{fu} = 1334 \text{N/mm}^2$$

$$C_{uf} = T_{uf} = \alpha_1 \beta_1 \Phi_c f_c^{'} cb = \Phi_f f_f A_f$$
$$= 0.781x0.855x1x1x46xcx2500 = 1x575.61x3990$$
$$c = 42.644mm$$

According to clause 8.4.1.4 concrete strain shall be assumed to have reached 0.0035 provided that the ratio of c/d satisfies the following equation:

$$\frac{c}{d} \ge \frac{7}{7 + 2000\varepsilon_{fu}} \rightarrow \frac{42.644}{150.5} = 0.28 \ge \frac{7}{7 + 2000x0.0207} = 0.145$$

$$M_r = C_u \left(d - \frac{c\beta_1}{2}\right)$$
$$= 0.781x0.855x1x46x42.644x2500\left(150.5 - \frac{0.855x42.644}{2}\right)$$
$$= 433.145KN.m$$

Shear Capacity According to CSA/S806–14.

Perimeter of critical section for shear: $b_o = 2\ (b_1 + b_2) = 2\ (450.50 + 450.50) = 1802$ mm

Factor to account for low–density concrete $\lambda = 1.0$

Factor accounting for shear resistance of cracked concrete: $\beta = b_1 / b_2 = 1.0$

$\alpha = 4.0$

Shear resistance attributed to the concrete factored by Φ_c:

$$v_c = 0.056\lambda\Phi_c \sqrt[3]{E_f \rho_f f_c'}$$
$$= 0.056x1x1x\sqrt[3]{64900x0.0151x46} = 1.995\text{N/mm}^2$$
$$v_c = (0.19 + \frac{d\alpha}{b_o})[0.147\lambda\Phi_c \sqrt[3]{E_f \rho_f f_c'}]$$
$$= (0.19 + \frac{150.5x4}{1802})[0.147x1x1x\sqrt[3]{64900x0.0151x46}] = 2.745\text{N/mm}^2$$
$$v_c = (1 + \frac{2}{\beta_c})[0.028\lambda\Phi_c \sqrt[3]{E_f \rho_f f_c'}]$$
$$= (1 + \frac{2}{1})[0.028x1x1x\sqrt[3]{64900x0.0151x46}] = 2.993\text{N/mm}^2$$

The minimum shear stresses according to the code equations is 1.995 N/mm2

Fraction of unbalanced moment transferred:

$$\gamma_V = 1 - \frac{1}{1 + \frac{2}{3}\sqrt{\frac{b_1}{b2}}} = 0.4$$

Polar moment of inertia:

$$j = \frac{d(c_1 + d)^3}{6} + \frac{d^3(c_1 + d)^3}{6} + \frac{d^3(c_2 + d)(c_2 + d)^3}{2}$$

j = 9429333893.8 mm^4

Distance from center line to edge of critical section:

e = (c+d)/2 = (300+150.5)/2=225.25 mm

$$M_n = \frac{j}{\gamma_v e}(v_c - \frac{V_u}{b_o d_{av}})$$
$$= \frac{9429333893.8}{0.4x225.25}(1.995 - \frac{140}{1802x150.5}) = 154.782\text{KN.m}$$

Horizontal force lead to unbalanced moment $V_h = M_n / H$ = 139.109 / 1.35 = 114.7 KN

Shear Capacity According to ACI 440.1 R–15.

$$n = \frac{E_f}{E_c} = \frac{64900}{4500\sqrt{46}} = 2.13$$
$$k = \sqrt{2\rho n + (\rho n)^2} - \rho n = 0.224$$
$$v_c = \frac{4}{5} kd\sqrt{f_c'} = \frac{4}{5} x0.224x150.5\sqrt{46} = 1.21\text{N/mm}^2$$

$$M_n = \frac{j}{\gamma_v e}(v_c - \frac{V_u}{b_o d_{av}})$$
$$= \frac{9429333893.8}{0.4x225.25}(1.21 - \frac{140}{1802x150.5}) = 72.973\text{KN.m}$$

Horizontal force lead to unbalanced moment $V_h = M_n / H = 72.973 / 1.35 = 54.1$ KN

GFRP–RC specimen (G3–subjected to high gravity load)

Design for flexure according to CSA/S806–14

$d_x = h_s$ – cover – d_b / 2 = 200 – 30 – 19.5/2 = 160.5mm

$d_y = h_s$ – cover – d_b – d_b / 2 = 200 – 30 – 19.5 – 19.5/2 = 140.5mm.

$d_{av} = (d_x + d_y) / 2 = (160.5 + 140.5)/2 = 150.5$ mm.

$\alpha_1 = 0.85 - 0.0015 f_c' = 0.85 - 0.0015(46) = 0.781 \geq 0.67$

$\beta_1 = 0.97 - 0.0025 f_c' = 0.97 - 0.0025(46) = 0.855 \geq 0.67$

According to clause 8.4.2.3, the spacing between reinforcement shall not be greater than the minimum of three times the slab thickness (600 mm) or 300 mm. 14 Bars No.20 with spacing = 173mm were used as flexural reinforcement.

$$A_f = 14x285 = 3990mm^2 \geq A_{f\,\text{Min}} = \frac{400}{E_f} A_g = 3081.66mm^2$$

$$\rho_f = A_f / A_c = 3990 / (2500 * 150.5) = 0.0106 (1.06\%)$$

From equilibrium and strain compatibility

$$\frac{\varepsilon_{cu}}{\varepsilon_{cu} + \varepsilon_{fu}} = \frac{c_b}{d} \rightarrow c_b = 21.77\text{mm}$$

$$C_u = T_u = \alpha_1 \beta_1 \Phi_c f_c' c_b b = \Phi_f f_{fu} A_{fb}$$
$$= 0.781x0.855x1x46x21.77x2500 = 1x1334xA_{fb}$$
$$A_{fb} = 1253.19mm^2$$

$\rho = 0.0106$ (1.06%) > $\rho_b = 0.0033$ (0.33%) (Compression failure)

According to CAS–S806 its recommend to design FRP members to be over reinforcement, in this case the concrete will crushing without rapture of the reinforcement and that will give a warning.

From equilibrium and strain compatibility

$$f_f = \frac{1}{2} E_f \varepsilon_{cu} \left(\sqrt{1 + \frac{4\alpha_1 \beta_1 \Phi_c f_c'}{\rho_f \beta_1 \Phi_f E_f \varepsilon_{cu}}} - 1\right)$$
$$= 705.65 \text{N/mm}^2 \le f_{fu} = 1334 \text{N/mm}^2$$

$$C_{uf} = T_{uf} = \alpha_1 \beta_1 \Phi_c f_c' cb = \Phi_f f_f A_f$$
$$= 0.781x0.855x1x1x46xcx2500 = 1x705.65x3990$$
$$c = 36.656mm$$

According to clause 8.4.1.4 concrete strain shall be assumed to have reached 0.0035 provided that the ratio of c/d satisfies the following equation:

$$\frac{c}{d} \ge \frac{7}{7 + 2000\varepsilon_{fu}} \rightarrow \frac{36.656}{150.5} = 0.244 \ge \frac{7}{7 + 2000x0.0207} = 0.145$$

$$M_r = C_u \left(d - \frac{c\beta_1}{2}\right)$$
$$= 0.781x0.855x1x46x36.656x2500\left(150.5 - \frac{0.855x36.656}{2}\right)$$
$$= 379.526KN.m$$

Shear Capacity According to CSA/S806–14.

Perimeter of critical section for shear: $b_o = 2\ (b_1 + b_2) = 2\ (450.50 + 450.50) = 1802$ mm

Factor to account for low–density concrete $\lambda = 1.0$

Factor accounting for shear resistance of cracked concrete: $\beta = b_1 / b_2 = 1.0$

$\alpha = 4.0$

Shear resistance attributed to the concrete factored by Φ_c:

$$v_c = 0.056\lambda\Phi_c \sqrt[3]{E_f \rho_f f_c'}$$
$$= 0.056x1x1x\sqrt[3]{64900x0.0106x46} = 1.772 \text{N/mm}^2$$

$$v_c = \left(0.19 + \frac{d\alpha}{b_o}\right)\left[0.147\lambda\Phi_c \sqrt[3]{E_f \rho_f f_c'}\right]$$
$$= \left(0.19 + \frac{150.5x4}{1802}\right)\left[0.147x1x1x\sqrt[3]{64900x0.0106x46}\right] = 2.437 \text{N/mm}^2$$

$$v_c = \left(1 + \frac{2}{\beta_c}\right)\left[0.028\lambda\Phi_c \sqrt[3]{E_f \rho_f f_c'}\right]$$
$$= \left(1 + \frac{2}{1}\right)\left[0.028x1x1x\sqrt[3]{64900x0.0106x46}\right] = 2.657 \text{N/mm}^2$$

The minimum shear stresses according to the code equations is 1.772 N/mm2

Fraction of unbalanced moment transferred:

$$\gamma_V = 1 - \frac{1}{1 + \frac{2}{3}\sqrt{\frac{b_1}{b2}}} = 0.4$$

Polar moment of inertia:

$$j = \frac{d(c_1 + d)^3}{6} + \frac{d^3(c_1 + d)^3}{6} + \frac{d^3(c_2 + d)(c_2 + d)^3}{2}$$

j = 9429333893.8 mm^4

Distance from center line to edge of critical section:

e = (c+d)/2 = (300+150.5)/2=225.25 mm

$$M_n = \frac{j}{\gamma_v e}(v_c - \frac{V_u}{b_o d_{av}})$$

$$= \frac{9429333893.8}{0.4x225.25}(1.772 - \frac{180}{1802x150.5}) = 115.940\text{KN.m}$$

Horizontal force lead to unbalanced moment $V_h = M_n / H$ = 115.940 / 1.35 = 85.90 KN

Shear Capacity According to ACI 440.1 R–15.

$$n = \frac{E_f}{E_c} = \frac{64900}{4500\sqrt{46}} = 2.13$$

$$k = \sqrt{2\rho n + (\rho n)^2} - \rho n = 0.191$$

$$v_c = \frac{4}{5} kd\sqrt{f_c'} = \frac{4}{5} x0.191x150.5\sqrt{46} = 1.04\text{N/mm}^2$$

$$M_n = \frac{j}{\gamma_v e}(v_c - \frac{V_u}{b_o d_{av}})$$

$$= \frac{9429333893.8}{0.4x225.25}(1.04 - \frac{180}{1802x150.5}) = 39.0\text{KN.m}$$

Horizontal force lead to unbalanced moment $V_h = M_n / H$ = 39.0 / 1.35 = 28.9 KN

GFRP–RC specimen (G4 – with high concrete compressive strength)

Design for flexure according to CSA/S806–14

$d_x = h_s$ – cover – d_b / 2 = 200 – 30 – 19.5/2 = 160.5mm

$d_y = h_s$ – cover – d_b – d_b / 2 = 200 – 30 – 19.5 – 19.5/2 = 140.5mm.

$d_{av} = (d_x + d_y) / 2$ = (160.5 + 140.5)/2 = 150.5 mm.

$\alpha_1 = 0.85 - 0.0015 f_c' = 0.85 - 0.0015(92) = 0.712 \geq 0.67$

$\beta_1 = 0.97 - 0.0025 f_c' = 0.97 - 0.0025(92) = 0.740 \geq 0.67$

According to clause 8.4.2.3, the spacing between reinforcement shall not be greater than the minimum of three times the slab thickness (600 mm) or 300 mm. 14 Bars No.20 with spacing = 173mm were used as flexural reinforcement.

$$A_f = 14x285 = 3990mm^2 \geq A_{f\,\mathrm{Min}} = \frac{400}{E_f} A_g = 3081.66mm^2$$

$$\rho_f = A_f / A_c = 3990/(2500*150.5) = 0.0106\,(1.06\%)$$

From equilibrium and strain compatibility

$$\frac{\varepsilon_{cu}}{\varepsilon_{cu} + \varepsilon_{fu}} = \frac{c_b}{d} \rightarrow c_b = 21.77\mathrm{mm}$$

$$C_u = T_u = \alpha_1 \beta_1 \Phi_c f_c^{'} c_b b = \Phi_f f_{fu} A_{fb}$$
$$= 0.712x0.740x1x92x21.77x2500 = 1x1334xA_{fb}$$
$$A_{fb} = 2002.61mm^2$$

ρ = 0.0106 (1.06%) > ρ_b = 0.0033 (0.53%) (Compression failure)

According to CAS–S806 its recommend to design FRP members to be over reinforcement, in this case the concrete will crushing without rapture of the reinforcement and that will give a warning.

From equilibrium and strain compatibility

$$f_f = \frac{1}{2} E_f \varepsilon_{cu} \left(\sqrt{1 + \frac{4\alpha_1 \beta_1 \Phi_c f_c^{'}}{\rho_f \beta_1 \Phi_f E_f \varepsilon_{cu}}} - 1\right)$$
$$= 911.92\mathrm{N/mm^2} \leq f_{fu} = 1334\mathrm{N/mm^2}$$

$$C_{uf} = T_{uf} = \alpha_1 \beta_1 \Phi_c f_c^{'} cb = \Phi_f f_f A_f$$
$$= 0.712x0.740x1x1x92xcx2500 = 1x911.92x3990$$
$$c = 30.018mm$$

According to clause 8.4.1.4 concrete strain shall be assumed to have reached 0.0035 provided that the ratio of c/d satisfies the following equation:

$$\frac{c}{d} \geq \frac{7}{7 + 2000\varepsilon_{fu}} \rightarrow \frac{30.018}{150.5} = 0.199 \geq \frac{7}{7 + 2000x0.0207} = 0.145$$

$$M_r = C_u(d - \frac{c\beta_1}{2})$$

$$= 0.712x0.740x1x92x30.018x2500(150.5 - \frac{0.740x30.018}{2})$$

$$= 507.067KN.m$$

Shear Capacity According to CSA/S806–14.

Perimeter of critical section for shear: $b_o = 2\ (b_1 + b_2) = 2\ (450.50 + 450.50) = 1802$ mm

Factor to account for low–density concrete $\lambda = 1.0$

Factor accounting for shear resistance of cracked concrete: $\beta = b_1 / b_2 = 1.0$

$\alpha = 4.0$

Shear resistance attributed to the concrete factored by Φ_c:

$$v_c = 0.056\lambda\Phi_c\sqrt[3]{E_f\rho_f f_c'}$$

$$= 0.056x1x1x\sqrt[3]{64900x0.0106x92} = 2.232\text{N/mm}^2$$

$$v_c = (0.19 + \frac{d\alpha}{b_o})[0.147\lambda\Phi_c\sqrt[3]{E_f\rho_f f_c'}]$$

$$= (0.19 + \frac{150.5x4}{1802})[0.147x1x1x\sqrt[3]{64900x0.0106x92}] = 3.071\text{N/mm}^2$$

$$v_c = (1 + \frac{2}{\beta_c})[0.028\lambda\Phi_c\sqrt[3]{E_f\rho_f f_c'}]$$

$$= (1 + \frac{2}{1})[0.028x1x1x\sqrt[3]{64900x0.0106x92}] = 3.348\text{N/mm}^2$$

The minimum shear stresses according to the code equations is 2.232 N/mm2

Fraction of unbalanced moment transferred:

$$\gamma_V = 1 - \frac{1}{1 + \frac{2}{3}\sqrt{\frac{b_1}{b2}}} = 0.4$$

Polar moment of inertia:

$$j = \frac{d(c_1 + d)^3}{6} + \frac{d^3(c_1 + d)^3}{6} + \frac{d^3(c_2 + d)(c_2 + d)^3}{2}$$

$j = 9429333893.8\ \text{mm}^4$

Distance from center line to edge of critical section:

$e = (c+d)/2 = (300+150.5)/2 = 225.25$ mm

$$M_n = \frac{j}{\gamma_v e}(v_c - \frac{V_u}{b_o d_{av}})$$
$$= \frac{9429333893.8}{0.4x225.25}(2.232 - \frac{140}{1802x150.5}) = 179.656\text{KN.m}$$

Horizontal force lead to unbalanced moment $V_h = M_n / H = 179.656 / 1.35 = 133.011$ KN

Shear Capacity According to ACI 440.1 R–15.

$$n = \frac{E_f}{E_c} = \frac{64900}{4500\sqrt{92}} = 1.50$$
$$k = \sqrt{2\rho n + (\rho n)^2} - \rho n = 0.163$$
$$v_c = \frac{4}{5} kd\sqrt{f_c'} = \frac{4}{5} x0.163x150.5\sqrt{92} = 1.25\text{N/mm}^2$$

$$M_n = \frac{j}{\gamma_v e}(v_c - \frac{V_u}{b_o d_{av}})$$
$$= \frac{9429333893.8}{0.4x225.25}(1.25 - \frac{140}{1802x150.5}) = 77.149\text{KN.m}$$

Horizontal force lead to unbalanced moment $V_h = M_n / H = 77.149 / 1.35 = 57.147$ KN

Appendix (B):

Flexural and Shear Capacity of Connections with FRP Shear Reinforcement

Design criteria:

Concrete properties:

Strain before crunching = 0.0035.

Clear cover = 30 mm.

Sand coated GFRP bars properties:

Modulus of elasticity = 64.9 GPa.

Ultimate tensile strength = 1334 MPa.

Bar diameter = 19.5 mm.

Bar area =285 mm^2.

Sand coated GFRP stirrups properties:

Ultimate tensile strength of the straight portion of the FRP stirrups = 504 MPa.

Modulus of elasticity of the straight portion of the FRP stirrups = 45000MPa.

Stirrups spacing = 75mm.

Stirrups diameter = 9.5 mm.

Bend radius = 40 mm.

Stirrups area = 71 mm^2.

GFRP–RC specimen (G5–GCS–4.5d)

Design for flexure according to CSA/S806–14

$d_x = h_s$ – cover – d_b / 2 = 200 – 30 – 19.5/2 = 160.5mm

$d_y = h_s$ – cover – d_b – d_b / 2 = 200 – 30 – 19.5 – 19.5/2 = 140.5mm.

$d_{av} = (d_x + d_y) / 2 = (160.5 + 140.5)/2 = 150.5$ mm.

$\alpha_1 = 0.85 - 0.0015 f_c' = 0.85 - 0.0015(45) = 0.783 \geq 0.67$

$\beta_1 = 0.97 - 0.0025 f_c' = 0.97 - 0.0025(45) = 0.858 \geq 0.67$

According to clause 8.4.2.3, the spacing between reinforcement shall not be greater than the minimum of three times the slab thickness (600 mm) or 300 mm. 14 Bars No.20 with spacing = 173mm were used as flexural reinforcement.

$$A_f = 14x285 = 3990mm^2 \geq A_{f\,\mathrm{Min}} = \frac{400}{E_f} A_g = 3081.66mm^2$$

$$\rho_f = A_f / A_c = 3990 / (2500 * 150.5) = 0.0106 (1.06\%)$$

From equilibrium and strain compatibility

$$\frac{\varepsilon_{cu}}{\varepsilon_{cu}+\varepsilon_{fu}}=\frac{c_b}{d}\rightarrow c_b=21.77\text{mm}$$

$$C_u=T_u=\alpha_1\beta_1\Phi_c f_c^{'}c_b b=\Phi_f f_{fu}A_{fb}$$
$$=0.783x0.858x1x45x21.77x2500=1x1334xA_{fb}$$
$$A_{fb}=1231.70mm^2$$

ρ = 0.0106 (1.06%) > ρ_b = 0.0033 (0.33%) (Compression failure)

According to CAS–S806 its recommend to design FRP members to be over reinforcement, in this case the concrete will crushing without rapture of the reinforcement and that will give a warning.

From equilibrium and strain compatibility

$$f_f=\frac{1}{2}E_f\varepsilon_{cu}(\sqrt{1+\frac{4\alpha_1\beta_1\Phi_c f_c^{'}}{\rho_f\beta_1\Phi_f E_f\varepsilon_{cu}}}-1)$$
$$=698.62\text{N/mm}^2\le f_{fu}=1334\text{N/mm}^2$$

$$C_{uf}=T_{uf}=\alpha_1\beta_1\Phi_c f_c^{'}cb=\Phi_f f_f A_f$$
$$=0.783x0.858x1x1x45xcx2500=1x698.62x3990$$
$$c=36.927mm$$

According to clause 8.4.1.4 concrete strain shall be assumed to have reached 0.0035 provided that the ratio of c/d satisfies the following equation:

$$\frac{c}{d}\ge\frac{7}{7+2000\varepsilon_{fu}}\rightarrow\frac{36.927}{150.5}=0.245\ge\frac{7}{7+2000x0.0207}=0.145$$

$$M_r=C_u(d-\frac{c\beta_1}{2})$$
$$=0.783x0.858x1x45x36.927x2500(150.5-\frac{0.858x36.927}{2})$$
$$=375.386KN.m$$

Shear Capacity According to CSA/S806–14.

<u>Inside the shear reinforcement zone</u>

Perimeter of critical section for shear: b_o = 2 (b_1+ b_2) = 2 (450.50 +450.50) =1802 mm

Factor to account for low–density concrete λ = 1.0

Factor accounting for shear resistance of cracked concrete: $\beta = b_1 / b_2$ = 1.0

α = 4.0

Shear resistance attributed to the concrete factored by Φ_c:

$$v_c = (1+\frac{2}{\beta_c})[0.028\lambda\Phi_c\sqrt[3]{E_f\rho_f f_c'}]$$

$$= (1+\frac{2}{1})[0.028x1x1x\sqrt[3]{64900x0.0106x45}] = 2.638\text{N/mm}^2$$

Shear resistance from shear reinforcements:

$$f_{fv} = 0.004\ E_{fv} = 180\text{N/mm}^2$$

$$f_{fv} = \frac{(0.05\, r_b / d_b + 0.3)\, f_{fv}}{1.5} = 171.537 \le f_{fbend}$$

$$v_{sf} = \frac{A_f\ \phi_f\ f_{fv}}{b_o\ S_{fv}} = 1.44\text{N/mm}^2$$

The Total shear resistance from shear reinforcements and concrete

$$v_r = 0.5\ v_c + v_s = 2.759\text{N/mm}^2$$

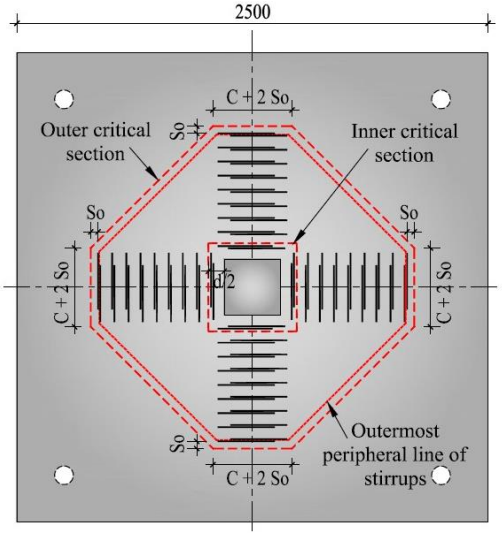

Fraction of unbalanced moment transferred:

$$\gamma_V = 1 - \frac{1}{1+\frac{2}{3}\sqrt{\frac{b_1}{b2}}} = 0.4$$

Polar moment of inertia:

$$j = \frac{d(c_1+d)^3}{6} + \frac{d^3(c_1+d)^3}{6} + \frac{d^3(c_2+d)(c_2+d)^3}{2}$$

j = 9429333893.8 mm^4

Distance from center line to edge of critical section:

e = (c+d)/2 = (300+150.5)/2=225.25 mm

$$M_n = \frac{j}{\gamma_v e}(v_c - \frac{V_u}{b_o d_{av}})$$
$$= \frac{9429333893.8}{0.4x225.25}(2.759 - \frac{140}{1802x150.5}) = 234.716\text{KN.m}$$

Horizontal force lead to unbalanced moment $V_h = M_n / H$ = 234.716 / 1.35 = 173.864 KN

Outside the shear reinforcement zone

Perimeter of critical section for shear at distance 4.5d:

b = 5348 mm

$$j = \frac{d}{3}\sum length(x_i^2 + x_i x_j + x_j^2) = 3.57x10^{11} mm^4$$

$$v_c = (1 + \frac{2}{\beta_c})[0.028\lambda\Phi_c \sqrt[3]{E_f \rho_f f_c'}]$$
$$= (1 + \frac{2}{1})[0.028x1x1x\sqrt[3]{64900x0.0106x45}] = 2.638\text{N/mm}^2$$

$$M_n = \frac{j}{\gamma_v e}(v_c - \frac{V_u}{b_o d_{av}})$$
$$= \frac{3.57x10^{11}}{0.4x858}(2.638 - \frac{140}{5348x150.5}) = 119.83\text{KN.m}$$

Horizontal force lead to unbalanced moment $V_h = M_n / H$ = 119.83 / 1.35 = 88.764 KN

Shear Capacity According to ACI 440.1 R–15.

Inside the shear reinforcement zone

$$n = \frac{E_f}{E_c} = \frac{64900}{4500\sqrt{45}} = 2.15$$
$$k = \sqrt{2\rho n + (\rho n)^2} - \rho n = 0.192$$
$$v_c = \frac{2}{5} kd\sqrt{f_c'} = \frac{2}{5} x0.192x150.5\sqrt{45} = 0.52\text{N/mm}^2$$

Shear resistance from shear reinforcements:

$$f_{fv} = 0.004\ E_{fv} = 180\text{N/mm}^2$$
$$f_{fv} = \frac{(0.05 r_b / d_b + 0.3)\ f_{fv}}{1.5} = 171.537 \le f_{fbend}$$
$$v_{sf} = \frac{A_f\ \phi_f\ f_{fv}}{b_o\ S_{fv}} = 1.44\text{N/mm}^2$$

$$M_n = \frac{j}{\gamma_v e}(v_c - \frac{V_u}{b_o d_{av}})$$
$$= \frac{9429333893.8}{0.4x225.25}(1.96 - \frac{140}{1802x150.5}) = 150.58\text{KN.m}$$

Horizontal force lead to unbalanced moment $V_h = M_n / H = 150.58 / 1.35 = 111.54$ KN

Outside the shear reinforcement zone

$$M_n = \frac{j}{\gamma_v e}(v_c - \frac{V_u}{b_o d_{av}})$$
$$= \frac{3.57x10^{11}}{0.4x858}(0.53 - \frac{140}{5348x150.5}) = 35.69\text{KN.m}$$

Horizontal force lead to unbalanced moment $V_h = M_n / H = 35.69 / 1.35 = 26.4$ KN

GFRP–RC specimen (G6–GCS–2d)

Design for flexure according to CSA/S806–14

$d_x = h_s$ – cover – d_b / 2 = 200 – 30 – 19.5/2 = 160.5mm

$d_y = h_s$ – cover – d_b – d_b / 2 = 200 – 30 – 19.5 – 19.5/2 = 140.5mm.

$d_{av} = (d_x + d_y) / 2 = (160.5 + 140.5)/2 = 150.5$ mm.

$\alpha_1 = 0.85 - 0.0015 f_c' = 0.85 - 0.0015(45) = 0.783 \geq 0.67$

$\beta_1 = 0.97 - 0.0025 f_c' = 0.97 - 0.0025(45) = 0.858 \geq 0.67$

According to clause 8.4.2.3, the spacing between reinforcement shall not be greater than the minimum of three times the slab thickness (600 mm) or 300 mm. 14 Bars No.20 with spacing = 173mm were used as flexural reinforcement.

$$A_f = 14x285 = 3990mm^2 \geq A_{f\,\text{Min}} = \frac{400}{E_f} A_g = 3081.66mm^2$$

$$\rho_f = A_f / A_c = 3990 / (2500 * 150.5) = 0.0106 (1.06\%)$$

From equilibrium and strain compatibility

$$\frac{\varepsilon_{cu}}{\varepsilon_{cu} + \varepsilon_{fu}} = \frac{c_b}{d} \rightarrow c_b = 21.77\text{mm}$$

$$C_u = T_u = \alpha_1 \beta_1 \Phi_c f_c' c_b b = \Phi_f f_{fu} A_{fb}$$
$$= 0.783x0.858x1x45x21.77x2500 = 1x1334xA_{fb}$$
$$A_{fb} = 1231.70mm^2$$

$\rho = 0.0106$ (1.06%) > $\rho_b = 0.0033$ (0.33%) (Compression failure)

According to CAS–S806 its recommend to design FRP members to be over reinforcement, in this case the concrete will crushing without rapture of the reinforcement and that will give a warning.

From equilibrium and strain compatibility

$$f_f = \frac{1}{2} E_f \varepsilon_{cu} \left(\sqrt{1 + \frac{4\alpha_1 \beta_1 \Phi_c f_c^{'}}{\rho_f \beta_1 \Phi_f E_f \varepsilon_{cu}}} - 1\right)$$

$$= 698.62 \text{N/mm}^2 \leq f_{fu} = 1334 \text{N/mm}^2$$

$$C_{uf} = T_{uf} = \alpha_1 \beta_1 \Phi_c f_c^{'} cb = \Phi_f f_f A_f$$

$$= 0.783x0.858x1x1x45xcx2500 = 1x698.62x3990$$

$$c = 36.927mm$$

According to clause 8.4.1.4 concrete strain shall be assumed to have reached 0.0035 provided that the ratio of c/d satisfies the following equation:

$$\frac{c}{d} \geq \frac{7}{7 + 2000\varepsilon_{fu}} \rightarrow \frac{36.927}{150.5} = 0.245 \geq \frac{7}{7 + 2000x0.0207} = 0.145$$

$$M_r = C_u \left(d - \frac{c\beta_1}{2}\right)$$

$$= 0.783x0.858x1x45x36.927x2500\left(150.5 - \frac{0.858x36.927}{2}\right)$$

$$= 375.386KN.m$$

Shear Capacity According to CSA/S806–14.

<u>Inside the shear reinforcement zone</u>

Perimeter of critical section for shear: $b_o = 2\ (b_1 + b_2) = 2\ (450.50 + 450.50) = 1802$ mm

Factor to account for low–density concrete $\lambda = 1.0$

Factor accounting for shear resistance of cracked concrete: $\beta = b_1 / b_2 = 1.0$

$\alpha = 4.0$

Shear resistance attributed to the concrete factored by Φ_c:

$$v_c = \left(1 + \frac{2}{\beta_c}\right)\left[0.028\lambda\Phi_c \sqrt[3]{E_f \rho_f f_c^{'}}\right]$$

$$= \left(1 + \frac{2}{1}\right)\left[0.028x1x1x\sqrt[3]{64900x0.0106x45}\right] = 2.638 \text{N/mm}^2$$

Shear resistance from shear reinforcements:

$$f_{fv} = 0.004 \; E_{fv} = 180 \text{N/mm}^2$$

$$f_{fv} = \frac{(0.05\, r_b / d_b + 0.3)\, f_{fv}}{1.5} = 171.537 \leq f_{fbend}$$

$$v_{sf} = \frac{A_f \; \phi_f \; f_{fv}}{b_o \; S_{fv}} = 1.44 \text{N/mm}^2$$

The Total shear resistance from shear reinforcements and concrete

$$v_r = \; 0.5 \; v_c \; + \; v_s = 2.759 \text{N/mm}^2$$

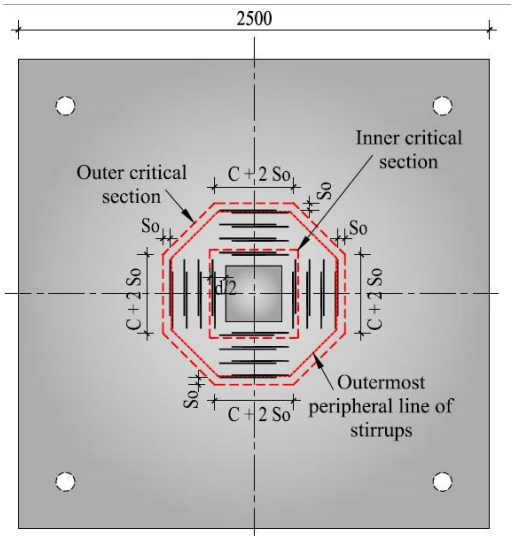

Fraction of unbalanced moment transferred:

$$\gamma_V = 1 - \frac{1}{1 + \frac{2}{3}\sqrt{\frac{b_1}{b2}}} = 0.4$$

Polar moment of inertia:

$$j = \frac{d(c_1 + d)^3}{6} + \frac{d^3(c_1 + d)^3}{6} + \frac{d^3(c_2 + d)(c_2 + d)^3}{2}$$

j = 9429333893.8 mm^4

Distance from center line to edge of critical section:

e = (c+d)/2 = (300+150.5)/2=225.25 mm

$$M_n = \frac{j}{\gamma_v e}(v_c - \frac{V_u}{b_o d_{av}})$$

$$= \frac{9429333893.8}{0.4x225.25}(2.759 - \frac{140}{1802x150.5}) = 234.716 \text{KN.m}$$

Horizontal force lead to unbalanced moment $V_h = M_n / H$ = 234.716 / 1.35 = 173.864 KN

Outside the shear reinforcement zone

Perimeter of critical section for shear at distance 4.5d:

b = 5348 mm

$$j = \frac{d}{3}\sum length(x_i^2 + x_i x_j + x_j^2) = 490233331541.25mm^4$$

$$v_c = (1+\frac{2}{\beta_c})[0.028\lambda\Phi_c\sqrt[3]{E_f \rho_f f_c^{'}}]$$

$$= (1+\frac{2}{1})[0.028x1x1x\sqrt[3]{64900x0.0106x45}] = 2.638\text{N/mm}^2$$

$$M_n = \frac{j}{\gamma_v e}(v_c - \frac{V_u}{b_o d_{av}})$$

$$= \frac{490233331541.25}{0.4x483}(2.638 - \frac{140}{5348x150.5}) = 107.839\text{KN.m}$$

Horizontal force lead to unbalanced moment $V_h = M_n / H$ = 107.839 / 1.35 = 79.88 KN

Shear Capacity According to ACI 440.1 R–15.

Inside the shear reinforcement zone

$$n = \frac{E_f}{E_c} = \frac{64900}{4500\sqrt{45}} = 2.15$$

$$k = \sqrt{2\rho n + (\rho n)^2} - \rho n = 0.192$$

$$v_c = \frac{2}{5} kd\sqrt{f_c^{'}} = \frac{2}{5} x0.192x150.5\sqrt{45} = 0.52\text{N/mm}^2$$

Shear resistance from shear reinforcements:

$$f_{fv} = 0.004\ E_{fv} = 180\text{N/mm}^2$$

$$f_{fv} = \frac{(0.05 r_b / d_b + 0.3)\ f_{fv}}{1.5} = 171.537 \le f_{fbend}$$

$$v_{sf} = \frac{A_f\ \phi_f\ f_{fv}}{b_o\ S_{fv}} = 1.44\text{N/mm}^2$$

$$M_n = \frac{j}{\gamma_v e}(v_c - \frac{V_u}{b_o d_{av}})$$

$$= \frac{9429333893.8}{0.4x225.25}(1.96 - \frac{140}{1802x150.5}) = 150.58\text{KN.m}$$

Horizontal force lead to unbalanced moment $V_h = M_n / H$ = 150.58 / 1.35 = 1117.54 KN

Outside the shear reinforcement zone

$$M_n = \frac{j}{\gamma_v e}(v_c - \frac{V_u}{b_o d_{av}})$$
$$= \frac{490233331541}{0.4x483}(0.53 - \frac{140}{3224x150.5}) = 23.70\text{KN.m}$$

Horizontal force lead to unbalanced moment $V_h = M_n / H = 23.70 / 1.35 = 17.55$ KN

GFRP–RC specimen (G8–GCS–4.5d with high gravity load)

Design for flexure according to CSA/S806–14

$d_x = h_s$ – cover – d_b / 2 = 200 – 30 – 19.5/2 = 160.5mm

$d_y = h_s$ – cover – d_b – d_b / 2 = 200 – 30 – 19.5 – 19.5/2 = 140.5mm.

$d_{av} = (d_x + d_y) / 2 = (160.5 + 140.5)/2 = 150.5$ mm.

$\alpha_1 = 0.85 - 0.0015 f_c' = 0.85 - 0.0015(51) = 0.774 \geq 0.67$

$\beta_1 = 0.97 - 0.0025 f_c' = 0.97 - 0.0025(51) = 0.843 \geq 0.67$

According to clause 8.4.2.3, the spacing between reinforcement shall not be greater than the minimum of three times the slab thickness (600 mm) or 300 mm. 14 Bars No.20 with spacing = 173mm were used as flexural reinforcement.

$$A_f = 14x285 = 3990mm^2 \geq A_{f\,\text{Min}} = \frac{400}{E_f} A_g = 3081.66mm^2$$

$$\rho_f = A_f / A_c = 3990 / (2500*150.5) = 0.0106(1.06\%)$$

From equilibrium and strain compatibility

$$\frac{\varepsilon_{cu}}{\varepsilon_{cu} + \varepsilon_{fu}} = \frac{c_b}{d} \rightarrow c_b = 21.77\text{mm}$$

$$C_u = T_u = \alpha_1 \beta_1 \Phi_c f_c' c_b b = \Phi_f f_{fu} A_{fb}$$
$$= 0.774x0.843x1x51x21.77x2500 = 1x1334xA_{fb}$$
$$A_{fb} = 1355.73mm^2$$

$\rho = 0.0106$ (1.06%) > $\rho_b = 0.0033$ (0.36%) (Compression failure)

According to CAS–S806 its recommend to design FRP members to be over reinforcement, in this case the concrete will crushing without rapture of the reinforcement and that will give a warning.

From equilibrium and strain compatibility

$$f_f = \frac{1}{2} E_f \varepsilon_{cu} \left(\sqrt{1 + \frac{4\alpha_1 \beta_1 \Phi_c f_c^{'}}{\rho_f \beta_1 \Phi_f E_f \varepsilon_{cu}}} - 1\right)$$
$$= 737.77/\text{mm}^2 \le f_{fu} = 1334\text{N/mm}^2$$

$$C_{uf} = T_{uf} = \alpha_1 \beta_1 \Phi_c f_c^{'} cb = \Phi_f f_f A_f$$
$$= 0.774x0.843x1x1x51xcx2500 = 1x737.77x3990$$
$$c = 35.429mm$$

According to clause 8.4.1.4 concrete strain shall be assumed to have reached 0.0035 provided that the ratio of c/d satisfies the following equation:

$$\frac{c}{d} \ge \frac{7}{7 + 2000\varepsilon_{fu}} \rightarrow \frac{35.429}{150.5} = 0.235 \ge \frac{7}{7 + 2000x0.0207} = 0.145$$

$$M_r = C_u \left(d - \frac{c\beta_1}{2}\right)$$
$$= 0.774x0.843x1x51x35.429x2500\left(150.5 - \frac{0.843x35.429}{2}\right)$$
$$= 399.1KN.m$$

Shear Capacity According to CSA/S806–14.

<u>Inside the shear reinforcement zone</u>

Perimeter of critical section for shear: b_o = 2 (b_1+ b_2) = 2 (450.50 +450.50) =1802 mm

Factor to account for low–density concrete λ = 1.0

Factor accounting for shear resistance of cracked concrete: $\beta = b_1 / b_2$ = 1.0

α = 4.0

Shear resistance attributed to the concrete factored by Φ_c:

$$v_c = \left(1 + \frac{2}{\beta_c}\right)\left[0.028\lambda\Phi_c \sqrt[3]{E_f \rho_f f_c^{'}}\right]$$
$$= \left(1 + \frac{2}{1}\right)\left[0.028x1x1x\sqrt[3]{64900x0.0106x51}\right] = 2.750\text{N/mm}^2$$

Shear resistance from shear reinforcements:

$$f_{fv} = 0.004\ E_{fv} = 180\text{N/mm}^2$$
$$f_{fv} = \frac{(0.05 r_b / d_b + 0.3)\ f_{fv}}{1.5} = 171.537 \le f_{fbend}$$
$$v_{sf} = \frac{A_f\ \phi_f\ f_{fv}}{b_o\ S_{fv}} = 1.44\text{N/mm}^2$$

The Total shear resistance from shear reinforcements and concrete

$$v_r = 0.5\, v_c + v_s = 2.815 \text{N/mm}^2$$

Fraction of unbalanced moment transferred:

$$\gamma_V = 1 - \frac{1}{1 + \frac{2}{3}\sqrt{\frac{b_1}{b2}}} = 0.4$$

Polar moment of inertia:

$$j = \frac{d(c_1 + d)^3}{6} + \frac{d^3(c_1 + d)^3}{6} + \frac{d^3(c_2 + d)(c_2 + d)^3}{2}$$

j = 9429333893.8 mm^4

Distance from center line to edge of critical section:

e = (c+d)/2 = (300+150.5)/2=225.25 mm

$$M_n = \frac{j}{\gamma_v e}(v_c - \frac{V_u}{b_o d_{av}})$$

$$= \frac{9429333893.8}{0.4x225.25}(2.815 - \frac{180}{1802x150.5}) = 225.161\text{KN.m}$$

Horizontal force lead to unbalanced moment $V_h = M_n / H$ = 225.161 / 1.35 = 166.786 KN

Outside the shear reinforcement zone

Perimeter of critical section for shear at distance 4.5d:

b = 5348 mm

$$j = \frac{d}{3}\sum length(x_i^2 + x_i x_j + x_j^2) = 3.57x10^{11} mm^4$$

$$v_c = (1 + \frac{2}{\beta_c})[0.028\lambda\Phi_c \sqrt[3]{E_f \rho_f f_c^{'}}]$$

$$= (1 + \frac{2}{1})[0.028x1x1x\sqrt[3]{64900x0.0106x51}] = 2.75\text{N/mm}^2$$

$$M_n = \frac{j}{\gamma_v e}(v_c - \frac{V_u}{b_o d_{av}})$$

$$= \frac{3.57x10^{11}}{0.4x858}(2.75 - \frac{180}{5348x150.5}) = 120.51\text{KN.m}$$

Horizontal force lead to unbalanced moment $V_h = M_n / H$ = 120.51 / 1.35 = 89.268 KN

Shear Capacity According to ACI 440.1 R–15.

Inside the shear reinforcement zone

$$n = \frac{E_f}{E_c} = \frac{64900}{4500\sqrt{51}} = 2.02$$

$$k = \sqrt{2\rho n + (\rho n)^2} - \rho n = 0.187$$

$$v_c = \frac{2}{5} kd\sqrt{f_c'} = \frac{2}{5} x0.187x150.5\sqrt{51} = 0.53\text{N/mm}^2$$

Shear resistance from shear reinforcements:

$$f_{fv} = 0.004 \; E_{fv} = 180\text{N/mm}^2$$

$$f_{fv} = \frac{(0.05 r_b / d_b + 0.3) f_{fv}}{1.5} = 171.537 \le f_{fbend}$$

$$v_{sf} = \frac{A_f \; \phi_f \; f_{fv}}{b_o \; S_{fv}} = 1.44\text{N/mm}^2$$

$$M_n = \frac{j}{\gamma_v e}(v_c - \frac{V_u}{b_o d_{av}})$$

$$= \frac{9429333893.8}{0.4x225.25}(1.97 - \frac{180}{1802x150.5}) = 137.04\text{KN.m}$$

Horizontal force lead to unbalanced moment $V_h = M_n / H$ = 137.04 / 1.35 = 101.51 KN

Outside the shear reinforcement zone

$$M_n = \frac{j}{\gamma_v e}(v_c - \frac{V_u}{b_o d_{av}})$$

$$= \frac{3.57x10^{11}}{0.4x858}(0.53 - \frac{180}{5348x150.5}) = 32.39\text{KN.m}$$

Horizontal force lead to unbalanced moment $V_h = M_n / H$ = 32.39 / 1.35 = 23.99 KN